Diffraction résonnante des rayons X dans des systèmes multiferroïques

Marta Ainhoa Elzo Aizarna

► **To cite this version:**

UNIVERSITÉ DE GRENOBLE

THÈSE

Pour obtenir le grade de

DOCTEUR DE L'UNIVERSITÉ DE GRENOBLE

Spécialité : **Physique de la Matière Condensée et du Rayonnement**

Arrêté ministériel : 7 août 2006

Présentée par

Marta ELZO AIZARNA

Thèse dirigée par **Jean-Marc TONNERRE**
codirigée par **Stéphane GRENIER** et **Nicolas JAOUEN**

préparée au sein du **Laboratoire MCMF – Institut Néel – CNRS**
et de la **ligne SEXTANTS – synchrotron SOLEIL**
dans **l'École Doctorale de Physique de Grenoble**

Etudes de systèmes multiferroïques nanostructurés par la diffraction résonante des rayons X

Thèse soutenue publiquement le **28 septembre 2012**,
devant le jury composé de :

M. Michel VIRET
Directeur de Recherche, CEA-Saclay, Rapporteur
M. Sylvain RAVY
Directeur de Recherche, Synchrotron SOLEIL, Rapporteur
Mme Sophie De Brion
Maître de Conférence, Institut Néel Université Joseph Fourier, Examinatrice
M. Jean-Marc TONNERRE
Directeur de Recherche, Institut Néel, Membre
M. Stéphane GRENIER
Chargé de Recherche, Institut Néel, Membre
M. Nicolas JAOUEN
Chargé de Recherche, Synchrotron SOLEIL, Membre

Université Joseph Fourier / Université Pierre Mendès France /
Université Stendhal / Université de Savoie / Grenoble INP

Remerciements

J'ai remercie mes rapporteurs de thèse Michel Viret et Sylvain Ravy pour avoir accepté d'évaluer mon travaille de thèse. J'ai remercie aussi Sophie de Brion pour avoir été l'examinatrice de thèse et pour les conseils sur la manganites.

Stéphane Grener et Nicolas Jaouen, merci pour avoir été mes directeurs de thèse. Stéphane merci beaucoup pour avoir eu toujours ta porte ouvert pour mes questions, et pour m'avoir introduire dans cette monde de synchrotroniste. Nico, merci pour m'avoir faire découvrir les différent s synchrotrons europèens et leur alentours (des traversés á travers des champs dans la campagne anglaise pour arriver dans un pub par exemple). Je voudrais remercier aussiJean Marc Tonnerre pour son énergie et son enthousiasme lors de nos travaills sur RESOXS et ses conseils expérimentaux.

Je remercie également tout les membres du département MCMF et des lignes synchrotron ou j'ai travaillé. Je tiens un souvenir spéciale pour l'équipe SIN, pour m'avoir accueillir ses trois années, et pour nos bonnes moments à la cafet avec des croisants les lundis matin. Je voudrais spécialement remercier Yves Joly ainsi que Oana Bunao lors des mes simulation avec le programme FDMNES. Je remercie le SERAS et Stéphanie Garaudée pour leur aide lors de mon travaille sur RESOXS. Merci aussi à Frédérique Gay et Jaques Marcus pour leur soutienne avec mes mesures de résistivité. J'ai garde aussi à remercier les personnel de SOLEIL pour avoir organiser tous mes ordres de missions au dernière moment et les personnes de la ligne SEXANTS toujours pour une accueille si chaloreuse. J'ai voudrais remercier Silvana Mercone pour son énergie et aide lors de nos expériences sur les films minces de manganites. Sans toi ses manips auront pas étés les mêmes.

Il faut à tout prix que je salue les thésardes et stagiaires qui m'on accompagnée ses dernières trois années. Emmanuelle Jal pour nos discussions discussions sur tout et de rien et sur pourquoi nous avons décidé de faire une thèse sur une telle technique. A Vinicius pour avoir apporté ton coté internationalle et á ta femme pour m'avoir apporté de si bon gâteaux.... Cécile pour m'avoir aidé la première année et m'avoir expliquer le fonctionnement du labo. Il faut pas que j'ai oublie les 'vieux' ceux qui été lors de mon première année, Simon, Pierre, Isaam, Marcio... vos conversations sont uniques.... Et bien sur les 'nouveaux', Anne, Mehdi, Vincent, Adrien, Josephine... Nous avons partagé des très bons moments, à la cafet, à H2, nos conversations sur le points des plats, nos bières de mercredi, et nos sortie de kayak, ski.... Sans une groupe comme cela la thèse aura pas été pareille.

Je ne peux pas oublier la famille, mes parents pour leur soutien téléphonique ces trois années et m'avoir encouragé tout le long des mesétudes. Je doit pas

oublier mes amies grenobloises, Mélisa, Emilie, le groupe Basque-Espagnole, c'est toujours bien de retrouver un petit chez soir à des kilometres de chez soi.

Et en fin je peux pas finir cette page sans remercier Tristan, pour avoir été a coté de moi, pour avoir supporter la Marta électrique les dernières jours de rédaction, eskerrikasko maitia.

0

Contents

Chapter 1

Résumé en Français

Dans ce travail de thèse nous avons étudié des systèmes multiferroïques. Ces systèmes montrent plusieurs ordres (ferromagnétique (FM), ferroélectrique (FE), antiferromagnétiques (AFM)). Une des motivations principales pour l'étude de ces types de systèmes est la possibilité d'utiliser le couplage magnétoélectrique pour contrôler un axe facile d'aimantation avec un champ électrique. Pour cela il est nécessaire d'avoir un matériau ferromagnétique couplé avec un système ferroélectrique. On peut l'obtenir de différentes manières: en utilisant un système multiferroïque dont les deux ordres coexistent, ou en couplant un matériau ferromagnétique avec un ferroélectrique formant alors un multiferroïque composite. Les propriétés des ses composés sont assez complexes et il n'y pas beaucoup de méthodes expérimentales qui permettent de les étudier. La diffusion résonante des rayons X est une technique qui permet de résoudre les structures électroniques et atomiques de ces systèmes, tel qu'il est expliqué dans ce manuscrit. La diffraction résonante des rayons X combine la spectroscopie et la diffraction, offrant ainsi une sélectivité chimique et une sélectivité spatiale. Cette thèse est un travail expérimental de recherche fondamentale qui a pour but d'explorer la faisabilité d'expériences de diffraction résonante sur des systèmes multiferroïques.

Ce manuscrit et divisé en plusieurs chapitres:

Introduction

Le premier chapitre est une introduction qui place dans son contexte le travail de cette thèse, et présente les éléments qui l'ont motivé.

La diffusion resonante des rayons X

Ce chapitre est dedié à l'aspect fondamental de l'interaction rayons X - matière. Quelques conventions sont d'abord introduites, notamment sur la polarisation des photons. Un traitement quantique de la diffusion résonante

est développé, et en particulier le développement multipolaire de l'amplitude de diffusion dans la base linéaire et circulaire de la polarisation du photon, pour des systèmes magnétiques et des systèmes avec une anisotropie uniaxiale. Pour ces derniers, à partir du facteur de diffusion on donne une expression analytique des ratio d'anisotropie pour les polarisations linéaire et circulaire.

Reflectivité résonante

La réflectivité est une technique qui permet d'étudier des systèmes stratifiés, faire des reconstructions électroniques aux interfaces et résoudre des empilements magnétiques. Dans ce travail, nous avons developpé un formalisme optimisé pour la simulation de la réflectivité résonante. Nous avons développé un formalisme de matrices de propagation aux interfaces dans une base d'ondes propres. Avec cette approche, la matrice de propagation est très simple ce qui fait que les calculs matriciels pour résoudre les problèmes de réflectivité deviennent plus faciles. Ce formalisme a été développé pour deux types de systèmes: des couches minces magnétiques et des systèmes avec une anisotropie uniaxiale. Pour le premier cas nous montrons un exemple d'application, et pour le deuxième cas nous proposons des systèmes sur lesquels ce formalisme pourrait être utilisé.

Films minces de $PbTiO_3$

Un multiferroïque composite peut être formé par l'assemblage d'un film mince ferroélectrique et d'un film mince magnétique. Nous avons ainsi étudié $PbTiO_3$ (PTO) sur $DyScO_3$. Dans PTO, la ferroélectricité est dûe à des déplacements relatifs des atomes au sein de la maille cristalline. L'absorption des rayons X au seuil K de l'atome de transition (dans notre cas le Ti) s'avère être une bonne sonde pour l'étude de la ferroélectricité dans le cas de cristaux massifs. Par contre, dans des films minces, des domaines de tailles nanométriques apparaissent dûs aux contraintes induites par le substrat dans la couche ferroélectrique. La diffraction résonante au seuil K du Ti en géométrie rasante est alors la technique idéale pour résoudre la ferroélectricité dans de tels films minces. Des mesures expérimentales sont combinées avec des simulations FDMNES. Les mesures ont été effectuées dans des lignes de lumière synchrotron au seuil K du Ti (domaine des X durs). Afin de tenir compte de la structure en domaines lors des simulations, le programme FDMES est exécuté sur des macro-cellules de plusieurs cellules unitaires chacune.

Couplage entre un cristal massif de BiFeO$_3$ et un film mince ferro-magnétique (Co)

BiFeO$_3$ est le seul système multiferroïque qui montre les deux ordres (magnétique et électrique) à température ambiante. L'ordre magnétique apparaît sous forme de cycloïde antiferromagnétique avec une periodicité de 64 nm. Dans des cristaux massifs de BFO, pour une polarisation ferroélectrique donnée, trois cycloïdes antiferromagnétiques peuvent se propager. Nous avons étudié des monocristaux mono-domaines ferroélectriques et multi-domaines ferroélectriques. Pour une éventuelle application au stockage de données, un film mince de Co est déposé sur le BFO, afin d'étudier l'effet que la cyloïde antiferromagnétique a sur l'ordre ferromagnétique du Co. Sur des cristaux mono-domaine FE, nous avons utilisé la diffraction résonante aux petits angles pour étudier l'influence de la cycloïde sur la couche ferromagnétique. On s'attend à voir la cycloïde créer une structure en forme de $zig - zag$ dans la couche de Co. En conditions de diffraction résonante, le signal de cette structure doit apparaître sous forme de pics satellites à côté du pic spéculaire. L'observation de ces pics aux seuils L$_{2,3}$ du Co et L$_{2,3}$ du Fe montre effectivement qu'une telle structure existe dans le Co. Des études en température montrent bien la corrélation des pics satellites du Co et du Fe, ce qui apporte donc une confirmation de l'existence d'un couplage avec la cycloïde présente dans le BFO. Nous avons aussi effectué des simulations qui ont permis d'expliquer nos mesures et qui montrent la propagation des cycloïdes. Simulations et mesures coïncident seulement en supposant la présence simultanée de différentes cycloïdes. De nouveaux axes de recherche sont alors ouverts: l'étude de ce système sous champ magnétique et électrique appliqués.

Pour des cristaux multi-domaines FE, une autre approche a été utilisée: la microscopie électronique par photoémission (PEEM). Cette technique est sensible au magnétisme et à la ferroélectricité via la polarisation (circulaire ou linéaire) des photons incidents. Appliquée à des échantillons multi-domaines FE, on montre une corrélation entre les domaines FE et AFM, et aussi le fait que plusieurs domaines AFM coexistent dans un même domaine FE.

Films minces de PrCaMnO$_3$

Cette partie est consacrée à l'étude de films minces de PrCaMO$_3$ (PCMO) sur LaAlO$_3$. Ce système présente un ordre de charge qui a été la motivation de ce travail. D'un côté l'ordre de charge pourrait créer un moment ferroélectrique et ainsi former un nouveau type de système multiferroïque ; d'un autre côté cet ordre de charge pourrait être un cas particulier d'onde de densité de charge (CDW). Dans cette approche, nous avons étudié le com-

portement de films minces de PCMO sous un courant électrique appliqué. La diffraction résonante des rayons X au seuil K du Mn se révèle être une bonne méthode pour l'étude des ordres de charges dans de tels systèmes. Nos résulats expérimentaux sont intrigants: on observe différents comportements selon différentes réflections. À ce stade, nous attribuons ces variations de comportement à une possible mixité de phase, chaque phase répondant différemment à l'application d'un courant électrique.

Outils expérimentaux

En dernière partie, le lecteur trouvera un résumé des différentes lignes de lumière où il est possible de conduire des expériences de diffraction résonante, soit dans les X durs ou les X mous. Ce chapitre est aussi consacré à des développements instrumentaux effectués sur le diffractomètre X mous RE-SOXS actuellement installé sur la ligne SEXTANTS du Synchrotron Soleil. En particulier, pendant cette thèse nous avons developpé et testé un nouveau porte-échantillon qui permet d'appliquer un courant/champ électrique pendant les expériences de diffraction résonante.

Conclusion

Pendant cette thèse, nous avons exploré et observé la faisabilité d'expériences de diffraction résonante sur des systèmes muliferroïques nanostructurés. Nous avons montré différentes approches pour étudier ces types de systèmes: la réflectivité résonante et la diffraction résonante à différents seuils. Pour la réflectivité, nous avons développé un formalisme optimisé pour simuler des expériences. En diffraction, nous avons montré l'importance non seulement du choix de l'énergie du photon incident, seuil K ou $L_{2,3}$, mais aussi le choix de la condition de diffraction (géométrie rasante, géométrie spéculaire). Pour une analyse complète des nos expériences nous avons vu que des simulations sont indispensables. Le besoin de nouveaux développements expérimentaux a aussi été mis en évidence, notamment dans le domaine des mesures sous champ ou courant électrique appliqué.

Chapter 2

Introduction

2.1   General background and motivation

In my fourth year of university, at the university of the Basque Country I had a course on quantum mechanics. I remember that we were only 7 students in class, all of us trying to figure out what the teacher was talking about with, "talkak, teorema optikoa, fermiren urrezko erregela". I did not know what all those theorems were for, if there could ever be useful to me. At that moment I could not imagine that those formulae explained the main part of my thesis, that is, resonant x-ray scattering. Once in France, when Stéphane Grenier who was to become my PhD co-supervisor, told me about Resonant diffraction, I realized that this technique combined two aspect of physics that had always intriguid me: diffraction and spectroscopy.

This thesis has not only been about resonant scattering, but about resonant scattering applied to 3d transition metal oxides, with multiferroic properties. In the next two paragraphs I give an overview of transition metal oxides and resonant scattering, pointing out the aspects of each topic that intrigued and attracted me to begin this adventure that is a PhD. At the end of this introduction I give a very brief summary of what is treated in each chapter of the manuscript.

Transition metals show many fascinating and intriguing properties, some known from ancient history as magnetism, and others discovered in the past century, as superconductivity. Among the many characteristics they present, some allow to store information as Random Access Memories (RAM). This can be achieved using the so called colossal magnetoresistance of perovskite type manganites in M-RAM systems or with the ferroelectric polarization in FE-RAM systems. Magnetic memories are the most commonly used and they require a large amount of energy to create the magnetic fields that write the data. To overcome this problem, scientists have been looking for ways to control magnetic moments with an electric field. One way to achieve this is to have the ferroelectric and magnetic orders in one same system. Multiferroic materials show these two properties, but most of them are low temperature multiferroics or antiferromagnetic. Another way would be to create composite multiferroics, for instance a manganite sample which shows colossal magnetoresistance with a ferroelectric sample.

Many experimental techniques allow to study multiferoic systems: neutron scattering, x-ray scattering, microscopy, spectroscopy methods, transport measurements, raman spectroscopy etc. Among all these I was proposed to use Resonant X-ray Diffraction (RXD). With RXD one studies the electronic structure of an atom: the shape of its orbitals, the oxidation state, the magnetization, as well as any periodic patterns: crystallographic, exotic magnetic arrangements, orbital ordering, ferroelectric domains... In addi-

tion, X-rays give access to a wide range of systems from nano metric systems to single crystals. Because of all this reasons, X-ray resonant scattering is a very well suited technique for the study of multiferroic materials. An eloquent anecdote about it is the 2012 workshop on multiferroics where 20% of the talks where about resonant scattering. This percentage is very high compared to the common number of RXD contributions in conference and workshops.

2.2 Present thesis

One of the main motivations to study multiferroic systems is the control of a net magnetic polarization with an electric field. In order to control this mechanism, it is essential to have a proper fundamental comprehension of the coupling between electric and magnetic orders. In this framework my thesis consisted in studying 3d transition metal oxides, especially multiferroicity, with resonant X-ray diffraction. This thesis is the result of three year work between two research groups. One is the *Surface Interface et Nanostructures* group (SIN) group Néel Institute in Grenoble and the other the Sextants beamline at Synchrotron SOLEIL under the supervision of Nicolas Jaouen. All experiments presented in this thesis were performed in synchrotron facilities (ESRF, Soleil, Diamond ligh source, SLS).

This manuscript is divided into six chapters. The first chapter is an introduction to resonant scattering, the second one shows the formalism I developed for reflectivity curves analysis, the third, fourth and fifth one are experimental chapters for three different materials and in the last chapter I give a brief summary of the presents state of resonant scattering beamlines in Europe. Before developing each chapter I would like to summarize the goals of each of them.

Chapter 1 I introduce resonant x-ray diffraction, I give a quantum mechanical treatement of the process as well as the conventions used throughout the thesis. At the end, I develop scattering terms in two polarization states and study the signals from magnetic or electronic orders by means of the anisotropy ratios.

Chapter 2 In this chapter, the reflectivity phenomenon is treated. I develop a boundary propagation matricial method based on eigen-waves for which the polarization of the wave does not change while it propagates in the medium. I develop this method for two cases, a magnetic system and a system with uniaxial anisotropy and I present an experimental example of the magnetic case and a simulated example for the uniaxial system. This

method has been coded in a matlab environmental.

Chapter 3 Here I propose a way to address the ferroelectric phases with RXD in very thin films of the common ferroelectric $PbTiO_3$ (PTO). Epitaxial PTO thin films on top of $DyScO_3$ show new ferroelectric polarizations and domains. I have combined hard X-ray resonant scattering experiments with *ab initio* simulations of absorption and diffraction to study these new ferroelectric phases.

Chapter 4 I have studied the coupling between a soft ferromagnetic layer and a single crystal of the mutliferroic $BiFeO_3$. $BiFeO_3$ is the only known multiferroic that shows both magnetic and electric orders at room temperature. It is antiferromagnetic and since a ferromagnetic layer is needed for data acquisition we have coupled a thin ferromagnetic layer with the single crystal. This study have been done in the soft X-ray range.

Chapter 5 In this chapter I started the study of thin film manganites under applied electric current. The motivation was that $PrCaMnO_3$ thin films on LAO show charge ordering that could be approach charge density waves and be at the origin of multiferroicity. The goal was to observe the behavior or the Charge ordered peaks under the influence of applied electric current. We installed the necessary set-up on synchrotron beamlines to perform RXD experiments under applied electric current. There are intriguing experimental observations in this study.

Chapter 6 In this last chapter I wanted to give an overview of the presents day state of the art of instrumentation for resonant scattering in europe. I list the synchrotron beamlines that allow to perform this type of experiments as well as the diffractometers and the sample environments in each beamline. During this thesis I have worked on a soft X-ray diffractometer, RESOXS, installed at synchrotron SOLEIL. I have especially been involved in the development of a new sample holder which allows to apply an electric field/current which was used for the Co/BFO study for the first time.

Chapter 3

Basics of Resonant X-ray Scattering

3.1   Introduction

In this chapter we present an introduction to the photon-matter interaction, in particular the scattering of x-rays. In the first part we introduce conventions that are consistently kept throughout the manuscript. The second part introduces the basics of resonant x-ray scattering. The third part consists in some original development of the basics previously introduced to a level that is of interest either for some of the research in the following chapters or for the general interest in the development of resonant x-ray scattering. Specifically, we show the magnetic and anisotropic scattering amplitude developed onto the basis of the circular and linear polarization, and evaluate the formula of the anisotropy ratios.

3.2   Conventions, definitions and useful expressions

3.2.1   Phase of a propagating wave

The electromagnetic radiation can be approached as a superposition of plane waves. There are two choices for the dependence of the phase with space or time, that is, $\pm i(\mathbf{k} \cdot \mathbf{r} - \omega t)$. Hereafter, we choose to write the phase of a propagating wave of energy $\hbar\omega$ and wave vector $\mathbf{k}$ as:

$$e^{i(\mathbf{k}\cdot\mathbf{r}-\omega t)} \tag{3.1}$$

Physicist and neutron crystallographers adopt this convention. The alternative choice, $e^{-i(\mathbf{k}\cdot\mathbf{r}-\omega t)}$, is usual in the field of x-ray crystallography.

Sticking with this convention is important. The sign for the space and time evolution of the phase imposes the signs of various other quantities. With such convention, if a complex number is introduced in the phase as a coefficient to the spatial term, $+i\mathbf{k} \cdot \mathbf{r}$, like an index of refraction, or time term, $-i\omega t$, like a lifetime, its imaginary part must have the same sign, $+$ and $-$ respectively, for the exponential to be damped. There are implications that are less evident. For instance, this convention will apply consistently when considering the perturbation terms introduced in the treatment of the resonant scattering, for instance when introducing the lifetime of the intermediary processes in the denominator of the resonant corrections.

3.2.2 Diffraction vector

A scattering event at position $\mathbf{r}$, that does not change the energy of the wave, is proportional to:

$$
\begin{aligned}
& \left(e^{i(\mathbf{k}_f \cdot \mathbf{r} - \omega_f t)}\right)^* e^{i(\mathbf{k}_i \cdot \mathbf{r} - \omega_i t)} \\
\propto\; & e^{-i(\mathbf{k}_f - \mathbf{k}_i) \cdot \mathbf{r} - i(\omega_f - \omega_i)t} \\
\propto\; & e^{-i\mathbf{Q} \cdot \mathbf{r}}
\end{aligned}
$$

which introduces the scattering, or diffraction vector $\mathbf{Q}$ defined as:
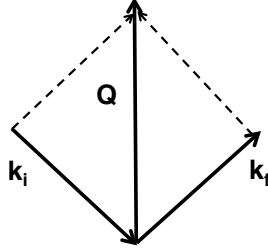
Figure 3.1: Diffraction vector

$$
\mathbf{Q} \equiv \mathbf{k}_f - \mathbf{k}_i \tag{3.2}
$$

The minus sign in the exponential has no profound meaning, it is added only for conveniency in the drawing of the vectors. We will also use

$$
\mathbf{q} \equiv \mathbf{Q}/2\pi \tag{3.3}
$$

which has the advantage of being simply the inverse of d, the inter reticular distance, thereby avoiding the unnecessary 2π mental calculus gymnastics.

3.2.3 Photon polarization

The polarization of the photon in quantum electrodynamics is equivalent to the unit vector in the direction of the electric field of the classical electromagnetic description. Now, the polarization of the photon corresponds to its intrinsic angular momentum, or spin; the polarization state corresponds to the angular momentum along the propagation of the photon. A right (left) circular polarization corresponds to the angular momentum projected along the direction is +1 (-1) as shown in Fig 3.2.
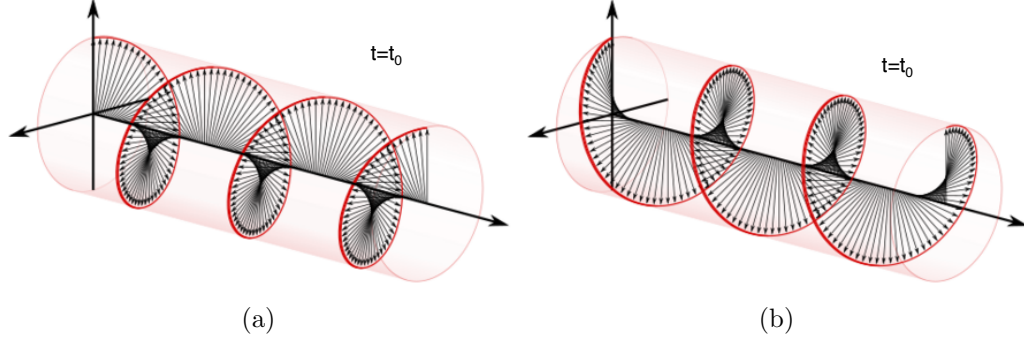
Figure 3.2: Cirular polarized waves, at a given time (a) Left-handed C^- (b) Right-handed C^+

In third generation synchrotrons, x-rays beams can be prepared with nearly all photons having the same polarization. The radiation coming from a bending magnet is linearly polarized, whereas the radiation from a insertion device can be linearly or circularly polarized with a good approximation. The optics on the beamline can change the polarization of the beam.

Circular right and left polarizations

When an electromagnetic beam is circularly polarized the electric field rotates around the propagation vector $\boldsymbol{k}$. With a propagation vector along the z direction and considering that the phase along y is shifted by $\pi/2$ with respect to the phase along x, the amplitude for a circular polarization is:

$$C^{\pm} = \mp \frac{1}{\sqrt{2}} \begin{pmatrix} 1 \\ \pm i \\ 0 \end{pmatrix} \tag{3.4}$$

The overall $\mp$ sign ensures that the momentum is ± 1 along the direction of propagation with respect to the common definition of spherical harmonics $Y_{l,m}$. C^+ (C^-) stands for right (left) circular polarization. One obtains a source of circular polarization from an insertion device with alternate magnets poles, or thanks to a quarter wave plate inserted in the optical path of the linearly polarized beam. The circular polarization rate impinging the sample typically is 99% at the SEXTANT beamline of Synchrotron Soleil, which is an insertion device, meaning that one photon's state is, say, $\sqrt{0.99}|C^+\rangle \pm \sqrt{0.01}|C^-\rangle$.

Linear σ and π polarizations

Bending magnets provide only linear polarizations; insertion devices can be configured for linear polarization. Linear polarization states have zero angular momentum projected along the propagation direction. When scattering is considered, the σ polarization is defined as the linear polarization of the beam that is perpendicular to the scattering plane; the π polarization is the linear polarization that lies in the scattering plane (see Figure 3.3). Representing the scattering event in a referential, with 2θ the scattering angle, the polarization σ, and π have for components:

$$\sigma = (-1, 0, 0) \tag{3.5}$$
$$\pi = (0, \sin\theta, \cos\theta) \tag{3.6}$$
$$\pi' = (0, -\sin\theta, \cos\theta) \tag{3.7}$$
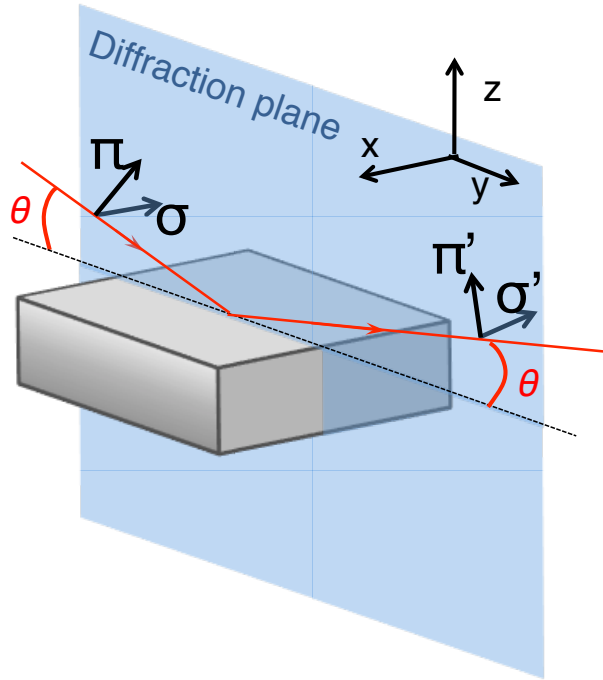
Figure 3.3: Scattering geometry, and definition of the referential: x is perpendicular to scattering plane, therefore parallel to σ, y cuts the scattering angle into two, $\sigma = \sigma'$.

The relation between σ, π and $C^{\pm}$ is then:

$$C^{\pm} = \mp 1/\sqrt{2}(\sigma \pm i\pi) \tag{3.8}$$

3.2.4   Photon wavelength and energy

A useful relation between the wavelength and the energy of X-rays is given by:

$$\lambda[\text{Å}] = \frac{12.398\ [\text{keV} \cdot \text{Å}]}{\text{E}\ [\text{keV}]} \tag{3.9}$$

with E the energy of the X-rays and λ the wavelength, having $hc/e = 12.398$ [keV · Å]. Typically *hard* X-rays have wavelength in the range of 0.1 to 1 nm, which is well tuned to diffracting interatomic distances. The waves with λ between 1 and 10 nm are called *soft* x-rays. This range corresponds to nanometric structures that might appear in a solid, like orbital or magnetic orderings.

3.3   Photon - Matter interaction

As a photon impinges a material several events may take place with a probability that depends mostly on the energy of the photon. Figure 3.4 shows the total and partial cross-section for coherent scattering, incoherent scattering and absorption. Coherent scattering is a photon-in photon-out process with no change of energy, incoherent scattering is a photon-in photon-out process with a gain or a loss of energy, and absorption is a photoelectric process.

The absorption phenomena is energy dependent, and is very useful when studying electronic properties of the outer shells of the atom, like a valence state, or local atomic displacements with methods like Extended X-ray Absorption Fine Structure, X-ray Anomalous Near-Edge Structure (XANES). When we use diffraction, we focus on periodic behavior, like in crystals, and superstructures in crystals like electronic multipolar orderings (orbital ordering) or magnetic structures. The formalism of the diffraction depends on the strength of the scattering amplitude. For a soft-energy or for a large high quality crystal one uses a so-called dynamical theory that takes multiple scattering into account. Usually one prefers to approximate the scattering as a weak enough phenomena so that a photon is only scattered once, the so-called kinematical approximation.

In the following sections, we present generalities on the absorption cross-section, the optical theorem, the initial steps toward the description of resonant x-ray scattering, and the expansion of the resonant scattering amplitude into multipolar terms of the electronic configuration. Then we will recall the basic definitions of diffraction.
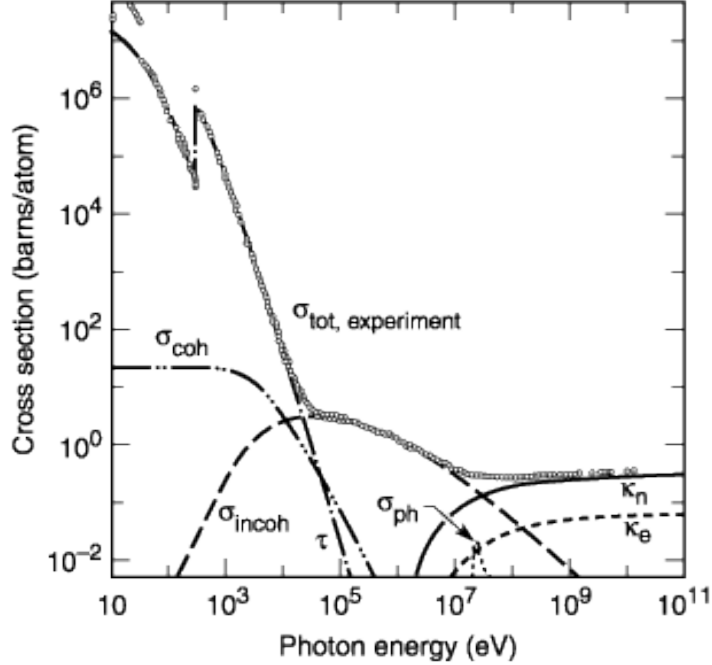
Figure 3.4: Various cross-sections for the photon-matter interaction in carbon as a function of energy. Approximating the total absorption cross-section σ_{tot} with the absorption cross-section is generally valid below 10 keV. ($\tau = \sigma_{\mathrm{abs}}$) atomic photo-effect like electron ejection, photon absorption; (σ_{coh}) coherent scattering, Rayleigh scattering, atom neither ionized nor excited; (σ_{incoh}) incoherent scattering, Compton scattering off an electron; (κ_{n}) pair production, nuclear field; (κ_{e}) pair production, electron field, (σ_{ph}) photonuclear absorption. Taken from the "x-ray data booklet" and [J. Phys. Chem. Ref. Data 9, 1023 (1980)].

3.3.1 Absorption

Photoelectric process

The absorption of a photon can be observed thanks to the so-called "photo-electric effect". The electron leaves the atom when the energy of the photon is large enough to overcome the interaction energy between the nucleus and the electron. If the energy of the photon is not large enough, but still close, the atom will absorb the photon and form an excited state, also called an "exciton", in which the electron can still be considered bound to the nucleus

but promoted to a higher energy shell. One takes advantage of this process in resonant x-ray spectroscopy. This effect probes the unoccupied states, and thereby provides a probe of the electronic configuration of the atom. It is a matter of current research to describe this multi-electronic behavior. From this excited state, the atom decays by re-emitting a photon of the same energy (resonant scattering), or by exciting other inner shells and ejecting secondary electrons (Auger electrons) as well as emitting photons of lower energy (fluorescence).

Absorption coefficient

One introduces the linear absorption coefficient μ and considers an infinitesimal sheet of thickness dz. The attenuation of the beam through the sample is given by μdz and the intensity changes from z to $z + dz$ is:

$$I(z + dz) - I(z) = -I(z)\mu dz \tag{3.10}$$

which gives:

$$I = I(0)e^{-\mu z} \tag{3.11}$$

Absorption cross-section

The absorption coefficient comes from the atomic absorption cross-section:

$$\mu[\mathrm{m}^{-1}] = \rho\sigma_{\mathrm{abs}}[\mathrm{m}^{-3}\mathrm{m}^2] \tag{3.12}$$

The cross section has the dimension of a surface, ρ is the atomic density.

In X-ray absorption spectroscopy (XAS) experiments, the energy of the incident beam is tuned through the absorption edge of an atom. This way one excites a core electron to an empty electronic state. The absorption edges are indexed increasingly according to the energy and angular momentum numbers describing the core levels. Each edge is named with a letter indicating the energy level K for n=1, L for n=2 etc and a number designing the total angular momentum L$_1$ for 2s, L$_2$ for $2p_{1/2}$, L$_3$ for $2p_{3/2}$... In this thesis we have worked either at the K edges for the hard x-ray experiments or in the L$_{2,3}$ edges at the soft x-ray range. In figure 3.5 we show these transition edges.

3.3.2   Scattering amplitude

The scattering length

The wave function of a particle after being scattered is asymptotically [1]:
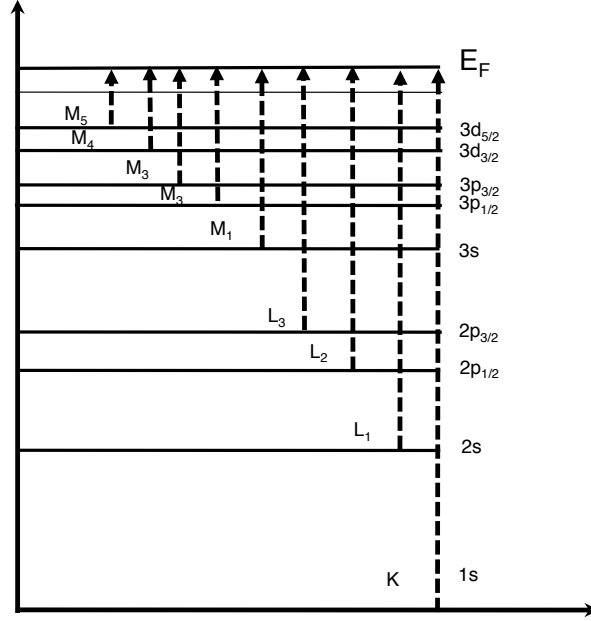
Figure 3.5: Absorption edges indexed by the energy and the angular momentum of the inner shell.

$$\psi \simeq e^{ikx} + \frac{b}{r} e^{ikr} \tag{3.13}$$

where b is called the scattering length and r is the distance to the scatterer. The dependence in $1/r$ ensures the conservation of the flux independently of the distance to the scatterer. The scattering length is often normalized to the scattering length of one free electron $r_0 = \frac{e^2}{mc^2}$:

$$b = -r_0 f \tag{3.14}$$

introducing the scattering amplitude f, which is the scattering length in unit of r_0, or "electron unit". This normalization comes from the approximation that only electrons contribute to the scattering, the scattering being inversely proportional to the mass of the charged particle.

The cross-section, which has the dimension of a surface is:

$$\sigma_{\text{scat}} = 4\pi |b|^2 \tag{3.15}$$

from which the scattering length could also be introduced, the cross-section being a classical concept as well.

Scattering length and absorption cross-section

Following Landau [1], in a very general quantum mechanical treatment of scattering, a general result gives that the imaginary part of the scattering length is related to the total cross-section at $Q = 0$ as:

$$\sigma_{\text{tot}}^{\epsilon} = \frac{4\pi}{k}\text{Im } b^{\epsilon\epsilon}(0). \tag{3.16}$$

This result is referred to as the "optical theorem". The scattering length is to be evaluated with no change in the polarization state ($\epsilon \to \epsilon$). For soft and hard x-rays below 20 keV, the total cross-section consists mainly of the absorption cross-section (see Fig. 3.4):

$$\sigma_{\text{abs}}^{\epsilon} \simeq \frac{4\pi}{k}\text{Im } b^{\epsilon\epsilon}(0). \tag{3.17}$$

This relation requires that the imaginary part of the scattering length be positive, and thus the scattering amplitude in electron unit be negative. The scattering amplitude is then written as :

$$f(\boldsymbol{Q}, E) = f_0(\mathbf{Q}) + f'(E) - if''(E) \tag{3.18}$$
$$\text{with } f_0 > 0 \text{ and } f'' > 0$$

where f_0 is scattering from electrons as if they were free, Thomson scattering and the energy dependent terms are the correcting terms due to their binding to the nucleus. Because f'' is often given positive in tables we add the negative sign in the expression 3.18.

3.3.3   Theoretical approach to resonant scattering

Generality on the formalism

The following development is after Sakurai's reference textbook on Modern Quantum Mechanics [2], we mention without going into detail the successive steps through the basis of quantum electrodynamics of resonant scattering. The scattering is described by a change of the wave function from an initial state to a final state under an interaction with a field during the time $T = t - t_0$. The transition amplitude for this scattering is formally written:

$$c_n(t) = \langle n| \; e^{iHt/\hbar}U(t, t_0)e^{-iHt_0/\hbar}|i\rangle \tag{3.19}$$

where U(t,t$_0$) is the time-evolution operator $U = e^{-\frac{i}{\hbar}H(t-t_0)}$, H being the interaction Hamiltonian. The probability for the transition from $|i\rangle$ to $|n\rangle$

during the time T is $|c_n(t)|^2$, the total cross-section is this probability per time unit:

$$\sigma_{ni} = \frac{|c_n(t)|^2}{T}$$

Now the resolution of the problem consists in treating the interaction as a perturbation V of the unperturbated system with an Hamiltonian H_0, that is $H = H_0 + V$.

First and second order perturbation

At the first order, one can approximate $U \approx U_0 - \frac{i}{\hbar}e^{-\frac{i}{\hbar}H_0(t-t_0)}V(t-t_0)$, where $U_0 = e^{-i\frac{H_0(t-t_0)}{\hbar}}$ with a constant perturbation V turned on at t=0 which leads to:

$$
\begin{align}
c_n^{(0)}(t) &= \delta_{ni} \tag{3.20} \\
c_n^{(1)}(t) &= -\frac{i}{\hbar}V_{ni}\int_0^t dt' e^{i(E_n-E_i)t'/\hbar} \\
&= \frac{V_{fi}}{E_n - E_i}(1 - e^{i(E_n-E_i)t}) \tag{3.21} \\
c_n^{(2)}(t) &= \frac{1}{\hbar}\sum_m \frac{V_{nm}V_{mi}}{E_m - E_i}\int_0^t (e^{i(E_n-E_i)t'} - e^{i(E_n-E_m)t'})dt'
\end{align}
$$

with $V_{ni} = \langle n|V|i\rangle$. The δ_{ni} function corresponds to a "no-event", the initial and final state are the same, it corresponds therefore to the non-interacting incident field. The minus sign after the δ_{ni} function is due to the negative phase evolution with time in the exponential. The resonance effects are described in the second order term of the Dyson series that takes place in two steps.

Fermi golden rule

Then the cross-section for a transition between the two different states is:

$$
\begin{align}
\sigma_{ni} &= \frac{|c_n(t)|^2}{T} \approx \frac{2\pi}{\hbar}|\tau_{ni}|^2\rho(E_n) \tag{3.22} \\
\tau_{ni} &= V_{ni} + \lim_{\eta \to 0}\sum_n \frac{V_{nm}V_{mi}}{E_m - E_i + i\eta}
\end{align}
$$

where η is not the lifetime of the intermediary state but a mathematical parameter introduced for the calculation of the integral over time and necessaty

when $V_{mn}V_{mi} \neq 0$. Relation 3.22 is the so-called Fermi golden rule, $\rho(E_n)$ is the density of final states. One should keep explicit the minus sign in τ coming from $c_n(t)$ for a correct treatment in case of interfering events either with the incident field or with a second scattering event. Sakurai [2] arrived to this last expression using several assumption not shown here. Here we feel that we have the relevant developments for a good understanding of the basics needed in this thesis. Usually, papers at the interface between theory and experiments, like Hannon's and Blume's [3] papers start at the Fermi golden rule, and continues with the following expression of the interaction Hamiltonian.

The Hamiltonian for the interaction

The Hamiltonian that describes the atom in interaction with an electromagnetic field is

$$
\begin{aligned}
H &= H_0 + H_r + H' \\
H_0 &= \sum_j \frac{1}{2m} \boldsymbol{P}_j^2 + \sum_{ij} V(r_{ij}) \\
H_r &= \sum_{k\lambda} \hbar\omega_k (a^+_{(k\omega)} a_{(k\omega)} + \frac{1}{2}) \quad (3.23) \\
H' &= \frac{e^2}{2m} \sum_j \mathbf{A}^2(\mathbf{r}_j) - \frac{e}{m} \sum_j \mathbf{A}(\mathbf{r}_j) \cdot \mathbf{P}_j \\
&= V_1 + V_2 \quad (3.24)
\end{aligned}
$$

with H_0 the free atom contribution, H_r the radiation field, and H' the interaction part with $\boldsymbol{r}_j$ the position of electrons and $\mathbf{P}_j$ their momentum, $-e$ is the charge of the electron. We have not included terms dependent on the spin, the magnetic interaction we are dealing with in this thesis is purely electric in nature and comes from V_2.

A quantized electro-magnetic field

For a quantized electromagnetic wave, the potential vector $\mathbf{A}$ is written in terms of the annihilation and creation operators, one gets [4]:

$$
\mathbf{A} = \sum_u \sum_\mathbf{k} \sqrt{\frac{\hbar}{2\epsilon_0 V \omega_\mathbf{k}}} \left[a_{(\mathbf{k}u)} \epsilon_u e^{i(\mathbf{k}\cdot\mathbf{r}-\omega t)} + a^\dagger_{(\mathbf{k}u)} \epsilon_u^* e^{-i(\mathbf{k}\cdot\mathbf{r}-\omega t)} \right] \quad (3.25)
$$

with $\mathbf{k}$ the wave vector, ϵ_u are two perpendicular unit polarizations, $u = 1, 2$, V is a so-called quantification volume, a mathematical trick that disappears
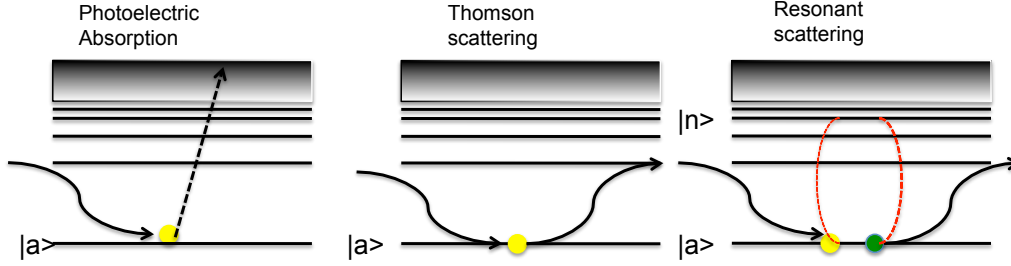
Figure 3.6: A quantum mechanical description of the interaction of a photon with an atomic electron.

in final expressions, and a and $a^\dagger$ the annihilation and creation operators with the properties: $a|n\rangle = \sqrt{n}|n-1\rangle$ and $a^+|n\rangle = \sqrt{n+1}|n+1\rangle$ with $|n\rangle$ the state with n photons in the field. In our case, we can consider $n = 1$ as the photons are not entangled. We are in Coulomb gauge, $\nabla \cdot \mathbf{A} = 0$.

Interaction Hamiltonian within the second order perturbation of the scattering amplitude

Considering only scattering events, that is with a photon in and a photon out, the first order term can only be given by V_1 which annihilates the photon in and creates the photon out. The second order term can only be given by V_2, which annihilates a photon thereby giving the energy to the atom, and creates a photon out thereby de-exciting the atom. One gets the scattering cross-section as given by Fermi's Golden rule, eq. 3.22:

$$\frac{2\pi}{\hbar} \left| -\langle n|V_1|i\rangle - \sum_n \frac{\langle n|V_2|m\rangle\langle m|V_2|i\rangle}{\hbar\omega + E_i - E_m + i\frac{\Gamma_n}{2}} \right|^2 \rho(E_n) \qquad (3.26)$$

where $\rho(E_n) = \frac{V\omega^2}{(2\pi)^3\hbar c^3}$ is the density of final states. The sum is done over all possible states with energy E_n. For now on we separate in the total initial energy the energy of the photon $\hbar\omega$ and the initial energy of the atom E_i, that is $E_i \rightarrow \hbar\omega + E_i$. For resonant elastic X-ray scattering the initial and final states of the atom have the same energy, and are considered the same. In figure 3.6 we show the three processes mentioned above (photoelectric effect, Thomson scattering and resonant scattering). Note that despite that the scattering is due to electrons the negative sign of its charge does not play any role in the scattering, at first and second order.

Thomson scattering

The term $\langle n|V_1|i\rangle$ describes the scattering by electrons as if they were free, the so called Thomson scattering. By including the constants from $\frac{2\pi}{\hbar}\rho(E_n)$ into the matrix element one can write an effective scattering length:

$$b^{(1)} = -\frac{e^2}{4\pi\epsilon_0 mc^2}\left(\epsilon'^* \cdot \epsilon\right)\langle f|e^{-i\mathbf{Q}\cdot\mathbf{r}}|i\rangle \tag{3.27}$$

$$= -r_0\left(\epsilon'^* \cdot \epsilon\right)f_0(Q) = -r_0\left(\epsilon'^* \cdot \epsilon\right)\int\rho(\mathbf{r})e^{-i\mathbf{Q}\cdot\mathbf{r}}d\mathbf{r} \tag{3.28}$$

The scattering length of the atom for Thomson scattering is the product of r_0 times the form factor, which is the expectation value, or the time average for the $e^{-i\mathbf{Q}\cdot\mathbf{r}}$ term; it is the Fourier transform of the electronic density. It is usually a real number because of the usual center of symmetry in the electron distribution.

Resonant corrections

The second term in eq. 3.26 describes the creation of intermediary states during the interaction of the atom with the field. By including the constants from $\frac{2\pi}{\hbar}\rho(E_f)$ into the matrix element one can write an effective resonant scattering length:

$$b^{(2)} = -\frac{r_0}{m}\sum_m\frac{\langle n|\mathbf{p}\cdot\epsilon^{*\prime}e^{-i\mathbf{k}'\cdot\mathbf{r}}|m\rangle\langle m|\mathbf{p}\cdot\epsilon e^{i\mathbf{k}\cdot\mathbf{r}}|i\rangle}{\hbar\omega + E_i - E_m + i\frac{\Gamma_m}{2}} \tag{3.29}$$

Considering the dipolar approximation, one supposes that the wavelength of the photon is large compared to one of the orbital of the electron in the initial and final state. In the matrix element, the exponential is then approximated to one. Physically it means that one supposes that the phase of the photon does not change significantly in a volume of the size of the smallest electrons orbitals involved in the resonance. Writting $\langle m|\mathbf{p}|i\rangle = -\frac{m}{i\hbar}(E_m - E_i)\langle m|\mathbf{r}|i\rangle$, and $\langle n|\mathbf{p}|m\rangle = -\frac{m}{i\hbar}(E_i - E_m)\langle n|\mathbf{r}|m\rangle$, one gets:

$$b^{(2)} = -r_0 m\sum_n\left(\frac{E_m - E_i}{\hbar}\right)^2\frac{\langle n|\mathbf{r}\cdot\epsilon^{*\prime}|m\rangle\langle m|\mathbf{r}\cdot\epsilon|i\rangle}{\hbar\omega + E_i - E_m + i\frac{\Gamma_n}{2}} \tag{3.30}$$

$$= -r_0\left(f' - if''\right) \tag{3.31}$$

f' and f'' are the dispersion corrections and they are dependent of the energy. f' is the Kramers-Krönig transform of f'', and vice-versa. One can verify

that the imaginary part of the scattering length goes as λ^2 when $\omega >> \omega_0$, which correctly gives an absorption coefficient going as λ^3, (Figure 3.4). To summarize, one gets to the second order in the perturbation:

$$
\begin{aligned}
b &= -r_0 \left(f_0 + f' - if'' \right) \\
f_0 &= (\epsilon'^* \cdot \epsilon) \int \rho(\mathbf{r}) e^{-i\mathbf{Q}\cdot\mathbf{r}} d\mathbf{r} \\
f' - if'' &= m \sum_m \left(\frac{E_m - E_i}{\hbar} \right)^2 \frac{\langle n|\mathbf{r}\cdot\epsilon^{*'}|m\rangle\langle m|\mathbf{r}\cdot\epsilon|i\rangle}{\hbar\omega + E_i - E_m + i\frac{\Gamma_m}{2}}
\end{aligned}
\qquad (3.32)
$$

We'll use this approximation in this thesis.

Now we have all the information to calculate the scattered intensity by an atom. The cross section is proportional to the probability that an interaction will occur and the differential cross section gives how efficiently the particles in the sample scatter the incident beam. The scattered intensity is:

$$
I_{sc} = I_0 N \Delta\Omega \left(\frac{d\sigma}{d\Omega} \right)
\qquad (3.33)
$$

where I_0 is the incident photons per second, $\Delta\Omega$ is the solid angle and N is the particles per unit area in the sample.

3.3.4 Multipolar development of the scattering amplitude

The relation 3.32 does not make any assumption on the electron orbitals, their shape, their orientation within the local symmetry of the resonant atom or if the atom carries a magnetic moment. Templeton and Templeton observed at the resonance an anisotropy in the x-ray scattering [5], similar to the birefringence occuring in anisotropic crystals with light, and Gibbs and coworkers discovered x-ray resonant scattering depending on the magnetic moment and its orientation thereby launching a new area of characterization of magnetic crystals in 1988 [6]. Both scattering occurs with a change in the polarization of the photon. In order to associate a particular dependence of the scattering with the polarization and the local symmetry, including uniaxial symmetry defined by a magnetic moment, a useful framework has been laid down in 1988 by Hannon following Gibbs reports [3], in which the scattering amplitude, within the approximations of dipolar transitions and uniaxial symmetry, takes the form:

$$
\hat{f}_{\epsilon'\epsilon} = (\boldsymbol{\epsilon'^*} \cdot \boldsymbol{\epsilon})\, F_0 - i(\boldsymbol{\epsilon'^*} \times \boldsymbol{\epsilon}) \cdot \boldsymbol{u}\, F_1 + (\boldsymbol{\epsilon'^\star} \cdot \boldsymbol{u})(\boldsymbol{\epsilon} \cdot \boldsymbol{u})\, F_2
\qquad (3.34)
$$

where $\boldsymbol{\epsilon}$ and $\boldsymbol{\epsilon'^*}$ are the polarization vector of the incoming and outcoming waves and $\boldsymbol{u}$ is the unit vector describing the anisotropy (magnetic or electronic). The term F_1 describes the magnetism and the term F_2 will describe a uniaxial electronic anisotropy, or a spin-orbit coupling. In the following we describe the F terms.

Isotropic term F_0

Then one also adds the resonant terms:

$$F_0 \;=\; -r_0 f_0 + (3/4k)[F_{11} + F_{1\bar{1}}]$$

$$(3.35)$$

The magnetic term F_1

Lets consider a magnetic media. In this case from equation 3.34 we have:

$$\hat{f}_{\boldsymbol{\epsilon'\epsilon}} = (\boldsymbol{\epsilon'^*} \cdot \boldsymbol{\epsilon})\, F_0 - i(\boldsymbol{\epsilon'^*} \times \boldsymbol{\epsilon}) \cdot \boldsymbol{u}\, F_1 \qquad (3.36)$$

with

$$F_0 \;=\; -r_0 f_0 + (3/4k)[F_{11} + F_{1\bar{1}}]$$
$$F_1 \;=\; (3/4k)[F_{11} - F_{1\bar{1}}]$$

where the polarization vectors of the incoming and outgoing photons, $\boldsymbol{\epsilon}$ and $\boldsymbol{\epsilon'}$ respectively, are unit vectors equivalent to the electric field vector of the classical description, $\boldsymbol{\epsilon} = \boldsymbol{E}/E$. The function F_{1m} are proportional to the probability of absorption of a photon with a change of m in the atomic angular momentum projected along $\boldsymbol{u}$. The unit vector $\boldsymbol{u}$ is the quantification axis, here it is chosen to correspond to the direction of the local magnetic moment. The term F_1 contains the magnetic signal, which lies in the difference $F_{11} - F_{1\bar{1}}$ corresponding to the difference in absorption with the angular momentum change $\Delta m = \pm 1$. Expression (3.36) corresponds to an atom whose electronic configuration, including the spin, can be described in a point group symmetry as low as C_{4h} [3, 7, 8], which is enough to describe an uniaxial asymmetry defined by the unit vector $\boldsymbol{u}$. It typically describes a cubic symmetry broken by a magnetic moment $\boldsymbol{u} = \boldsymbol{m}/m$. It implies that we neglect the spin-orbit interaction in the valence shell. Here, the local cubic symmetry is only broken by the magnetic moment. Finally, the expression (3.36) also implies that we restrict ourselves to the approximation of a dipolar transition, that is $l = 1$ and $m = 0, \pm 1$; higher order in the multipolar expansion are neglected.
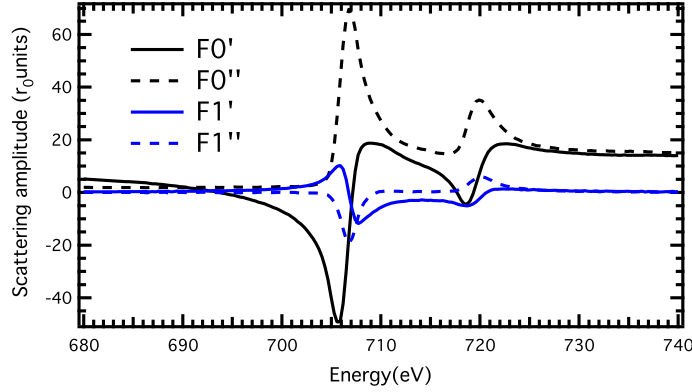
Figure 3.7: Real (') and imaginary (") parts of the scattering length (in r_0 unit) at the Fe L_3 edge.

As example we show real and imaginary parts of F0 and F1 for Fe atoms in Fig 3.7. These factors were obtained after experimental X-ray absorption measurements of X-ray magnetic circular dichroism that provide the imaginary part and Kramers Kronig transform of the imaginary part to give the real part [9].

The quadrupolar term, uniaxial symmetry.

For a non magnetic system with a uniaxial anisotropy from eq 3.34

$$\hat{f} = (\boldsymbol{\epsilon}'^{\star} \cdot \boldsymbol{\epsilon}) \ F_0 + (\boldsymbol{\epsilon}'^{\star} \cdot \boldsymbol{u})(\boldsymbol{\epsilon} \cdot \boldsymbol{u}) \ F_2 \tag{3.37}$$

The tensor has dimension 2 on the basis defined by the two polarization vectors, usually noted σ and π and defined as the components perpendicular and parallel to the scattering plane respectively. F_0 and F_2 relates to the scattering factors expressed in a cartesian referential as:

$$F_0 = \frac{1}{3}(2f_{\perp} + f_{\parallel}) \tag{3.38}$$

$$F_2 = f_{\parallel} - f_{\perp} \tag{3.39}$$

In this framework, F_0 is the isotropic and F_2 the quadrupolar term in the electronic configuration expansion. Typically, in a reconstructed interface, the resonant atom may undergo a change in its environment departing from a cubic symmetry to an uniaxial anisotropy as it sits along the normal, from the interface. It corresponds to a point group symmetry as low as C_{4h} [7, 8],

which is enough to describe an uniaxial asymmetry. It would describe for instance Jahn-Teller Mn ions in $LaMnO_3$, as a first approximation, where $\boldsymbol{u}$ defined the axis of higher symmetry, the long Mn-O distance. We believe that for this presentation this point group is a good trade-off between simplicity and generality. Lower symmetries are considered elsewhere [7, 8].

As example we show real and imaginary parts of F0 and F2 for $YBa_2Cu_3O_7$ in Fig 3.8. These factors were obtained after experimental X-ray absorption measurements of X-ray linear dichroism that provide the imaginary part and Kramers Kronig transform of the imaginary part to give the real part [9].
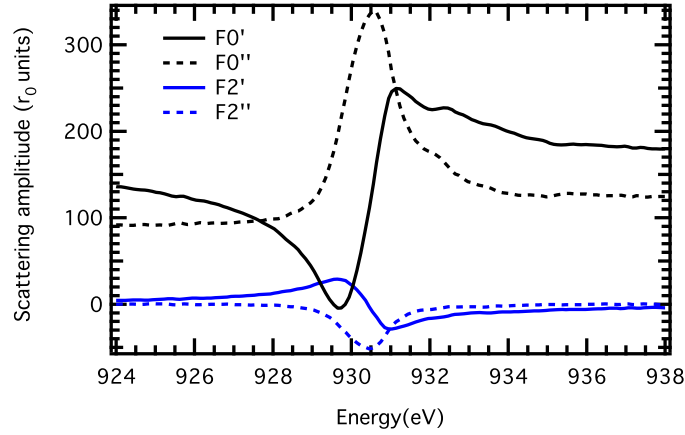
Figure 3.8: Real (') and imaginary (") parts of the scattering length (in r_0 unit) at the Cu L_3 edge for the YBCO "molecule".

3.3.5   Diffraction

In practice photons diffract from an organised assembly of atoms. We will focus on the kinematical approximation. The kinematical approximation considers the interaction between the crystal and the atom weak, in other words, the scattering process happens just once. A crystal can be considered as a assembly of atomic layers spaced at a distance d as shown in fig 3.9. The elastic scattering is coherent, that is, it shows interferences between sites, that is the "wave"-side of the photon. A crystal has a scattering factor $F(\boldsymbol{Q})$. The intensity of the diffracted beam is proportional to the square of the scattering from $F(\boldsymbol{Q})$:

$$F^{crystal}(\boldsymbol{Q}) = \sum_{\boldsymbol{r_j}} f_j(\boldsymbol{Q})e^{-i\boldsymbol{Q}\cdot\boldsymbol{r_j}} \sum_{\boldsymbol{R_n}} e^{-i\boldsymbol{Q}\cdot\boldsymbol{R_n}} \tag{3.40}$$
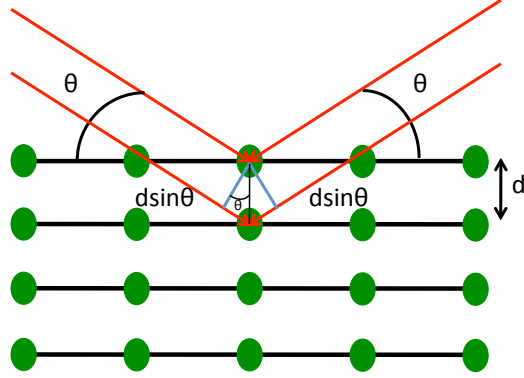
Figure 3.9: Diffraction from an assembly of atoms

with f_j the scattering amplitude of one atom, $\boldsymbol{Q}$ the scattering vector, $\boldsymbol{R_n}$ the lattice vectors and $\boldsymbol{r_j}$ the position of the atoms.

Here we consider parallel lattice planes separated by a distance d as shown in 3.9. From here we see that the difference of the path of two incident beams from adjacent planes is $2d \sin \theta$, where θ is the angle the beam makes with the surface plane of the sample, it is known as the Bragg angle. There is a constructive interference when the radiation of the neighbor planes when the distance d is an integer of the wavelength of the beam. This gives Bragg's law:

$$2d \sin \theta = n\lambda \tag{3.41}$$

A crystal is a three dimensional system and in crystallography the crystals are defined by the crystal axes $\boldsymbol{a_1, a_2, a_3}$. Bragg's law considers a set of planes, called the crystallographic planes which are equidistant planes that fulfill certain conditions: one of them passes through the origin, and the adjacent one intercept the crystallographic axis on the points $\boldsymbol{a1}/h$, $\boldsymbol{a2}/k$, $\boldsymbol{a3}/l$. The integers hkl are the Miller indices.

Reciprocal vectors are defined as:

$$\boldsymbol{a_1^*} = \frac{\boldsymbol{a_2} \times \boldsymbol{a_3}}{\boldsymbol{a_1} \cdot (\boldsymbol{a_2} \times \boldsymbol{a_3})}, \boldsymbol{a_2^*} = \frac{\boldsymbol{a_3} \times \boldsymbol{a_1}}{\boldsymbol{a_1} \cdot (\boldsymbol{a_2} \times \boldsymbol{a_3})}, \boldsymbol{a_3^*} = \frac{\boldsymbol{a_1} \times \boldsymbol{a_2}}{\boldsymbol{a_1} \cdot (\boldsymbol{a_2} \times \boldsymbol{a_3})} \tag{3.42}$$

now we define the reciprocal lattice vector $\boldsymbol{G_{hkl}}$ being a linear combination of the reciprocal lattice vectors.

$$\boldsymbol{G_{hkl}} = h\boldsymbol{a_1^*} + k\boldsymbol{a_2^*} + l\boldsymbol{a_3^*} \tag{3.43}$$

From [4] we know that $F^{crystal}(\boldsymbol{Q})$ is going to be non-zero if:

$$\boldsymbol{Q} = 2\pi\boldsymbol{G} \tag{3.44}$$

This means that in order to have diffraction the scattering vector $\boldsymbol{Q}$ coincides with a reciprocal lattice vector. The intensity diffracted is proportional to the square of the scattering form $F(\boldsymbol{Q})$.

3.3.6   Dynamical effects

When a propagating beam passes from one to another medium its propagation direction also changes. The refractive index or index of refraction n of a medium describes how the light propagates. The index of refraction of a propagating wave in a medium has an imaginary part to describe the absorption. Following definition (3.1), the imaginary part of the index of refraction should be positive in order to describe a spatial attenuation:

$$n \;=\; n_r + in_i \quad n_i > 0 \tag{3.45}$$

We already see a resemblance between n and f, both have a imaginary part. In optics n is defined as the ratio of the speed of the light in the vacuum and the speed in the media. In our case, since we will study resonance phenomena the index of refraction has a real and imaginary part as shown in eq 3.45. The index of refraction gives the information we need to resolve the reflectivity that is related to the permitivity and magnetic properties of the sample. Reflectivity can be solved using classical physics and considering the matter-x-ray interaction dynamical. Maxwell equations relies physical properties to the electromagnetic waves propagating in the medium and the Snell law relates the index of refraction with the EM waves. In the next chapter we present two formalisms to treat reflectivity based on Maxwell wave theory.

3.4   Multipolar development on two polarization basis

In the following section, we develop the scattering amplitude onto the two most useful polarizations basis, the linear and the circular basis. It consists in calculating Hannon's eq:3.34 in the four possible channels, the two unchanged channels, for instance $\sigma \to \sigma$, $\pi \to \pi$, and the two cross channels, for instance $\sigma \to \pi$, and $\pi \to \sigma$. Then one can benefit from using matrix algebra, constructing the 2x2 matrix with the four channels. Hill and Mc Morrow had

presented the matrix expressed in the linear σ and π matrix [10]. We present the matrix expressed in the circular basis for it is the most used basis in soft x-ray experiments. This calculation is straightforward, but for some reasons, it is never presented in the literature, to the best of our knowledge, even when only circular polarizations are used. Of course one can alternatively transform circular polarization onto the linear basis and then apply Hill's expression before retransforming onto the circular basis.

3.4.1   The linear basis

We first start by rediscovering Hannon's equation into the linear σ and π polarization as presented by Hill and Mc Morrow in their reference paper on x-ray resonant magnetic scattering [10]. Eq. 3.34 calculated on the linear polarization basis for the four channels gives:

$$
\begin{aligned}
\sigma \to \sigma &= F_0 + F_2 u_x^2 \\
\sigma \to \pi' &= iF_1(u_y \cos\theta + u_z \sin\theta) - F_2 u_x(-u_y \sin\theta + u_z \cos\theta) \\
\pi \to \sigma &= -iF_1(u_y \cos\theta - u_z \sin\theta) - F_2 u_x(u_y \sin\theta + u_z \cos\theta) \\
\pi \to \pi' &= F_0 \cos 2\theta + iF_1 u_x \sin 2\theta - F_2(u_y^2 \sin^2\theta - u_z^2 \cos^2\theta)
\end{aligned}
$$

which gives the following matrix on the linear basis:

$$
\begin{aligned}
\hat{f}_{e'e}(\theta) &= \quad F_0 \begin{pmatrix} 1 & 0 \\ 0 & \cos 2\theta \end{pmatrix} \\
&\quad -iF_1 \begin{pmatrix} 0 & u_y \cos\theta - u_z \sin\theta \\ -u_y \cos\theta - u_z \sin\theta & -u_x \sin 2\theta \end{pmatrix} \\
&\quad +F_2 \begin{pmatrix} u_x^2 & -u_x u_y \sin\theta - u_x u_z \cos\theta \\ u_x u_y \sin\theta - u_x u_z \cos\theta & -u_y^2 \sin^2\theta + u_z^2 \cos^2\theta \end{pmatrix}
\end{aligned}
$$

$$(3.46)$$

If one does not write the anisotropy terms u from F_1 and F_2 in a different way, it considers that the uniaxial anisotropy in F_2 has a magnetic origin. In the case where there is no magnetic order (F_1=0), the F_2 term can either be magnetic or not magnetic. However if a system shows a magnetic order F_1 and a non magnetic uniaxial anisotropy F_2, the quantification vectors $\boldsymbol{u}$ describing the anisotropies have to be labeled in different ways. Here we will consider both (F_1 and F_2) as magnetic terms, except for the cases where there will be no F_1 – then in such cases F_2 will be considered non-magnetic.

The 3.46 is the formula (5) of Hill and Mc Morrow's paper [10], if one performs the change of referential: $z_1 \to u_y$, $z_2 \to u_x$ and $z_3 \to -u_z$. There is a sign mistake in the $\pi \to \pi'$ term of the F_2 term in ref. [10], which

reads $-F_2 \cos^2 \theta (z_1^2 \tan^2 \theta + z_3^2)$, but should read $-F_2 \cos^2 \theta (z_1^2 \tan^2 \theta - z_3^2)$ or $F_2(-z_1^2 \sin^2 \theta + z_3^2 \cos^2 \theta)$. One can check indeed that in the $\pi \to \pi'$ channel and for a magnetization along the (011), the scattering at $\theta = \pi/4$ must be zero as the magnetization is then parallel to the scattered beam.

3.4.2 The circular basis

Most resonant magnetic reflectivity experiments are performed with circular x-rays, eq:3.34 calculated on the circular polarization basis for the four channels gives:

$$
\begin{aligned}
C_+ \to C_+ &= F_0 \cos^2 \theta - i\frac{F_1}{2}(-u_x \sin 2\theta + i2u_y \cos \theta) + \frac{F_2}{2}[(u_x - iu_y \sin \theta)^2 + u_z^2 \cos^2 \theta] \\
C_- \to C_- &= F_0 \cos^2 \theta - i\frac{F_1}{2}(-u_x \sin 2\theta - i2u_y \cos \theta) + \frac{F_2}{2}[(u_x + iu_y \sin \theta)^2 + u_z^2 \cos^2 \theta] \\
C_- \to C_+ &= -F_0 \sin^2 \theta - i\frac{F_1}{2}(-u_x \sin 2\theta - i2u_z \sin \theta) + \frac{F_2}{2}[-(u_x + iu_z \cos \theta)^2 - u_y^2 \sin^2 \theta] \\
C_+ \to C_- &= -F_0 \sin^2 \theta - i\frac{F_1}{2}(-u_x \sin 2\theta + i2u_z \sin \theta) + \frac{F_2}{2}[-(u_x - iu_z \cos \theta)^2 - u_y^2 \sin^2 \theta]
\end{aligned}
$$

$$(3.47)$$

which gives the following matrix in the basis of the circular polarizations:

$$
\begin{aligned}
\hat{f}_{e'e}(\theta) = \quad & F_0 \begin{pmatrix} \cos^2 \theta & -\sin^2 \theta \\ -\sin^2 \theta & \cos^2 \theta \end{pmatrix} \\
& -i\frac{F_1}{2} \begin{pmatrix} -u_x \sin 2\theta + i2u_y \cos \theta & -u_x \sin 2\theta - i2u_z \sin \theta \\ -u_x \sin 2\theta + i2u_z \sin \theta & -u_x \sin 2\theta - i2u_y \cos \theta \end{pmatrix} \\
& +\frac{F_2}{2} \begin{pmatrix} (u_x - iu_y \sin \theta)^2 + u_z^2 \cos^2 \theta & -(u_x + iu_z \cos \theta)^2 - u_y^2 \sin^2 \theta \\ -(u_x - iu_z \cos \theta)^2 - u_y^2 \sin^2 \theta & (u_x + iu_y \sin \theta)^2 + u_z^2 \cos^2 \theta \end{pmatrix}
\end{aligned}
$$

$$(3.48)$$

3.5 Multipolar development of the scattering amplitude

Using the preceding developments of the scattering amplitudes one can deduce the intensities of reflected beams for a particular incident photon polarization and how they depend depend on the u_x, u_y and u_z components of the anisotropy. First we treat the Thomson scattering, then X-ray magnetic dichroism or x-ray natural dichroism and at last, the reflectivity analysis.

3.5.1 Thomson scattering of circularly polarized photons

Consider the first isotropic term of the Thomson scattering and the resonant terms with no anisotropy of any sort:

$$\hat{f}_{e'e} \;\; = \;\; F_0 \begin{pmatrix} \cos^2\theta & -\sin^2\theta \\ -\sin^2\theta & \cos^2\theta \end{pmatrix}$$

One sees that it is impossible to keep the pure circular polarization if a beam is scattered with a certain angle. This is an issue to consider when monochromotizing a beam. In the table 3.1 some calculations are performed for an incoming right circular polarized beam. The higher the energy requested, the more a purely circular incident light will be destroyed. It is a problem for hard x-ray beamline which can not use a source of circular light, but rather use phase plates after the monochromator in order to get a circular light. For soft x-ray beamline, the monochromator keeps a low angle, and therefore one can use a beam that is circularly polarized at the source, from the undulator. In particular we note that the incident circular polarization at the SEXTANTS beamline is still 99.6 % after being scattered by the monochromator. In fact, the purity in the incident circular polarization is mostly hampered by the insertion device that does not give a purely circular beam.

Table 3.1: Polarization rate of a perfectly C_+ polarized incident beam scattered at angle 2θ, for instance, by a monochromator

incident angle (deg)	polarization rate
0	C_+
3.5	99.6% C_+ 0.4% C_- (soft x-ray monochromator)
45	50% C_+ and 50% C_- that is σ
90	C-

Another remark is that backscattering ($\theta = 90°$) gives the opposite circular polarization, an effect that is also related to the time inversion of the circular polarization that is time-odd.

3.5.2 Forward scattering and absorption cross-section of polarized photons

The calculation of the forward scattering is used for the evaluation of the index of refraction as we will see in the next chapter. It is also important in

order to evaluate the absorption cross-section which is related to the imaginary part of the scattering length. Absorption experiments are very common in synchrotrons and specially in magnetism one uses the dichroism to obtain magnetic information of the sample. Here we will see how the most common polarizations of the synchrotron allow to observe different magnetic and electronic properties.

Linear basis and X-ray Linear Dichroism

X-ray linear dichroism (XLD) is one of such techniques which uses the linear σ and π polarizations to obtain magnetic and/or electronic properties of systems. From eq:3.46 and assuming an absorption experimental condition $\theta=0$ and $\epsilon'=\epsilon$, one gets for the forward scattering amplitude:

$$\hat{f}_{ee}(\theta = 0) \quad = \quad F_0 \begin{pmatrix} 1 & 0 \\ 0 & 1 \end{pmatrix} - iF_1 \begin{pmatrix} 0 & u_y \\ -u_y & 0 \end{pmatrix} + F_2 \begin{pmatrix} u_x^2 & -u_x u_z \\ -u_x u_z & u_z^2 \end{pmatrix}$$

$$(3.49)$$

From the previous expressions and using eq:3.14 $b = -r_0 f$ and eq:3.17 $\sigma_{\text{abs}} = \frac{4\pi}{\lambda}\text{Im}b^{\epsilon\epsilon}(0)$ we deduce the two atomic cross-sections for absorption in linear polarization:

$$\begin{aligned} \sigma_{\text{abs}}^{\sigma} &= \frac{\lambda r_0}{2}\text{Im}\{F_0 + u_x^2 F_2\} \\ \sigma_{\text{abs}}^{\pi} &= \frac{\lambda r_0}{2}\text{Im}\{F_0 + u_z^2 F_2\} \end{aligned} \quad (3.50)$$

where we recall that x is along σ's direction, and z is along π's direction (see Fig.3.3). Linear dichroism is a measurement in which two acquisition are made with σ and π polarizations and then they are substrated. This way one reveals the anisotropy.

$$\sigma_{\text{abs}}^{XLD} = \sigma_{\text{abs}}^{\sigma} - \sigma_{\text{abs}}^{\pi} = \frac{\lambda r_0}{2}(u_x^2 - u_z^2)\text{Im}\{F_2\} \qquad (3.51)$$

The F_2 term can have two denominations depending on its origin. If the F_2 term originates from a magnetic moment and a spin-orbit coupling, this is the "X-ray Linear Magnetic Dichroism" (XMLD). If there is no magnetic origin in the anisotropy, but rather a local atomic loss of symmetry, it is called "X-ray Linear Natural Dichroism" (XNLD). In both case the anisotropy is measurable as long as it does not lie along the direction of the photon, or exactly in between the two directions of the polarization.

Circular basis and X-ray Magnetic Circular Dichroism

X-ray magnetic dichroism is a very well known method to study magnetism. WE can see how it works considering that for circular polarized light the scattering form factor for an absorption case where $\theta=0$ is:

$$\hat{f}_{e'e}(\theta=0) = F_0 \begin{pmatrix} 1 & 0 \\ 0 & 1 \end{pmatrix} + F_1 \begin{pmatrix} u_y & 0 \\ 0 & -u_y \end{pmatrix} + \frac{F_2}{2} \begin{pmatrix} u_x^2 + u_z^2 & -(u_x + iu_z)^2 \\ -(u_x - iu_z)^2 & u_x^2 + u_z^2 \end{pmatrix}$$

$$(3.52)$$

And again combining eq:3.14 and eq:3.17 with the previous expressions one gets the two atomic cross-sections for absorption:

$$\sigma_{\text{abs}}^{C+} = \frac{\lambda r_0}{2} \text{Im}\{F_0 + u_y F_1 + \frac{F_2}{2}(u_x^2 + u_z^2)\}$$

$$\sigma_{\text{abs}}^{C-} = \frac{\lambda r_0}{2} \text{Im}\{F_0 - u_y F_1 + \frac{F_2}{2}(u_x^2 + u_z^2)\} \qquad (3.53)$$

The circular dichroism corresponds to a measurement of the absorption cross-section in the two circular polarization states and performing the subtraction to reveal only the anisotropy:

$$\sigma_{\text{abs}}^{XMCD} = \sigma_{\text{abs}}^{C+} - \sigma_{\text{abs}}^{C-} = \lambda r_0 u_y \text{Im}\{F_1\} \qquad (3.54)$$

The term F_1 can only be of magnetic origin, the technique is called "X-ray Magnetic Circular Dichroism" XMCD.

XMLD and XLD are absorption techniques, they do not consider any diffraction or reflectivity conditions. We will use XMLD/XNLD on chapter 6 on the X-PEEM study.

3.5.3 Reflectivity/diffraction intensities and anisotropy ratios

Now we use the multipolar development for the analysis of reflectivity. The analysis of the magnetic/electronic reflectivity/diffraction signal is usually performed on the so-called asymmetry ratio. It consists in isolating the signal coming from the anisotropy, thereby eliminating the strong charge signal. To achieve such results one measures twice the intensity reflected/diffracted, once with a definite direction of the magnetic moment or, of the photon's polarization, and a second time with one of these moments reversed. There are therefore two ways to calculate the ratio. One is to fix a given polarization ($p_{1,2}$) and to measure the reflectivity twice applying a field in two

opposite directions ($\pm u$) and the other one is with a fixed applied field to change the polarization of the incoming photons between the two reflectivity measurements.

The ratio for a fixed applied field is given by:

$$R_{p_1-p_2}^{\pm u \text{ fixed}} = \frac{I_{p_1}^{\pm u} - I_{p_2}^{\pm u}}{I_{p_1}^{\pm u} + I_{p_2}^{\pm u}} \tag{3.55}$$

The ratio for a fixed photon polarization is given by:

$$R_{p_{1,2}}^{u \ inv} = \frac{I_{p_{1,2}}^{+u} - I_{p_{1,2}}^{-u}}{I_{p_{1,2}}^{+u} + I_{p_{1,2}}^{-u}} \tag{3.56}$$

In appendix A, we give an analytical formulation of the anisotropy ratios corresponding to the two measurement geometries for linear and circular polarizations. These calculations are kinematical, that is we neglect the dynamical effect and the index of refraction is 1. This approximation is valid if one is only interested in the angular behavior of the reflectivity. We will find how the angular dependence of an anisotropy evolves with the angle. We find out also that measuring a circular dichroic signal is not necessary due to a magnetic moment.

The field is applied along one direction, this leads to three possible experimental configurations: **longitudinal**, **transversal** and **polar**. In Fig.3.10 we show these three configurations. With a longitudinal configuration the applied field is along the y direction, with a transversal configuration along the x direction and in the polar configuration along the z direction. We consider each particular case separately and discuss the expressions obtained. In our discussions we consider a saturation field and only the moments in the direction of the applied field contribute to the measurements.
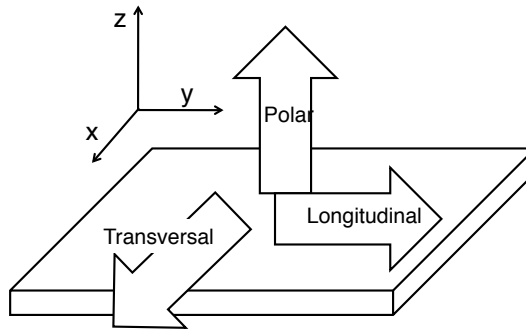

Figure 3.10: Definition of the transversal, longitudinal and polar directions.

3.5.4 Conclusion and Discussion

In the table 3.2 we summarize the anisotropy ratios and the information they give obtained at the appendix A. For each anisotropy ratio R three configurations are studied (Transversal, Longitudinal and Polar). We look at the x,y,z components of a Magnetic system as well as to the x,y,z components of a uniaxial anisotropy system. For example to study a magnetic system with the anisotropy along the x direction, $R_\sigma^{u\ inv}$ in the Polar configuration is the best option.

Table 3.2: Summary of the anisotropies ratios and the information we get from them. 🙂 means it is possible to study it, and 🙂 the best method.

Anisotropy		Magnetic			Uniaxial		
Ratio	Configuration	x	y	z	x	y	z
$R_{\sigma-\pi}^{\pm u}$	Trans	☺	⌢	⌢	⌢	⌢	⌢
	Long	⌢	⌢	⌢	⌢	☺	⌢
	Pol	⌢	⌢	⌢	⌢	⌢	☺
$R_\sigma^{u\ inv}$	Trans	⌢	⌢	⌢	⌢	⌢	⌢
	Long	⌢	⌢	⌢	⌢	⌢	⌢
	Pol	⌢	⌢	⌢	⌢	⌢	⌢
$R_\pi^{u\ inv}$	Trans	☺	⌢	⌢	⌢	⌢	⌢
	Long	⌢	⌢	⌢	⌢	⌢	⌢
	Pol	⌢	⌢	⌢	⌢	⌢	⌢
$R_{C\pm}^{u\ inv}$	Trans	☺	⌢	⌢	⌢	⌢	⌢
	Long	⌢	☺	⌢	⌢	⌢	⌢
	Pol	⌢	⌢	☺	⌢	⌢	⌢
$R_{C_+-C_-}^{\pm u}$	Trans	⌢	⌢	⌢	⌢	⌢	⌢
	Long	⌢	☺	⌢	⌢	⌢	⌢
	Pol	⌢	⌢	☺	⌢	⌢	⌢

We have seen there are several experimental configurations to study an anisotropy. We can either use circular or linear polarization or apply a magnetic or electric field. These techniques are very often used in synchrotron facilities specially with the XMCD related techniques. We conclude that at saturation field the best methods to look for a magnetic component are $R_\pi^{u\ inv\ TRANS}$ in the x direction, $R_{C\pm}^{u\ inv\ Long}$ in the y direction and $R_{C\pm}^{u\ inv\ POL}$ in the z direction. In the case of a non magentic uniaxial system one could only get clear information of the y and z directions performing $R_{\sigma-\pi}^{\pm u\ Long}$. The other component information is crossed with F_1 terms.

Sometimes to work on a saturation field may not be the best option.

Some intrinsic information on the samples magnetization may be destroyed. For this reason some experiments are performed at the remanence field. In this case one gets a reorientation of the magnetic moments from the saturation value to any other directions. This techniques is very much used in resonant magnetic reflectivity measurements to look for the components of the magnetic field in different directions. Here we show only the magnetic case (F_2=0) with the magnetic field applied in one of the three directions, The differences are:

$$
\begin{aligned}
I_{C_+}^{\pm u} - I_{C_-}^{\pm u} &= \pm 4\mathrm{Re}\{F_0 F_1^*\}(u_y \cos^3\theta - u_z \sin^3\theta) \\
I_{C_\pm}^{+u} - I_{C_\pm}^{-u} &= \pm 4\mathrm{Re}\{F_0 F_1^*\}(u_y \cos^3\theta - u_z \sin^3\theta) + \mathrm{Im}\{F_0 F_1^*\}u_x \sin 4\theta \\
I_\pi^{u} - I_\pi^{-u} &= 2\mathrm{Im}\{F_0 F_1^*\}u_x \sin 4\theta
\end{aligned}
$$

The first case shows that with an applied field in one direction and substracting two acquisitions from opposite circular polarizations the resulting data will be sensitive to the y direction of magnetization at small angles and to the z direction of the magnetization at higher angles. In the second case there would be the same angular dependence but there would also be an extra contribution from the x component of magnetization. The third case, using π polarization is the only term that is sensitive to just one component. For the study of a magnetic system using anisotropy ratios we propose the $R_{C_+ - C_-}^{\pm u \ Long \ Trans}$ to search for the y and z components and $R_\pi^{u \ inv \ Trans}$ for the x direction of magnetization.

Here we want to propose another way to study an anisotropy using these ratios. We have seen that the application of a saturation field in a given direction condemns the study to the anisotropy in that direction. Here we propose a way to look at the x and y components at the same time. Instead of applying a magnetic field (and in consequence affecting to all moments) and performing $R_{C_\pm}^{u \ inv}$, one could turn the sample around the z direction 180° and perform two acquisitions with the same photon polarization $R_{C_\pm}^{z \ rot}$ (see Fig. 3.11). This way one is sensitive to both the y and x directions of the anisotropy.

To use our second method, one needs a rotation of 180° for the azimuthal angle. The anisotropy ratios are often used in the soft x-ray range where the diffractometers are in vacuum. Not many chambers have a precise motorized azimuthal rotation and therefore for an experimental point of view this method may not be the best choice. For example in RESOXS diffractometer at synchrotron Soleil, one can perform this kind of rotation, but manually. It is not a very precise rotation and probably one will have to realign the sample
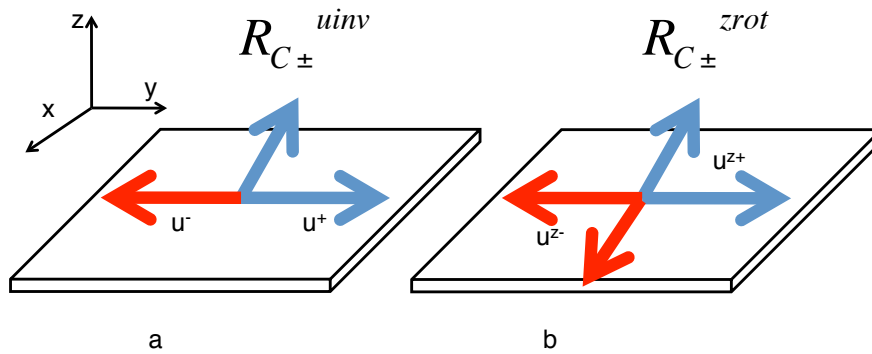
Figure 3.11: (a) Classical anisotropy ratio study $R^{u\ inv}_{C\pm}$ applying and reversing a field along the y direction. (b) Rotating the sample around the z direction. In the second case one changes at the same time both the magnetization in the y and x directions.

after. This would take too much time, and in synchrotron experiments time is something very precious.

Bibliography

[1] L. D. Landau, E. M. Lifshitz, and L. P. Pitaevskii, *Quantum Machanics*. Pergamon Press, 1984.

[2] J. Sakurai, *Modern Quantum Mechanics*. Addison-Wesley, 1994.

[3] J. P. Hannon, G. T. Trammell, M. Blume, and D. Gibbs, "X-ray resonance exchange scattering," *Phys. Rev. Lett.*, vol. 61, pp. 1245–1248, Sep 1988.

[4] J. Als-Nielsen and D. McMorrow, *Elements of Modern X-Ray Physics*. Wiley, 2001.

[5] D. H. Templeton and L. H. Templeton, "Polarization anisotropy of anomalous scattering," *Acta Crystallographica Section A*, vol. 40, no. 397, 1984.

[6] D. Gibbs, D. R. Harshman, E. D. Isaacs, D. B. McWhan, D. Mills, and C. Vettier, "Polarization and resonance properties of magnetic x-ray scattering in holmium," *Phys. Rev. Lett.*, vol. 61, pp. 1241–1244, Sep 1988.

[7] M. Blume, *Resonant Anomalous X-Ray Scattering, Theory and Applications*. Materlik, Sparks and Fisher, 1994.

[8] N. Stojic, N. Binggeli, and M. Altarelli, "Mn l[sub 2,3] edge resonant x-ray scattering in manganites: Influence of the magnetic state," *Physical Review B (Condensed Matter and Materials Physics)*, vol. 72, no. 10, p. 104108, 2005.

[9] C. T. Chen, Y. U. Idzerda, H.-J. Lin, N. V. Smith, G. Meigs, E. Chaban, G. H. Ho, E. Pellegrin, and F. Sette, "Experimental confirmation of the x-ray magnetic circular dichroism sum rules for iron and cobalt," *Phys. Rev. Lett.*, vol. 75, pp. 152–155, Jul 1995.

[10] J. P. Hill and D. McMorrow, "X-ray resonance exchange scattering:polarization dependence and correlation functions," *Acta Cryst*, vol. 52, pp. 236–244, 1996.

[11] J. E. Lorenzo, "*To be published*,"

Chapter 4

Eigen-Wave Formalisms of Resonant Reflectivity

4.1   Introduction

In case of layered materials, reflectivity is a technique of choice to characterize the properties along the growth axis. The aim of reflectivity is to determine structural properties, like atom densities, thicknesses and roughnesses of monolayers, thin films or multilayers. The technique is common in all fields on hard or soft matter. One can determine a magnetic profile within the layers with polarized neutrons reflectivity, but to obtain a chemically specific information, including on the magnetic profile or on local atomic anisotropy due to displacements, one can tune the energy of x-rays in order to work in the resonance regime. X-ray reflectivity data are then analyzed with simulations based on a classical Maxwell approach to solve the propagation of the waves in the media and with a quantum mechanical description for the atomic interactions. Parratt formalism is mostly applied on all kind of systems, when no magnetism or anisotropy is present. When dealing with magnetism, the most used formalism is the one proposed by Zak *et al.* [1], originally written for optics (Kerr, Faraday effects) but used just as well in the x-ray range.

While studying Zak's formalism to understand all the steps and evaluate the approximations performed, we came to realize that a slightly different formalism could be derived by using eigen-waves throughout all the steps, thereby gaining in simplicity (a little), in logic and coherence (same polarization basis throughout all the formalism steps) and in computing speed (a lot). This study was also beneficial to the development of a similar formalism for materials with an electronic anisotropy. In this case, we also realized that we could extend the Parratt formalism, leading to a much simpler formalism, and a much faster code. Both formalisms have been coded in a Matlab environment program called Dyna whose development was started just near the beginning of this thesis in our group. In this chapter, we present the two formalisms, the methods and applications.

4.2   Boundary Propagation matrices method

In the first of the following sections, we present the principles and successive steps of the boundary-propagation matrices (BPM) method. In the second section, we present the case of a magnetic system, and in a third the case of an anisotropic system, whose anisotropy is along the normal to the surface of the sample. The core of the formalism was published in [2].

4.2.1 Principles of the method

In our Boundary Propagation matrices method we will use the so-called eigen-waves as propagating waves. Eigen-waves are waves that do not change their polarization state as they propagate. We calculate the indices of refraction corresponding to a wave that does not change its polarization state, using Maxwell equations. Then one determines from the indices of refraction the polarization state they correspond to, which gives us the eigen-waves. Then one has to determine the matrix that solves the reflectivity at each interface: This matrix projects the two eigen-waves, onto planar components of the electric and magnetic fields. The boundary conditions are solved equating the planar components with those of the next medium (Snell's law). The roughness of the interface is also considered. Then, one gets the propagation matrix, which is diagonal thanks to the use of eigen-waves, until the next interface is reached, and so on. To summarize, the method consists in the following steps:

1. Determine constitutive equations

2. Calculate the indices of refraction

3. Identify the eigen-waves

4. Determine the boundary matrix

5. Determine the propagation matrix

6. Apply roughness corrections

7. Multiply matrices throughout the stack of layers

Let's give some details on these steps:

4.2.1.1 Constitutive equations, permittivity, permeability

The constitutive equations describe the response of a material to an exciting field. The responses are described by the electric induction field $\mathbf{D}$ in response to the electric field $\mathbf{E}$, and the magnetic induction $\mathbf{B}$ in response to the magnetic field $\mathbf{H}$[1]. In the general case we assume that the medium has a linear, tensorial and dispersive response to the electric field and a simple

---

[1]The names of the fields are a question of context and maybe a question of taste too: $\mathbf{D}$ is also called "displacement field", $\mathbf{B}$ is also called "magnetic field" and $\mathbf{H}$ is also called "magnetizing field".

linear, scalar response to the magnetic field. The response is characterized by the electric permittivity $\hat{\epsilon}$ for the electric displacement, and the magnetic permeability μ for the magnetic induction:

$$D_i = \epsilon_{ij}E_j, \ \mathbf{B} = \mu\mathbf{H} \tag{4.1}$$

where ϵ_{ij} is a tensorial dielectric permittivity with $i, j = x, y, z$ which takes into account the process of magnetic resonant x-ray scattering. The relation between the dielectric permitivity ϵ and the scattering factor is:

$$\begin{aligned} \hat{\chi} &= \frac{4\pi}{k_0^2}\sum_a n_a\hat{f}_a \\ \hat{\epsilon} &= 1 + \hat{\chi} \end{aligned} \tag{4.2}$$

with n_a the number of atom a per unit volume, χ the dielectric susceptibility and $\hat{f}_a$ its scattering length.
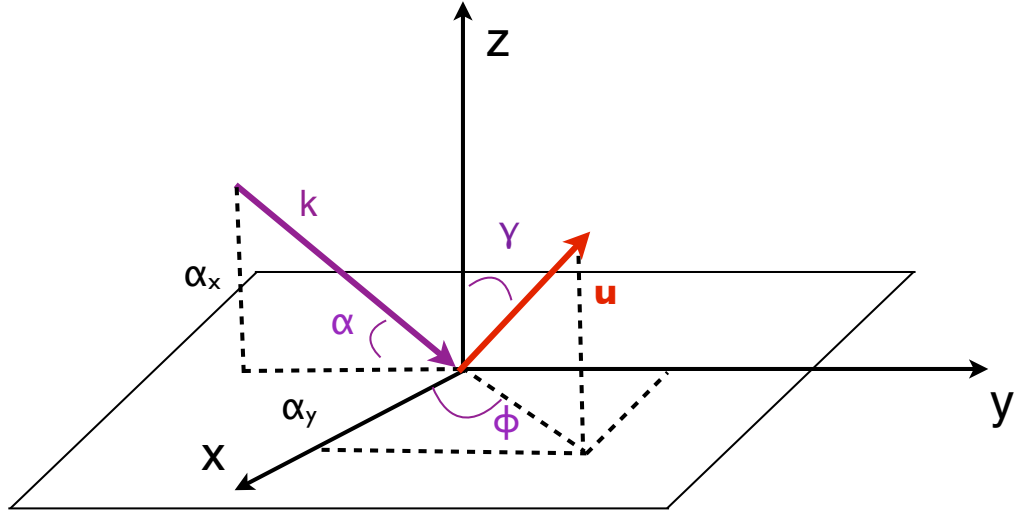

Figure 4.1: Definition of angles used throughout the formalism. Here, $\mathbf{k}$ is a unit vector, $\alpha_y = \cos\alpha$ and $\alpha_z = \sin\alpha$. The referential (x', y', z') is attached to the wave vector, with $x' = x$ and $\boldsymbol{k} = \hat{\boldsymbol{z}}'$, $\mathbf{u}$ is a unit vector describing the systems anisoptropy.

4.2.1.2   Index of refraction

The effect of the medium on the waves is essentially reduced to a change on the direction and amplitude of the wave vector, in addition to a reduction of the amplitude by absorption. Therefore, solutions to the propagation

equation are sought in the form of propagating plane waves with a wave vector that is changed to $\mathbf{k} = (n_x k_{0x}, n_y k_{0y}, n_z k_{0z})$ with k_0 the wave vector in vacuum, $k_0 = 2\pi/\lambda$, and defining $\mathbf{n}$, the index of refraction. The index $\mathbf{n}$ is imposed by Maxwell equations with the constitutive equations, and is obtained by combining Maxwell equations:

$$
\begin{aligned}
\bigtriangledown \times \mathbf{E} &= -\frac{\partial \mathbf{B}}{\partial t} \\
\bigtriangledown \times \mathbf{B} &= \hat{\epsilon} \mu \frac{\partial \mathbf{E}}{\partial t}
\end{aligned}
\tag{4.3}
$$

for a monochromatic plane wave with $\mathbf{k} = \frac{2\pi}{\lambda}\mathbf{n}$, leading to:

$$
\mathbf{n} \times (\mathbf{n} \times \boldsymbol{E}) + \hat{\epsilon}\mathbf{E} = 0,
\tag{4.4}
$$

which constrains the indices of refraction with respect to the permittivity [3]. Solving this equation, we obtain typically two indices of refraction, corresponding to two eigen-waves with polarizations p_1 and p_2.

4.2.1.3 Identifying the eigen-waves

Eigen waves are the waves with the indices of refraction obtained as explained before which do not undergo a change in their polarization state while propagating. Returning to Maxwell's equation and the relation $\mathbf{n} \times (\mathbf{n} \times \mathbf{E}) + \hat{\epsilon}\mathbf{E} = 0$, rewritten explicitly as $\mathbf{D} = \mathbf{n} \times (\mathbf{E} \times \mathbf{n})$ and with the explicit form of $\mathbf{n}$, one gets an expression of $\mathbf{D}$ which is equivalent to the photon polarization of the propagating wave in the medium. We will see that, for magnetic materials, $\mathbf{D}$ components ratio is i, and is kept constant while propagating, which identifies circular waves as eigen-waves for propagation.

4.2.1.4 Boundary conditions

Once the dielectric tensor $\hat{\epsilon}$ is calculated and the $\mathbf{D}_{p1}$ and $\mathbf{D}_{p2}$ eigen-waves known, we consider how boundary conditions at the interfaces can be treated for these waves. Maxwell equations impose conservation of the planar components of the "exciting" fields, the electric $\mathbf{E}$ and the magnetic $\mathbf{H}$ fields, at interfaces. From the constitutive equations and Maxwell equations we have:

$$
\begin{aligned}
\mathbf{E} &= \hat{\epsilon}^{-1}\mathbf{D} & (4.5) \\
\mathbf{H} &= \mathbf{n} \times \mathbf{E} = \mathbf{n} \times (\hat{\epsilon}^{-1}\mathbf{D}) & (4.6)
\end{aligned}
$$

where the exciting fields are written as a function of the electric induction field, which represents the propagating waves. Equations (4.5) and (4.6) are

six expressions for the electromagnetic fields components, but only the four planar components, say x and y, are concerned with the boundary conditions. One then introduces a matrix we call $\hat{A}_m$ whose "job" is all mathematical. It projects (or "decomposes") $\mathbf{D_m}$ of the eigen-waves amplitudes into the x and y planar component of the electric and magnetic fields in medium m:

$$A_m D_m = \begin{pmatrix} (\hat{\epsilon}_m^{-1}\mathbf{D}_m)_x \\ (\hat{\epsilon}_m^{-1}\mathbf{D}_m)_y \\ (\mathbf{n} \times \hat{\epsilon}_m^{-1}\mathbf{D}_m)_x \\ (\mathbf{n} \times \hat{\epsilon}_m^{-1}\mathbf{D}_m)_y \end{pmatrix} = \begin{pmatrix} E_{x,m} \\ E_{y,m} \\ H_{x,m} \\ H_{y,m} \end{pmatrix} \tag{4.7}$$

A_m is a 4x4 matrix, and there is one for each media. We will see two examples in the next sections, one for a magnetic medium, one for an anisotropic medium. The benefit of calculating the A matrix is that one can now use matrix algebra. The boundary conditions,

$$\begin{aligned} E_{x,m} &= E_{x,m+1} \\ E_{y,m} &= E_{y,m+1} \\ H_{x,m} &= H_{x,m+1} \\ H_{y,m} &= H_{y,m+1} \end{aligned}$$

or

$$\begin{aligned} (\hat{\epsilon}_m^{-1}\mathbf{D}_m)_x &= (\hat{\epsilon}_{m+1}^{-1}\mathbf{D}_{m+1})_x \\ (\hat{\epsilon}_m^{-1}\mathbf{D}_m)_y &= (\hat{\epsilon}_{m+1}^{-1}\mathbf{D}_{m+1})_y \\ (\mathbf{n} \times \hat{\epsilon}_m^{-1}\mathbf{D}_m)_x &= (\mathbf{n} \times \hat{\epsilon}_{m+1}^{-1}\mathbf{D}_{m+1})_x \\ (\mathbf{n} \times \hat{\epsilon}_m^{-1}\mathbf{D}_m)_y &= (\mathbf{n} \times \hat{\epsilon}_{m+1}^{-1}\mathbf{D}_{m+1})_y \end{aligned} \tag{4.8}$$

can be written more concisely as:

$$A_m D_m = A_{m+1} D_{m+1} \tag{4.9}$$

We see that the boundary conditions relate the permittivity of the media with the amplitude of the wave passing through the boundary with amplitude D_m and D_{m+1} in each medium. That is, knowing the amplitude in the mth layer eq:4.8 gives the amplitude in the $(m+1)^{th}$ layer:

$$D_{m+1} = A_{m+1}^{-1} A_m D_m \tag{4.10}$$

Now, instead of expressing the x and y component of each eigen-waves, we will refer to their amplitude D_m. The x and y components are found to

be proportional to this amplitude (see next sections). We will keep track of the amplitude of the eigen-waves with the vector $\mathbf{D}_m$

$$\mathbf{D}_m = \begin{pmatrix} D_m^{p_1\downarrow} \\ D_m^{p_2\downarrow} \\ D_m^{p_1\uparrow} \\ D_m^{p_2\uparrow} \end{pmatrix} \qquad (4.11)$$

where $D_m^p \downarrow\uparrow$ is the amplitude of the electric induction, or, the eigen-wave amplitude with p polarization, propagating downward or upward. We feel that there is no much confusion to use the letter D for this 4x1 vector because of its close relationship with the electric induction vectors of the waves.

4.2.1.5 Propagation

Now we consider the propagation of the waves within the medium. The change of the phase they undergo is $\phi = \frac{2\pi}{\lambda} n \alpha_z z$ and it is described by the propagation matrix P:

$$P_m(z) = \begin{pmatrix} e^{-i\phi^{p_1\downarrow}} & 0 & 0 & \\ 0 & e^{-i\phi^{p_2\downarrow}} & 0 & 0 \\ 0 & 0 & e^{-i\phi^{p_1\uparrow}} & 0 \\ 0 & 0 & 0 & e^{-i\phi^{p_2\uparrow}} \end{pmatrix}$$

with n the index of refraction, $\alpha_z z$ the position of the wave in the out-of-plane direction. P_m is diagonal, a benefit of describing the waves projected onto a basis of eigen-waves. It will ease the matrix algebra and the coding of the formalism. It is one obvious difference from Zak's formalism.

4.2.1.6 Matrix product to calculate the reflectivity

Finally, in case of a multilayer, one multiplies the matrices corresponding to the boundary conditions at each interface with the matrices corresponding to the propagation in each layer, see Figure 4.2. The polarization state in the final layer is:

$$\begin{aligned} D_f &= A_f^{-1} \left(\prod_m A_m P_m A_m^{-1} \right) A_0 D_i & (4.12) \\ &= M D_i & (4.13) \end{aligned}$$

The matrix M is a 4x4 matrix which relates the polarization states of the incoming and outgoing waves in the vacuum, to the transmitted waves into
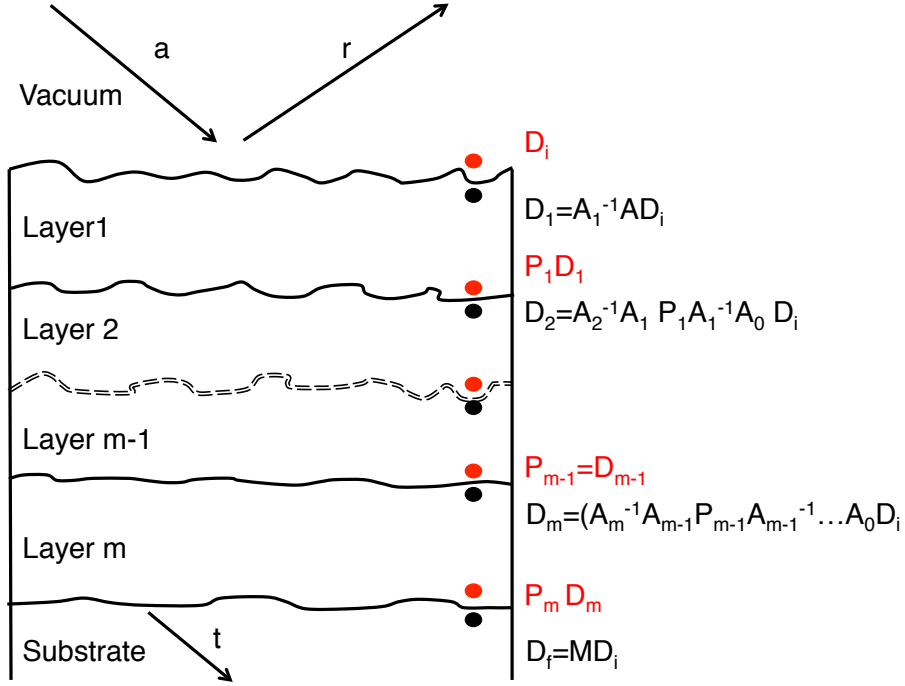
Figure 4.2: Scheme indicating the reflectivity process. $D_i = E_i$ is the polarization state of the electromagnetic field in the vacuum; $A_m^{-1}A_{m-1}$ relates the polarization states on both sides of an interface. P_m propagates the wave between the two interfaces of the m-th layer. a is the incoming beam, r the reflected beam and t the transmitted beam.

the last medium, defined as the medium in which there is no returning waves, like an homogeneous infinite substrate or vacuum.

We obtain a system of four equations. The system is solved by the conditions that the two amplitudes of the incident eigen-wave states are known, and the two amplitudes of the states coming upward from the last layer are zero (it is either vacuum or an infinite substrate in which the waves is only transmitted and nothing comes back):

$$D_i = M^{-1}D_f$$

or

$$\begin{pmatrix} a_{p_1} \\ a_{p_2} \\ r_{p_1} \\ r_{p_2} \end{pmatrix} = M^{-1} \begin{pmatrix} t_{p_1} \\ t_{p_2} \\ 0 \\ 0 \end{pmatrix} \tag{4.14}$$

where the unknowns are the reflectivity coefficients r for the two polarizations, t the transmittivity for each polarization state, and the inputs are a the initial polarization states of the incident photon expressed in the basis of the eigen-waves. We then have to solve the equations:

$$\begin{pmatrix} r_{p1} \\ r_{p2} \end{pmatrix} = \frac{1}{d} \times$$

$$\begin{pmatrix} M_{41}M_{34} - M_{31}M_{44} & M_{34}M_{42} - M_{32}M_{44} \\ M_{43}M_{31} - M_{41}M_{33} & M_{32}M_{43} - M_{33}M_{42} \end{pmatrix} \begin{pmatrix} a_{p1} \\ a_{p2} \end{pmatrix}$$

(4.15)

with $d = M_{44}M_{33} - M_{34}M_{43}$.

4.2.1.7 Roughness

The roughness of the interface is considered with a Debye-Waller treatment. Associated with this type of correction is the assumption that the roughness is stationary, the roughness σ is not dependent of the point under consideration. It is also supposed that the fluctuation of the thickness can vary laterally because of the roughness at the interface. The fluctuation has to be smaller than the thickness of the layer [4]. At the interface of the $m-1$ layer with the m layer, the matrix element of the matrix $A_m^{-1}A_{m-1}$ must be multiplied by $e^{\pm} = e^{-(k_m \pm k_{m+1})^2 \sigma^2/2}$. The $\pm$ stands for the matrix element that relies waves with the same or different direction of propagation. For a general case we have:

$$W_{m,m+1} = \begin{bmatrix} e^- & e^- & e^+ & e^+ \\ e^- & e^- & e^+ & e^+ \\ e^+ & e^+ & e^- & e^- \\ e^+ & e^+ & e^- & e^- \end{bmatrix}$$

W is not a matrix, but a table of values to be multiplied by each element of the matrix $A_m^{-1}A_{m-1}$.

4.2.2 X-ray Resonant Magnetic Reflectivity

In practice, this information allows the simulation of X-ray resonant magnetic reflectivity. X-ray resonant magnetic reflectivity (XRMR) yields the magnetization density across ultra-thin magnetic materials. Two specificities have established the technique as a complement to macroscopic techniques or polarized neutron scattering: a sensitivity to the orientation and the amplitude of the local magnetic moment with a spatial resolution below the nanometer,

and the selection of the chemical element contributing to the magnetization. XRMR has been applied to several types of thin films, multi-layers and superlattices to determine the distribution of the magnetic moment density along the growth axis. The technique has proven (i) to be efficient on single magnetic layer in the nanometer thickness range [5, 6], (ii) to have a spatial resolution in the subnanometer range [7, 8, 9] and (iii) to be sensitive to small modifications at antiferromagnetic interfaces [10]. Induced magnetization of non-magnetic elements has also been investigated [11]. The profile is averaged in both directions parallel to the plane but with a resolution about the Angström along the depth of the films. The sensitivity of resonant X-rays to all three components of the local magnetic moment has been exploited in various cases. For instance, Tonnerre *et al.* reported on the sensitivity to the moment normal to the surface, a timely application for the growing field of perpendicular magnets [8]. In this section we apply the Boundary Propagation method to the case of magnetic media to retrieve magnetization profiles in media such as thin films or multilayers on substrates, with magnetization in any direction. It can also be applied to magneto-optics if the magnetic correction to the permittivity is relatively small. Finally, we present an application of the formalism on a W/Fe/W trilayer.

4.2.2.1   Constitutive equations

In the case of a magnetic media the scattering amplitude is (see Chapter Basics):

$$\hat{f}_{e'e} = (\boldsymbol{e'^*} \cdot \boldsymbol{e}) \, F_0 - i(\boldsymbol{e'^*} \times \boldsymbol{e}) \cdot \boldsymbol{u} \, F_1 \qquad (4.16)$$

with $\boldsymbol{e}$ and $\boldsymbol{e'^*}$ the polarization vectors of the incoming and outcoming waves and $\boldsymbol{u}$ the vector describing the magnetic anisotropy. Let's rewrite $\hat{f}_{e'e}$ as a matrix to built the dielectric permittivity ϵ_{ij}. This is done by decomposing $\hat{f}_{e'e}$ in the x, y and z directions so that one can write $\hat{f}_{e'e}$ as $\boldsymbol{e'^*} \cdot \hat{f} \cdot \boldsymbol{e}$, which mathematically means that $\hat{f}$ is the scattering tensor written in the basis of the polarization vectors. With the referential in Figure 4.1 we get:

$$\hat{f} = \begin{pmatrix} F_0 & -iu_zF_1 & iu_yF_1 \\ iu_zF_1 & F_0 & -iu_xF_1 \\ -iu_yF_1 & iu_xF_1 & F_0 \end{pmatrix} \qquad (4.17)$$

In Figure 4.3 we show the dielectric terms of the Fe atom. These values were obtained from the experimental factors of the atomic form factor shown in the previous chapter Fig. 3.7. Using the relation between the permittivity and the scattering factor, expression (4.2) and together with expression
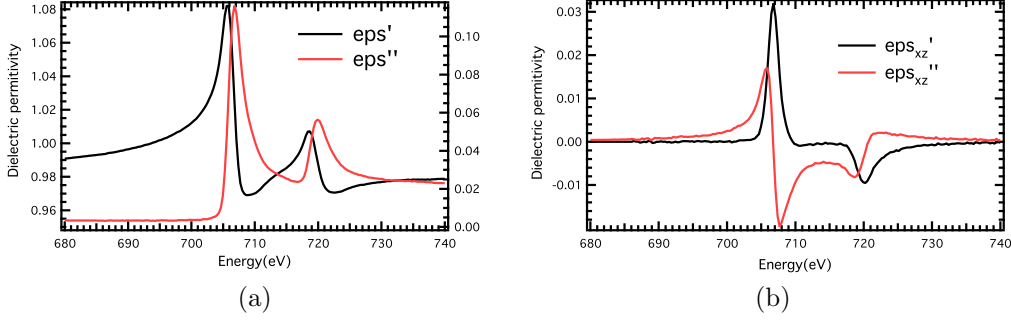
Figure 4.3: (a)Real and imaginary parts of the magnetic-independent dielectric tensor elements of Fe atoms near the $L_{2,3}$ edge.(b)Real and imaginary parts of the magnetic-dependent dielectric tensor elements of Fe atoms near the $L_{2,3}$ edge

(4.16), one derives the expression of the dielectric tensor for a magnetic system:

$$\hat{\epsilon} = \begin{pmatrix} \epsilon_{xx} & \epsilon_{xy} & \epsilon_{xz} \\ -\epsilon_{xy} & \epsilon_{xx} & \epsilon_{yz} \\ -\epsilon_{xz} & -\epsilon_{yz} & \epsilon_{xx} \end{pmatrix} \tag{4.18}$$

where

$$\begin{aligned}
\epsilon_{xx} &= 1 + \frac{4\pi}{k_0^2} \rho \, F_0 \\
\epsilon_{xy} &= -i\frac{4\pi}{k_0^2} \rho \, u_z \, F_1 \\
\epsilon_{xz} &= i\frac{4\pi}{k_0^2} \rho \, u_y \, F_1 \\
\epsilon_{yz} &= -i\frac{4\pi}{k_0^2} \rho \, u_x \, F_1
\end{aligned} \tag{4.19}$$

which gives an antisymmetric tensor whose diagonal terms are all equal. This expression of the dielectric function, in particular the antisymmetric nature derives directly from the scattering amplitude (eq. 4.16). Note that F_0 and F_1 are complex quantities.

We have now the first constitutive equation, an expression of the electric induction $\mathbf{D} = \hat{\epsilon}\mathbf{E}$.

Due to spin-orbit effects in the core-hole at the resonance, we assume that the origin of the magnetic scattering is purely electric. We will then assume $\mu = 1$, then $\boldsymbol{B}=\boldsymbol{H}$.

4.2.2.2   Index of refraction

The indices of refraction for such constitutive equations have to fulfill the equation (4.4), which is solvable if the determinant is zero:

$$|n^2 \delta_{ik} - n_i n_k - \epsilon_{ik}| = 0. \qquad (4.20)$$

To solve this equation, let's consider temporally a referential attached to a wave propagating along z', then $\boldsymbol{n} = n(0,0,1)$ and the solutions in this referential are:
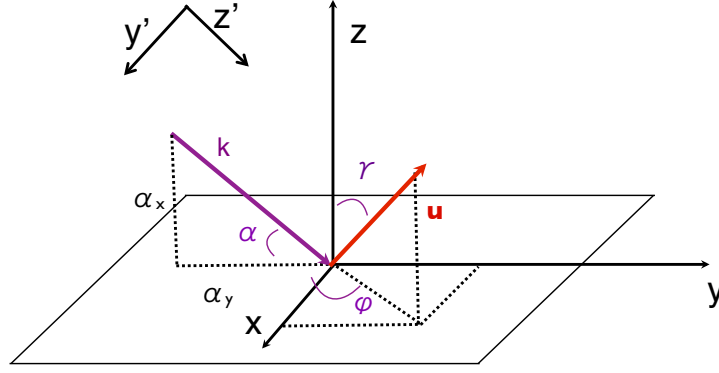

Figure 4.4: Definition of angles used throughout the formalism. Here, $\mathbf{k}$ is a unit vector, $\alpha_y = \cos \alpha$ and $\alpha_z = \sin \alpha$. The referential (x', y', z') is attached to the wave vector, with $x' = x$ and $\boldsymbol{k} = \hat{\boldsymbol{z}}'$. $\mathbf{u}$ is the unit vector describing the magnetization.

$$n^2 = \epsilon + \frac{\epsilon_{x'z'}^2 + \epsilon_{y'z'}^2 \pm \sqrt{(\epsilon_{x'z'}^2 + \epsilon_{y'z'}^2)^2 - 4\epsilon^2 \epsilon_{x'y'}^2}}{2\epsilon}$$

This equation has four solutions one pair is formed by each eigen-wave polarization, the two pairs corresponding to the two directions of propagation, upward and downward, that is incoming and outgoing.

To proceed with the development of the formalism, for now on, we limit our case to the approximation $\epsilon_{ij} << \epsilon$, neglecting second order of the off-diagonal terms of the permittivity (see Fig. 4.3). Its justification is based on experiments and calculations, but it should be checked for each case. By experience, one observes that this approximation is totally justified for soft x-rays, which is the regime the technique is the most employed. Indeed, even if the magnetic-dependent scattering amplitude is of the same order than r_0,

the most important term is the first order term. Therefore, an approximate form for one pair of the index of refraction gives:

$$n^\pm \approx \sqrt{\epsilon \pm i\epsilon_{x'y'}}$$

Expliciting the permittivity:

$$n^\pm = \sqrt{1 + \frac{4\pi}{k_0^2}\rho(F_0 \pm u_{z'}F_1)} \approx 1 + \frac{2\pi}{k_0^2}\rho(F_0 \pm u_{z'}F_1). \qquad (4.21)$$

In the referential of figure 4.4, the index of refraction only depends on the component of the magnetic moment that is along the propagation vector. In the general case the propagation of the wave can be in any direction. Then, generalizing, the index of refraction becomes:

$$n^\pm = \sqrt{1 + \frac{4\pi}{k_0^2}\rho(F_0 \pm \hat{\boldsymbol{k}} \cdot \boldsymbol{u}F_1)} \approx 1 + \frac{2\pi}{k_0^2}\rho(F_0 \pm \hat{\boldsymbol{k}} \cdot \boldsymbol{u}F_1) \qquad (4.22)$$

The planar component of the wave vector is conserved (Snell's law):

$$n_0\alpha_{y0} = n^+\alpha_y^+ = n^-\alpha_y^-$$

That is, in magnetic media, the wave vectors of the two eigen waves generally have different directions unless the local magnetization $\boldsymbol{u}$ is perpendicular to the propagation vector. We must now find the polarizations of the waves that have these indices of refraction.

4.2.2.3 Determining the eigen-waves

If we combine these expressions with $\boldsymbol{D} = \boldsymbol{n} \times (\boldsymbol{n} \times \boldsymbol{E})$ and writing the x', y' and z' components of the electric induction, we have:

$$\begin{aligned} D_{x'} &= (\epsilon \pm i\epsilon_{x'y'})E_{x'} \\ D_{y'} &= (\epsilon \pm i\epsilon_{x'y'})E_{y'} \\ D_{z'} &= 0 \end{aligned}$$

and equating with $D_i = \epsilon_{ij}E_j$, one finds the ratio:

$$D_{y'}/D_{x'} \approx \pm i \text{ associated with } n^\pm = \sqrt{\epsilon \pm i\epsilon_{x'y'}}$$

This is the same relation we find for the circular polarized waves (see eq 4.23). In conclusion, the eigen-waves propagating in a magnetic medium without spin-orbit coupling, with the permittivity as in expr. (4.19), and with the

approximation that $\epsilon_{ij} << \epsilon$ are circularly polarized waves. For now on we will express our eigen-waves p_1 and p_2 as $+$, $-$ or C^-, C^+. In that same temporally reference frame, the circular waves have for general components:

$$\mathbf{D}^{\pm} = \mp \frac{D_{x'}^{\pm}}{\sqrt{2}} \begin{pmatrix} 1 \\ \pm i \\ 0 \end{pmatrix} \tag{4.23}$$

In the laboratory referential depicted in Figure 4.4, the components of the waves become:

$$\mathbf{D}^{\pm} = \frac{D_x^{\pm}}{\sqrt{2}} \begin{pmatrix} \mp 1 \\ i\alpha_z^{\pm} \\ i\alpha_y^{\pm} \end{pmatrix} \tag{4.24}$$

These are the eigen-waves of a magnetic medium with the dielectric tensor having small antisymmetric off-diagonal terms, and constant diagonal terms. Circular polarized beams are easily obtainable in soft x-ray beamlines and most of reflectivity experiments are done with these polarizations. We will now continue with our formalism using C^+ C^- polarized waves. Let's derive A_m, that projects the circular waves onto x and y components of the electromagnetic fields so that we can apply the boundary conditions.

4.2.2.4   Boundary conditions

Following expression (4.7), we need to invert the antisymmetric dielectric tensor:

$$\hat{\epsilon}^{-1} = \frac{1}{|\epsilon|} \begin{pmatrix} 1 + \epsilon_{yz}^2 & -\epsilon_{xy} - \epsilon_{xz}\epsilon_{yz} & -\epsilon_{xy} + \epsilon_{xy}\epsilon_{yz} \\ \epsilon_{xy} - \epsilon_{xz}\epsilon_{yz} & 1 + \epsilon_{xz}^2 & -\epsilon_{yz} - \epsilon_{xy}\epsilon_{xz} \\ \epsilon_{xy} + \epsilon_{xy}\epsilon_{yz} & +\epsilon_{yz} - \epsilon_{xy}\epsilon_{xz} & 1 + \epsilon_{xy}^2 \end{pmatrix}$$

Keeping with our approximation that second order ϵ_{ij} are negligible, the inverse of the antisymmetric dielectric function becomes:

$$\hat{\epsilon}^{-1} \approx \frac{1}{\epsilon} \begin{pmatrix} 1 & -\epsilon_{xy} & -\epsilon_{xz} \\ \epsilon_{xy} & 1 & -\epsilon_{yz} \\ \epsilon_{xz} & \epsilon_{yz} & 1 \end{pmatrix} \tag{4.25}$$

Introducing this expression in Maxwell equations and using the eigen-waves found in equation (4.24) we write the x, y, z components of the electric

field as:

$$
\begin{aligned}
E_x^\pm &= D_x^\pm \frac{1}{\sqrt{2\epsilon}} \left(\mp 1 - i\epsilon_{xy}\alpha_z^\pm - i\epsilon_{xz}\alpha_y^\pm \right) \\
E_y^\pm &= D_x^\pm \frac{1}{\sqrt{2\epsilon}} \left(\mp \epsilon_{xy} + i\alpha_z^\pm - i\epsilon_{yz}\alpha_y^\pm \right) \\
E_z^\pm &= D_x^\pm \frac{1}{\sqrt{2\epsilon}} \left(\mp \epsilon_{xz} + i\epsilon_{yz}\alpha_z^\pm + i\alpha_y^\pm \right)
\end{aligned}
\tag{4.26}
$$

using equation (4.6) the x, y components of the magnetic field are:

$$
\begin{aligned}
H_x^\pm &= D_x^\pm \frac{1}{\sqrt{2\epsilon}} \, n^\pm (i \mp \epsilon_{xy}\alpha_z^\pm \mp \epsilon_{xz}\alpha_y^\pm) \\
H_y^\pm &= D_x^\pm \frac{1}{\sqrt{2\epsilon}} \, n^\pm \alpha_z^\pm (\pm 1 + i\epsilon_{xy}\alpha_z^\pm + i\epsilon_{xz}\alpha_y^\pm)
\end{aligned}
$$

From here we have the terms that will be used to built the A_m matrix. With a close look at the resulting expressions one can reduce the writing of the magnetic field planar components to $H_x^\pm = \mp i n^\pm E_x^\pm$ and $H_y^\pm = -\alpha_z^\pm n^\pm E_x^\pm$.

We can now build the boundary matrix A_m for the medium m:

$$
A_m = \tfrac{1}{\sqrt{2\epsilon}} \times
$$

$$
\begin{bmatrix}
A_x^{+\downarrow} & A_x^{-\downarrow} & A_x^{+\uparrow} & A_x^{-\uparrow} \\
A_y^{+\downarrow} & A_y^{-\downarrow} & A_y^{+\uparrow} & A_y^{-\uparrow} \\
-in^{+\downarrow}A_x^{+\downarrow} & in^{-\downarrow}A_x^{-\downarrow} & -in^{+\uparrow}A_x^{+\uparrow} & in^{-\uparrow}A_x^{-\uparrow} \\
-\alpha_z^+ n^{+\downarrow}A_x^{+\downarrow} & -\alpha_z^- n^{-\downarrow}A_x^{-\downarrow} & \alpha_z^+ n^{+\uparrow}A_x^{+\uparrow} & \alpha_z^- n^{-\uparrow}A_x^{-\uparrow}
\end{bmatrix}
$$

where

$$
\begin{aligned}
A_x^{\pm\downarrow} &= \mp 1 - i\epsilon_{xy}\alpha_z^\pm - i\epsilon_{xz}\alpha_y^\pm \\
A_y^{\pm\downarrow} &= \mp \epsilon_{xy} + i\alpha_z^\pm - i\epsilon_{yz}\alpha_y^\pm \\
A_x^{\pm\uparrow} &= \mp 1 + i\epsilon_{xy}\alpha_z^\pm - i\epsilon_{xz}\alpha_y^\pm \\
A_y^{\pm\uparrow} &= \mp \epsilon_{xy} - i\alpha_z^\pm - i\epsilon_{yz}\alpha_y^\pm
\end{aligned}
$$

4.2.2.5 Propagation

Thanks to our basis, the propagation matrix is diagonal:

$$
P_m(z) =
\begin{pmatrix}
e^{-i\phi^{+\downarrow}} & 0 & 0 & 0 \\
0 & e^{-i\phi^{-\downarrow}} & 0 & 0 \\
0 & 0 & e^{i\phi^{+\uparrow}} & 0 \\
0 & 0 & 0 & e^{i\phi^{-\uparrow}}
\end{pmatrix}
$$

$$
\tag{4.27}
$$

with $\phi = \frac{2\pi}{\lambda} n \alpha_z z$ the phase of the wave.

4.2.2.6   Reflectivity

Then the reflectivity intensities are directly obtained from expression (4.15). Note that if one want to use σ and π polarizations instead, as incident waves, we only apply the relation $C^\pm = \mp 1/\sqrt{2}(\sigma \pm i\pi)$ in order to use all the previous expressions.

4.2.2.7   Kerr effect

We mentioned that this method is also applicable to magneto optical kerr (MOKE) measurements if the magnetic correction to the permittivity is relatively smallI. Kerr Rotation is the rotation of the polarization plane and Kerr Ellipticity the appearance of elliptical polarization when linearly polarized light is reflected from samples that have a magnetization component parallel or antiparallel to the propagation direction of the light. [12]: Using our formalism the Kerr parameters for σ and π are:

$$\text{Kerr}(\sigma)_{\text{rot}} = \text{Re}\frac{M_{12}}{M_{11}} \quad \text{Kerr}(\sigma)_{\text{ellip}} = \text{Im}\frac{M_{21}}{M_{11}}$$

$$\text{Kerr}(\pi)_{\text{rot}} = \text{Re}\frac{M_{21}}{M_{22}} \quad \text{Kerr}(\pi)_{\text{ellip}} = \text{Im}\frac{M_{21}}{M_{22}}$$

4.2.3   XRMR of the ferromagnetic layer W/Fe/W

As an example of our formalism we analyzed room temperature (RT) hard non-resonant and soft resonant magnetic reflectivity obtained at the Fe L_3-edge (706.8 eV) for a trilayer W/Fe/W. This part of the study was performed jointly with Emmanuelle Jal, PhD student in the same group. The multilayer was grown on Al_2O_3 by Pulsed Laser Deposition (the tungsten layers are used as a buffer and as a protection from oxidation). In order to determine the structural parameters, hard X-ray specular reflectivity shown in Fig. 4.5 was measured with a laboratory X-ray source (Cu Kα). The results of the refinement are summarized in Table 4.1.

   As mentioned in the preceding chapter, the magnetic signal is extracted from two successive measurements of the reflectivity corresponding to reversing either the direction of the magnetization or the polarization of the incoming photon. There is a choice for two experimental configurations. For one configuration, one specific photon polarization is chosen, being right, left circular or σ and π linear, and the magnetic field is reversed between two

Table 4.1: Structural parameters obtained from the refinement of the hard X-ray reflectivity of the W/Fe/W trilayer.

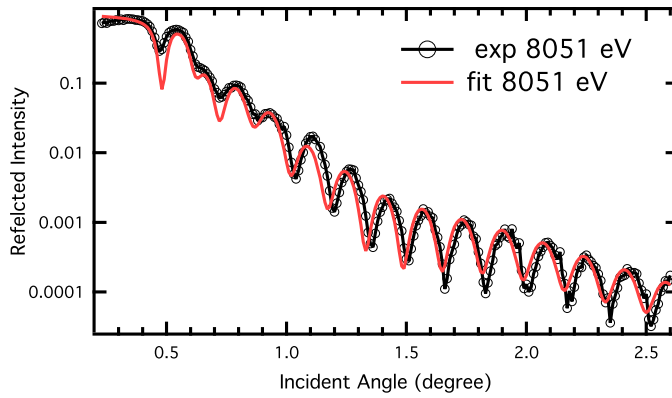| Layer	d(Å)	σ(Å)	ρ(mol cm^{-3})	ρ(g cm^{-3})
W	31.3	1.4	0.105	19.30
Fe	91.5	5.1	0.141	7.875
W	134.1	11.6	0.105	19.30
Al$_2$O$_3$		5.9	0.038	3.876

Figure 4.5: Experimental (symbols) and calculated (solid line) specular reflectivity for W/Fe/W at 8051 eV

measurements. For the second configuration, the applied field is fixed, and the reflectivity is successively measured with the left and right circular polarizations. It is also possible, as in a XMLD experiment, to measure the contrast induced by two perpendicular incident linear polarizations of the photon. Note that the two configurations are generally equivalent, but not always, in particular when the magnetization exhibits a transverse magnetic component. The direction of the applied magnetic field is chosen according to the properties of the magnetic hysteresis, for instance along an easy magnetization axis.

The soft X-ray resonant magnetic scattering measurements were taken by switching the direction of a saturating applied magnetic field on U4B of the National Synchrotron Light Source (USA). The magnetic field (0.04 T) was applied parallel to the surface of the sample, either in the scattering plane, the so-called longitudinal configuration, or transverse to the scattering plane, the transverse configuration. In the first configuration, circular polarized light was used, and linear π polarized light for the transverse configuration. Figure
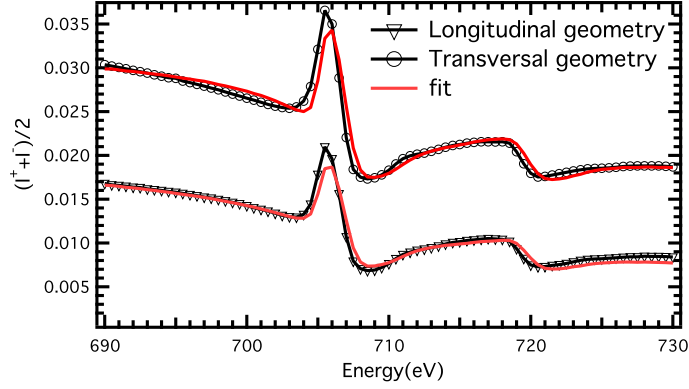
Figure 4.6: Experimental (symbols) and calculated (solid line) of the specular reflectivity vs energy for an incident angle of 10°deg. longitudinal geometry: applied field parallel to the surface, in the scattering plane, summing spectra for incident right and left circularly polarized light. Transversal geometry: incident π polarized light summing spectra from reversing a transverse field, applied parallel to the surface and perpendicular to the scattering plane (vertically offset by 0.01 for clarity)
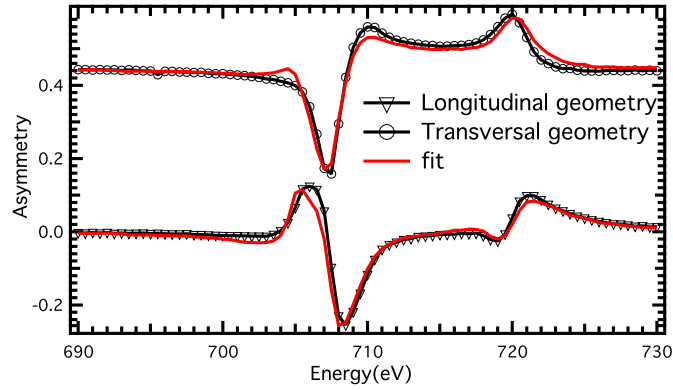
Figure 4.7: Experimental (symbols) and calculated (solid line) asymmetry ratio vs energy for an incident angle of 10deg for (open circle) circular polarized light and longitudinal applied field and, (triangles) for π polarized light and transverse applied field (vertically offset by 0.45 for clarity)

(4.6) shows the dependence of the averaged reflectivity $(I^+ + I^-)/2$ against photon energy measured at 10 deg for both configurations. The fits reproduce the resonant changes of intensity at the L_3 and L_2 edge as well as the variation apart from the resonance. For the simulations, the scattering factors for the iron at the L edges were obtained from the XMCD of Fe bcc which

relates to the imaginary part [13], and a KramersKronig transformation of the imaginary part to get the real part. Figure (4.7) displays the asymmetry $(I^+-I^-)/(I^++I^-)$ derived for both cases. The differences between the cases are ascribed to the different interplay between magnetization direction of the Fe layer and polarization state of the incident beam. The agreement between the fit and the experiment shows that the formalism can deal properly with different configurations.

Our formalism can also be applied to Magneto-Optical Kerr Effect (MOKE). Here we present simulations of soft X-ray MOKE, similar to the ones performed by Kortright *et al.* [14, 15]. These experiments consist in performing energy scans around the resonance energies of the magnetic atoms, at different values of the angle of incidence θ. These measurements are depth-sensitive and solve the magnetic profile in a multilayer. In comparison to reflectivity, the main experimental difference is that in these measurements there is need for polarization analysers, which limits the use of this technique to a few soft X-ray reflectometers (for instance RESOXS does not have). In addition, polarization anlysers decrease the intensity of the signal by orders of magnitude which would make the detection at high angles of any signal very hard. We show two simulations for the W/Fe/W trilayer with σ polarization and the Fe magnetic moments along the y axis. The results consist of Kerr rotation and Kerr ellipticity, presented in fig. 4.8.
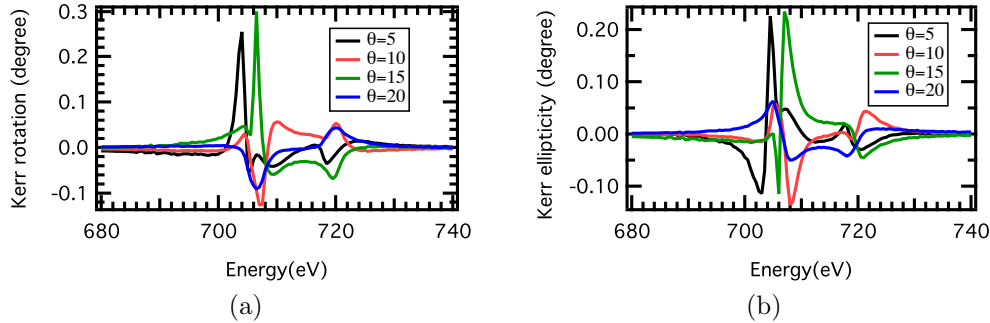

Figure 4.8: (a)Kerr rotation and (b)Kerr ellipticity from Kerr effect simulations of W/Fe/W trilayer for σ polarization and for different incoming angles.

4.2.4 Uniaxial system

Let's now consider a different type of system, one with no magnetism but still with an uniaxial anisotropy. In Figure 4.9, we see that an anisotropy in the

scattering can be due either to a distortion in a structure, or the orientation of a molecule adsorbed on a surface or to electronic correlations for instance implying some orbital ordering and concomitant with local structural distortions. We restrict the anisotropy to be out of plane with the in-plane directions that are equivalent, a more general formalism is possible, but has not been developed during the thesis.
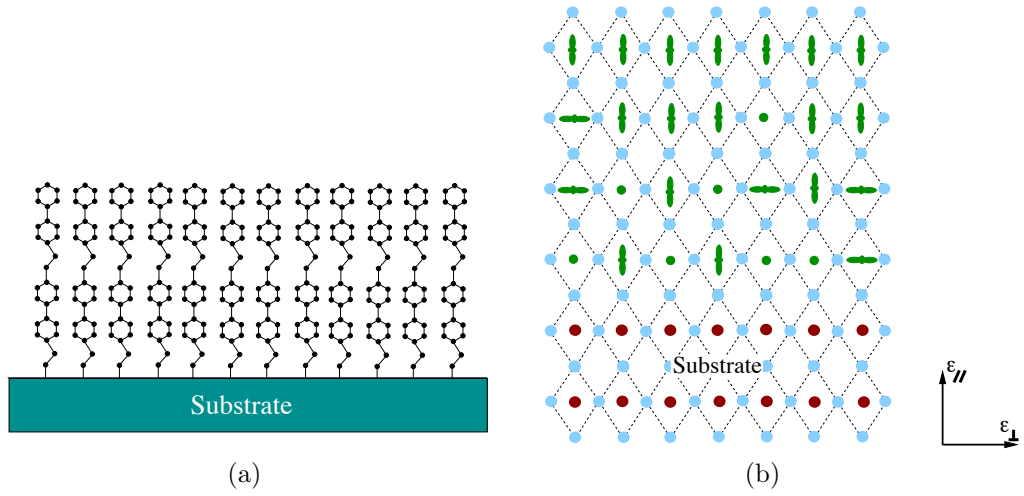

Figure 4.9: Two examples of uniaxial systems: (a) long molecules adsorbed on a surface, (b) electronic reconstruction at the interface between two 3d oxides.

We present the procedure of the method step by step. We will first present the properties of the system we want to study with its dielectric tensor and then we will proceed to evaluate the eigen-waves followed by the imposition of the boundary conditions, the roughness and propagation.

4.2.4.1 Generalities

We consider an uniaxial system with the anisotropy along the normal, the scattering length is, following the expression (3.34) [16]:

$$\hat{f} = (\boldsymbol{\epsilon'}^{\star} \cdot \boldsymbol{\epsilon})\, F_0 + [(\boldsymbol{\epsilon'}^{\star} \cdot \boldsymbol{u})(\boldsymbol{\epsilon} \cdot \boldsymbol{u}) - \frac{1}{3}u^2(\boldsymbol{\epsilon'}^{\star} \cdot \boldsymbol{\epsilon})]\, F_2 \qquad (4.28)$$

There is no F_1 because the system is supposed non-magnetic. F_2 describes the anisotropy. Let's first write the dielectric tensor ϵ_{ij} for this particular case. In the referential we considered, z is taken along the normal to the surface sample and it defines the axis of anisotropy. We consider that the

anisotropic dielectric permitivity defined as $D_i = \epsilon_{ij} E_k$, has a diagonal tensor of the form:

$$\epsilon = \begin{pmatrix} \epsilon_\perp & 0 & 0 \\ 0 & \epsilon_\perp & 0 \\ 0 & 0 & \epsilon_\| \end{pmatrix} \tag{4.29}$$

where we assume that the medium has, as lowest symmetry, an inherent anisotropy between the in-plane ($\perp$) and out-of-plane ($\|$) directions. By this, we impose an in-plane isotropy which should cover a large variety of systems. In the soft X-ray regime the direct magnetic scattering is negligible; we will assume that $\mu = 1$. The dielectric susceptibility and the dielectric permittivity are then given by eq:(4.2). This leads to:

$$\epsilon_\perp = 1 + \frac{4\pi}{k_0^2} \sum_a n_a f_{a\perp} \tag{4.30}$$

$$\epsilon_\| = 1 + \frac{4\pi}{k_0^2} \sum_a n_a f_{a\|} \tag{4.31}$$

4.2.4.2 Indices of refraction

Now we solve Fresnel equation:

$$(n^2 - \epsilon_\perp)[\epsilon_\| n_z^2 + \epsilon_\perp(n_x^2 + n_y^2) - \epsilon_\perp \epsilon_\|] = 0 \tag{4.32}$$

Two solutions are:

$$n = \sqrt{\epsilon_\perp}$$

$$\frac{n_z^2}{\epsilon_\perp} + \frac{n_x^2 + n_y^2}{\epsilon_\|} = 1$$

Considering the geometry of the reflectivity experiment, and defining x as perpendicular to the scattering plane, the x direction corresponds to σ polarization and the YZ plane contains the π polarization. Let's write the index of refraction in function of σ and π. By definition the σ polarization is perpendicular to the scattering plane then, $n^\sigma = \sqrt{\epsilon_\perp}$. n_y and n_z are in the scattering plane, therefore they are directly related to the π polarization with, $n_y = n^\pi \alpha_y$ and $n_z = -n^\pi \alpha_z$ whereas $n_x = 0$. Considering this we write the indices of refraction in the σ π basis as:

$$n^\sigma = \sqrt{\epsilon_\perp} \tag{4.33}$$

$$n^\pi = \frac{\sqrt{\epsilon_\perp \epsilon_\|}}{\sqrt{\epsilon_\| \alpha_z^2 + \epsilon_\perp \alpha_y^2}} \tag{4.34}$$

These are the indices of refraction of the eigen-waves that propagate in a medium whose permittivity is like in expression (4.29).
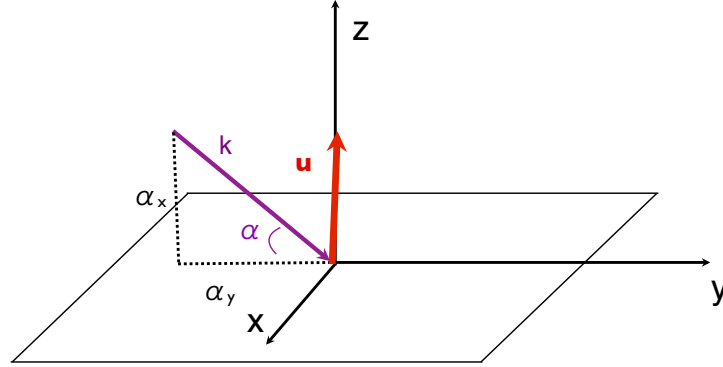
Figure 4.10: Referential with the uniaxial anisotropy $\mathbf{u}$ along the z direction.

4.2.4.3 Boundary conditions

To determine the projection matrix A_m we express explicitly the electromagnetic fields $\mathbf{E}$ and $\mathbf{H}$ as a function of the eigen-waves in Maxwell equations. The eigen-waves in this case are D^σ and D^π. In the referential we use, the waves are described as:

$$\mathbf{D}^\sigma = \begin{pmatrix} 1 \\ 0 \\ 0 \end{pmatrix} \quad \mathbf{D}^\pi = \begin{pmatrix} 0 \\ \alpha_z \\ \alpha_y \end{pmatrix} \tag{4.35}$$

The inverse of the dielectric tensor is:

$$\hat{\epsilon}^{-1} \;=\; \begin{pmatrix} \epsilon_\perp^{-1} & 0 & 0 \\ 0 & \epsilon_\perp^{-1} & 0 \\ 0 & 0 & \epsilon_\parallel^{-1} \end{pmatrix} \tag{4.36}$$

Applied to the polarized wave of expressions (4.35), relations (4.5) and (4.36) lead to:

$$\begin{aligned} E_x^\sigma &= \frac{D_\sigma}{\epsilon_\perp} \\ E_y^\pi &= \frac{D_\pi \alpha_z}{\epsilon_\perp} \\ E_z^\pi &= \frac{D_\pi \alpha_y}{\epsilon_\parallel} \end{aligned}$$

The magnetic field is then obtained using these three expressions and equa-

tion (4.6).

$$H_x^\sigma = n_\pi D_\pi \left[\frac{\alpha_y^2}{\epsilon_\parallel} + \frac{\alpha_z^2}{\epsilon_\perp} \right] \tag{4.37}$$

$$H_y^\pi = -n_\sigma D_\sigma \frac{\alpha_z}{\epsilon_\perp} \tag{4.38}$$

$$H_z^\pi = -n_\sigma D_\sigma \frac{\alpha_y}{\epsilon_\perp} \tag{4.39}$$

We can now build the boundary matrix for the medium m:

$$A_m = \begin{pmatrix} \frac{1}{\epsilon_\perp} & 0 & \frac{1}{\epsilon_\perp} & 0 \\ 0 & \frac{\alpha_z}{\epsilon_\perp} & 0 & -\frac{\alpha_z}{\epsilon_\perp} \\ 0 & \frac{1}{n_\pi} & 0 & \frac{1}{n_\pi} \\ -\frac{\alpha_z}{\sqrt{\epsilon_\perp}} & 0 & \frac{\alpha_z}{\sqrt{\epsilon_\perp}} & 0 \end{pmatrix} \tag{4.40}$$

4.2.4.4 Propagation

Within the eigen-wave basis the propagation matrix is diagonal:

$$P_m(z) = \begin{pmatrix} e^{i\phi_\sigma} & 0 & 0 & 0 \\ 0 & e^{i\phi_\pi} & 0 & 0 \\ 0 & 0 & e^{-i\phi_\sigma} & 0 \\ 0 & 0 & 0 & e^{i\phi_\pi} \end{pmatrix} \tag{4.41}$$

where $\phi = \frac{2\pi}{\lambda} n \alpha_z z$ the phase of the wave. If one wants to write the analytical form of the phase needs the angles α_z in function of the incoming angles α_{y0}. Combining the snell's law and using $\alpha_y^2 + \alpha_z^2 = 1$ one gets:

$$\alpha_z^\sigma = \sqrt{1 - \frac{\alpha_{y0}^2}{n_\sigma^2}} \quad \text{and} \quad \alpha_z^\pi = \sqrt{1 - \frac{\alpha_{y0}^2}{n_\pi^2}} \tag{4.42}$$

One then can write the phase of the propagating wave in a medium as:

$$\phi^\sigma = 2k_0 \sqrt{\epsilon_\perp - \alpha_{0y}^2} \tag{4.43}$$

$$\phi^\pi = 2k_0 \sqrt{\epsilon_\perp - \frac{\epsilon_\perp}{\epsilon_\parallel} \alpha_{0y}^2} \tag{4.44}$$

4.2.4.5 Roughness

For this system we use the same treatment for the roughness as before, Debye-Waller method. For a uniaxial system the table representing the roughness is expressed as:

$$W_{m,m+1} = \begin{bmatrix} e_\sigma^- & 0 & e_\sigma^+ & 0 \\ 0 & e_\pi^- & 0 & e_\pi^+ \\ e_\sigma^+ & 0 & e_\sigma^- & 0 \\ 0 & e_\pi^+ & 0 & e_\pi^- \end{bmatrix} \tag{4.45}$$

4.2.4.6 Reflectivity

The reflectivity can then be expressed as a matrix derived from the M matrix:

$$\begin{bmatrix} r_\sigma \\ r_\pi \end{bmatrix} = \tfrac{1}{d} \times$$

$$\begin{bmatrix} M_{41}M_{34} - M_{31}M_{44} & M_{34}M_{42} - M_{32}M_{44} \\ M_{43}M_{31} - M_{41}M_{33} & M_{32}M_{43} - M_{33}M_{42} \end{bmatrix} \begin{bmatrix} \sigma \\ \pi \end{bmatrix}$$

$$\tag{4.46}$$

with $d = M_{44}M_{33} - M_{34}M_{43}$.

In this case the boundary matrix A_m only has eight non zero values. If we solve the reflectivity for a medium m, we get for the σ and π reflected waves:

$$\begin{aligned} r_m^\sigma &= \frac{n_{(m-1)}^\sigma \alpha_{(m-1)z} - n_m^\sigma \alpha_{mz}}{n_{(m-1)}^\sigma \alpha_{(m-1)z} + n_m^\sigma \alpha_{mz}} \\[2em] r_m^\pi &= \frac{\dfrac{n_{(m-1)}^\pi \alpha_{(m-1)z}}{\epsilon_{m-1\perp}} - \dfrac{n_m^\pi \alpha_{mz}}{\epsilon_{j\perp}}}{\dfrac{n_{(m-1)}^\pi \alpha_{(m-1)z}}{\epsilon_{(m-1)\perp}} + \dfrac{n_m^\pi \alpha_{mz}}{\epsilon_{m\perp}}} \end{aligned} \tag{4.47}$$

For the magnetic media we have not deduced an analytical expression for the reflectivity at each interface. The reason is that the A_m matrix, for the magnetic case there are too many components that make the analytical treatment tedious as the reflectivity can change the polarization state of the wave.

4.2.5 Example

As an example we do not have an experimental result but a simulation of a system that show an uniaxial anisotropy. This system consist on a layer of

YBCO between two thin layers of $Pr_{0.5}Ca_{0.5}MnO_3$ with a substrate of MgO. The YBCO is simulated with two isotrope interfacial layers and a thicker medium layer with an uniaxial anisotropy. The value of this anisotropy can be modified in the program multiplying F_2 by a factor as. When as $= 0$ the medium is isotropic and as $= 1$ it has its maximum anisotropy. In figure 4.11 we show three curves with different values of as simulated with π polarization and at the L_3 edge of the Cu E=930eV . The big signal at $\theta = 45°$ most probalby is due to the $\cos^2(\theta)$ term of the thomson scattering (see eq:3.46). The well around $\theta = 21°$ gets stronger with the anisotropy. We assume that this peak reveals the information of the anisotropy of the system.
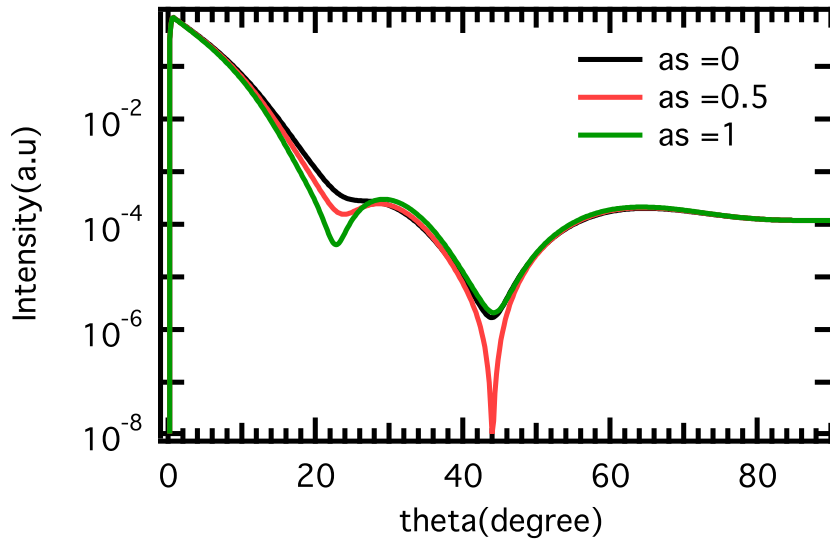
Figure 4.11: Simulation of a PCMO/YBCO/PCMO/MgO system with the BPM method for three anisotropy values

4.3   Parratt

Here we introduce another formalism to describe reflectivity from stratified homogeneous media: the Parrat method [17]. Parratt formalism consists of a recursion formula which starts at the bottom of the system, and recursively calculate the reflectivity at each interfaces and considering the multiple reflection of the photon, then adding the contribution of all the layers below. At the mth interface, the first being a thick substrate of vacuum, the reflectivity is:

$$R_m = \frac{r_m + R_{m+1}e^{\phi_{m+1}}}{1 + r_m R_{m+1}e^{\phi_{m+1}}} \tag{4.48}$$

Here r_m and ϕ_m are the reflectivity and phase terms obtained in the previous section, and R_m is the value calculated by the Parratt formalism. For a N-interface system with N a semi-infinite substrate the recursion starts with $R_{N+1} = 0$ and $R_N = r_m$. The terms r, R and ϕ have different values depending on the polarization states we are using. The roughness is introduced by a Debye-Waller treatment multiplying the $e^{\pm} = e^{-(k_m \pm k_{m+1})^2\sigma^2/2}$ terms to the r_m term.

Once all these terms are calculated one introduces them in the reflectivity expression (4.48).

4.3.1   Uniaxial system

As we have seen, the Parratt method requires the analytical term for the phase and for the reflectivity. For the uniaxial system, they have all been calculated in the BP matrices method section. The reflectivity for a medium m is:

$$r_m^\sigma = \frac{n_{(m-1)}^\sigma \alpha_{(m-1)z} - n_m^\sigma \alpha_{mz}}{n_{(m-1)}^\sigma \alpha_{(m-1)z} + n_m^\sigma \alpha_{mz}}$$

$$r_m^\pi = \frac{\dfrac{n_{(m-1)}^\pi \alpha_{(m-1)z}}{\epsilon_{m-1\perp}} - \dfrac{n_m^\pi \alpha_{mz}}{\epsilon_{j\perp}}}{\dfrac{n_{(m-1)}^\pi \alpha_{(m-1)z}}{\epsilon_{(m-1)\perp}} + \dfrac{n_m^\pi \alpha_{mz}}{\epsilon_{m\perp}}}$$

and the phase is:

$$\phi^\sigma = 2k_0\sqrt{\epsilon_\perp - \alpha_{0y}^2} \tag{4.49}$$

$$\phi^\pi = 2k_0\sqrt{\epsilon_\perp - \frac{\epsilon_\perp}{\epsilon_\parallel}\alpha_{0y}^2} \tag{4.50}$$

Once all the terms are calculated all is left to is to introduce them into the expression (4.48). From a computational point of view the Parratt method is much faster because the A matrices have already been inverted and the reflectivity takes an analytical form to a farther degree. The reflectivity has an analytical form. Furthermore the multiple scattering is taken into account as a geometric series whose sum is a well known academic exercise.

4.4 Discussion and Prospectives

The main difference between the BPM methods and Parratt formalism lies in the degree to which analytical calculation are attainable. With the BPM method the reflectivity at interfaces is solved by the code, whereas in the Parratt method it is solved analytically before the computing process. There are two main consequences: the Parratt method is much faster, but it has to be proved that the Parratt method is suitable for all systems including magnetic. Here we want to note that in the previous section we do not give a proper reflectivity solution for the magnetic case whereas for the uniaxial system we do see in expression 4.47). However it appears to be an interesting prospective to extend Parratt formalism to describe the magnetism thereby gaining an order of magnitude in the computing time. This was tried during this thesis but the big amount of factors to deal with made this treatment left aside for another time.

The eigen-wave Boundary-Propagation Matrices method is applicable to magneto-optics (for instance for Faraday effects, or MOKE simulations), as well as X-ray reflectivity on resonance or off resonance. Equivalent formalisms were presented by Mansuripur [18], Zak *et al.* [1], Bourzami *et al.* [19], and Qiu [20]. These formalisms are restricted to the antisymmetric dielectric tensor. Several approximations are added for not using eigenwaves throughout the formalism. For instance, the projection of circular waves into a linear basis within a magnetic layer required approximations on the direction of the waves in order to calculate the electric field. These approximations are observed to not be important for the cases we have been dealing with, it is however an unnecessary step within these formalisms. Apart from the approximation made on the homogeneity of the media inherent to choosing macroscopic Maxwell equations, the main approximation of the present formalism lies in the relative value of off-diagonal terms of the dielectric tensor. We can see in the example of a high-spin atom like Fe in the bulk *bcc* structure, in figure 4.3, that these terms may be at best in a ratio of 1:7 relative to the diagonal terms. One can also cite a seminal paper by Sacchi *et al.* who had presented results using a numerical approach to resolving Fresnel

equation [21].

The formalisms presented by Stepanov *et al.* in Ref. [22] and Lee *et al.* [23] combined the three terms of the scattering amplitude F_0 and F_1 and F_2. Doing this they included the possibility of having an electronic anisotropy in the valence shell, due to spin-orbit coupling. These formalisms must be used in such specific cases where there is a strong spin-orbit coupling in the valence shell. However, this effect is often absent or neglected in $3d$ metallic or oxide materials, because of a high symmetry point group and quenched orbital momentum. This will be a nice development to do using our boundary matrices method. However one can expect to have not commonly used polarizations as eigen-waves. We could expect to have unconventional polarizations: asymmetrical circular waves, one with its long axis along the π direction and the other along σ. Of course these are only conjectures and to obtain the real eigen-waves the entire process have to be calculated.

We also would like to propose another system that could be studied using eigen waves. A system with an electronic anisotropy **u** rotating in the YZ plane as presented in Fig. 4.12. We guess that the eigen-waves of this system are also σ and π polarized waves, and therefore Parrat can easily be expanded to anisotropy within the scattering plane.

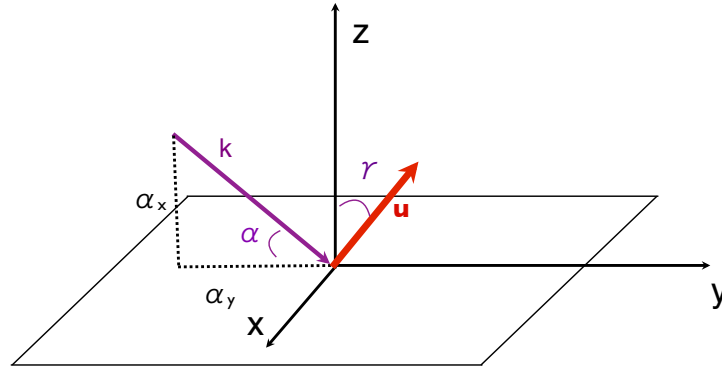
Figure 4.12: Referential with the uniaxial anisotropy **u** rotating in the YZ plane.

Bibliography

[1] J. Zak, E. R. Moog, C. Liu, and S. D. Bader, "Magneto-optics of multilayers with arbitrary magnetization directions," *Phys. Rev. B*, vol. 43, pp. 6423–6429, Mar 1991.

[2] M. Elzo, E. Jal, O. Bunau, S. Grenier, Y. Joly, A. Ramos, H. Tolentino, J. Tonnerre, and N. Jaouen, "X-ray resonant magnetic reflectivity of stratified magnetic structures: Eigenwave formalism and application to a w/fe/w trilayer," *Journal of Magnetism and Magnetic Materials*, vol. 324, no. 2, pp. 105 – 112, 2012.

[3] L. D. Landau, E. M. Lifshitz, and L. P. Pitaevskii, *Electrodynamics of continuous media.* Pergamon Press, 1984.

[4] N. L. and P. Croce, "Caractérisation des surfaces par réflexion rasante de rayons X. Application a l'étude du polissage de quelques verres silicates," *Rev. Phys. Appl.*, vol. 15, no. 3, pp. 761–779, 1980.

[5] C.-C. Kao, C. T. Chen, E. D. Johnson, J. B. Hastings, H. J. Lin, G. H. Ho, G. Meigs, J.-M. Brot, S. L. Hulbert, Y. U. Idzerda, and C. Vettier, "Dichroic interference effects in circularly polarized soft-x-ray resonant magnetic scattering," *Phys. Rev. B*, vol. 50, pp. 9599–9602, Oct 1994.

[6] A. Déchelette, J. M. Tonnerre, M. C. S. Lager, F. Bartolomé, L. Sève, D. Raoux, H. Fischer, M. Piecuch, V. Chakarian, and C. C. Kao, "Magnetic properties of bct $fe_x mn_{1-x}$ thin-film alloys investigated by linearly polarized soft-x-ray resonant magnetic reflectivity," *Phys. Rev. B*, vol. 60, pp. 6636–6645, Sep 1999.

[7] S. Roy, C. Sanchez-Hanke, S. Park, M. R. Fitzsimmons, Y. J. Tang, J. I. Hong, D. J. Smith, B. J. Taylor, X. Liu, M. B. Maple, A. E. Berkowitz, C.-C. Kao, and S. K. Sinha, "Evidence of modified ferromagnetism at a buried permalloy/coo interface at room temperature," *Phys. Rev. B*, vol. 75, p. 014442, Jan 2007.

[8] J. M. Tonnerre, M. D. Santis, S. Grenier, H. C. N. Tolentino, V. Langlais, E. Bontempi, M. Garcia-Fernandez, and U. Staub, "Depth magnetization profile of a perpendicular exchange coupled system by soft-x-ray resonant magnetic reflectivity," *Physical Review Letters*, vol. 100, no. 15, p. 157202, 2008.

[9] H. L. Meyerheim, J.-M. Tonnerre, L. Sandratskii, H. C. N. Tolentino, M. Przybylski, Y. Gabi, F. Yildiz, X. L. Fu, E. Bontempi, S. Grenier, and J. Kirschner, "New model for magnetism in ultrathin fcc fe on cu(001)," *Phys. Rev. Lett.*, vol. 103, p. 267202, Dec 2009.

[10] J. W. Freeland, J. Chakhalian, A. V. Boris, J.-M. Tonnerre, J. J. Kavich, P. Yordanov, S. Grenier, P. Zschack, E. Karapetrova, P. Popovich, H. N. Lee, and B. Keimer, "Charge transport and magnetization profile at the interface between the correlated metal $caruo_3$ and the antiferromagnetic insulator $camno_3$," *Phys. Rev. B*, vol. 81, p. 094414, Mar 2010.

[11] J. Geissler, E. Goering, M. Justen, F. Weigand, G. Schütz, J. Langer, D. Schmitz, H. Maletta, and R. Mattheis, "Pt magnetization profile in a pt/co bilayer studied by resonant magnetic x-ray reflectometry," *Phys. Rev. B*, vol. 65, p. 020405, Dec 2001.

[12] H.-C. Mertins, S. Valencia, D. Abramsohn, A. Gaupp, W. Gudat, and P. M. Oppeneer, "X-ray kerr rotation and ellipticity spectra at the $2p$ edges of fe, co, and ni," *Phys. Rev. B*, vol. 69, p. 064407, Feb 2004.

[13] J. Als-Nielsen and D. McMorrow, *Elements of Modern X-Ray Physics*. Wiley, 2001.

[14] K. S. Lee, D. E. Jeong, S. Kim, and J. Kortright, "Soft x-ray resonant magneto-optical kerr effect as a depth-sensitive probe of magnetic heterogeneity: A simulation approach," *Journal of Applied Physics*, vol. 97, p. 083519, Apr 2005.

[15] J. B. Kortright and S.-K. Kim, "Resonant magneto-optical properties of fe near its $2p$ levels: measurement and applications," *Phys. Rev. B*, vol. 62, pp. 12216–12228, Nov 2000.

[16] M. Blume, *Resonant Anomalous X-Ray Scattering, Theory and Applications*. Materlik, Sparks and Fisher, 1994.

[17] L. G. Parratt, "Surface studies of solids by total reflection of x-rays," *Phys. Rev.*, vol. 95, pp. 359–369, Jul 1954.

[18] M. Mansuripur, "Analysis of multilayer thin-film structures containing magneto-optic and anisotropic media at oblique incidence using 2x2 matrices," *Journal of Applied Physics*, vol. 67, no. 10, 1990.

[19] A. Bourzami, O. Lenoble, C. Féry, J. F. Bobo, and M. Piecuch, "Enhancement of polar kerr rotation in $fe/al2o3$ multilayers and composite systems," *Phys. Rev. B*, vol. 59, pp. 11489–11494, May 1999.

[20] Z. Qiu and S. Bader, "Surface magneto-optic kerr effect," *Review of Scientific Instrument*, vol. 71, no. 3, p. 1243, 2000.

[21] M. Sacchi and A. Mirone, "Resonant reflectivity from a ni(110) crystal: Magnetic effects at the ni $2p$ edges using linearly and circularly polarized photons," *Phys. Rev. B*, vol. 57, pp. 8408–8415, Apr 1998.

[22] S. A. Stepanov and S. K. Sinha, "X-ray resonant reflection from magnetic multilayers: Recursion matrix algorithm," *Phys. Rev. B*, vol. 61, pp. 15302–15311, Jun 2000.

[23] D. R. Lee, S. K. Sinha, D. Haskel, Y. Choi, J. C. Lang, S. A. Stepanov, and G. Srajer, "X-ray resonant magnetic scattering from structurally and magnetically rough interfaces in multilayered systems. i. specular reflectivity," *Phys. Rev. B*, vol. 68, p. 224409, Dec 2003.

Chapter 5

PbTiO$_3$ thin film ferroelectrics: experiments and simulations.

5.1 Introduction

On the path to studying multiferroics, we started a study on a ferroelectric thin film by Resonant X-ray Diffraction (RXD). The realization that RXD is extremely sensitive to small changes in the atomic structure, like in EXAFS, had made a study of ferroelectrics appealing, along other structural-electronic coupling like the Jahn-Teller effect in Manganites. However the choice of the right sample was not as easy as it seems for the ferroelectric propagation vector corresponds to main Bragg reflections, just like ferromagnetic reflections occur at the same position than structural Bragg reflections. Nevertheless our collaborator D. Mannix from the Institut Néel found a very interesting case and initiated the RXD study that we present in this section.

We had therefore two motivations to start this new thematic. One motivation was that multiferroics to be studied by resonant x-ray diffraction (RXD) may consist in one ferroelectric layer in case of a composite where the ferro orders develop in separate layers instead of one single material. The second motivation was the recent proposition of a new ferroelectric state due to a reduced size and substrate strain in thin film PbTiO$_3$ by the group of Noheda in Gröningen [1]. As the authors noted, a standard crystallographic structure refinement is impossible in thin film, which is why only qualitative conclusions had been drawn from the position in the reciprocal space of x-ray superstructure reflections from ferroelectric domains. We intended to use the potential of the resonant technique in order to give a more quantitative explanation to this new FE state. D. Mannix obtained two PbTiO$_3$ thin films from Noheda's group.

In this chapter, we describe our way towards the experimental determination of the polar structure at the atomic scale in thin ferroelectric (FE) films, using RXD. Our results are promising but not concluding because of an unexplained similar feature in the spectra of two diffraction reflections. We can however report in detail on the methodology, and on RXD simulations from various FE scenarii using the FDMNES code.

5.1.1 Origin of ferroelectricity

Ferroelectric materials are defined by their electric polarization that has to be both spontaneous and reversible by an applied electric field. Ferroelectrics are also characterized by a macrostructure consisting of domains with polarizations in different directions. With a certain accumulation of charges, the nucleation of one domain of reversed polarization creates a depolarization field whose energy can flip over neighbor dipoles.

Here we consider perovskite structured ferroelectrics. The general chem-

ical formula for a perovskite structure is ABO_3 and A and B are two cations where A is larger than B. Ideally, it has a cubical structure with the B atom in a 6-fold coordination surrounded by an Oxygen octahedron, and the A cation in a 12-fold coordination (see Figure 5.1). In the cubic structure there is no ferroelectricity, the systems are paraelectric and the phase transition to the ferroelectric state occurs at T_C, alongside a structural transition/distortion.
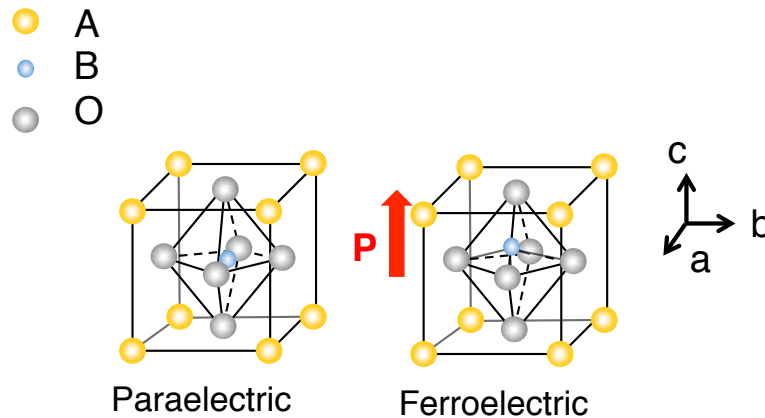

Figure 5.1: Perovskite structures for the paraelectric and ferroelectric states.

In conventional perovskite structured ferroelectrics, the origin of the polarization is a relative displacement of anions and cations in the unit cell as shown in figure 5.1. In the configuration where the Oxygen octahedra is distorted, the unit cell is no longer cubic but tetragonal. The displacement of the B cation is due to the hybridization of the atomic orbitals between neighboring atoms. In case of transition metal (TM) based compounds, this hybridization occurs because the high electronegativity of the oxygen atom attracts the electrons of the TM atom. Therefore the TM atom is depleted of its valence electrons, and the energy of the system is minimized if the TM atom is bound to one or more neighbor oxygens. The binding induces its displacement that creates the electric moment. It is considered that the TM atom and the O atom share some electron density. This electrical polarization appears in each unit cell, and it is the sum of all of them that creates the macroscopic polarization: ferroelectricity is a collective phenomenon.

Bulk perovskite ferroelectrics have very often been studied by X-ray absorption spectroscopy because it gives the information of the local electronic environment of the atom under study, most of the time the B cation[2, 3, 4]. One can therefore ask what happens to ferroelectricity when one dimension is reduced and if it is approachable by x-ray absorption. Before attacking this question we present the ferroelectric compound studied during this thesis.

5.1.2   PbTiO$_3$

In this thesis we have studied *lead titanate*, PbTiO$_3$ (PTO). PTO is a perovskite type ferroelectric with a distorted Oxygen octahedra as mentioned before [5, 6]. In the ferroelectric state it has a tetragonal structure (P4mm space group $a = 3.9036$ Å and $c = 4.144$ Å). Its transition from the paraelectric cubic phase to the ferroelectric tetragonal phase occurs at T$_C = 492°C$. In the tetragonal perovskite configuration the Ti is ionized and its electronic structure is:

$$Ti^{4+} = [Ar]4s^0 3d^0 4p^0 \tag{5.1}$$

As mentioned before, an important aspect is that the electronic density, occupied and unoccupied, of the Ti atoms is not isotropic anymore because of the preferred hybridization and the resulting displacement. This electronic anisotropy induces an anisotropy in the scattering amplitude of the Ti atoms. By characterizing the anisotropy in the scattering amplitude, one should be able to determine in return the anisotropy in the electronic density and therefore in the local structure around the Ti atoms. The goal of our experiment was to have the way to a method to study ferroelectric nanostructure and, in particular, to identify a ferroelectric phase in a strained thin film, not present in the bulk material.

5.2   Thin film ferroelectrics

The physical properties of ferroelectricity are very interesting from an application point of view. However, to use ferroelectric materials for an industrial application they have to be in the form of thin films. For this reason many studies have been done in the area of thin film ferroelectrics and the effect of the substrates on them [7, 8, 9, 10].

Here we will consider tetragonal ferroelectrics grown on cubic substrates. The orientation of the polarization of the FE system will depend on the lattice parameters of the FE (a,c) and the lattice parameter of the substrate (a_s). We consider three cases represented in figure 5.2 already studied by Foster *et al.* [11]. If the lattice parameter of the substrate is smaller than the lattice parameter of the film ($a_s \leq a$), the stress applied by the substrate will be compressive. The film will grow in the c-direction and the polarization will be out-of-plane (c phase). Such films split into 180° domains in order to decrease the depolarization field [12]. In the case where $a_s \simeq c$ the film will

grow with c in-plane, and therefore the polarization will be in-plane (a phase). In this systems a_1/a_2 domains can appear. Here only elastic considerations govern the domain scaling [13]. For intermediate situations ($a < a_s < c$), the film will be relaxed and it will create domains of c and a in a ratio such as to fit the substrate, and both elastic and depolarization effects compete with each other.
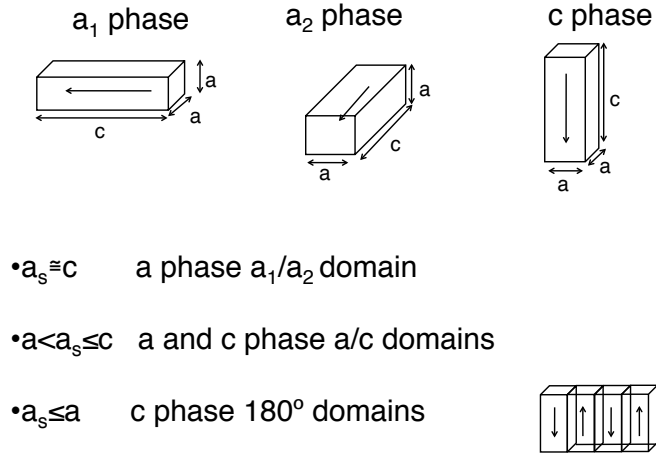

Figure 5.2: On the top part of the image we show the three possible phases. The three conditions considered for the substrate and film parameters there will be three different types of domains.

5.2.1 The case of PbTiO$_3$ on DyScO$_3$

Most of the substrates used apply a compressive strain on the film inducing an enhancement of the tetragonality. Hence the polarization is out of plane. Many of these studies were done on thin films grown on (001) SrTiO$_3$ (STO) substrates [14, 15]. STO is a very well known material with a cubic structure of lattice constant $a = 3.905$ Å. The films grown on STO show compressive strain, they are in the c phase and they form 180° stripe domains [12].

The use of different substrates with new lattice parameters opened a new path for new FE states. DyScO$_3$ (DSO) is one of these new substrates. It has a perovskite orthorhombic structure with the lattice parameters $a = 5.44$ Å, $b = 5.713$ Å and $c = 7.887$ Å. DSO [110] substrates have a pseudocubic structure with the in-plane parameter $a = 4.944$ Å.

The group of B.Noheda had synthesized several thin films of PTO on DSO [110] substrates [16, 1]. By Pulsed Laser Deposition (PLD) they grew samples with different thicknesses of PTO (5nm and 25-30nm). Some of the

samples had an electrode layer of SrRuO$_3$ $a = 3.930$ Å between the substrate and the film. With such a mismatch the PTO is expected to show a new polar displacement.

Grazing incidence X-ray Diffraction (GIXD) and Transmission Electron Microscopy (TEM) measurements on thin films of PbTiO$_3$ grown on DyScO$_3$ ucture with a periodicity of around 27 gure 5.3b [1]. These peaks arise from c domains, antiparallel to each other. polarizations arise from opposite dis-dy centered site of the perovskite unit

Figure 5.3. (a) Logarithmic reciprocal space maps in the HK0 scattering zone around the 010,100, 110 and 200 reflections for the film grown with a SRO electrode. [Intensities from low to high: blue (b), green (g), yellow (y), red (r), white (w)] [16](b) High resolution TEM of epitaxial PbTiO3 thin films with 90° domains with P alternating between in-plane and out-of-plane [1].

5.2.1.1   5nm thick PTO film on DSO

A new ferroelectric phase was proposed in a 5 nm thick PTO thin film grown on DSO [16]. The group of Noheda *et al* concluded by x-ray diffraction in grazing incidence that the ferroelectric polarization had an out of plane and an in plane components because they observed satellite peaks around all reciprocal space directions (Fig. 5.4). The in-plane modulation was calculated

to be $\simeq 20$ nm for the samples grown with SRO and $\simeq 30$ nm for the samples without SRO. The in plane component of the polarization was claimed to be oriented tail-to-tail or head-to-head since it produced a modulation parallel to the in-plane reciprocal lattice vector. The domain formation was controlled by the depolarization field. They proposed two ferroelectric configurations that were compatible with the results observed (see Figure 5.4).
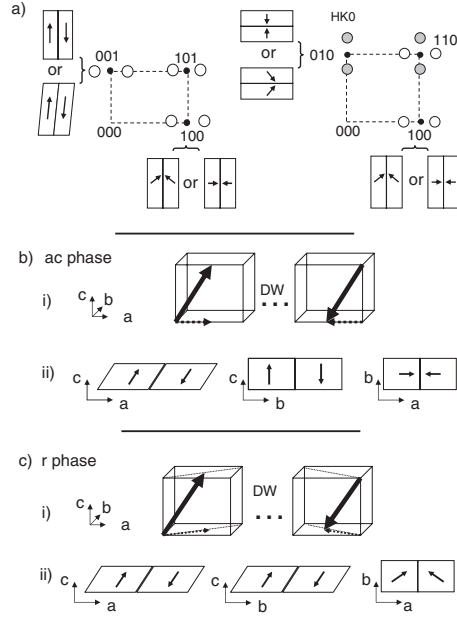

Figure 5.4: Schematic representation of the observed reciprocal space maps and their implication for the polar domain orientation; Polar symmetry for (b) ac phase, and (c) the r phase. In (b) and (c): (i) shows the sketch of the polar shifts in two unit cells at both sides of the domain wall and (ii) represents the projections of the polarization in the (100) pseudocubic planes for the proposed phases and domain configurations. [16].

These models were only propositions. With diffraction they were not able to give a quantitative solution to this new FE state. In the next section we will discuss how to address this with resonant x-ray diffraction.

5.2.1.2 25nm thick PTO film on DSO

The case for 25nm-thick layer is different from the 5nm case. The domains are dominated by strain and they appear in the $a/c/a$ pattern [1]. In this 90° domains the width of the a domains is the smallest possible in order to keep the horizontal coherency of the film. This was seen by X-ray diffraction by
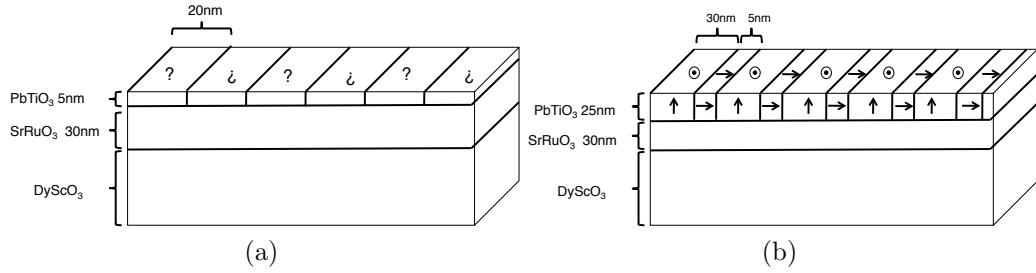
Figure 5.5: (a) Sheme of the 5nm thick PTO/DSO sample. The ferroelectricity of the sample is unknown. (b) Scheme of the 25nm thick sample with ac domains.

which the modulations through reciprocal space showed a 28 nm periodicity. The Bragg peak corresponding to the c lattice parameter of bulk PTO was observed in the in-plane direction, showing the presence of a domains.

Transmission electron Microscopy (TEM) images supported the scenario of the $a/c/a$ pattern, see Fig. 5.3b. The width of the a domains was found to be 6nm whereas the periodicity of the $a/c/a$ pattern was observed to be 27nm. Both TEM and X-ray diffraction gave very similar values for the periodicities.

Figure 5.5 shows a scheme of the two samples.

5.3   Resonant X-ray Diffraction on PTO/DSO

In this section we evaluate the potential of Resonant X-ray Diffraction (RXD) and how it gives a more quantitative view of the displacement of the Ti atoms within their O environment. The spectroscopy basis of RXD is sensitive to the atomic environment by means of the tensorial dielectric response to the incoming beam, while the diffraction effect will spatially select the periodicity of interest. The atomic displacements in ferroelectric materials and the appearance of domains make x-ray resonant diffraction a well adapted technique to study them.

We chose to work at the K-edge of the Ti atom, the 1s core electron transitions. This transition is in the hard x-ray range with an energy of $E = 4.966$ keV. In the case of an isotropic atom, the electronic transition with the largest probability is the dipolar term for which the angular momentum of the atom changes by one unit, $l = \pm 1$ and the electronic transition is from 1s⇒4p. In perovskite ferroelectric systems the electronic structure of the Ti is not isotropic: the hybridization of the orbitals allows new electronic

transitions as the 1s⇒3d-2p, 3d-2p being the hybridized orbital. This is the
sensitivity we will use in order to look for this new atomic displacement seen
in thin film PTO/DSO.

Depending on the displacement of the Ti atom, the spectroscopic signa-
ture of the RXD will have a particular form. Combining the experiments
with simulation of the FDMNES program we propose a new methodology to
study thin film ferroelectrics.

5.3.1 Experiments

The experimental results shown in this section were all taken at X-Mas,
the british Cooperative Research Group (CRG) beamline at the ESRF, in
collaboration with D. Mannix of the Institut Néel.

During this experiment the polarization of the incoming photon was kept
linear and horizontal. The diffraction configuration always was in grazing
incidence, the diffraction plane is in the surface plane. Figure 5.6 shows the
two configurations we used. The "vertical" configuration, in which the sam-
ple is vertical, corresponds to the so-called σ polarization (the polarization
of the incoming photon is perpendicular to the diffraction plane) and the
horizontal configuration corresponds to the π polarization (the polarization
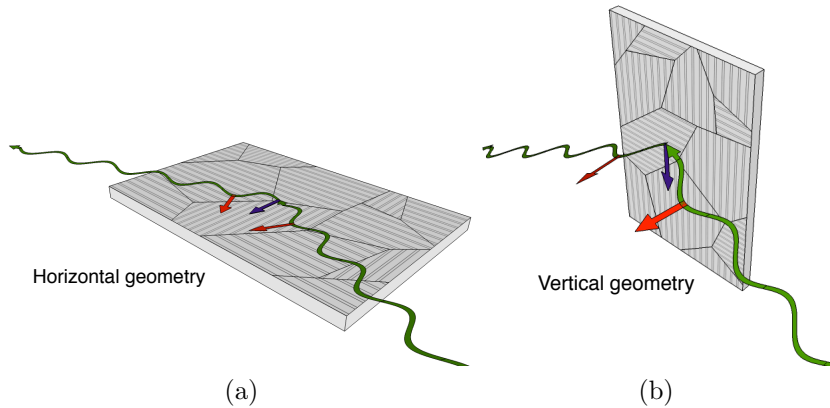of the incoming photon is in the diffraction plane).

Figure 5.6: Polarization configurations for the PTO experiments at XMas
beamline. the red arrows represent the polarization of the beam and the
blue arrow the diffraction vector. (a)Horizontal configuration equivalent to
π polarization.(b) vertical configuration, equivalent to σ polarization

In our experiments we studied two samples, one was a 5nm-thick PTO
layer on DSO with a buffer layer of 25 nm of SRO and the other a 30nm-thick

layer of PTO on DSO with a 25nm thick buffer layer of SRO.

The goal of the experiments was to perform RXD on the 5nm-thick layer in order to solve the new FE phase predicted by Noheda. Unfortunately we could not get any information from this sample. This could be explained with a damaged layer of PTO. For a thicker sample (30nm) a refinement of the reflectivity using Parratts formalism, with the program Dyna, showed a less dense layer of around 9nm (see Fig.5.7). The parameters of the refinement are presented in the table 5.1. We notice that it is absolutely necessary to introduce a layer that has a density ρ smaller than the one of the PTO to obtain a good agreement between the experiment and the simulation. This layer can be either because an oxidation state or a loss of Pb atoms from the layer.
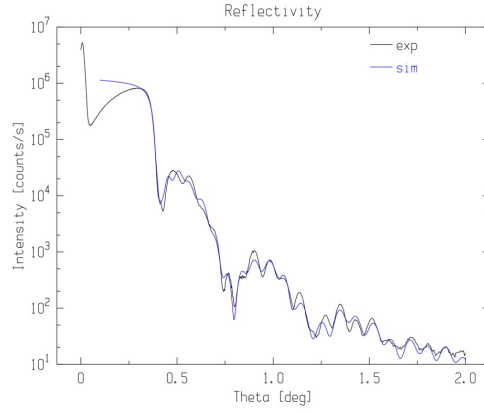

Figure 5.7: Reflectivity experiment (black curve) and simulation (blue curve) for a 30nm thick sample of PTO/DSO.

Table 5.1: estimated values of the reflectivity study. PTO* : PTO probably oxidized or with possible loss of Pb atoms.

	$\rho(g/cm^3)$	Thickness (nm)
PTO*	5.435	3.24
PTO*	4.991	2.988
PTO*	5.712	3.184
PTO	8.126	23.089
SRO	7.592	23.041
DSO	8.112	1000000000

We tried to perform reflectivity measurements on the 5nm thick layer but we did not get any information. To explain this one could assume that in

a very thin layer there also exists a damaged layer. Then, one could expect that in a 5nm thick PTO film, the damaged layer could be thick enough and therefore the signal from the film too small inexsistent. However we had some interesting results on the 30nm thick layer. In the following, all the results that we present will be from the 30nm thick layer.

We explored the reciprocal space in the HKL directions looking for satellite peaks. The satellites will appear around those position in the reciprocal space (HKL) that have at least one component parallel to the direction of the polarization. To get information of the atomic displacements we will perform energy scans of the satellite peaks.

5.3.2 Results

Figures 5.8 and 5.9 show two reciprocal space maps around $(0\ 0\ 0.9525)+(\pm 0.06 \pm 0.06\ 0)$ and $(1\ 1\ 0)+(\pm 0.05 \pm 0.05\ 0)$. Both maps show satellite peaks, which means that the displacement vector in the system has components in the x, y and z directions. This is consistent with what was observed by Noheda *et al.* The periodicity observed from these peaks is $d = 2\pi/\Delta H$. In our data ΔH=0.02 then $d = 30$ nm. The diffraction peaks are indexed to the PTO film.
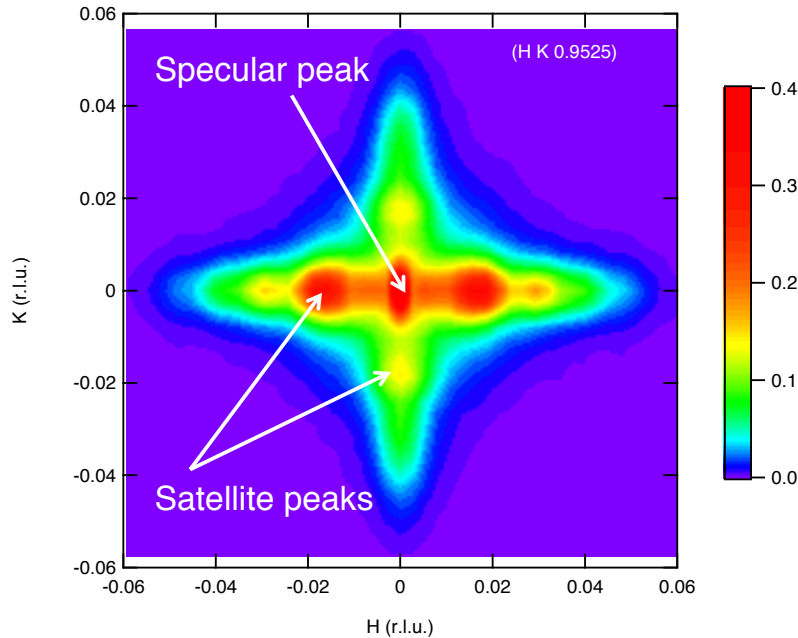

Figure 5.8: HK mesh around the 001. The symmetry evidences that the domains propagate in a and b directions
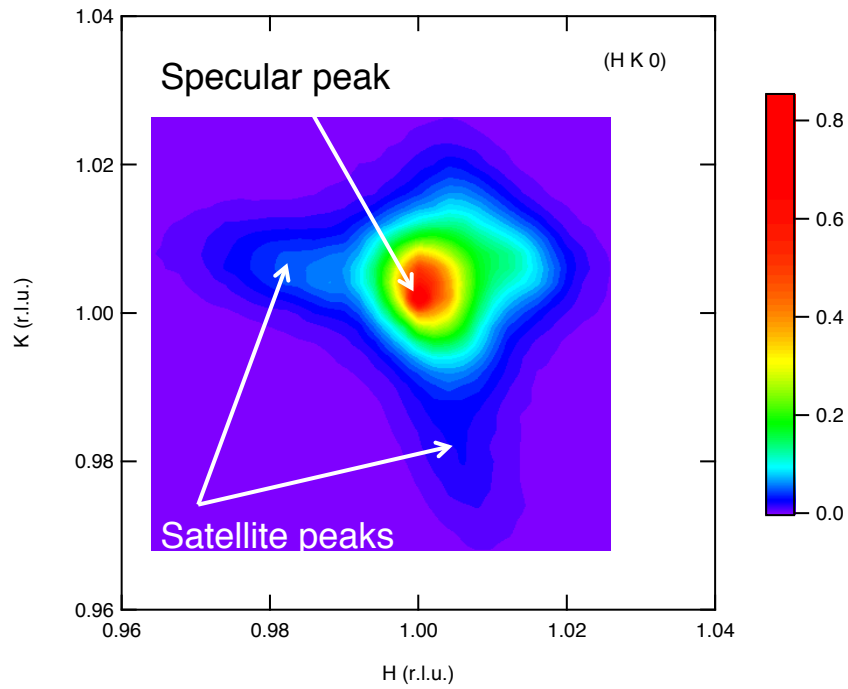
Figure 5.9: HK mesh around the (1 1 H). The symmetry evidences that the domains propagate in a and b directions

The symmetry in Fig. 5.8 originates from twin domains that are totally equivalent but have grown in two perpendicular directions. Therefore the (HKL) reflections will be superposed with (KHL) reflections. This scheme is validated in Figure 5.10 where figure 5.10a shows two energy scans at two equivalent satellite peaks (0.98 0 0) and (0 0.98 0) for π polarization and Figure 5.10b shows the same behavior at (0.98 1.007 0) and (1.005 0.98 0) positions for σ polarization, they are respectively similar in shape.
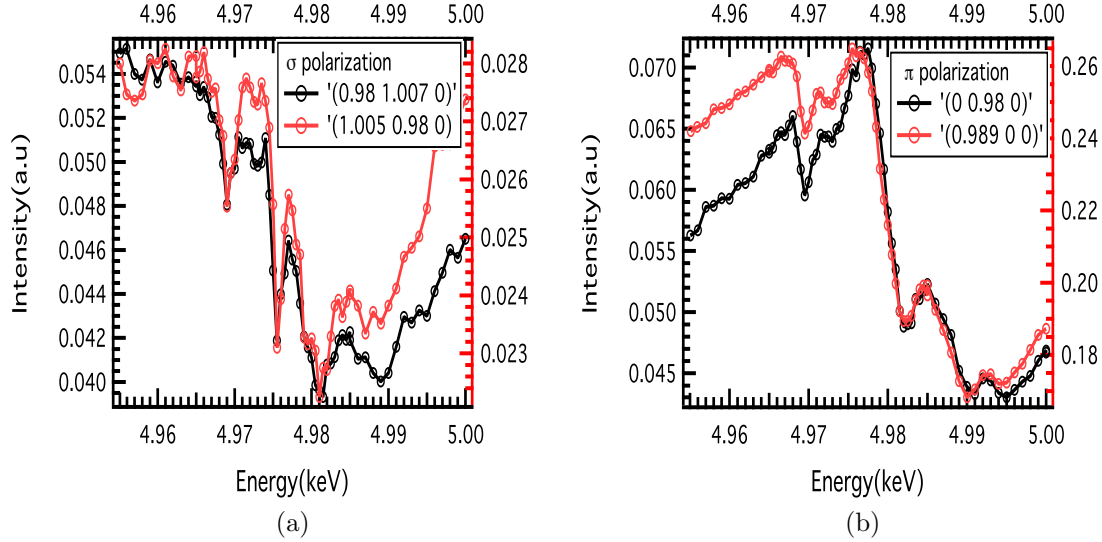
Figure 5.10: RXS spectra at the same geometry at equivalent HKL values because of the twin domains of the sample (a) σ and (b) π polarization.

Let's have a closer look at the spectroscopic signatures of the spectrum. We will focus on two main features that we called Δ and Ω. In Figure 5.11 we point out the two features at E_Ω=4.969 keV and E_Δ=4.9755 keV.

The Δ feature is only seen in vertical geometry (sigma polarization) and on *two* satellites (see figure 5.11). The signature of the peak is very large and we expect that it has something to do with the directions of the moments and the polarization of the incoming wave. Could it be a spurious feature? Usually spurious features appear as a sudden increase in intensity while sweeping the incident energy, not like here a sudden decrease. Here the signal It also appears at two different positions, thereby diminishing the odd of a multiple scattering effect, whereby a second condition of inner diffraction appears as a loss in intensity in the primary reflection. We have therefore considered the feature to be real, even though we keep in mind that the sudden decrease is not usual.
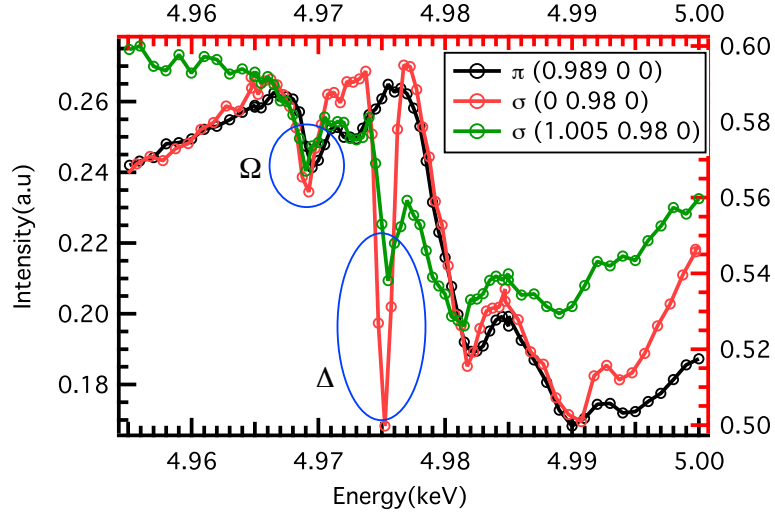
Figure 5.11: Energy scans at the satellite peak for σ and π polarizations. For σ polarization there is a Δ peak observable in two reciprocal space positions (red and green curves) whereas in π polarization there is no such feature (black curve).The Ω feature appears at both geometries.

In Figure 5.12a we show two RXS spectra around the (100) reflection. One is measured at the main Bragg peak (black curve) and the other at the satellite position $(100) - (\delta 00)$(red curve), pointed out in Fig 5.12b. From Fig.5.12a we see that Ω feature appears at both positions and Fig. 5.11 shows that it comes out in both σ and π geometries. However, its intensity is much stronger in the satellite position than at the main Bragg reflection (see figure 5.12a). On the main Bragg position it is hardly detectable. Since it gains intensity at the satellite peak we consider Ω to be a spectroscopic signature of the FE arrangement.

In Fig. 5.13 we summarize in a reciprocal space representation the reflections observed experimentally and the features they show. The red dots are the satellite peaks.
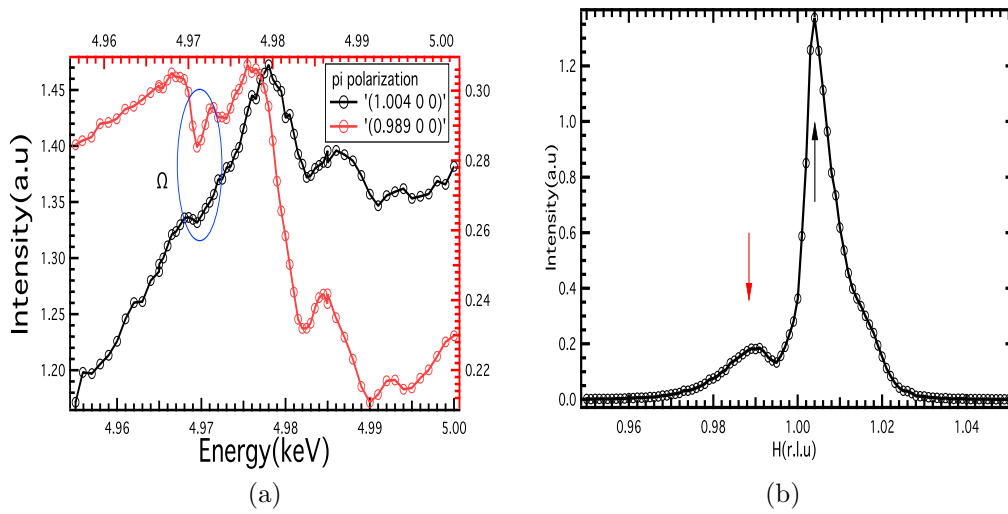
Figure 5.12: (a)Energy scans at two sites in the reciprocal space at the main Bragg reflection (black) and the satellite position (red) around the (1 0 0) for π polarization (b) reciprocal space scan around (H 0 0)
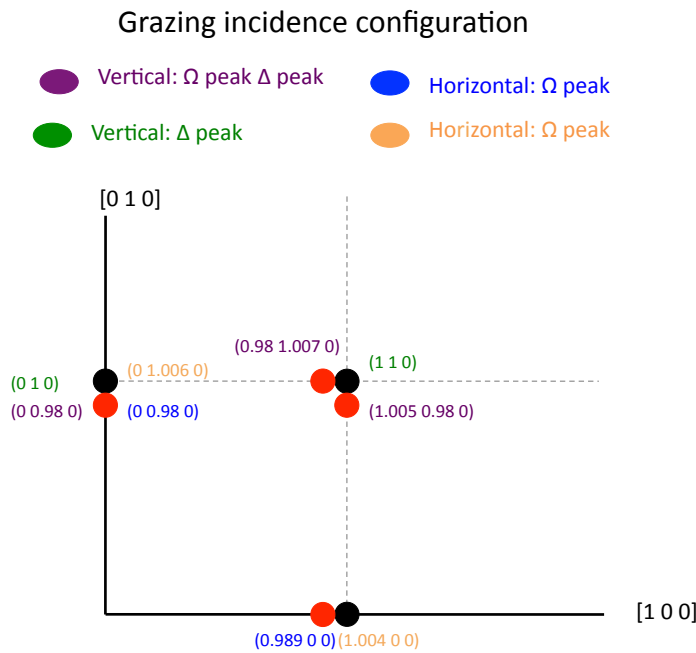

Figure 5.13: reciprocal space representation with the reflections and the energy features found on these reflections.

5.4   Simulation on PTO/DSO

To interpret our experimental data we performed *ab initio* simulations of absorption and resonant diffraction with the FDMNES program. First, we simulated the absorption spectra of bulk systems and compared it to the existing data and other simulations in the literature in order to obtain a good starting set of simulation parameters (the size of the cluster of nearby atoms for instance). We used these parameters to perform the resonant diffraction simulations. When simulating the resonant diffraction spectra we considered the domains reported by Noheda *et al.* on the 25 nm-thick PTO/DSO systems and tried several positions of the atoms in order to simulate the new FE phase described by this group in order to qualify the adequacy and the sensitivity of the resonant diffraction technique.

5.4.1   FDMNES: simulation tool

In the case of PTO, the ferroelectricity has its origin in the atomic displacements. The atomic structure is reflected in the electronic structure of the valence and band states, hence in the scattering of resonant x-rays. We simulated the resonant spectra using the program FDMNES developed by Y. Joly in our group [17]. FDMNES has *ab initio* methods that calculate ground and excited electronic states of a crystallographic or molecular structure, and transitions between them, thus the resonant x-ray scattering cross-section around ionization edges. One of the most important features of the program is the choice between two methods of monoelectronic calculations. One is the so called Green multiple-scattering formalism with the "muffin tin" approximation: a spherical cluster is defined around the excited atom inside which the potential is assumed to be spherically symmetric. Beyond this sphere the potential is constant and continuity of the potential is enforced between the spheres and the interstitial region. The other method is based in a Finite Difference Method (FDM) and involves the numerical resolution of Schrödinger equation. With this method one can define more realistic potential, in particular anisotropic potentials. However, this latter method needs huge computing resources.

FDMNES gives the spectral information of the crystal under study. Simulations are performed optimizing different parameters in the crystal environment and the calculation mode. In Table 5.2 below we show some of the parameters which are possible to change and their meaning.

Table 5.2: Various entries and parameters for the FDMNES simulations.

Parameters	Meaning
Cluster radius	The final states are calculated inside a sphere, whose radius is defined by the user. Only the atoms inside this sphere are considered.
Structure	The crystal structure of the system is introduced.
Atom	An electronic configuration is used by default for all the atoms.
Multipolar development	By default only the dipolar component is calculated. This can be modified taking into account the quadrupole, octupole, nondipole, nonquadrupole, terms.
Relativity	It is possible to perform a relativistic calculation for heavy atoms
Screening	By default, the screening is one electron on the first non fully occupied valence orbital of the absorber. It is also possible to modify this value or the number of the orbital.

5.4.2 Bulk simulation: absorption

FDMNES has already been used to simulate absorption spectra from TiO_2-rutile [18] and $PbTiO_3$ under high pressure [4]. X-ray absorption near edge spectroscopy spectra (XANES) show different peaks or features realizing a signature of the electronic structure. In Figure 5.14 we show three remarkable features that appear in a perovskite type structure at the K-edge (peak α, β and γ) in the pre-edge region, a spectrum measured by Jaouen *et al.* [4].

The origin of peak α, β and γ were proposed to be the following:

α: Transition metal (TM) $1s$ electron quadrupole transition to the $3d$ unoccupied states of the same TM,

β: TM $1s$ electron dipole transition to the $4p - 3d$ orbitals of the same TM, due to some hybridization of the two angular momentum states in a non centro-symetric environment.

γ: the dipole-allowed transition of the $1s$ TM electron to the TM $3d$ originated molecular orbitals (MO) of neighboring octahedra.

A starting point of our simulations was to find the same conclusions using the FDMNES program and qualify the use of its parameters. We started simulating the paraelectric state where the unit cell is cubic and the
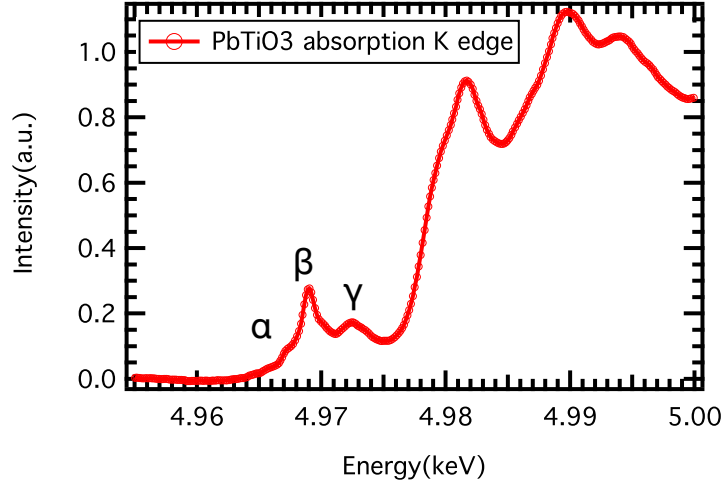
Figure 5.14: Absorption spectrum of PTO bulk crystal. This data comes from [4]

atoms sit on the perfect perovskite positions. It is during the transition from paraelectric to ferroelectric that the feature β appears Fig. 5.15a. We attribute this to the $p - d$ orbitals hybridization. When the Ti and the O atoms are displaced from their paraelectric cubic positions to the ferroelectric positions, the $p - d$ orbitals hybridize thanks to the loss of the centro-symetry. The peak α appears very clearly when the quadrupolar terms is considered, which means that it is due to a quadrupolar transition from a $1s$ orbital to a $3d$ orbital. There is also a small dipolar contribution. The origin of the peak γ is a transition from the $1s$ TM orbital to the molecular orbitals of the neighboring atoms. We deduced that from the fact that it appears only when a big cluster radius is used Fig. 5.15b. Table 5.3 summarizes these results.

Table 5.3: Re-discovering the origin of the remarkable features in the XANES spectrum using FDMNES.

Peak	Origin	When it appears
α	quadrupolar transition + some dipolar contribution	small cluster perfect position
β	$p - d$ orbitals hybridation dipolar	atoms displaced from cubic position
γ	transition 1s-3d Molecular orbitals dipolar	Neighbor atoms considered (large cluster)

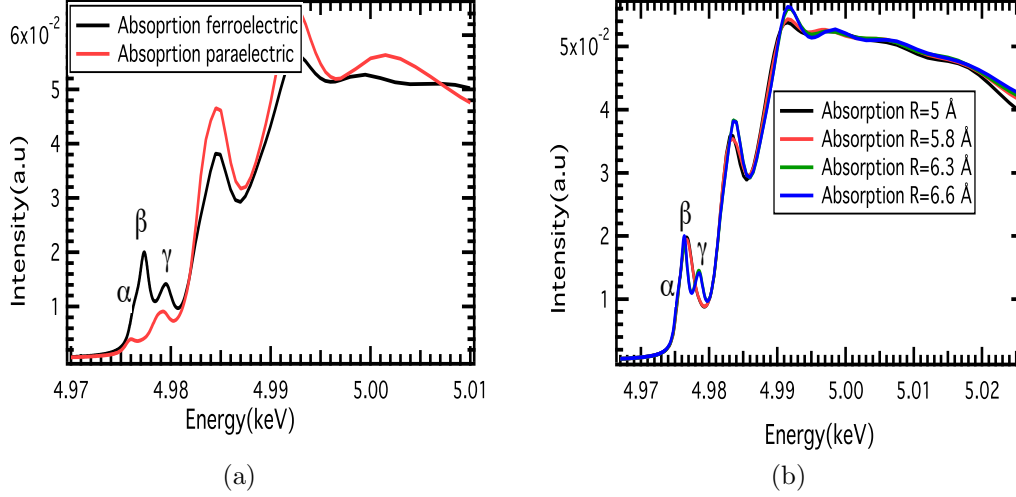Figure 5.15: Absorption simulations of bulk PTO. Figure (a) puts in evidence the hybridization of p-d orbitals in the FE state from peak β. In (b) one sees that only with a big cluster radius R=6.3 Å the peak γ appears.

We ran simulations changing the parameters mentioned above in order to find the best agreement with experimental data or other simulations. The crystal structure found in the literature for the FE state is [5]: space group P4mm and unit cell parameters in Å are $a = 3.90$, $b = 3.90$ and $c = 4.144$ and $\alpha = 90°$, $\beta = 90°$ and $\gamma = 90°$, and with the atom positions in the unit cell listed in Table 5.8.

Table 5.4: Atomic positions of the bulk paraelectric and ferroelectric structures proposed by Ramirez *et al.* [5].

	Cubic PE state			Tetragonal FE state		
Ti	$x=0$	$y=0$	$z=0.5$	$x=0$	$y=0$	$z=0.5382$
O$_1$	$x=0.5$	$y=0.5$	$z=0.0$	$x=0.5$	$y=0.5$	$z=0.1162$
O$_2$	$x=0$	$y=0.5$	$z=0.5$	$x=0$	$y=0.5$	$z=0.6091$
Pb	$x=0$	$y=0$	$z=0$	$x=0$	$y=0$	$z=0$

With these crystallographic parameters the best agreement between experiments and simulations was found with the parameters shown in table 5.5. All calculations were performed with the muffin tin method. This method is less accurate than the FDM method, but it is much faster. Our system requires a big cluster radius in order to consider the MO transitions. For example if one calculation with the Green method takes half a day, the same

calculation with the DFM method takes a week.

Table 5.5: Best found parameters for the FDMNES parameters to match experimental data from bulk samples.

Parameters	Best found values
Cluster radius	6.7 Å
Structure	Tetragonal FE state
Atom	Ti orbital 3d 1.33 e^- orbital 4s 0.67e^-
Multipolar development	dipole and quadrupole
Relativity	relativistic calculation
Screening	orbital 3d 0.8

To search for a solution for the Noheda's new FE phase, FDMNES is the tool of choice. It is possible to perform simulations with different positions of the atoms. As shown in Figure 5.4 Noheda's group proposed different possible configurations for the FE polarizations, which means that the atoms are displaced in different directions from the bulk positions.
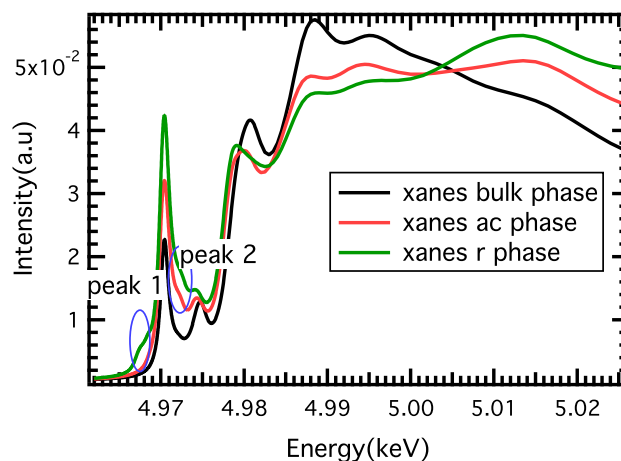

Figure 5.16: Absorption simulations of three possible FE phases. The first one corresponds to the bulk system and the other two are the possibilities proposed by Noheda.

In Figure 5.16 we show three absorption simulations, one for the bulk system, another for the *r phase* and the last one for the *ac phase*. Here what we see is that the XANES spectrum show different behaviors for the three

cases. The *r phase* shows an extra peak (peak 1) that does not appear in the other two cases and both the *ac* and *r phase* show the same extra peak (peak 2). With a close look to the position of the peaks, one sees that *peak*1 is at the same position as peak α. We remember that peak α is a transition from the 1*s* orbital to the unoccupied 3*d* state of the same TM. One can explain the appearance of these new peaks by imaging that the new displacements make the system less symmetric and therefore generate new hybridization states. These hybridization states would allow electronic transition with energies different from the previous ones. Since in the *r* phase, the Ti atom is displaced along the *x*, *y* and *z* the symmetric breaking is the largest and several new possible transition states could have been created, giving rise to *peak*1 and *peak*2.

Unfortunately, as explained above, we were not able to perform neither absorption nor resonant diffraction in the 5 nm thick sample, probably for lack of photon flux, and the probable destruction of the thin layer. Therefore we cannot answer the specific question raised by Noheda. Instead we provide a simulation of spectrum using the same FDMNES parameters obtained for the bulk system. Because of domains the XANES spectra would be an average over the sample. This problem can be overcome using resonant X-ray diffraction.

5.4.3 Thin film simulation: diffraction

Up to now we have considered bulk systems or the new possible FE phases, but we did not consider the diffraction by the FE domain periodicity. In FE thin films there are FE domains and we have seen in our experiments that diffraction clearly originates from their periodicity. Here we present RXD simulations of FE domains as well as two approaches to reproduce the domains. The simplest method would consist in using the scattering factors f_{phase1} and f_{phase2} obtained from bulk simulations of two different FE phases. Then we would use them to simulate the diffraction patterns of the FE domains: $I = \sum f_1 \exp(iq_1 r_1) + \sum f_2 \exp(iq_2 r_2)$. Unfortunately the FDMNES program does not provide a way to add crystallographic factors at will. The method then consists in creating a macro cell, built from aligning several unit cells forming two different domains, over which the domain patterns will be reproduced.

5.4.3.1 Creating macro cells

To reproduce the reflections due to domains, we run FDMNES oven a set of unit cells containing the domain structure. We know from literature the ratio

between *a phase* and *c phase* is 1/6. Figure 5.17 shows an illustration of unit cell patterns used for the calculation. In this set the *a*-phase is tetragonal with $c > a$, and the displacement of the atoms is either in the x direction for the ca_1 *domains* or y direction for the ca_2 *domains*. The amplitudes of the displacements are the tetragonal FE state values presented in Table5.8.
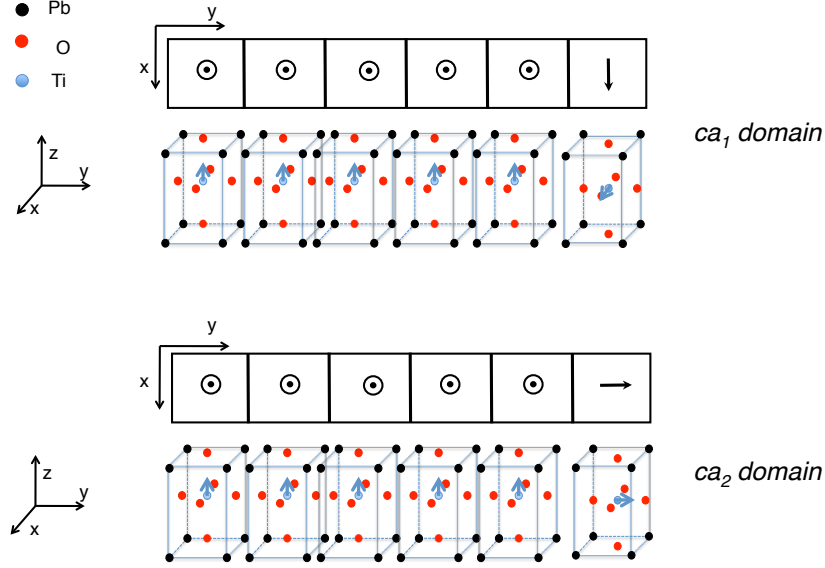

Figure 5.17: An example of two different patterns of unit cells which were used as input for the calculation of domain reflections

We need to know which reflections in our model are equivalent to our experimental reflections in the real sample. FDMNES has its own referential and there is a way to calculate the diffraction vector of the RXD reflections in the laboratory frame. In the table below we show four cases for (HKL) and five diffraction channels with the corresponding direction of the scattering vector in FDMNES.

In the table, ϵ and ϵ' are the polarizations of the incoming and outgoing waves and β the Bragg angle.

In grazing incidence geometry, the scattering vector nearly lies in the surface plane. Only the reflections shown in blue in the table fulfill this condition. Since we modeled the domains propagating in the y direction, we should have correspondence with the reflections of type (0 K 0). The $\pi - \pi'$ 90° channel also has to be taken into consideration since grazing incidence geometry implies $\sin \beta \simeq 0$ so the scattering vector is in the plane. This also implies that the $\pi - \pi'$ 90° and $\pi - \pi'$ 0° should be equivalent.

Table 5.6: The polarization of the diffraction vector for FDMNES reflections for four HKL values and five channels.

FDMNES reflections		
HKL	reflection	Polarization
	$\epsilon\ \epsilon'\ \chi$	
H 0 0	$\sigma\ \sigma\ 0$	$-\vec{j}$
	$\sigma\ \sigma\ 45$	$\vec{k}$ and $-\vec{j}$
	$\sigma\ \sigma\ 90$	$\vec{k}$
	$\pi\ \pi\ 0$	$\sin\beta\vec{k} + \cos\beta\vec{i}$ / $-\sin\beta\vec{k} + \cos\beta\vec{i}$
	$\pi\ \pi\ 90$	$-\sin\beta\vec{j} + \cos\beta\vec{i}$ / $\sin\beta\vec{j} + \cos\beta\vec{i}$
0 K 0	$\sigma\ \sigma\ 0$	$-\vec{j}$
	$\sigma\ \sigma\ 45$	$\vec{k}$
	$\sigma\ \sigma\ 90$	$\vec{k} + \vec{i}$
	$\pi\ \pi\ 0$	$-\sin\beta\vec{i} + \cos\beta\vec{j}$ / $-\sin\beta\vec{i} + \cos\beta\vec{j}$
	$\pi\ \pi\ 90$	$-\sin\beta\vec{k} + \cos\beta\vec{j}$ / $\sin\beta\vec{k} + \cos\beta\vec{j}$
0 0 L	$\sigma\ \sigma\ 0$	$-\vec{j}$
	$\sigma\ \sigma\ 45$	$\vec{i}$
	$\sigma\ \sigma\ 90$	$\vec{j} + \vec{i}$
	$\pi\ \pi\ 0$	$-\sin\beta\vec{j} + \cos\beta\vec{k}$ / $\sin\beta\vec{j} + \cos\beta\vec{k}$
	$\pi\ \pi\ 90$	$\sin\beta\vec{i} + \cos\beta\vec{k}$ / $-\sin\beta\vec{i} + \cos\beta\vec{k}$
H K 0	$\sigma\ \sigma\ 0$	$\vec{i}\text{-}\vec{j}$
	$\sigma\ \sigma\ 45$	$\vec{k}$
	$\sigma\ \sigma\ 90$	$2\vec{i} - \vec{j} + 2\vec{k}$
	$\pi\ \pi\ 0$	$-\sin\beta\ 2(\vec{i}\text{-}\vec{j}) + \cos\beta\ (\vec{i}+\vec{k})$ / $\sin\beta\ 2(\vec{i}\text{-}\vec{j}) + \cos\beta\ (\vec{i}+\vec{j})$
	$\pi\ \pi\ 90$	$\sin\beta\ 2\ \vec{k} + \cos\beta\ (\vec{i}+\vec{j})$ / $-\sin\beta\ 2\vec{k} + \cos\beta\ (\vec{i}+\vec{j})$

5.4.4 Comparing simulations and experiments

For the sake of convenience and to try to make easier the comparison between the experiments and the simulation, we labelled all experimental features with greek letters and simulation features with latin letters. The absorption features are α, β and γ, the diffraction feature Ω and Δ for experiments and D and G for diffraction simulations.

We compare the (010) reflection of the two simulated patterns in the $\pi-\pi'$ channel with the experimental $(010) - (0\delta0)$ spectra with π polarization in Figure 5.18. The matching between simulation and experiment is satisfactory for the a_2c domain (Fig. 5.18b) but not for the a_1c domain (Fig. 5.18a). The simulation of the a_2c domain reproduces the spectroscopic signature around

the G feature in a clear way. However, the D feature of the simulation seems to have no experimental correspondence.
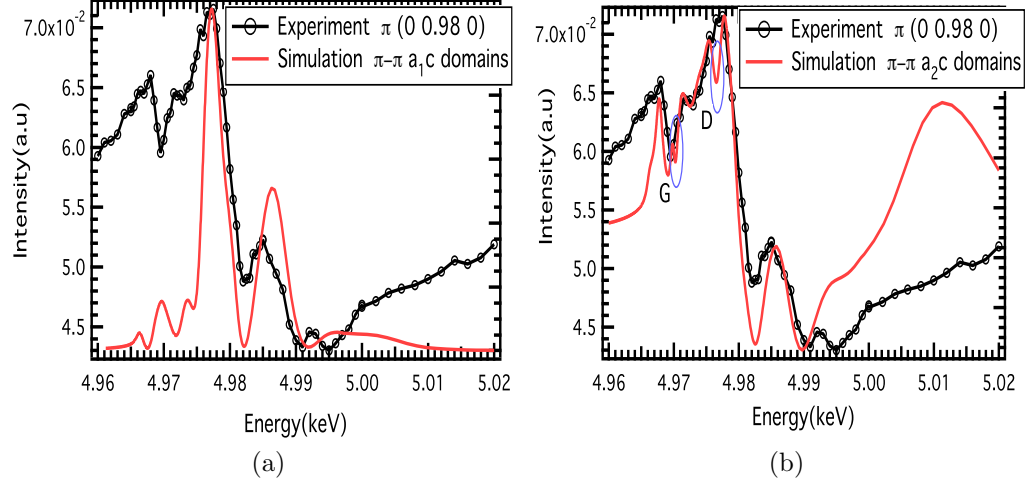

Figure 5.18: Comparison between experiment and simulation (a) for the a_1c domain and (b) a_2c domain.

In the experiments we saw that the Δ feature only appears with σ polarization. In order to understand its origin, we compared the $\sigma - \sigma$ channel simulation with the experimental data in Figure 5.19a. We see that the Δ feature is reproduced whereas the Ω feature does not appear. We observed that the energy of the D and Δ peaks is the same by comparing the experimental spectrum in σ polarization with the simulation in the $\pi - \pi'$ channel (see Fig. 5.19b). We compared these two curves just to show the energy correspondence of the two features. At this stage we do not have an explanation for this. We tried to optimize the fit between the experiments and simulation changing the amplitude of the atoms displacements in the a phase unit cell (the polarization in the surface plane). These simulations did not fit better with the experiments, and we decided to keep the model we used at the beginning.

We have also looked if there is any similarity between the Δ, Ω diffraction peaks and the α, β, γ peaks from absorption. First we have looked at the absorption simulation of the *a_2c domain*. The shape of the absorption spectrum (see Fig. 5.20) is different from the bulk absorption as well as from the 5 nm thick sample simulations (see Fig. 5.20 and 5.16). There is no sign of the α, β, γ peaks in this spectrum probalby because of the very different ferroelectric configuration. However if we look at the energy of G and D

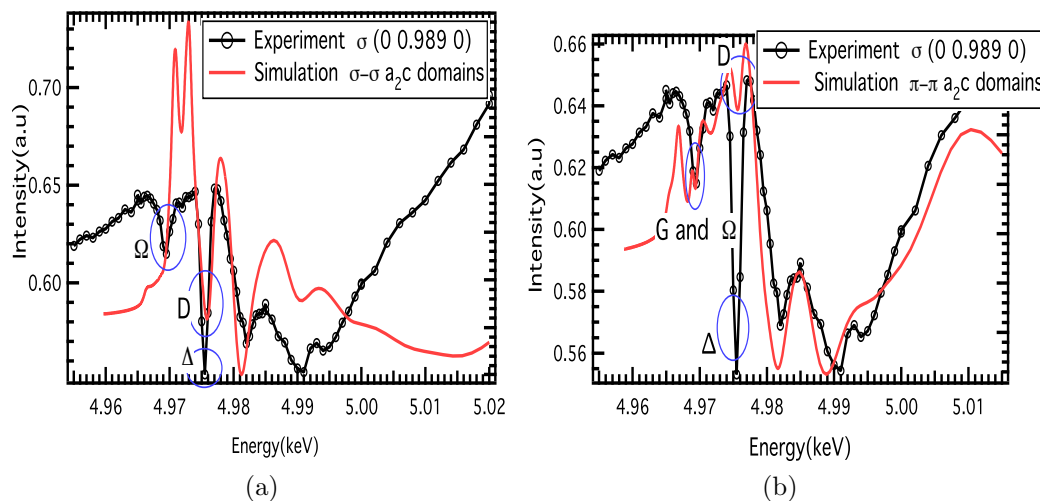Figure 5.19: Comparison between experiment with σ polarization and simulation of the a_2c domain (a) in the $\sigma - \sigma$ cannel and (b)in the $\pi - \pi'$ channel

(simulation peaks from diffraction) they match quite well with the β and γ experimental absorption peaks.
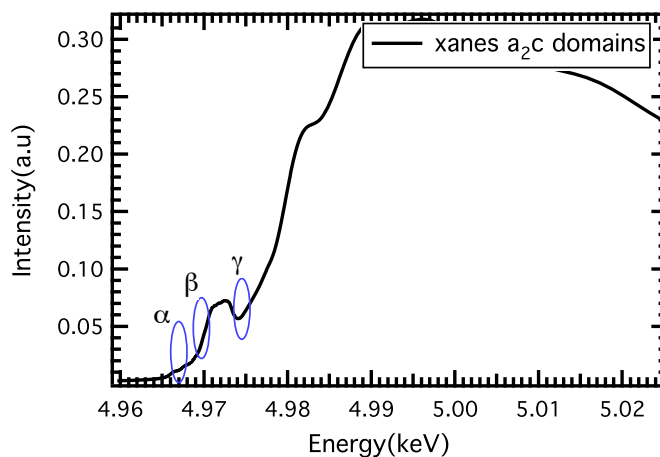

Figure 5.20: Absorption simulation of the a_2c domains. One sees there is no resemblence between the bulk absorption and the simulation no sign of the (α,β, γ peaks)

We summarize the peaks' positions treated in this chapter in Table 5.7. The Δ, C and β peaks have the same energy. We attribute them the same spectroscopic origin: a transition from $1s$ atomic orbital to $3d$ molecular

orbital. The Ω, B and G peaks have another origin: a transition from $1s$ to $p - d$ hybridized orbital.

Table 5.7: Energy positions of the Ω, Δ, β, γ, G and D features.

Peak	RXD experiments		Absorption simulation		RXD simulation	
	Ω	Δ	β	γ	G	D
Energy(keV)	4.969	4.9755	4.970	4.9747	4.9701	4.976

The best simulation is obtained with a macrocell of six tetagronal unit cells. The unit cell parameters are the same for all six of them a = b = 3.9Å and c = 4.144Å. The first five cells have the ferroelectric polarization out of plane and for the last one the polarization is in plane, with relative displacements of:

Table 5.8: Atomic positions of the macro cell ca_2 *domain* for the fist five unit cells and for the last unit cell.

	Ferroelectric displacements first five cells			Ferroelectric displacements last cells		
Ti	$x=0$	$y=0$	$z=0.5382$	$x=0$	$y=0.53820$	$z=0.5$
O_1	$x=0.5$	$y=0.5$	$z=0.1162$	$x=0.5$	$y=0.6162$	$z=0$
O_2	$x=0$	$y=0.5$	$z=0.6091$	$x=0$	$y=0.1162$	$z=0.5$
Pb	$x=0$	$y=0$	$z=0$	$x=0$	$y=0$	$z=0$

5.5   Conclusion

In this chapter we have proposed a new method to study thin film ferro-electrics. We showed that with resonant x-ray scattering we can observe the spectroscopic signature of FE structures as well as new possible FE phases that may appear in thin films due to strain from the substrate. The combination of experiments with FDMNES simulations is a great tool to study the atomic displacements in ferroelectric systems. The need of a diffraction technique is essential to look at domain patterns. If no FE domains existed only X-ray absorption experiments will be enough to look at the FE order as already shown for single crystals by Jaouen et al. [4]

In particular, we have studied PTO/DSO systems in which new FE phases had been proposed in the literature. FDMNES absorption simulations of the new FE phase proposed XANES would help to solve the phase. This new phase was proposed for a 5nm thick sample, but during our experiments we

could only study 25 nm thick samples. These systems show FE domains and we realized RXD experiments as well as simulations with FDMNES. We successfully reproduced these FE patterns by building up a macro cell. Comparing the energies of the peaks from absorption and RXD, we proposed the origins of the experimental peaks in the RXD spectra.

To our knowledge the new ferroelectric phase on 5nm thick PTO/DSO samples it is not yet solved. We think that hard x-ray absorption and XRD experiments would allow to give the answer to the atom displacement in the unit cell.

Bibliography

[1] A. H. G. Vlooswijk, B. Noheda, G. Catalan, and A. Janssens, "Smallest 90 domains in epitaxial ferroelectric films," vol. 91, Sep 2007.

[2] B. Ravel and E. A. Stern, "Local disorder and near edge structure in titanate perovskites," *Physica B: Condensed Matter*, vol. 208-209, pp. 316 – 318, 1995.

[3] B. Ravel, E. A. Stern, R. Vendrinskii, and V. Kraizman, "Local disorder and phase transitions of batio$_3$," *Ferroelectrics*, vol. 206-207, pp. 407–430, 1998.

[4] N. Jaouen, A. C. Dhaussy, J. P. Itié, A. Rogalev, S. Marinel, and Y. Joly, "High-pressure dependent ferroelectric phase transition in lead titanate," *Phys. Rev. B*, vol. 75, p. 224115, Jun 2007.

[5] R. Ramirez, H. Vincent, R. J. Nelmes, and A. Katrusiak, "X-ray studies of pbtio3 under hydrostatic pressure," *Solid State Communications*, vol. 77, no. 12, pp. 927 – 929, 1991.

[6] R. Nelmes and W. Kuhs, "The crystal structure of tetragonal pbtio$_3$ at room temperature and at 700 k,"

[7] S. Venkatesan, A. Vlooswijk, B. J. Kooi, J. T. M. De Hosson, and B. Noheda, "Substrate influence on the shape of domains in epitaxial pbtio3 thin films," *Journal of Applied Physics*, vol. 102, p. 104105, Nov 2007.

[8] G. Rossetti, L. E. Cross, and K. Kushida, "Stress induced shift of the curie point in epitaxial pbtio3 thin films," *Applied Physics Letters*, vol. 59, no. 20, p. 3, 1991.

[9] N. A. Pertsev, A. G. Zembilgotov, and A. K. Tagantsev, "Effect of mechanical boundary conditions on phase diagrams of epitaxial ferroelectric thin films," *Phys. Rev. Lett.*, vol. 80, pp. 1988–1991, Mar 1998.

[10] K. J. Choi, M. Biegalski, Y. L. Li, A. Sharan, J. Schubert, R. Uecker, P. Reiche, Y. B. Chen, X. Q. Pan, V. Gopalan, L.-Q. Chen, D. G. Schlom, and C. B. Eom, "Enhancement of ferroelectricity in strained batio3 thin films," *Science*, vol. 306, no. 5698, pp. 1005–1009, 2004.

[11] C. M. Foster, W. Pompe, A. C. Daykin, and J. S. Speck, "Relative coherency strain and phase transformation history in epitaxial ferroelectric thin films," *Journal of Applied Physics*, vol. 79, no. 3, pp. 1405–1415, 1996.

[12] S. K. Streiffer, J. A. Eastman, D. D. Fong, C. Thompson, A. Munkholm, M. V. Ramana Murty, O. Auciello, G. R. Bai, and G. B. Stephenson, "Observation of Nanoscale 180° Stripe Domains in Ferroelectric $PbTiO_3$ Thin Films," *Phys. Rev. Lett.*, vol. 89, p. 067601, Jul 2002.

[13] W. Pompe, X. Gong, Z. Suo, and J. Speck, "Elastic energy release due to domain formation in the strained epitaxy of ferroelectric and ferroelastic films," *Journal of Applied Physics*, vol. 74, Nov 1993.

[14] D. D. Fong, G. B. Stephenson, S. K. Streiffer, J. A. Eastman, O. Auciello, P. H. Fuoss, and C. Thompson, "Ferroelectricity in ultrathin perovskite films," *Science*, vol. 304, no. 5677, pp. 1650–1653, 2004.

[15] S. Venkatesan, A. Vlooswijk, B. J. Kooi, A. Morelli, G. Palasantzas, J. T. M. De Hosson, and B. Noheda, "Monodomain strained ferroelectric $pbtio_3$ thin films: Phase transition and critical thickness study," *Phys. Rev. B*, vol. 78, p. 104112, Sep 2008.

[16] G. Catalan, A. Janssens, G. Rispens, S. Csiszar, O. Seeck, G. Rijnders, D. H. A. Blank, and B. Noheda, "Polar domains in lead titanate films under tensile strain," *Phys. Rev. Lett.*, vol. 96, p. 127602, Mar 2006.

[17] Y. Joly, "X-ray absorption near-edge structure calculations beyond the muffin-tin approximation," *Phys. Rev. B*, vol. 63, p. 125120, 2001.

[18] D. Cabaret, Y. Joly, H. Renevier, and C. Natoli, "Pre-edge structure analysis of ti k-edge polarized x-ray absorption spectra in tio2 by full-potential xanes calculations," *JOURNAL OF SYNCHROTRON RADIATION*, vol. 6, no. 3, pp. 258–260, 1999.

[19] R. V. Vedrinskii, V. L. Kraizman, A. A. Novakovich, P. V. Demekhin, and S. V. Urazhdin, "Pre-edge fine structure of the 3d atom K-edge x-ray absorption spectra and quantitative atomic structure determinations for

ferroelectric perovskite structure crystals," *J. Phys. Cond-Mat.*, vol. 10, pp. 9561–9580, 1998.

Chapter 6

Exchange magnetic coupling between a soft ferromagnetic layer and BiFeO$_3$

6.1   Introduction

The possibility to control a net magnetic moment with an electric field draws the attention of many scientists. In some cases these two orders are coupled, and it is possible to control a net magnetic moment with an electric field and vice-versa. This effect is the *magnetoelectric effect*. Pierre Curie already predicted the coexistence of the magnetic and ferroelectric orders in one system. However it wasn't until 1959 that the real field of multiferroics started with the remark done by Landau and Lifshitz in a volume of *Course of Theoretical Physics* [1]:   *Let us point out two more phenomena, which, in principle, could exist. One is piezomagnetism, which consists of linear coupling between a magnetic field in a solid and a deformation (analogous to piezoelectricity). The other is a linear coupling between magnetic and electric fields in a medium, which would cause, for example, a magnetization proportional to an electric field. Both these phenomena could exist for certain classes of magnetocrystalline symmetry. We will not however discuss these phenomena in more detail because it seems that till present, presumably, they have not been observed in any substance.*

Soon after, the magnetoelectric coupling was observed by Astrov [2]. However, by the seventies the research on multiferroics slowed down, and it was later that people started again to be interested in this subject when theoretical predictions came out [3] while experimental achievements had discovered two different types of multiferroics: *Type I Multiferroics* and *Type II Multiferroics*. In 2003, the research on multiferroics has really taken off when Ramesh and his group synthesized thin films of BiFeO₃ [4].

To understand how the combination of magnetism and ferroelectricity appears in one system it is necessary to go back to the origin of each order. Magnetic order is mostly due to the presence of localized electrons in partially filled d or f orbitals of transition metals or rare earth ions, while ferroelectricity can have many different origins as it was already mentioned in the previous chapter. This separates multiferroic materials into two groups.

The first ones are the so called *Type I Multiferroics*. In these multiferroic materials, ferroelectricity and magnetism have different origins and their transition temperatures are usually far from each other. In most cases the magnetic transition temperature is lower than the ferroelectric transition temperature T_c. The electric polarization P is very large with values around $P \sim 10 - 100\,\mu\mathrm{C/cm}^2$. However, magnetoelectric coupling is quite small. The second type are the so called *Type II Multiferroics*, in which magnetism causes ferroelectricity, implying a large magnetoelectric coupling. However the ferroelectric polarization is rather small $P \sim 10^{-2}\,\mu\mathrm{C/cm}^2$ and most of them are low temperature multiferroics.

In this chapter, we present our work on BiFeO$_3$ single crystals. In the first part, we study monodomain FE single crystals coupled with a soft ferromagnetic layer. We use soft x-ray resonant scattering along with kinematical simulations to explain the effect that BiFeO$_3$ has on the Co's magnetization. In the second part we study multidomain FE single crystals with X-ray photoemission electron microscopy. We look at the ferroelectric and antiferromagnetic domain structures. This study has been a collaboration with Michel Viret form CEA Saclay.

6.1.1 Magnetic coupling between a soft ferromagnetic layer and BiFeO$_3$

Among all multiferroics, BiFeO$_3$ (BFO) is a material of choice, since it has both magnetic and ferroelectric orders at room temperature. BFO has a rhombohedrally distorted perovskite structure with space group $R3c$ [5]($a = 3.96$ Å and $\alpha = 89.4°$). The ferroelectric polarization is due to a perovskite distortion along the (111) direction driven by the Bi^{3+} *lone pairs*. The Curie temperature is 1100 K with an electrical spontaneous polarization $P = 90 \, \mu C/cm^2$ [6]. It is a G-type antiferromagnet, in which the Fe magnetic moments form a cycloidal structure of 64 nm periodicity 6.1. This cycloidal
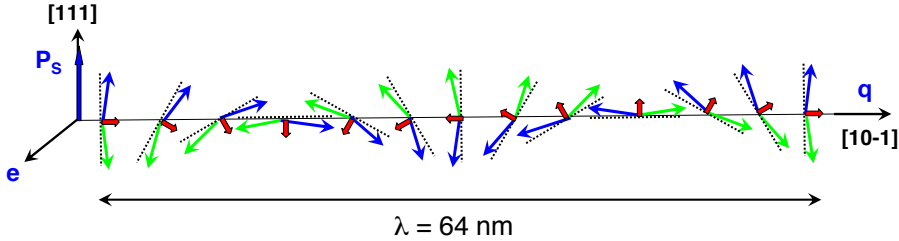
Figure 6.1: Cycloid structure of BiFeO$_3$.

structure yields no net macroscopic magnetization. However it has been reported that the cycloidal structure is destroyed under high magnetic field of 20 T [7]. The antiferromagnetic structure has a Néel temperature of 640 K [8]. The antiferromagnetic and the electric polarizations vectors are linked and the magnetic moments rotate in a plane containing the polarization vector P and the cycloidal propagation vector. [9]. Because of the rhombohedral symmetry, there are three equivalent directions for the cycloid propagation for a given ferroelectric polarization, namely: $\vec{q_1}[\bar{1}10]$, $\vec{q_2}[10\bar{1}]$ and $\vec{q_3}[0\bar{1}1]$ (see Fig. 6.2).
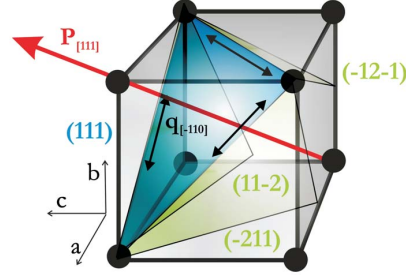
Figure 6.2: BFO unit cell in the case of a ferroelectric polarization along the (111) direction (red arrow), the three propagation directions of the associated cycloids (black arrows) and the three planes in which the magnetic moments of the cycloids rotate: $(\bar{1}2\bar{1})$, $(11\bar{2})$ and $(\bar{2}11)$ (light-green).

One of the goals of multiferroic materials is to control an easy axis of magnetization with an electric field. Data storage is done using net magnetic moments and since BFO is AFM (no net magnetic moment) one of the ways to achieve this is to couple a soft FM layer with BFO. The magnetoelectric coupling present in BFO allows to change the AFM order by applying an electric field. Then, if a FM layer is coupled to the AFM order it could be possible to act on the FM moments via the electric field. With BFO, this coupling would happen with the moments of the cycloidal structure. During this thesis we have adressed this issue in two different systems: monodomain ferroelectric single crystals and multidomain ferroelectric single crystals.

Systems with single crystal BFO and a FM layer have already been synthesized and studied by Lebeugle *et al.* [10] by neutron diffraction and magnetic measurements. For the FM layer they used 20 nm thick of Py (NiFe). In this case the FM material was a thin layer, so the magnetic moments should lie on the surface plane, since the demagnetization factor would prevent any out of plane components of magnetization. But with BFO beneath the FM layer, the group of M.Viret [10] observed an easy axis of magnetization within the sample plane. This was seen by Magneto-optical Kerr Effect (MOKE) measurements. This could not be attributed to an in-plane demagnetization factor, so it was claimed to be caused by the coupling with the underlying AFM order of the BFO. They proposed the FM layer to follow the cycloidal structure creating a magnetic wriggle.

In Magnetism, different exchange couplings exist. The most common is the *exchange-bias* effect. This coupling arises at the interface between a ferromagnetic thin film and an antiferromagnet. One of the main characteristic of this coupling is that it is a unidirectional exchange anisotropy. This refers to the presence of a preferred direction of the FM magnetization that

originates from the exchange coupling of the moments in the FM to uncompensated pinned moments of the AFM. In consequence, the hysteresis loop of the FM later is shifted along the field axis. One could expect to have an exchange-bias interaction in our system. However, Lebeugle *et al.* observed a preferred axis of anisotropy (easy axis) of magnetization which is a sign of a uniaxial exchange anisotropy, and the hysteresis loop is not shifted in the field axis. Moreover, it is known that in transition metal oxides the exchange coupling is not a direct interaction with the adjacent atoms but an indirect interaction, also called *superexchange.* This kind of interactions was first studied by Anderson [11] in 1950, with an interaction between the Mn^{2+} cations separated by an O^{2-} anion.

Therefore, in our case, the exchange interaction between the $BiFeO_3$ and the FM layer can be described as a superexchange. Superexchange is a strong antiferromagnetic coupling between two next-to-nearest neighbor cations (Fe^{3+}) through a non-magnetic anion (O^{2-}). This local interfacial exchange coupling between the $BiFeO_3$ and a FM layer can be written in the form of $E_{ex} = \frac{1}{2}J_{ex}\vec{S}_F\vec{S}_{cant}$ where $\vec{S}_{cant}$ is the local canting of the Fe^{3+} moment describing the cycloid. Because of exchange coupling, the cycloids will tend to imprint the cycloidal structure on the FM layer. However, since the length scale of the cycloid (64 nm) is comparable to the exchange length of the FM layer (around 15 nm), the FM layer is not likely to adopt a cycloidal structure. Instead, Lebeugle *et al.* proposed that the coupling should induce a wriggle in the FM layer. They estimated an angle of $1.5°$ for the canting of the FM moments in the wriggle. The periodicity of this incommensurate structure on the FM layer is expected to be the same as the cycloid periodicity. In figure 6.3 we show an image of the coupling.
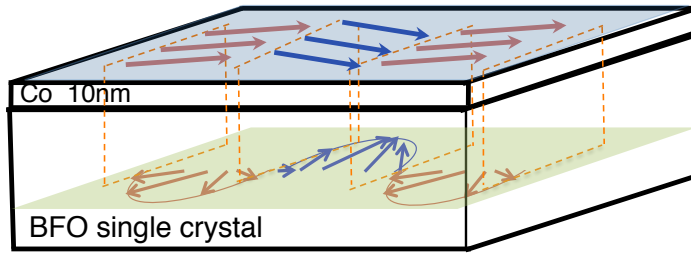

Figure 6.3: Sketch of the antiferromagnetic superexchange coupling between the cycloidal structure of BFO and the FM layer (Co) deposited on top of the BFO. The Co magnetic moments follow the cycloidal structure creating a *zig-zag* structure.

The study of the effect of the cycloidal structure on a soft ferromagnetic layer deposited on a BFO single crystal, can be done with monodomain FE

or multidomain FE single crystlas. For monodomain FE samples we use Soft X-ray Resonant Magnetic Scattering. In comparison with neutron diffraction, with X-rays it is possible to look at 10 nm-thick matter. In addition, in the soft x-ray range the cross sections are highest for the transition metals, and the sensitivity to magnetism is large. The periodic structures we will be looking at are typically of dimensions that match the soft x-ray range and therefore can be accessed by soft x-rays diffraction in grazing incidence geometry. In the case of multidomain FE samples, the magnetic and electric domain should be of the same size and one might expect to have a different behaviour of the magnetic coupling compared to monodomain FE systems. In these systems, magnetic scattering is not a good technique since the multidomain state is equivalent to a powder state for which it is impossible to perform magnetic scattering experiments. For this reason, one needs a local probe as a microscopy technique that is sensitive to both electric and magnetic properties. This is obtained using X-ray Photoemission Electron Microscopy. (X-PEEM)

For a real application point of view, it is more suitable to study thin films. However, a fundamental comprehension of the mechanism that creates the coupling is crucial. In thin films, when the strain induced by the substrate is large enough, the cycloidal structure is supressed [12], but the coupling with a thin FM layer is still possible via an exchange-bias process such as described by Malozemov's model that relies on surface roughness and lateral AFM domain walls [13, 14]. In both cases – thin films and crystals – the coupling involves the Fe moments of the cycloid and the moments of the FM layer. The physics behind the coupling is the same in both cases: this is why it is important, for a fundamental point of view, to study the coupling with single crystals.

6.1.1.1   Sample preparation

All the samples studied during this thesis were synthesized by floating zone technique at CEA Saclay SPEC/IRAMIS by Michel Viret and Dorothée Colson. The samples are mostly monodomain when they grow and it is during the extraction from the preparation chamber that some become multidomain ferroelectric. This because BFO is also a piezoelectric material, which means that strain (structural defects) create FE domains. They grow along the (010) direction and their typical size is around $0.5\,mm \times 1.5\,mm \times 0.05\,mm$. We show a picture of a sample in figure 6.4.

For XRMS measurements, we deposited 10 nm of Co on top of monodomain samples in a Molecular Beam Epitaxy (MBE) chamber. In order to have an even surface for the deposition, samples are polished with ionized
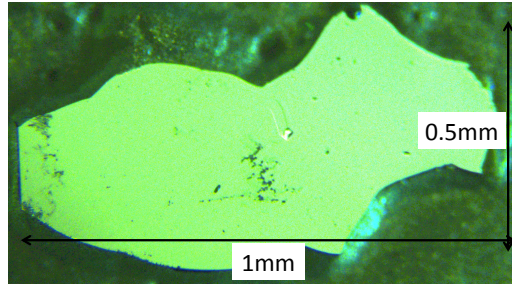
Figure 6.4: Picture of a single crystal BFO sample on silver paint

argon gas for about 20 s. During the process, the Ar atoms hit the surface of the samples and remove the unwelcome roughness. The deposition is done by heating high purity Co which evaporates into the chamber and collects onto the samples at a rate of about 3 Å/s.

6.2 Coupling in the case of long-range magnetic order: XRMS experiments on Co/BFO monodomain ferroelectric samples

In figure 6.5 we show two images of $BiFeO_3$ single crystals in the monodomain FE state. These pictures were taken by Polarized Light Microscopy (PLM) that is only sensitive to the in-plane ferroelectric polarizations. The two images were taken with inverse polarizations and there is only small difference between them: a minor ferroelectric domain (surrounded in red in the picture). This minor domain will not contribute in our studies.

In this section we focus on monodomain ferroelectric systems. Since the coupling with the Co layer occurs at the sample surface, it is important to consider how the Fe moments are ordered at the BFO surface. All three cycloids q_1,q_2,q_3 have a 64 nm periodicity. But since the sample grew along the (010)-direction, the periodicity of cycloids q_1 and q_3 appears larger at the surface (90 nm) for they are 45° tilted to the surface plane, while cycloid q_2 – which is parallel to the surface plane – simply yields a 64 nm-periodical footprint. A simple geometrical analysis is presented in Fig. 6.6.
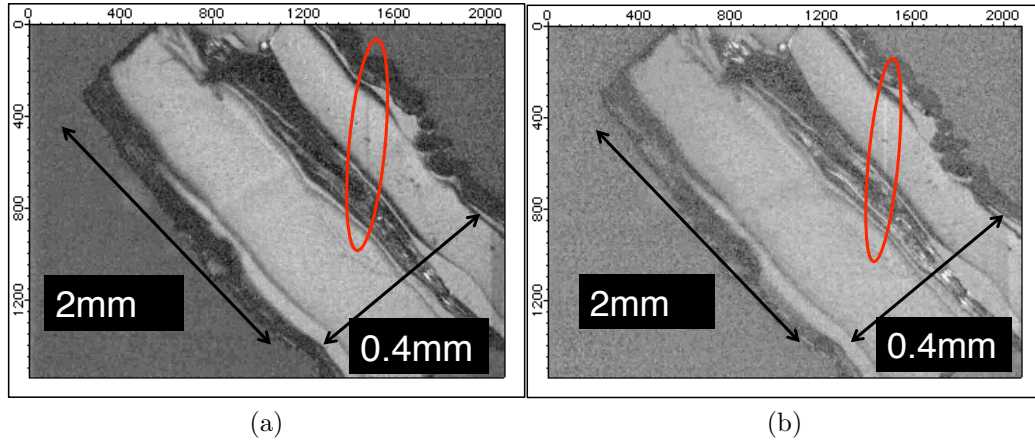
Figure 6.5: Two polarized light microscopy images of a monodomain ferroelectric bulk crystal. The thin line in (a)black and (b)white is a minor ferroelectric domain.
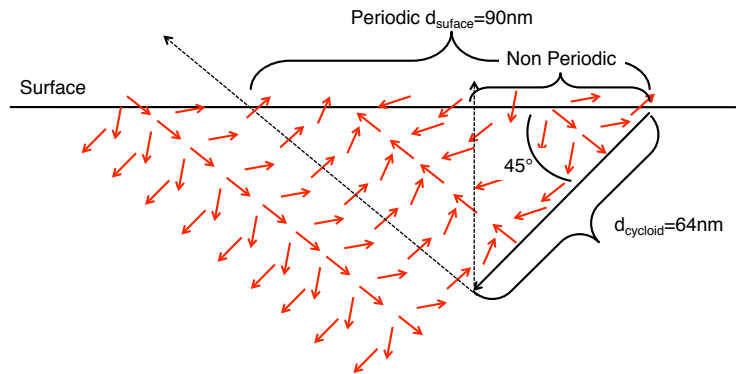

Figure 6.6: The projection of a cycloid on the surface plane of the sample. The periodicity on the surface is $\mathrm{d}_{surface} = \mathrm{d}_{cycloid}/\cos 45°$ with $\mathrm{d}_{cycloid} = 64\,\mathrm{nm}$

6.2.1   Soft x-ray scattering

The periodicities in BFO can be access in grazing incidence geometry by soft x-ray resonant magnetic scattering (XRMS) as already shown in the case of magnetic domains by Durr [15]. XRMS gives the reciprocal space information as well as the chemical selectivity. In the following, we will treat the reciprocal space and the chemical selectivity contributions. In the expression for the diffracted intensity we see that both contributions are coupled.

$$I = |\sum_{r_j} f_j(\boldsymbol{Q}, \boldsymbol{E}) e^{i\boldsymbol{Q} \cdot \boldsymbol{r_j}}|^2 \qquad (6.1)$$

6.2.1.1 Scanning the reciprocal space

With a diffraction geometry as in figure 6.7 in which the direction of the incoming beam is perpendicular to the periodicities under study it is possible to scan the reciprocal space in the x and z directions. This is done by combining the motor displacements of the diffractometer θ (sample rotation) and 2θ (detector). In Co/BFO systems the magnetic coupling occurs at the surface plane. Therefore we are looking at periodicities that are in the XY plane (surface plane), following the notation from figure 6.7 the component of the scattering vector in the x direction is given by:
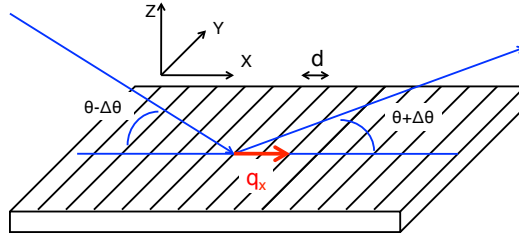
Figure 6.7: Rocking curve geometry. The detector is fixed at $2\theta = 2 \times \theta$. The sample is turned around the Y axis from $-\Delta\theta$ to $+\Delta\theta$.

$$q_x = 2\,\frac{\sin\theta\sin\Delta\theta}{\lambda} \qquad (6.2)$$

with $\mathbf{Q} \equiv \mathbf{k}_f - \mathbf{k}_i$ the scattering vector where $\mathbf{q} \equiv \mathbf{Q}/2\pi$ and $k = 2\pi/\lambda$. Then, the periodicity is $d = 1/q_x$. To search the information along q_x we choose to perform rocking curves. In a rocking curve we realize a rotation of the sample around the specular position ($\theta_i = \theta_f$) with the detector fixed. With:

$$\theta_i = \theta - \Delta\theta \qquad (6.3)$$
$$\theta_f = \theta + \Delta\theta \qquad (6.4)$$
$$\qquad (6.5)$$

θ is the incidence angle of the specular reflection, the detector being at $2\theta = 2 \times \theta$.

6.2.1.2   Chemical selectivity & reciprocal space information

We have already shown that the chemical selectivity is given by the energy-dependent terms of the scattering form factor. Let us rewrite the scattering form factor as:

$$\hat{f}_{e'e} = (\boldsymbol{e'^*} \cdot \boldsymbol{e})(f_0 + f' - if'') - \underbrace{i(\boldsymbol{e'^*} \times \boldsymbol{e}) \cdot \boldsymbol{u}(m' - im'')}_{\text{fmag}} \qquad (6.6)$$

With $\boldsymbol{e'^*}$ and $\boldsymbol{e^*}$ the polarization of the incoming and outcoming beam, $\boldsymbol{u}$ the quantification of the magnetic moment of each atom, f the scattering amplitude and m the magnetic scattering amplitude. The diffracted beam will only have a contribution from the f_{mag} term when the energy of the incident beam corresponds to the energy of an electronic transition. In the soft X-ray range, for transition metals, these energies are the $L_{2,3}$ edges. For instance, performing rocking curves at different energies we will have the information from the magnetic periodicity in the x-direction. In figure 6.8 we present three possible scenarii that may happen during the experiments. The first case corresponds to a configuration in which the magnetism is invisible for the photon – the energy of the incoming beam being far from the resonance. In this case, the rocking curve only gives the total specular peak. In the second example, the incoming beam "sees" the magnetism, but since there is no particular magnetic order the rocking curve is similar to the first case. For the third case there is a magnetic periodicity in the x-direction and the energy of the incoming beam corresponds to an electronic transition of the magnetic atrom. In this configuration, the rocking curve has satellite peaks around the specular peak. The position of the satellite peaks $(1/d)$ gives the periodicity of the magnetic pattern (d). The aim of our study is to look for satellite peaks that will be due to the cycloidal structure of the BFO or the wriggle in the Co thin layer.
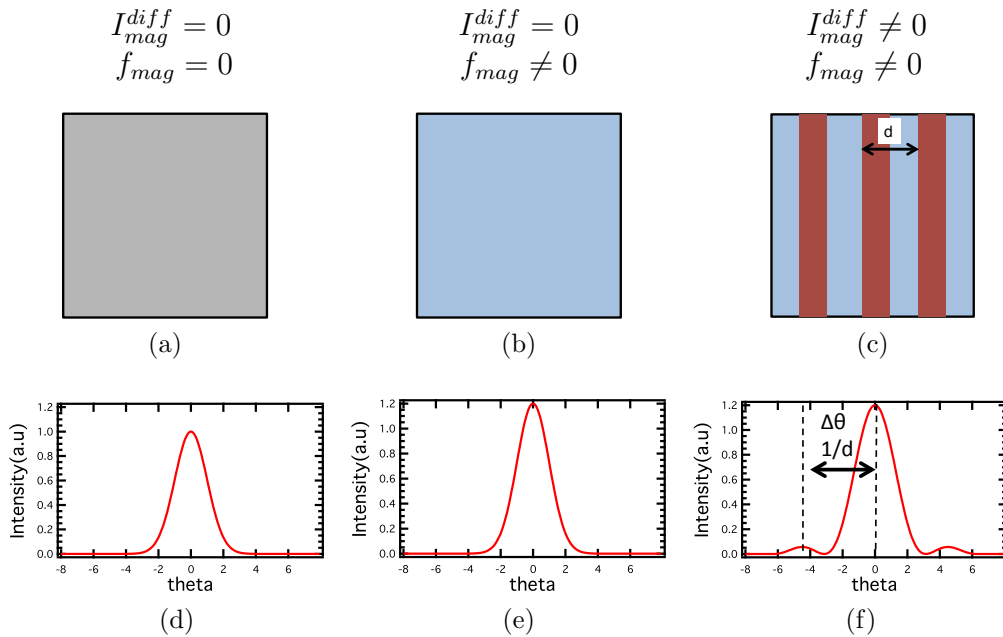
Figure 6.8: Here we show three possible scenarii of XRMS that may happen during the experiments. On the top part we show how the incoming beam "sees" the sample and on the bottom part what the rocking curve gives. (a)The energy of the incoming beam is far form the resonance: the magnetism is invisible and the rocking curve only gives a specular peak (d). (b)The photon sees the magnetism but since there is no magnetic order the rocking curve gives the specular peak with a resonance contribution (e). (c)The photon sees the magnetism and since there is a magnetic ordering we have the specular peak with satellite peaks around it (f).

6.2.2 Results

All XRMS experiments were performed with similar samples: Monodomain ferroelectric single crystals with a 10 nm-thin layer of Co deposited on top. Up to four different samples have been studied, all of them giving the same results – either at synchrotron SOLEIL or at Diamond light source. At SOLEIL, the experiments were performed with RESOXS diffractometer, which is presented in detail in the last chapter. At diamond light source, we worked at the I06 beamline with either RASOR diffractometer or with a 2-circle diffractometer for a temperature dependence study. In these two diffractometers, the detection is done either by a photodiode or a by total electron yield (TEY).

At the Fe edge we only see diffracted photons, whereas at the Co edge we measure both the photoelectrons and the diffracted X-rays. The TEY

counts the photoelectrons coming from the very surface of the system, since their penetration length is extremely small. Indeed, Fig. 6.9 illustrates that the photoelectrons coming from the BFO layer do not cross the 10 nm layer of Co.

The spectra of figure 6.9 give information on the degree of oxidation. For example, the XRMS spectrum at the Fe edge is typical of an oxide, with some characteristic anomalies on both sides of the peaks. Signature of oxidation can also be seen at the Co edge – pointed out by circles in the figure – which means the Co is partially oxidized.
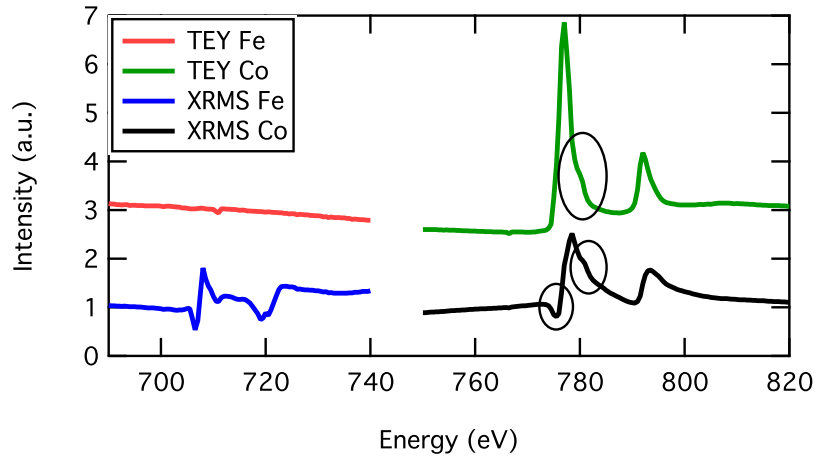
Figure 6.9: Comparison between the TEY and the XRMS data. The TEY spectrum of Fe is flat because the electrons coming out from the BFO do not cross the 10 nm Co layer. The XRMS data shown here were taken at $q_x = 0$.

6.2.2.1   Experimental conditions

The rocking curve geometry chosed for these experiments implies a fixed angle for the detector. The experiments were performed at fixed energy, with energies of a wavelength in the soft x-ray range between 1.5 and 1.8 nm. The magnetic orders under study have a periodicity of around 64 nm. Looking at the relation for q_x from eq:6.2, we can evaluate $\Delta\theta$ – the position of the satellite peaks – for a given λ and 2θ. In table 6.1 we show the values for $\Delta\theta$ for an incoming photon of energy 774 eV.

The geometry of the diffraction experiment limits the angle of the detector to $2\theta > \theta$. In table 6.1 we see that for small angles up to $2\theta = 10°$, it is not possible to reach the satellite peaks for both periodicities because $\Delta\theta > 2\theta/2$. We also see that at higher angles $2\theta = 28°$ the satellite peaks are close to

Table 6.1: Calculated values for $\Delta\theta$ in deg at $E = 774\,\text{eV}$

2θ	$10°$	$12°$	$14°$	$18°$	$22°$	$28°$
p=64 nm	8.24	6.87	5.88	4.85	3.75	2.96
p=90 nm	5.85	4.87	4.18	3.25	2.67	2.1

the specular specular peak ($\theta=2\theta/2$) and it may even not be possible to see them. During the experiments the best compromise was found at at value for 2θ between $10°$ and $12°$. This is shown in figure 6.10 were we show several rocking curves at values of 2θ from $9°$ to $20°$. We see that at angles bigger than $13°$ there are no satellite peaks observed. The position of the peaks does not correspond to the ones expected from table 6.1. This is explained later considering the azimuthal angle.
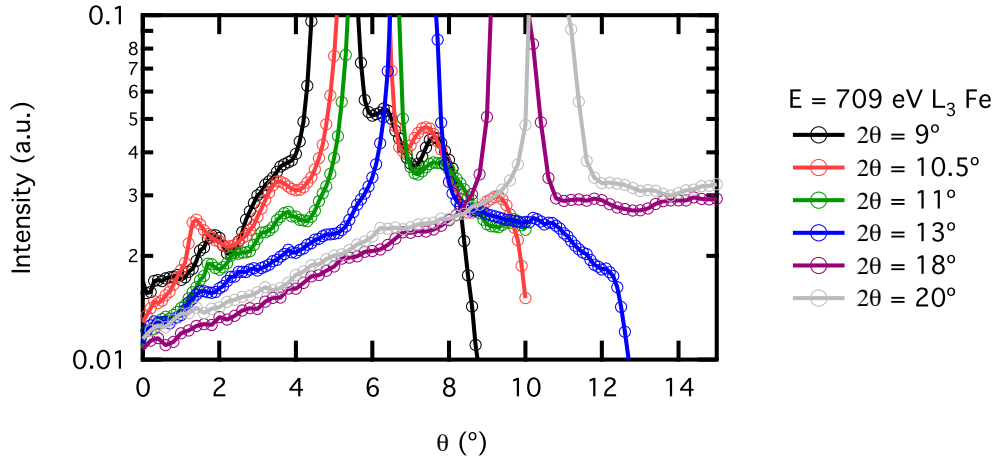
Figure 6.10: Rocking curves at different fixed values of the detector (2θ)

The size of the incoming beam was around $50\,\mu\text{m}$ in the vertical direction and $200\,\mu\text{m}$ in the x-direction. The projection of the beam in the surface sample for $13°$ is $222\,\mu\text{m}$. The penetration depth of soft X-rays at the $L_{2,3}$ energy edges of 3d metals is around $20\,\text{nm}$ at the resonance and around $490\,\text{nm}$ far from the resonance. Since the Co layer is only about $10\,\text{nm}$, we are sure the beam will go through the Co layer and get to the BFO.

In magnetic diffraction only the component of the magnetization with a periodicity along the diffraction vector contributes in the f_{mag} term of the scattering form factor of eq:6.6. $\boldsymbol{u}$ is the quantification vector of the magnetic moment of each atom. In our case, the coupling between the Co and the BFO is expected to imprint a modification on the Co layer. This modification can be expressed as an added term to its magnetic moments

as $\boldsymbol{u} = \boldsymbol{u_0} + \delta\boldsymbol{u}$ where the extra term $\delta\boldsymbol{u}$ is periodic. The stimated small canting of the Co moments ($\approx 1.5°$) make this extra term small compared to the Co magnetic moment $\delta\boldsymbol{u} < \boldsymbol{u_0}$. This, along with the fact that there is only 10nm of Co will make the XRMS signal of the Co very weak and hard to detect. On the contrary for the BFO the entire magnetic moments of the Fe atoms contribute to the XRMS signal, but since the signal has to cross the Co layer, this will considerably decrease the intensity. For these reasons, the beam has to be very bright and very well focussed. Indeed, slits are even necessary to optimize the signal by removing some parasitic photons. The slits are in front of the detector, and their size is about $1\,\mu$m-thick in the horizontal direction and $1\,$mm-long in the vertical direction at Diamond Light Source and $200\,\mu$m $\times 2\,$mm in RESOXS diffractometer.

6.2.2.2   XRMS results

Diffraction spectra of rocking curves at $2\theta = 12°$ for the Fe $L_{2,3}$ edges are shown in Fig. 6.11. At the resonance of Fe at $E = 708\,$eV there are satellite peaks around the specular peak. The position of these peaks in the reciprocal space are: $q_x = 0.0035\,$nm^{-1} for the first peak and $q_x = 0.007\,$nm^{-1} for the second peak, corresponding to periodicities of $285\,$nm and $142\,$nm. These two values are far from the cycloidal structure periodicities which are $64\,$nm or $90\,$nm. This is because in this simple approach of X-ray diffraction we do not take into account the azimuthal angle of the incoming beam. We will come later to this (see section 6.2.2.4). These satellite peaks are the direct signature of the cycloidal structure in BFO, confirming that XRMS is a relevant technique for this kind of study.

As explained in the introduction, the aim of the study was to see the effect of the cycloid structure on the soft ferromagnetic layer of Co. In Fig. 6.12, we display rocking curves recorded at the Co L_3 edge $E = 779\,$eV showing satellite peaks. These satellite peaks – compared to the ones at the Fe edge – are broad shoulder-like bumps from which no precise position can be extracted. However, if we take the middle of the peaks we see that their reciprocal space position $q_x = 0.003\,$nm^{-1} is not the same as the peaks at the Fe edge. This periodicity (about $333\,$nm) is slightly larger than the one observed at the Fe edge. Noteworthy, the existence of these diffraction peaks is the direct probe of the coupling between the BFO cycloidal structure and the Co thin layer. In the case where no magnetic structure would exists, we would be in the case of figure 6.8 b and there would be no satellite peak.

Here we shall recall that the canting of Co moments is expected to be very small ($1.5°$) with only $10\,$nm of Co that scatters. Moreover, exchange coupling is stronger at the interface with BFO, and we might expect it to
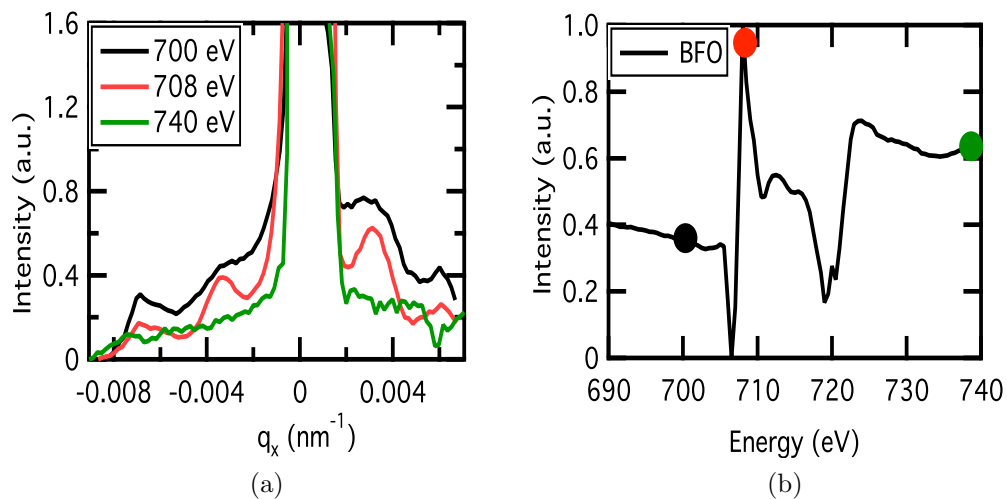
Figure 6.11: (a)Energy dependence of the peaks around Fe edge. (b)XRMS spectrum at $q_x = 0$ at the Fe $L_{2,3}$ edges.
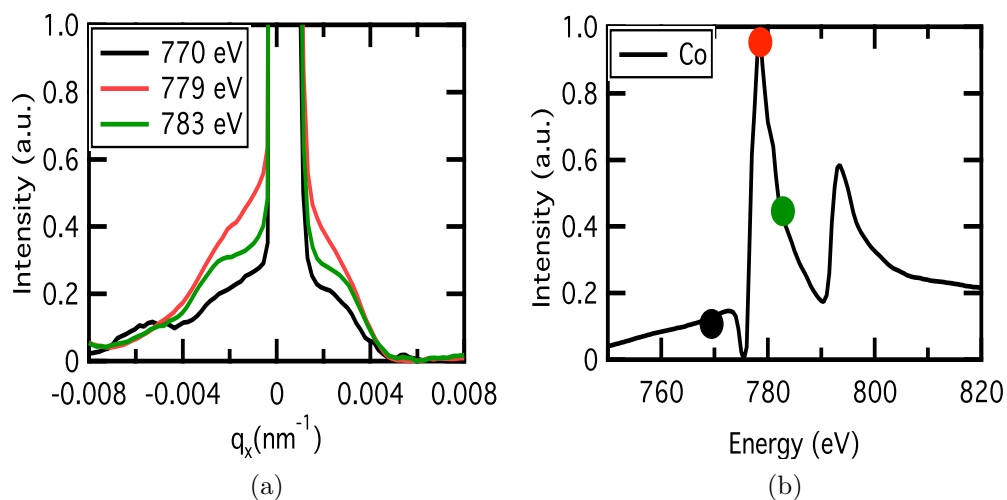

Figure 6.12: (a)Energy dependence of the peaks around Co edge.(b)XRMS spectra at $q_x = 0$ at the Co $L_{2,3}$ edges.

decrease at the top of the Co layer, allowing a certain relaxation of the Co wriggle. Since XRMS is a long range method, the total yield of diffraction is an average over the entire layer. All these facts may explain the broader peaks at the Co edge than at the Fe edge.

In figure 6.13 we show XRMS spectra at the Fe $L_{2,3}$ edges : one at the

satellite peak position and one at the specular position. In both cases, the shape of the spectrum is very different from the a metallic Fe crystal. This is not surprising, since Fe is here oxidized and its electronic structure is very anisotropic because of the polar displacement and the hybridization between neighbor atoms.The intensity of the spectra are not significant since they were normalized between 0 and 1. The spectrum at the specular position shows thinner peaks than the one at the satellite peak position.
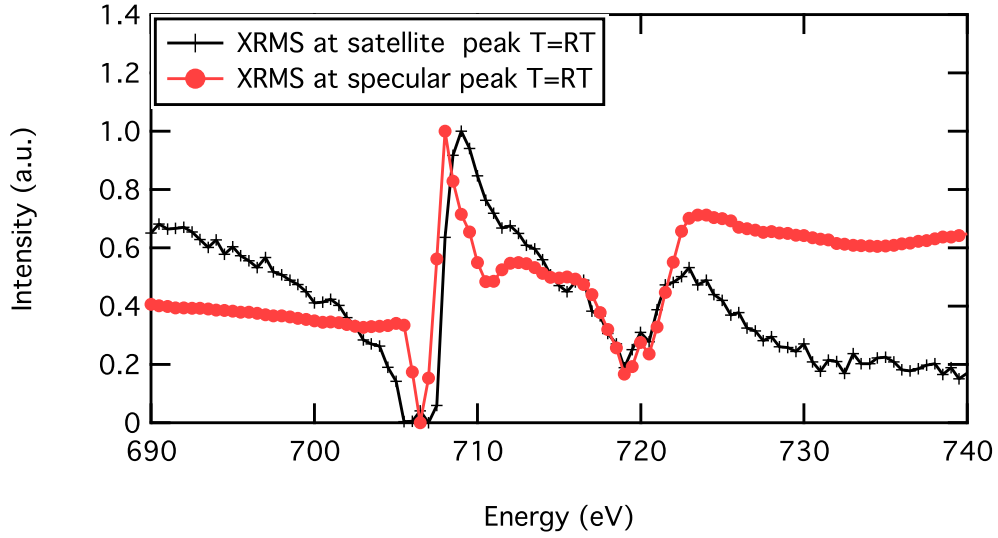
Figure 6.13: XRMS spectra at RT, one at the specular peak and the other one at the satellite position.

6.2.2.3   Study of the satellite peaks as a function of the temperature

One of the ways to prove that the satellite peaks in the Co edge are due to the coupling with the antiferromagnetic order of the BFO, is to heat the system above the T_N of BFO – which is known from neutron diffraction ($T_N = 640$ K). Not many experimental endstations allow to perform soft X-ray diffraction measurement under high temperature. We perform this experiments at Diamond Light Source in I06 beamline in a small 2-circle diffractometer. In figure 6.14a we show the temperature behavior of the satellite peaks at the Co L_3 transition energy. When temperature approaches T_N, the satellite peaks disappear, getting to a non antiferromagnetic configuration. This confirms the new magnetic nature of the Co thin layer.

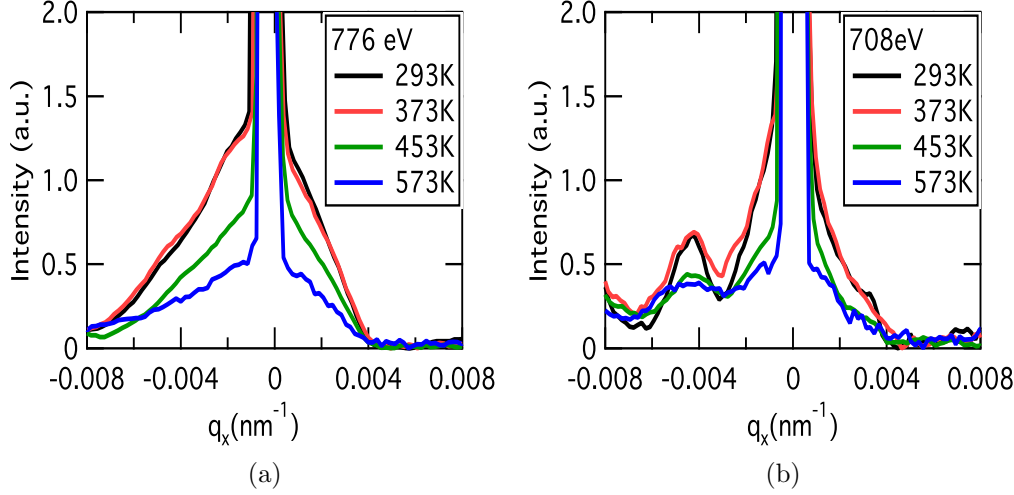The same behavior is observed at the Fe edges 6.14b. In our experiments,

Figure 6.14: XRMS spectra at different temperatures (a)at the Co L_3 edge and (b)at the Fe L_3 edge.

the position of the peaks remain the same while the sample is heated, meaning that the periodicity of the cycloids does not change with temperature. This is different from what has been observed in neutron experiments by Ramazanoğlu *et al.* [16], where they reported that the cycloid period slowly grew with increasing temperature. They observed the change of the periodicity above 400 K. In our experiments, above 400 K the satellite peaks were too small to get a precise position of them. We will like to recall that, the aim of the study was not to study the behaviour of the cycloidal structure with temperature but to emphasize the coupling between the BFO cycloidal structure and the Co layer.

In Fig. 6.15 we show the intensity of the satellite peaks as a function of temperature at the Fe L_3 edge. We superpose our experimental data with neutron diffraction data from [17] for $BiFeO_3$ crystals. We observe a similar behaviour in both cases.

In figure 6.16 there are two spectra at the Fe edges at $T = 563$ K. It can already been observed that at this temperature (below the Néel temperature) the shape of the spectrum at the satellite peak is not very clear. At this temperature, the AFM order is almost inexistent, which means that there will not be much diffraction at this position. At the specular position, the spectrum is also very different from the one at room temperature. This spectrum resembles that of a metal, but it is not metallic since the resonance peaks are splitted in two (see figure 6.16), a direct footprint of the oxidized
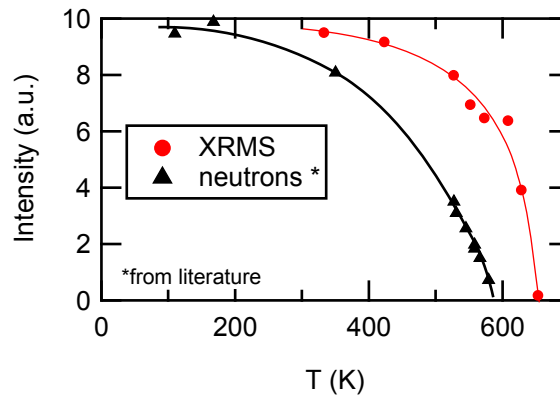
Figure 6.15: Comparison of the temperature dependance of the satellite peak intensity with neutron experiments from [17] (black) and our experiments (red).

state of the material. At this temperature, the electronic environment of Fe is not very different from the one at room temperature [17], since the displacement of the atoms is not different enough to change the electronic order. The contribution from the satellite peak is weak due to the fact that at this temperature the background is too high and covers up the information. We still see a resonance at the L_3 edge $E = 708\,\text{eV}$.
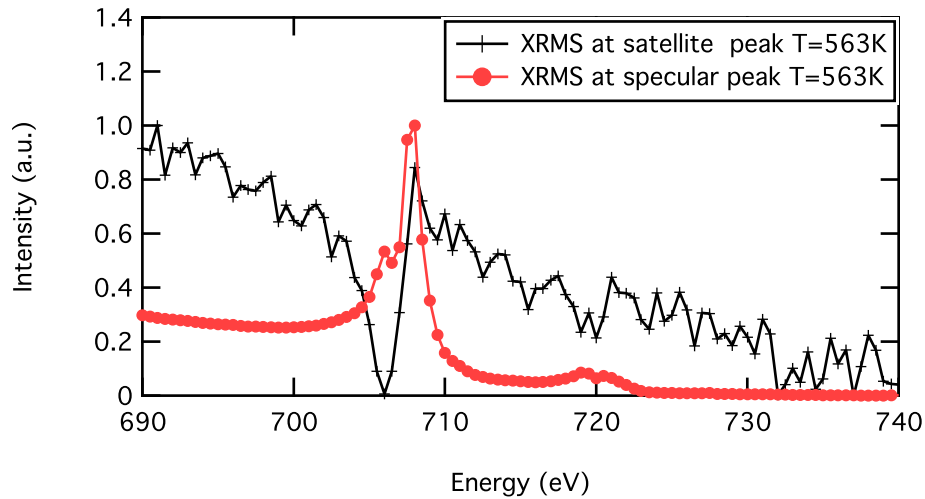
Figure 6.16: XRMS spectra at RT, one at the specular peak and the other one at the satellite position.

6.2.2.4 Explanation of the satellite peaks positions as a function of the azimuthal angle

Until now, we have studied the appearance of the satellite peaks as a function of energy and temperature. However, we have not properly studied their position in the reciprocal space. In order to have a proper interpretation, we need an azimuthal study. The azimuthal angle is the angle between the in-plane scattering vector and the incoming photon. Let us first remember that in single crystal BFO there are three directions of propagation of the cycloid for one ferroelectric polarization. It has been shown earlier that in some rocking curves two satellite peaks appear (see figure 6.11a) and that the periodicities obtained are higher that the ones expected. The fact that there are two peaks could be explained as being 1st and 2nd order diffraction peaks. However, the intensities are quite similar and the second peak is not always at the double position. For this reason, the hypothesis of a 2nd order peak was eliminated.

In fact, one has to consider that the X-rays might be diffracted by several cycloids at the same time each of them with a different propagation direction. In Fig. 6.17 there are three rocking curves recorded at RASOR diffractometer for three different azimuthal angles and different polarizations. We observe that the shape and position of the satellites are strongly affected by the azimuthal angle: in one case there is only one well-defined peak ($\chi = 54.295°$), whereas in another case we see two not-well-defined peaks ($\chi = 0°$).
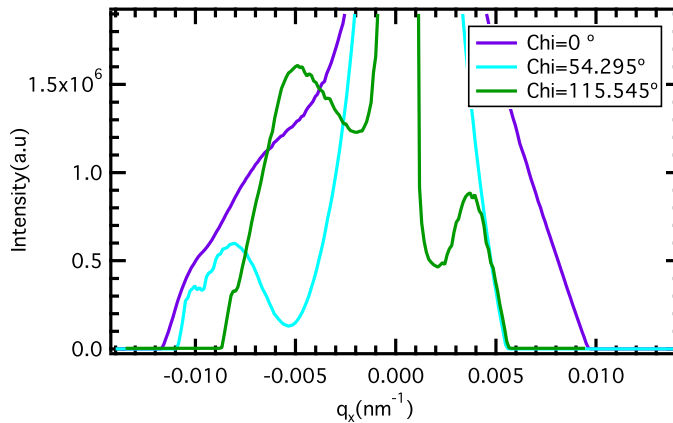

Figure 6.17: XRMS for three azimuthal angles. The black spectrum has two not-well-defined peaks, while in the red and green spectra the peaks are much better defined. Each of them give a different periodicity.

If we consider that the surface of the sample looks like figure 6.18, there

are three domains – each with a different propagation direction – and different periodicities. Considering an azimuthal angle χ, the periodicity for each propagation vector as seen by an incoming photon is (see fig 6.2):
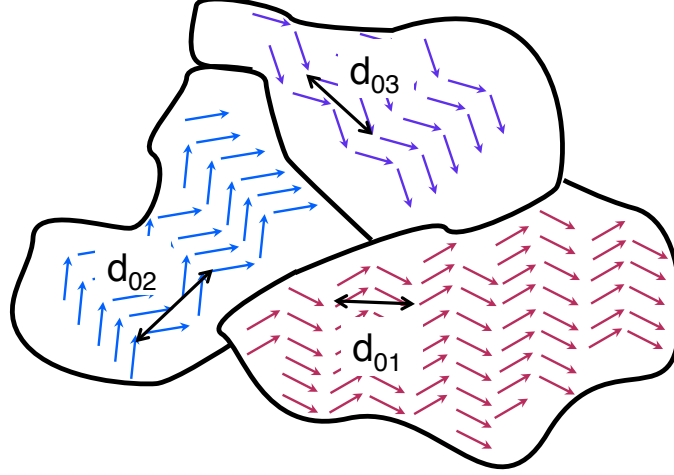

Figure 6.18: An image of the sample surface considering the three directions of propagation with its corresponding angles

$$d_1 = \frac{d_{01}}{\cos \chi} \text{ for the cycloidal propagating along the } [1\bar{1}0]$$

$$d_2 = \frac{d_{02}}{\cos(\chi - 45)} \text{ for the cycloidal propagating along the } [10\bar{1}]$$

$$d_3 = \frac{d_{03}}{\cos(\chi + 45)} \text{ for the cycloidal propagating along the } [0\bar{1}1]$$

Where d_0 is the proper periodicity of the cycloidal at the surface plane with: $d_{01} = 64$nm, $d_{02} = 90$nm and $d_{03} = 90$nm.

To have a better understanding of these cycloidal structures and their contribution to the XRMS spectra we performed simulations of the rocking curves as a function of azimuthal angle. This will be the objective of the next section.

6.2.3   Simulations of x-ray scattering of BFO and Co

In order to better understand the recorded scattering diagrams, we use the kinematical approximation of X-ray diffraction. Despite that this approximation may seem rather rough in soft X-rays, we will see that it is sufficient

to successfully explain our scattering data. We simulated the intensity of the diffracted beam and the position of the peaks as a function of the azimuthal angle.

As shown by Lebeugle *et al.* [10], since the periodicity of the cycloids is of the order of the exchange length of the Co, the magnetic moments do not adopt a cycloidal structure, but one can imagine that only a small wriggle appears in the Co layer. With our diffraction geometry, we are only sensitive to the periodicities on the surface plane and therefore only the projection of the magnetic moments in the sample plane (XY plane) will be considered. In figure 6.19 we show the surface view of the BFO and of the Co thin film.
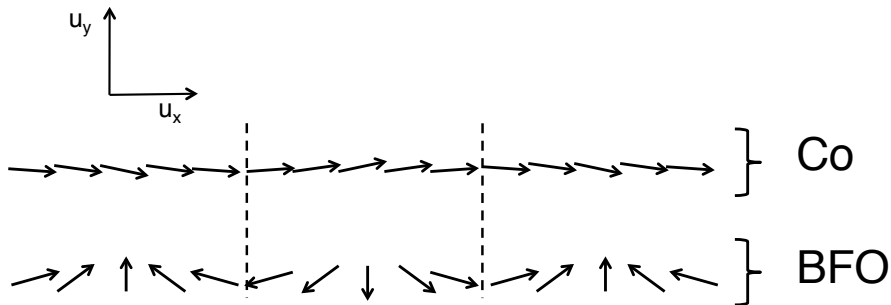

Figure 6.19: The bottom part represents the cycloidal structure projected at the surface plane. The top line is the wriggle of the Co.

Let us have a closer look to the Co magnetization. Co is a magnetic material with moments ordered in a ferromagnetic pattern. The Co intrinsic magnetic moments are coupled to the magnetic moments of Fe describing the cycloid structure. Magnetic diffraction is produced by the periodic extra components $u_{x\_cycloid}$ and $u_{y\_cycloid}$ that result from the coupling with underlying cycloids (see Fig. 6.20). These two components are represented as two sine functions describing a magnetic cycloid.
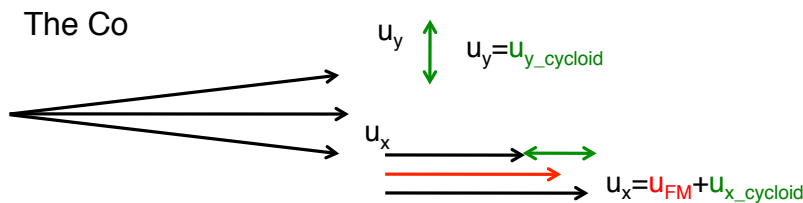

Figure 6.20: Sketch of the Co moments in the XY plane.

From the two images above, we can write the cycloid magnetization in the

XY plane as a combination of two sine waves propagating in the x direction.

$$u_{\text{x\_cycloid}} = u_{\text{x0}} \cos(\tau x) \tag{6.7}$$

$$u_{\text{y\_cycloid}} = u_{\text{y0}} \sin(\tau x) \tag{6.8}$$

where $\tau = \frac{1}{d}$ and $d = \frac{d_0}{\cos \chi}$ from page 128.

This model gives the information of the position of the satellite peaks in the reciprocal space for each azimuthal angle. In figure 6.21 we display a polar graph in which the polar axis is the azimuthal angle and the linear axis is the position of the peaks. For a given azimuthal angle we see there can be several peaks that appear at different positions in the reciprocal space.
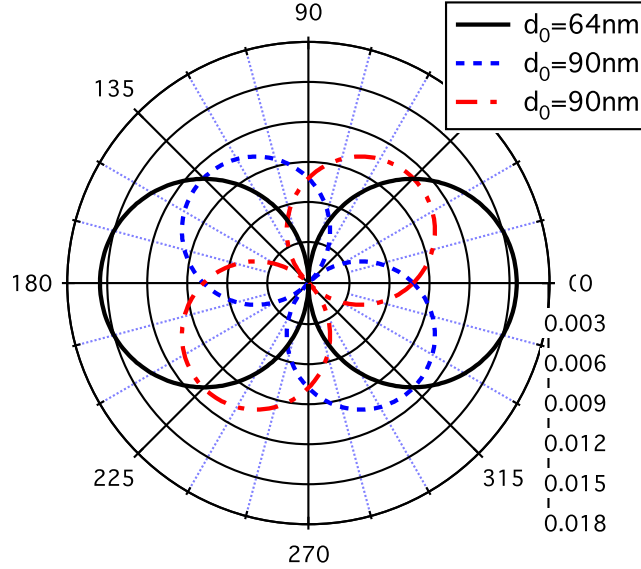

Figure 6.21: Polar graph of our simulations. The radial axis is the position of the satellite peaks in the reciprocal direction q_x and the polar axis the azimuthal angle in degrees. Each curve represents a cycloid with a certain direction of propagation.

6.2.4   Comparison between simulation and experiments

In order to check if our model explains the experimental data and to understand properly the meaning of the satellite peaks we have to compare the simulations with the data. In figure 6.22 we present a polar graph with

three azimuthal angles pointed out, alongside experimental spectra for three azimuthal angles.
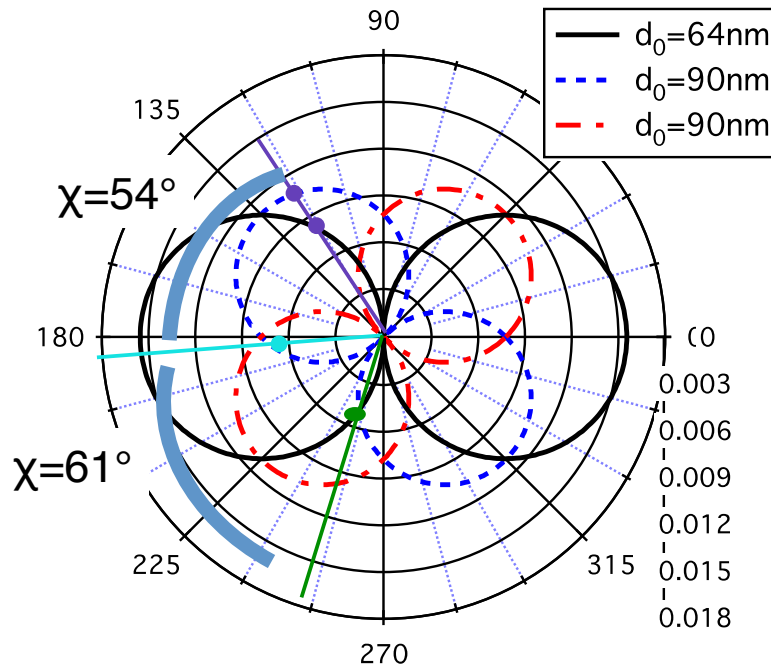
(a)
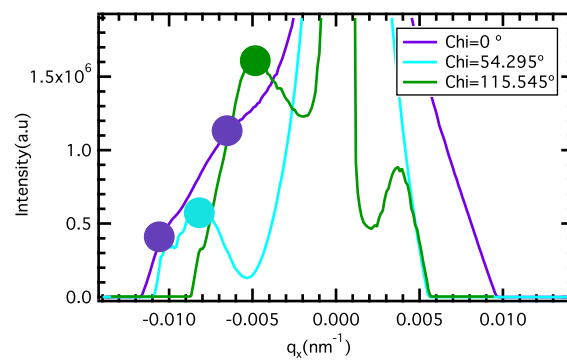
(b)

Figure 6.22: (a): polar plot of satellite peaks positions. (b): three experimental spectra for three different azimuthal angles.

The violet curve of the experimental data matches with the simulated position drawn in violet dots. In this configuration, two cycloids diffract:

one with a minimum periodicity at the surface d_0 of 90 nm and the other with a periodicity of 64 nm. The light blue curve only has one peak which corresponds to the second azimuthal in the polar graph with the light blue dot. In this case only one cycloid with a d_0 periodicity of 90 nm is diffracted. For the third case (green curve), there is also one single peak. In this case it comes from two cycloids one with a d_0 periodicity of 90 nm and the other with 64 nm as pointed out in the polar graph by the green dot. This geometrical model successfully accounts for the azimuthal angle dependance of the satellite peaks of our experimental spectra.

6.2.4.1 Simulation of the relative intensity of the satellite peaks

Within the kinematical approximation, we can simulate the intensity of the satellite peaks. We write the scattering factor in the polar basis as:

$$
\begin{aligned}
\hat{f}_{\boldsymbol{e'e}}(\theta) \;=\; & F_0 \begin{pmatrix} \cos^2\theta & -\sin^2\theta \\ -\sin^2\theta & \cos^2\theta \end{pmatrix} \\
& -i\frac{F_1}{2} \begin{pmatrix} -u_x\sin 2\theta + i2u_y\cos\theta & -u_x\sin 2\theta - i2u_z\sin\theta \\ -u_x\sin 2\theta + i2u_z\sin\theta & -u_x\sin 2\theta - i2u_y\cos\theta \end{pmatrix}
\end{aligned} \tag{6.9}
$$

with $\boldsymbol{u}$ the magnetization of the Co or of the Fe in BFO and θ the scattering angle. If the model of eq 6.8 is introduced in the scattering form factor, one can compute the diffracted intensity and get a simulation of the diffracted intensity peaks as shown in figure 6.23.
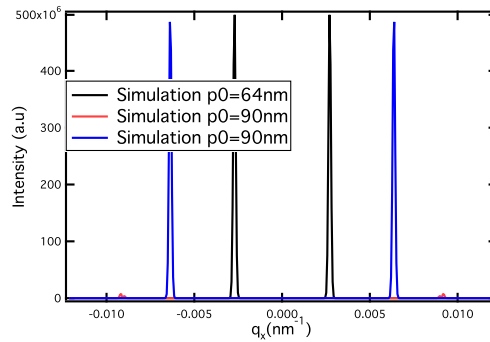

Figure 6.23: Simulation of the satellite peaks for three directions of propagation of the cycloids.

No dichroic effect has been observed in any XRMS experiments performed during this thesis (Fig.6.24). By *dichroism effect* we mean a change in the

diffracted intensity of the satellite peaks for opposite circular polarizations. In our simulations, we do not have any dichroic effect neither (as shown in figure 6.25), confirming the validity of our model.
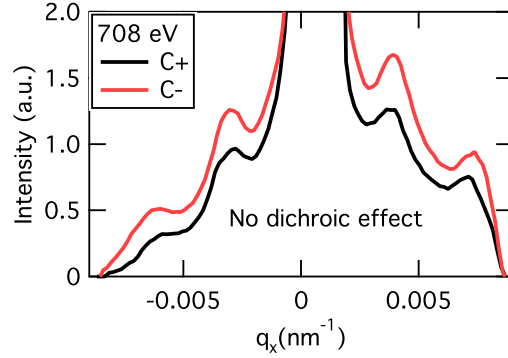

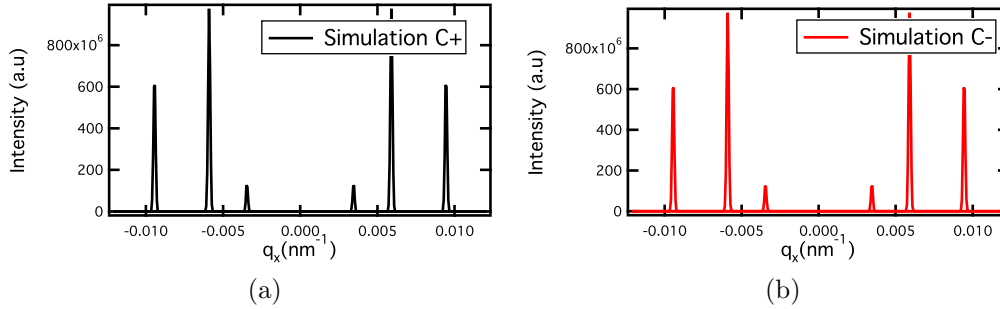Figure 6.24: XRMS experimental data for two polarizations at the Fe edge.

Figure 6.25: Polar simulations of the satellites with (a)right (C^+) and (b)left (C^-) circular polarizations.

The absence of any dichroic effect can also be explained with hands as in section A.2 where we saw that circular dichroism is produced by the u_y and u_z components of magnetization. In our model, the u_y contribution is very small and u_z is considered equal to zero. Likewise, in our diffraction experiments we look at the q_x component of the diffraction vector neglecting any out-of-plane contribution.

6.2.5   Conclusion and perspectives

With XRMS we proved that there is magnetic coupling between a soft ferromagnetic layer of Co and a $BiFeO_3$ single monodomain ferroelectric crystal.

We demonstrated that the easy axis of magnetization observed by Lebeugle *et al.* was due to the new magnetic order imposed by the cycloidal structure beneath the Co layer. We studied the behavior of the satellite peaks as a function of temperature and at different energies.

With our model we explained the position and the number of satellite peaks around the specular position. We concluded that several cycloids diffract at the same time, either at the same or at different reciprocal space positions. In the case where only one pair of satellite peaks appears, it is because either the apparent periodicities of the other two cycloids are too large, dumping the spectral content into the specular peak or too small to be detected with our diffraction geometry.

Our kinematical approximations have confirmed that the u_z contribution of magnetization does not contribute to our experiments because our model explains the experimental without any u_z component of magnetization.

As perspectives beyond this work, there are two main areas that remain to be explored, which have already been started in this thesis. One would be to evaluate the energy of the coupling by applying a magnetic field, and the other to observe the behavior of the satellite peaks under applied electric field. We now present the results of some preliminary experiments in these directions.

6.2.5.1   Behaviour of the satellite peaks under applied magnetic field

One of the ways to measure the energy of the exchange interaction is to apply a magnetic field and see at which value of the field the peaks disappear. With our system this would consist in measuring the behaviour of the satellite peaks under different directions of the applied magnetic field. We eventually performed these experiments at SOLEIL synchrotron. RESOXS diffractometer allows to apply a magnetic field up to H = 0.2T with two different configurations – transverse or longitudinal – as shown in Fig. 6.26 (see Tools). In both configurations the magnetic field is in the surface plane. It is perpendicular to the X-ray direction in the transverse configuration, and parallel to the X-rays in the longitudinal configuration.

From the work done by Lebeugle [10], we know there is an easy and a hard axis of magnetization on the FM thin layer. The easy axis is along the [010] direction, and the hard axis along the [100] direction, the [010] being the long axis of the sample. In the experimental configuration, we chose the long axis of the sample to be in the X-ray direction therefore having the field applied along the easy axis in the longitudinal configuration, and along the hard axis in the transverse configuration. We applied up to 1750 G in both
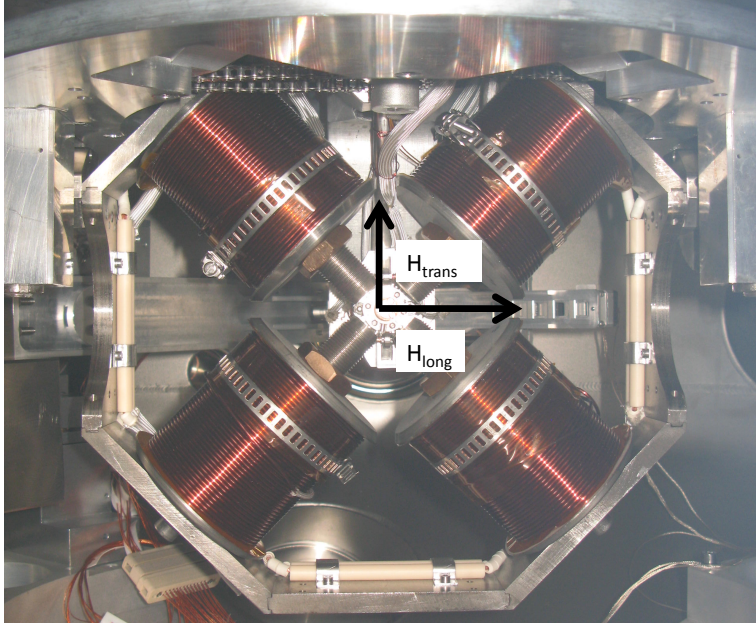
Figure 6.26: RESOXS magnetic coils. The coils allow to apply a magnetic field in the transverse and longitudinal directions.

configurations, and observed how the peaks vanish. The first applied field was 1000 G in the transverse configuration. We observed a dramatic decrease of the peak intensity and after this, we remeasured the rocking curve at zero applied magnetic field and we never got back to the initial intensity. This can be explained by the magnetic training. The training effect implies that during the application of the magnetic field, the ferromagnetic layer does not reverse homogeneously because of the symmetry of the AFM material that is below. The symmetry of the AFM system is crucial for the training effect [18]. The training effect occurs in systems where the antiferromagnetic component has several equivalent easy magnetic axes. In contrast, when the AFM system only has uniaxial magnetic anisotropy, there is no training effect observed.

In figure 6.27 we show two rocking curves at the resonance of the Co for different applied fields with the two configurations (longitudinal and transverse). The behavior of these two systems is quite similar: magnetic field suppresses the magnetic signal of the Co layer by overcoming the coupling with BFO cycloids. But it is hard to obtain a quantitative conclusion.
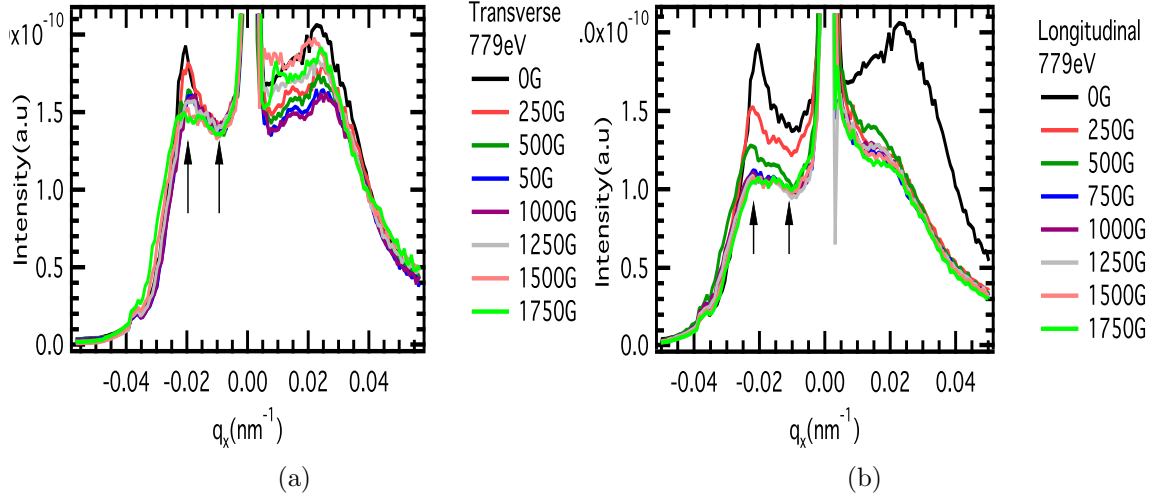
Figure 6.27: Rocking curves at different applied magnetic fields in the (a) Transverse configuration and (b) Longitudinal configuration.

In figure 6.28 we show the intensity of the satellite peak in function of the applied field. These values are calculated by substrating the intensity at the well to the intensity at the peak (the two arrows in Fig. 6.27). In our experiments we observe that in transversal geometry the intensity decreases faster that with the field applied in the longitudinal direction. These are only preliminary results and further studies such as micromagnetic simulations and more precise experimental results would be needed for better quantitative conclusions.

The important point of this study is that under applied magnetic field the satellite peaks disappear, supporting the fact that the wriggle in the Co layer is due to exchange coupling with the AFM order of BFO. The Co layer has no longer a magnetic pattern and the experimental conditions are the same as in figure 6.8b.

6.2.5.2   Application of an electric field on Co/BFO system in XRMS

The coupling proven before is the mechanism which is going to allow to control magnetization via and electric field. In order to observe this mechanism it is necessary to perform resonant magnetic scattering experiments under applied electric field. During this thesis we have created and built a new sample holder for RESOXS endstation that allows to apply an electric field (see Chapter Tools).

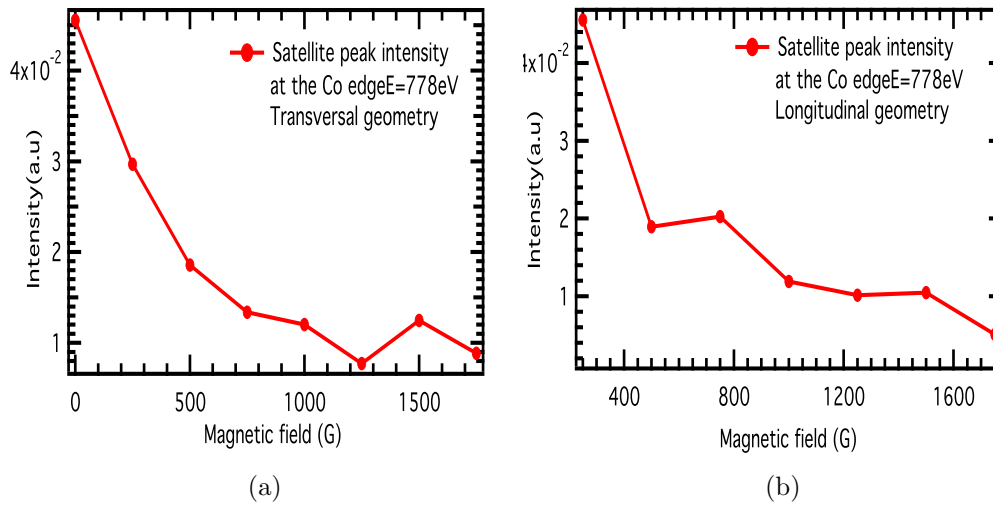In figure 6.29 we show an image of our electrical contact system. The

Figure 6.28: (a) Intensity of the satellite peaks in function of the applied magnetic field for the (a) Transverse configuration and (b) Longitudinal configuration.
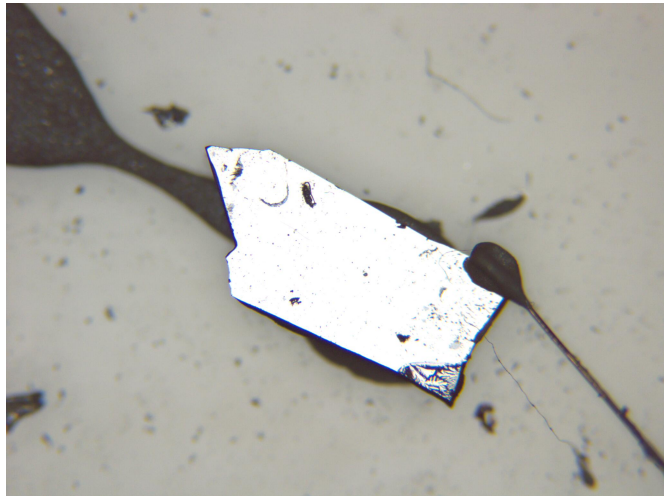

Figure 6.29: Picture of a sample with electrical contacts on it.

sample is $1\,mm \times 0.4\,mm.05\,mm$. It is deposited on top of electrical conductive epoxy glue (which is also a good thermal conductor). Electrical contacts on the Co layer are done using thin gold wire and a very small drop of epoxy. Electric field is applied on the vertical direction which is the (010) direction as shown in figure 6.30. The electric polarization of BFO is in the (111) or

equivalent directions.This means that the electric field is applied at 54.44°
to it. When electric field is applied the electrical polarization will follow the
electric field and it will flip to another other equivalent polarization state.
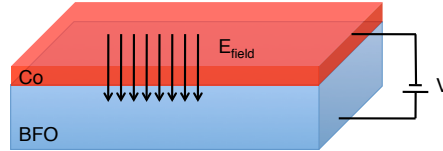

Figure 6.30: This schema shows how the electric field is applied on our
system.

Our experimental results are shown in figure 6.31 where we show two
curves, one at zero applied electric field an another after a $30\,kV/cm$ electric
field had been applied. During this experiment no information from the
satellite peaks could be obtained. However, we see a clear splitting of the
specular peak. This means that after having applied electric field the sample
"breaks" into several domains, becoming multidomain ferroelectric. This
effect has already been reported in literature [9] and the change in reflectivity
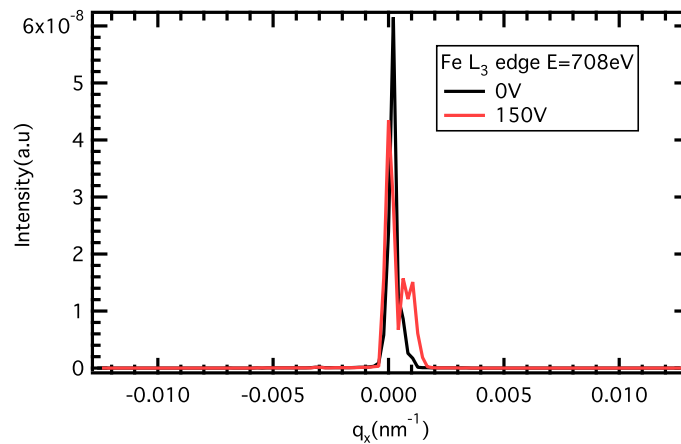is simply due to the buckling of the crystal as reported by Lebeugle *et al*.

Figure 6.31: XRMS spectra at the Fe edge under applied electric field.

6.3 Direct imaging of both ferroelectric and antiferromagnetic domains in multiferroic BiFeO$_3$ single crystal using X-ray Photoemission Electron Microscopy

In the previous section we studied ferroelectric monodomain BFO single crystal. Now we will focus on the study of multi-domain ferroelectric BFO single crystals. In monodomain system there is only one FE polarization, whereas in multidomain systems, there are eight possible electric polarizations as shown in Fig. 6.32. The aim of the work is to see if there is any correlation between FE and AFM domains, and to study the coupling with a soft ferromagnetic layer.
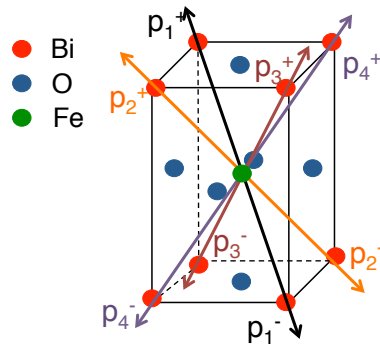

Figure 6.32: Sketch of a unit cell of BiFeO$_3$ with all 8 possible electric polarizations.

In figure 6.33 we show two images taken by polarized microscopy of a multidomain BFO single crystal. The FE domains appear by structural defects and are surrounded in red in fig. 6.33. This is not surprising since BFO is also a piezoelectric material, which means that strain (structural defects) create FE domains and defects appear when extracting the crystal from the growth chamber.

With these systems we focus our work on the study of the correlation between FE and AFM domains. In BFO thin films this has already been studied by the Ramesh group [19]. They showed that FE and AFM domains had the same shape, as shown in figure 6.34. The ferroelectric domain size on thin films is around $1\,\mu$m, whereas in bulk samples the FE domain size is much larger – around $1\,$mm (see figure 6.33a). This raises the question of what happens to AFM domains in mutlidomain FE single crystals. Do they follow the FE domains or are there multiple domains in one FE domain?

(a)   (b)
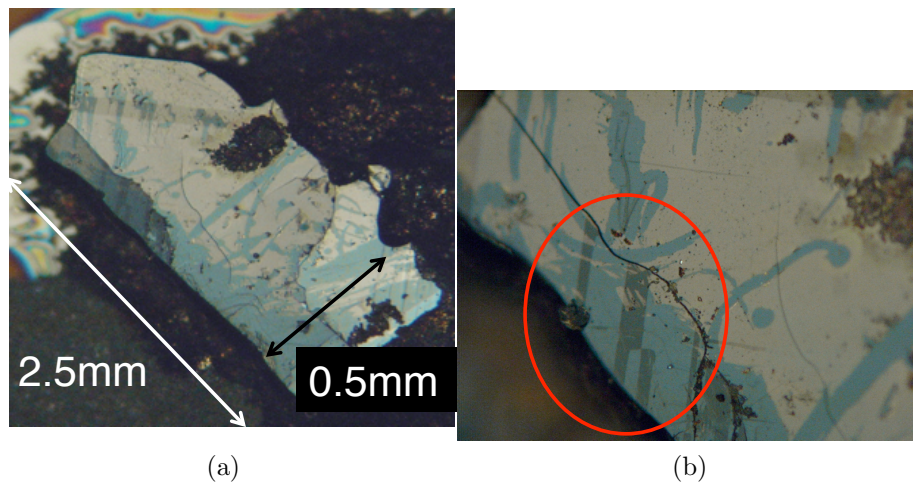
Figure 6.33: (a)Picture of a multidomain FE BFO crystal. (b)The area surrounded in red points out typical rectangular ferroelectric domains. Areas with light color are Au deposited on top in order to evacuate the built up charges.

To address this question we use a local probe method: X-ray Photoemission Electron Microscopy (X-PEEM) that allows to study both magnetic and electric properties.
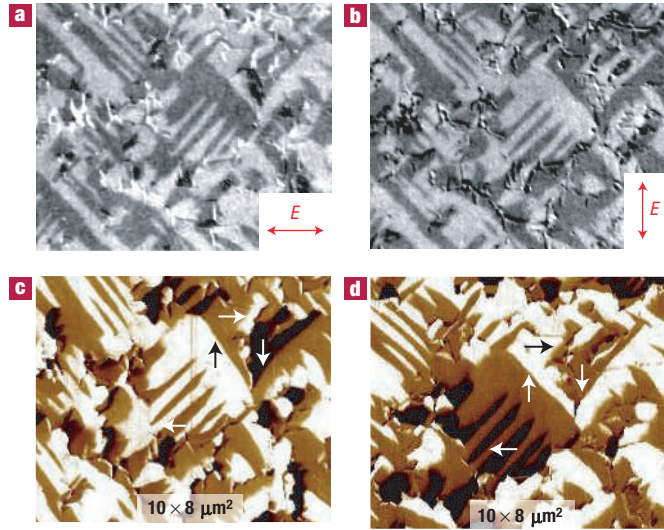
Figure 6.34: PEEM and in-plane PFM images taken on the same area of a BiFeO$_3$ film. PEEM images before (a) and after (b) 90° in-plane rotation between the two images. In-plane PFM images before (c) and after (d) 90° in-plane rotation. The arrows show the direction of the in-plane component of ferroelectric polarization [19].

6.3.1 X-Ray Photoemission electron microscopy

X-Ray Photoemission electron microscopy is a microscopy technique based on the imaging method and the dichroic effect. The physical process that occurs in X-PEEM is the photoelectric effect, which is a photon-in electron-out process (see section 3.3.1). The energy of the incoming photon is tuned to an atomic resonance in the soft X-ray regime – the L$_{2,3}$ edge in the case of transition metals. The incoming photon is absorbed by an atom and the excess of energy is transferred to an electron, which is expelled from the atom, leaving the atom ionized. This process is the photoelectric effect (see Fig. 3.6). With X-PEEM, the photoelectrons coming out from the atom are collected in the microscope giving the X-PEEM image which has the magnetic and electronic information of the system.

An X-PEEM microscope consists of a series of electrostatic or magnetic lenses with magnification onto a phosphor screen as shown in fig 6.35. The X-rays coming from the synchrotron source are moderately focussed, in order to have an extended field of vision in the microscope. The photoelectrons are pulled out to the objective lens by an applied voltage of around 15 kV between the sample and the lens. The energy resolution is given by the beamline

monochromator, and the spatial resolution is determined by three factors: spherical aberration, chromatic aberration and diffraction. In practice, the chromatic aberration dominates.

Chromatic aberration is due to the energy spread of the inelastic tail (about $4\,eV$) of the electrons. However, the portion of electrons that most contribute to the intensity is the secondary electron tail in the 0-20 eV kinetic energy range. To reduce the energy spread, there is an aperture that acts like a filter for high energy electrons. The low energy portion of inelastic electrons is properly focussed and then transmitted through the aperture. With this method we achieve a spatial resolution of about 20 nm. However, a better spatial resolution can be achieved by further reducing the energy spread of the photoelectrons. This is done by using an ultraviolet radiation with its energy slightly higher that the workfunction. This way a spatial resolution of 8,nm can be obtained.

X-ray Photoemission Electron Microscopy (PEEM)
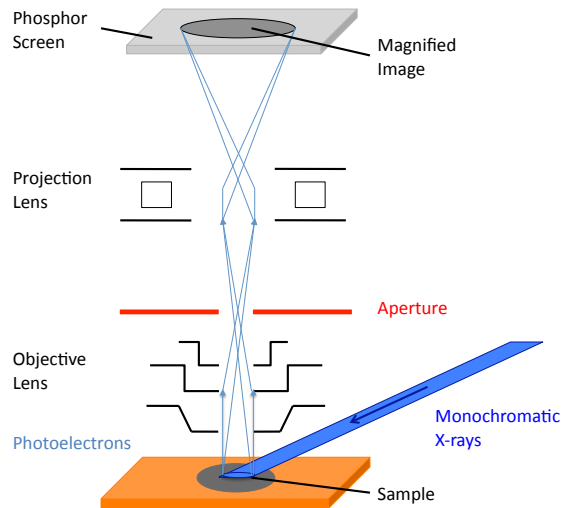
Figure 6.35: Sketch of a PEEM microscope

6.3.1.1   X-ray Magnetic Linear Dichroism XMLD, Magnetic contrast

We have already seen how the dichroic effect gives information about the magnetic and/or electronic anisotropies in a system. Here we will focus on AFM and FE anisotropies which are detectable by X-ray magnetic linear dichroism (XMLD) and X-ray natural linear dichroism (XNLD) respectively. Let us rewrite the absorption cross-section as presented in section 3.5.2.

$$\sigma_{\text{abs}} = \underbrace{\lambda r_0 u_y \text{Im}\{F_1\}}_{\text{XMCD}} + \underbrace{\frac{\lambda r_0}{2}(u_x^2 - u_z^2)\text{Im}\{F_2\}}_{\text{XMLD}} \qquad (6.10)$$

With linear polarized light, the magnetic contrast or dichroic signal depends on the mutual orientation of the X-ray polarization and the AFM vectors. In a X-PEEM image of XMLD/XNLD, a white color indicates that the vector that describes the anisotropy is parallel to the X-ray polarization vector and a dark color perpendicular. When the contrast is grey the anisotropy vector is in-between the parallel and the perpendicular component of the X-ray polarization.

6.3.2 Experimental issues

The main experimental challenge of these experiments was to deal with the large charge build-up effect that can hinder the X-PEEM signal. To overcome this problem we have evaporated 2 nm of gold onto the surface sample. Then this gold thin film is grounded, so that build-up charges evacuate. However, since X-PEEM is a surface sensitive method, the gold layer cannot cover the entire surface. We uncovered parts of the sample by lithography, corresponding to circular areas in Fig. 6.33.

In the microscope at the SIM beamline of the Swiss Light Source, the incident angle of the X-rays with the sample is 16° (see Fig. 6.36). In this configuration, Vertical linear polarization (VLP) is equivalent to π polarization and Horizontal linear polarization (HLP) is almost equivalent to σ polarization, one will call it an in-pure σ polarization. σ polarization would correspond to the polarization of the incoming beam perpendicular to the surface plane.
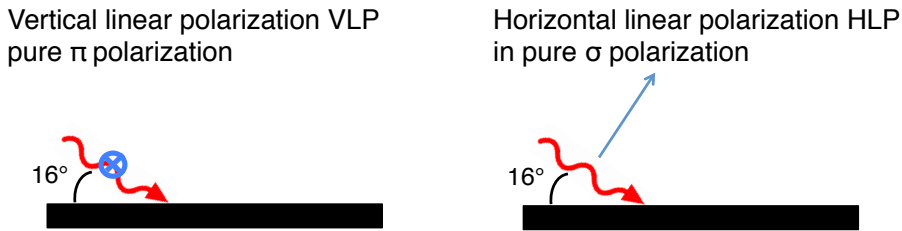

Figure 6.36: X-PEEM configurations for the SIM beamline experimental setup (top view).

From eq:6.10 one sees that XMLD is only sensitive to the x and z components of the anisotropy if one uses pure σ and π polarizations. However, since

in our case there is an angle of 16° between the incoming beam and the surface plane, X-PEEM is sensitive to the three components of the anisotropy. HLP being sensitive to the z and y components and VLP to the x component, the combination of VLP and HLP is therefore sensitive to all three components.

We have seen that the XNLD and XMLD contrast come from the difference of two acquisitions between σ and π polarizations. W also used another method to study the AFM order, which consist on using the extra freedom the incoming 16° angle gives to address with HLP the z and y components of the AFM order. The dichroic information is obtained by substracting two images with different photon energies.

In BiFeO$_3$ the ferroelectric information comes from XNLD measurements, therefore one has to address the O edges where the magnetic contribution could be considered negligible. In the soft X-ray range one can tune the energy of the incoming photon to the O K edge at $E = 543.1$ eV. On the contrary, the AFM order is seen by XMLD and therefore at the Fe L$_{2,3}$ edges $E_{L_2} = 719.9$ eV and $E_{L_3} = 706.8$ eV.

6.3.3   Results

Now we present results from X-PEEM experiments on BFO multidomain FE single crystals. The samples used in these experiments were grown by the same method as the monodomain FE crystals (see section 6.1.1.1). We present the XNLD and XMLD images of the FE and AFM domains along with absorption spectra. We show the absorption spectra after the X-PEEM images because one needs them to differenciate FE and AFM domains.

6.3.3.1   Imaging the FE domains

Ferroelectric domains can be observed not only by X-PEEM but also by polarized light microscopy (PLM). The FE contrast in PLM comes from the birefringence of the polarized light by FE domains. This way, with PLM one can differentiate monodomain ferroelectric from multidomain ferroelectric single crystals. One can also choose interesting areas of the sample to study, before going to the synchrotron beamline. As an example, in Fig. 6.37a we show an image taken by PLM. The bright and dark area correspond to domains of different ferroelectric polarizations. Since the incoming light imprints the sample at normal incidence, the contrast of the image only results from the in-plane component of the FE polarization directions. With PLM no perpendicular information can be measured.
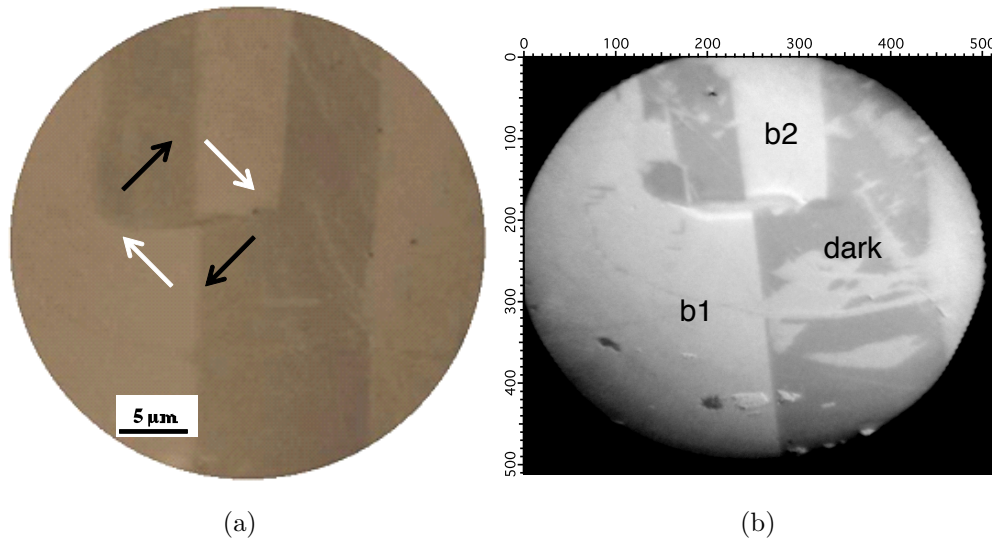
Figure 6.37: (a)Optical PLM image of FE multidomaincBFO. (b)XLD X-PEEM image of FE multidomain BFO

To get a complementary 3D information of the polarization, one needs X-PEEM experiments. Thanks to the a-symmetrical configuration of the X-PEEM (16° of incidence) the combination of HLP and VLP allows to have contrast between domains of same in-plane but different out-of-plane components of polarization, as well as between different in-plane components. This is illustrated in Fig.6.38 where we show the expected X-PEEM contrast colors for the eight possible FE polarizations.

In Fig. 6.37 we show PLM and X-PEEM images of the same region of a sample. The PLM image shows two contrasts, one dark and one light color coming from two opposite direction of the out of plane direction of the polarization. The X-PEEM shown is the difference between VLP and HLP at the O K edge. In the X-PEEM image we can distinguish one dark color and two bright colors (b1 and b2). We attribute the two bright colors to different out-of-plane components of the polarization (for example, p_1^- and p_1^+).

We also show the absorption spectra of different regions obtained from images at the O K edge. The chosen regions are the two bright areas b1 and b2 and the dark area. The curves are shifted in the vertical direction for clarity. The dichroic signal is present at $E = 530\,\text{eV}$ and $E = 532.5\,\text{eV}$.
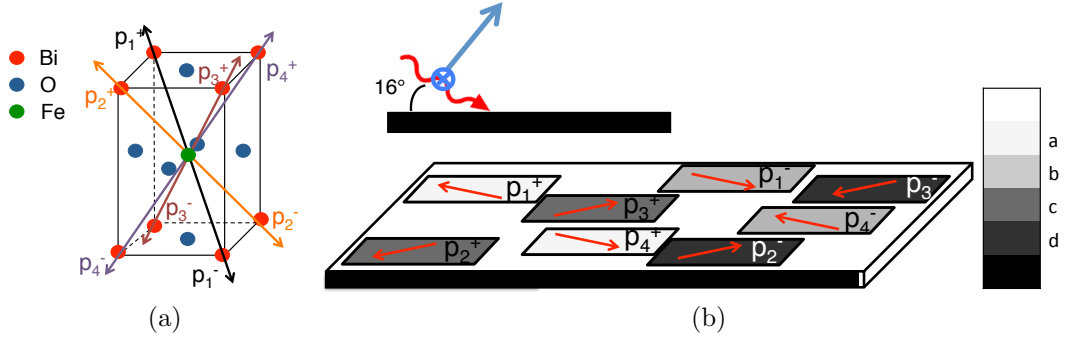
Figure 6.38: (a)BFO unit cell with the eight possible ferroelectric polarizations. (b)Contrast colors of the eight possible ferroelectric polarizations. Arrows represent the-in plane direction and the $\pm$ the out-of-plane component of the ferroelectric polarization. Between two domains of same in-plane component but different out-of-plane component, the color difference is small ; for example, from light grey p_1^- (color b) to lighter grey p_1^+ (color a).
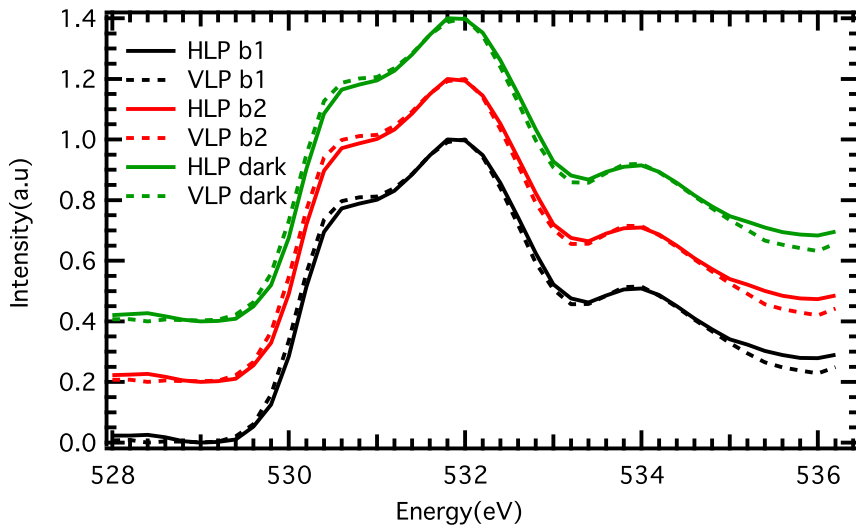
Figure 6.39: Absorption spectra at the O K edge for the three areas showing different XNLD contrast in X-PEEM images.

6.3.3.2   Imaging the AFM domains of BiFeO$_3$

In multiferroic materials, both antiferromagnetism and ferroelectricity participate to the contrast at the Fe edges when using linear polarization. The proportion of each term is hard to estimate and depends on the orientations of

their respective vectors, their magnetic moment and exchange/crystal field. Figure 6.40a is an image containing AFM contrast obtained by subtracting two images measured at the two resonance energies of the Fe $L_{2,3}$ edges with HLP. The magnetic signal being much smaller than the ferroelectric one, the obtained image is of worse quality than those taken at the O K edge in pure XNLD. Any surface irregularity, impurity, charge pockets or weak XMLD effect generate a contrast that masks the interesting signal. It is therefore hard to visualize the real topology of AFM domains in $BiFeO_3$. By comparing the image of the FE domain structures Fig. 6.37b, some correlations are visible as the border between the different FE domains can be seen in the XMLD image. This border is pointed out by two green arrows in figure 6.40a. On the left side (Fig. 6.40b), we show a simple sketch of the image to highlight the line that separates the two FE domains.

(a)   (b)
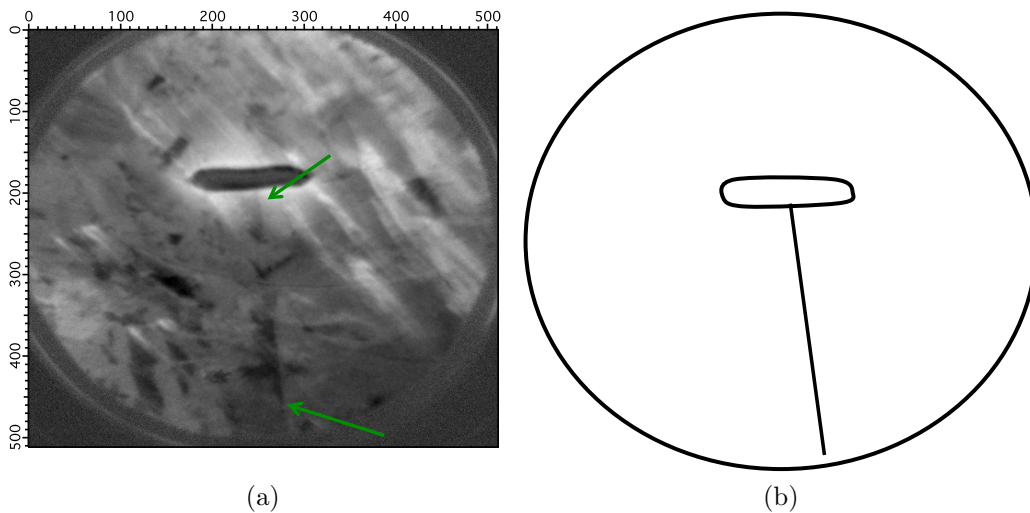
Figure 6.40: XMLD X-PEEM image at Fe L_2 and L_3 with HLP. (a) the green arrows point out the line semparating the FE domains. (b) sketch of the XMLD image reproducing the border between the FE domains.

Since the magnetic contrast depends on the mutual orientation of the X-ray polarization and the AFM vectors, only an azimuthal study can get the true AFM signal. In Fig. 6.41 we show a sketch with a representation of two experimental conditions. In this picture p_1, p_2 and p_3 are three AFM vectors from the same FE polarization and the blue arrow is the photon polarization. With XMLD, when the anisotropy vector is parallel to the polarization of the photon the contrast is white, dark if it is perpendicular, and grey if it is in-between. Now let us consider only the in-plane components of the AFM vectors. In the first case of our sketch, the p_1 vector gives a white

contrast and the other two grey contrasts. On the contrary, when the system is turned 45° with the same photon polarization, one has grey contrast for the p_1 vector, white for the p_2 and black for the p_3. One has to keep in mind that this picture is not the real expected contrasts. In practice, there are several parameters that could complicate the comprehension of the contrast, such as the intrinsic azimuthal angle or the out-of-plane contribution.
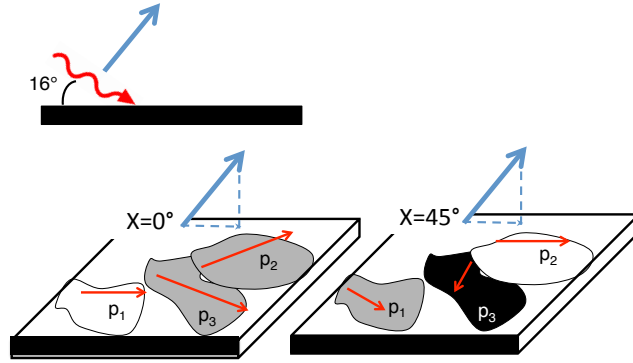

Figure 6.41: XMLD X-PEEM image contrast for two azimuthal angles 0° and 45°. The blue arrow represents the polarization of the photon, and p_1, p_2 and p_3 the AFM vectors.

In Fig 6.42 we show four XMLD images of the same area taken at four different azimuthal angles, in which the gradual rotation of this angle from 0° to 45° induces a progressive change of the images contrast in certain areas (surrounded by red and blue). In other regions, the contrast does not change, indicating that the information is masked. Besides, in some regions, the angular variation of the contrast is opposite, meaning that their AFM vectors are differently oriented. Some areas (in red) change from black to light grey, whereas the other regions (in blue) change from light grey to dark gray. What is observed experimentally corresponds with our sketch of Fig. 6.41. Therefore, one can conclude that several AFM domains exist in a single FE domain.

One also sees that a certain ∨-shape domain appears in both FE domains (surrounded by the red circle). The angle between the in-plane components of the ferroelectric polarizations is 90° and since the direction of propagation of the cycloids are perpendicular to the ferroelectric polarization, the equivalent cycloids will form a 90° angle at the domain edge. This is what is observed in this particular case.

Our observations are different from what was observed in thin films where the AFM and FE domains were equal as shown in figure 6.34. The FE domain size is much smaller in thin films than in single crystals. This might be one
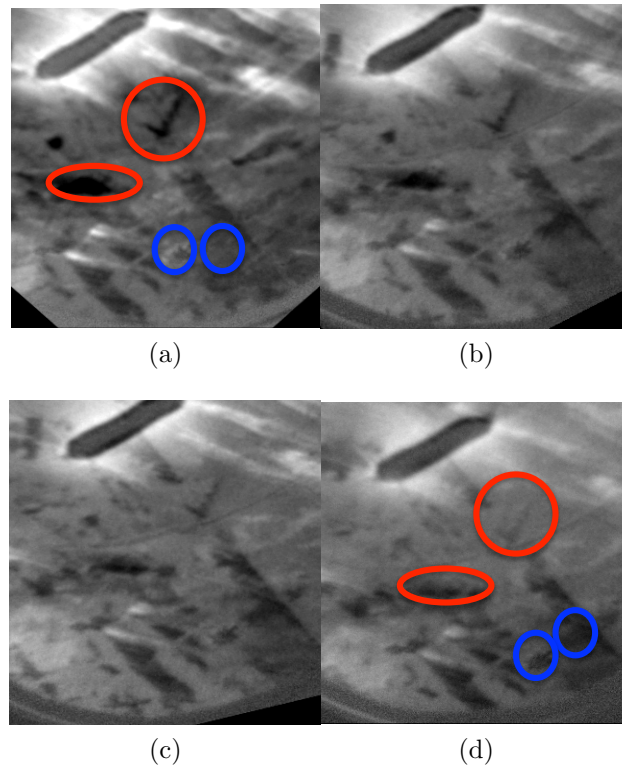
Figure 6.42: Four XMLD images of the same area for four azimuthal angles. (a)0°(b)15°(c)30°(d)45°. The areas surrounded in red change color from 0° to 45° from dark to white and the one in red blue $vice-versa$.

of the reasons why there are several AFM domain propagation directions in one same Fe domain.

In order to support these results we also recorded several absorption spectra at the Fe $L_{2,3}$. These spectra were obtained by taking the spectroscopic information of a certain area from an X-PEEM image. This way it it possible to obtain XAS from the AFM domains located with the azimuthal study. The XAS of the Fe $L_{2,3}$ edges splits into two. This splitting corresponds to the energy level degeneracy from the multiplet structure.

If we look at the Fe $L_{2,3}$ edges, we can obtain a dichroic affect by comparing the spectra for two azimuthal angles. If we look closely at the $L_{2,3}$ at 0° and 45°, we observe a small dichroic effect .

Figure 6.43: X-ray absorption spectra at the Fe L_2 edge, recorded from areas surrounded by red and blue in Fig. 6.42d and 6.42a. We present the spectra obtained by rotating the in-plane angle 0° (a) and 45° (b), respectively. The insets show zooms on the spectra around the two main peaks, evidencing a small but measurable difference in their intensities.

6.3.4   Conclusion

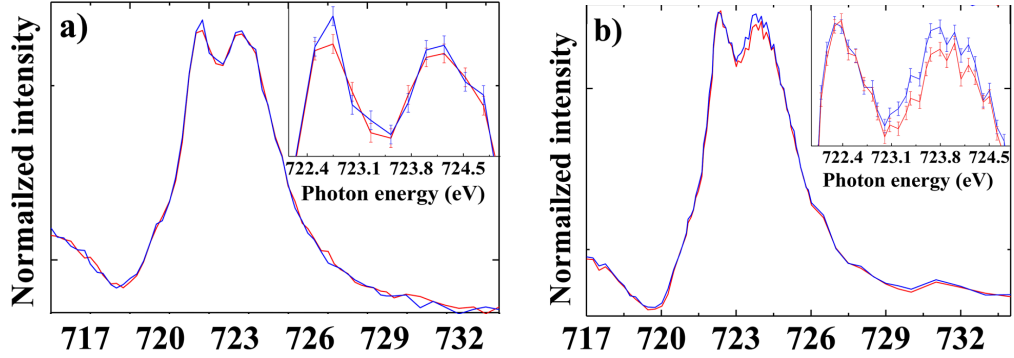As a conclusion, with X-PEEM we have observed in one same experiment FE and AFM domains of single crystal BFO. We showed evidence the existence of a correlation between these two and that several antiferromagnetic domains coexist in one same ferroelectric domain. This is the opposite of what was observed with thin films, where Zhao *et al.* reported the same FE and AFM domain size in thin films.

The next step in this study is the observation of FM domains in a thin ferromagnetic layer deposited on top of a multidomain FE single crystal. The idea will be to first observe and locate opposite FE domains and perform XMLD/XNLD measurements as the ones presented in this chapter. Then, a thin FM layer would be deposited and XMCD measurement are carried out on the same spot of the sample. The magnetic coupling between the AFM structure and the FM layer induces a change in the thin layer magnetization which would be detectable in X-PEEM images.

6.4   General conclusion

In this chapter we have studied two states of $BiFeO_3$ single crystals: monodomain ferroelectric and multidomain ferroelectric. With monodomain ferroelectrics we focussed on the study of the coupling between a soft ferromagnetic layer and single crystal BFO. In the multidomain, we looked at the correlation between the FE and AFM domains.

The coupling between the soft ferromagnetic layer of Co and BFO monodomain FE single crystals have been studied by soft X-ray resonant magnetic scattering. We have seen that in grazing incidence geometry it is sensitive to magnetic periodicities in the surface plane. This way, we were able to observe a magnetic pattern on the Co layer because of the cycloidal structure of the BFO underneath. To support our experimental data, we realized kinematical simulations of the diffracted intensities. The magnetic cycloidal and the *zig-zag* structures were modeled by two sinusoidal waves. Azimuthal dependence of the magnetic periodicities has allowed to explain the experimental data and the fact that several cycloids can diffract at the same time, each with a different periodicity on the surface plane.

The second part of our study has been dedicated to the study of the correlation between the FE and the AFM domains. We have addressed this problem with X-PEEM at the O K edge and the Fe $L_{2,3}$ edges. Our experimental results have shown that the FE and AFM domains are correlated, but – in contrast to what was observed in thin films – several AFM domains may coexist in one same FE domain. One has to keep in mind that the size of the FE domains is much larger in single crystals than in thin films.

As perspectives, in the monodomain FE case, applied electric and magnetic fields studies have to be done these has already been tried in this thesis without giving any successful results. A new PhD grant is to be started on domain walls study. In the multidomain FE case, the next step will be to perform the same measurements as performed here, but this time with a soft ferromagnetic layer.

Bibliography

[1] L. D. Landau, E. M. Lifshitz, and L. P. Pitaevskii, *Electrodynamics of continuous media*. Pergamon Press, 1984.

[2] J. E. T. F. D. N. Astrov, "The magnetoelectric effect in antiferromagnetics," *Sov. Phys.JETP*, 1960.

[3] N. A. Hill, "Why Are There so Few Magnetic Ferroelectrics?," *The Journal of Physical Chemistry B*, vol. 104, no. 29, pp. 6694–6709, 2000.

[4] J. Wang, J. B. Neaton, H. Zheng, V. Nagarajan, S. B. Ogale, B. Liu, D. Viehland, V. Vaithyanathan, D. G. Schlom, U. V. Waghmare, N. A. Spaldin, K. M. Rabe, M. Wuttig, and R. Ramesh, "Epitaxial BiFeO3 Multiferroic Thin Film Heterostructures," *Science*, vol. 299, no. 5613, pp. 1719–1722, 2003.

[5] C. Michel, J.-M. Moreau, G. D. Achenbach, R. Gerson, and W. James, "The atomic structure of BiFeO3," *Solid State Communications*, vol. 7, no. 9, pp. 701 – 704, 1969.

[6] J. R. Teague, R. Gerson, and W. James, "Dielectric hysteresis in single crystal BiFeO3," *Solid State Communications*, vol. 8, no. 13, pp. 1073 – 1074, 1970.

[7] Y. F. Popov, A. M. Kadomtseva, S. Krotov, and D. V. e. a. Belov, "Features of the magnetoelectric properties of BiFeO3 in high magnetic fields ," *Low Temperature Physics*, vol. 27, p. 2, June 2001.

[8] J. Moreau, C. Michel, R. Gerson, and W. James, "Ferroelectric BiFeO3 X-ray and neutron diffraction study," *Journal of Physics and Chemistry of Solids*, vol. 32, no. 6, pp. 1315 – 1320, 1971.

[9] D. Lebeugle, D. Colson, A. Forget, M. Viret, A. M. Bataille, and A. Gukasov, "Electric-Field-Induced Spin Flop in $BiFeO_3$ Single Crystals at Room Temperature," *Phys. Rev. Lett.*, vol. 100, p. 227602, Jun 2008.

[10] D. Lebeugle, A. Mougin, M. Viret, D. Colson, and L. Ranno, "Electric Field Switching of the Magnetic Anisotropy of a Ferromagnetic Layer Exchange Coupled to the Multiferroic Compound $BiFeO_3$," *Phys. Rev. Lett.*, vol. 103, p. 257601, Dec 2009.

[11] P. W. Anderson, "Antiferromagnetism. theory of superexchange interaction," *pr*, vol. 79, pp. 350–356, Jul 1950.

[12] H. Béa, M. Bibes, S. Petit, S. Fusil, C. Deranlot, J. Kreisel, and A. Barthélémy, "Structural distortion and magnetism of BiFeO3 epitaxial thin films: A Raman spectroscopy and neutron diffraction study," *Philosophical Magazine: Letters*, Mar 2007.

[13] Lebeugle, D. and Mougin, A. and Viret, M. and Colson, D. and Allibe, J. and Béa, H. and Jacquet, E. and Deranlot, C. and Bibes, M. and Barthélémy, A., "Exchange coupling with the multiferroic compound $bifeo_3$ in antiferromagnetic multidomain films and single-domain crystals," *Phys. Rev. B*, vol. 81, p. 134411, Apr 2010.

[14] Béa, H. and Bibes, M. and Ott, F. and Dupé, B. and Zhu, X.-H. and Petit, S. and Fusil, S. and Deranlot, C. and Bouzehouane, K. and Barthélémy, A., "Mechanisms of exchange bias with multiferroic $bifeo_3$ epitaxial thin films," *Phys. Rev. Lett.*, vol. 100, p. 017204, Jan 2008.

[15] A. Y. S. Durr H.A Dudzik E. S.S Dhesi J.B Goedkoop G. van der Laan M.Belakhovsky, C. Mocuta, "Chiral Magnetic Domain Strucutres in Ultrathin FePd Films," *SCIENCE*, vol. 284, no. 5423, pp. 2166–2168, 1999.

[16] M. Ramazanoglu, W. Ratcliff, Y. J. Choi, S. Lee, S.-W. Cheong, and V. Kiryukhin, "Temperature-dependent properties of the magnetic order in single-crystal $BiFeO_3$," *Phys. Rev. B*, vol. 83, p. 174434, May 2011.

[17] I. P.Fischer, M.Polomska and M.Szymanki, "Temperature dependance of the crystal and magnetic structures of BiFeO3," *J.Phys.C:Solid St.Phys*, vol. 13, pp. 1931–40, 1980.

[18] A. Hoffmann, "Symmetry Driven Irreversibilities at Ferromagnetic-Antiferromagnetic Interfaces," *Phys. Rev. Lett.*, vol. 93, p. 097203, Aug 2004.

[19] T. Zhao, A. Scholl, F. Zavaliche, K. Lee, M. Barry, A. Doran, M. P. Cruz, Y. H. Chu, C. Ederer, N. A. Spaldin, R. R. Das, D. M. Kim,

S. H. Baek, C. B. Eom, and R. Ramesh, "Electrical control of antiferromagnetic domains in multiferroic BiFeO3 films at room temperature," *Nature Materials*, vol. 5, Sep 2006.

Chapter 7

$Pr_{1-x}Ca_xMnO_3$ charge ordered manganites under applied electric current

7.1 Charge ordering, a novel multiferroic mechanism, and the CDW model

The manganite perovskite has a very rich phase diagram on doping with 2+ or 3+ cations showing various magnetic phases, in particular a ferromagnetic metallic (FM) phase, and an antiferromagnetic insulating (AFI) phase. This latter phase is stable near half doping and is attributed to a localization of the charges on the manganese atoms together with an orbital ordering of the 3d orbitals that set the pathway for the pattern of magnetic moments. The general ideas on this phase date back to the 50's with the Goodenough's paper [1]. This AFI phase shows however a colossal magnetoresistance, the highly insulating manganite becomes metallic with the application of a few Tesla magnetic field [2].

In the recent years the AFI phase has raised some novel, and sometime controversial research. Several contradicting crystallographic methods have proposed either a checkerboard organization of formally Mn^{4+} and Mn^{3+} atoms in which the charge is localized on the Mn atoms (site centered) thereby confirming Goodenough's model [3, 4] or a Zener polaron model in which the charge is localized between the Mn (bond centered) [5]. A great deal of interest has followed this controversy notably because it was argued that the bond centered model could form a novel mechanism for multiferroicity based on charge-ordering [6]. This multiferroicity would thus have an electronic origin which is well known to strongly interact with a magnetic field, for instance showing colossal magnetoresistance. That's not all: In addition to this exciting prospect, another physics was proposed for the charge ordered phase, suggesting that it could just be a weakly or delocalized charge density wave (CDW) [7, 8]. In the CDW model one expects a nonlinear collective charge transport occurring in the CO phase above a critical applied current corresponding to a CDW sliding. Non linear behavior in manganite single crystals have been reported [11, 12, 13]

These were studies based on bulk systems. Then we have extended our research to strained thin films, since only few studies have reported on CDW on manganite thin films. Fisher *et al.* [9], reported the absence of CDW in PCMO film on NGO in 2010. In such systems, the strain induced by the substrate can completely change the properties of the film.

As it is now well understood that resonant diffraction reveals superstructures reflections related to the checkerboard organization of the electron-lattice coupling, we started a study of a charge/orbitally ordered manganite under applied current which would fit well in our research on multiferroicity by RXD. Our goal was to characterize the ordered phase as the material en-

ters a non-linear regime in its resistivity. We expected to have a close insight on the ordered phase, and the atomic environment of the Mn atoms. How is the local structure changed by the applied current? Could we see the non-linear behavior together with the local environment of the Mn atoms? Could we interpret our results with respect to the well-known mixing of metallic and insulating phases, or to a particular structural change around the Mn atom, like the loss of the Jahn-Teller distortions accompanying the non-linear behavior?

This chapter describes our attempts at characterizing RXD superstructure reflections at a synchrotron beamline on a manganite thin film with simultaneous applied current and resistivity measurements. Despite some difficulties with samples and experiments, we have some preliminary intriguing results. These results may be compared to the current-induced metallic behavior in $Pr_{0.5}Ca_{0.5}MnO_3$ thin films observed by Padhan *et al.* [10] who discussed the competition between Joule heating and nonlinear conduction mechanisms. These authors concluded that two mechanisms were at play: local heating and nonlinear conduction. The origin of these behavior were explained "with a model based on local thermal instabilities in the metallic percolation regions resulting from the phase-separation system and a modification in the long range charge-ordered state" [10]. At the present stage of our study, we clearly have seen an effect based on Joule heating. However, the absence of a thermal effect on several superstructure reflections is still puzzling, and may point as well to a phase separation effect.

In the first section, we recall some information on the crystallographic structure of the bulk and the thin film manganite. We will then give a summary on the work by Nelson *et al.* [14] on which we based our study. Nelson's studies describe the observation of RXD superstructures on thin films, without applied current. Their samples were thicker than ours which might have conditioned our results. We finally present our results on two samples.

This study has been a collaboration with Silvana Mercone of the Laboratoire des Sciences des Procédés et Matériaux (Villetaneuse), Wilfrid Prellier of the Crismat (Caen) and Sophie de Brion of the Institut Néel.

7.2 Bulk and Thin Film Structures

7.2.1 Bulk crystallography

Because of the large interest on charge and orbital ordering in manganites and the colossal magnetoresistance associated to it, several groups have grown

and refined the crystallographic positions of manganites near half doping. Table 7.2 shows the lattice parameters of bulk manganites, especially our system (Pr,Ca) and the prototypical (La,Ca) system, that order in charge (formally Mn^{3+}/Mn^{4+}) and orbital ($e_g\ 3x^2 - r^2/e_g\ 3y^2 - r^2$) at low temperature. One notes the differences between systems and doping, and the quite small discrepancies between the same systems.

Table 7.1: Lattice parameters from crystallographic refinements of single or powder crystals of the bulk $Pr_{1-x}Ca_xMnO_3$ compounds and related materials. References: Jirak *et al.* [15], Goff *et al.* [4], Daoud-Aladine *et al.* [5], Rodriguez *et al.* [16], Radaelli *et al.* [17].

bulk	a	b	c	γ	T	Ref.
$Pr_{0.5}Ca_{0.5}MnO_3$	5.395	5.403	7.612	90	RT	[15]
$Pr_{0.5}Ca_{0.5}MnO_3$	5.435	2x5.435	7.4889	90.069	10K	[4]
$Pr_{0.5}Ca_{0.5}MnO_3$	5.3949	5.4052	7.6064	90	RT	[18]
$Pr_{0.5}Ca_{0.5}MnO_3$	5.4335	2x5.4348	7.4819	90	10K	[18]
$Pr_{0.6}Ca_{0.4}MnO_3$	5.415	5.438	7.664	90	RT	[15]
$Pr_{0.6}Ca_{0.4}MnO_3$	5.4210	5.4460	7.6480	90	RT	[5]
$Pr_{0.6}Ca_{0.4}MnO_3$	5.4315	2x5.4485	7.6370	90.076	185 K	[5]
$La_{0.5}Ca_{0.5}MnO_3$	5.4309	5.4211	7.6400	90	RT	[16]
$La_{0.5}Ca_{0.5}MnO_3$	5.4750	2x5.44425	7.5194	89.95	20 K	[16]
$La_{0.5}Ca_{0.5}MnO_3$	5.4355	5.4248	7.6470	90	RT	[17]
$La_{0.5}Ca_{0.5}MnO_3$	5.4763	2x5.4466	7.5247	90	1.5 K	[17]

The space group of the high temperature phase, the phase that is not electronically long-range ordered, is *Pbnm*. In this space group, reflections of the type $(h00)$ and $(0k0)$ with h and k odd are forbidden. In the low temperature, charge and orbitally ordered phase, the symmetry is lowered and different space groups have been proposed. Without going into the details of this different propositions, one always observes that the high temperature forbidden reflections are now allowed. One also observed $(0\frac{k}{2}0)$ reflections related to the orbital ordering that doubles the unit cell along the k direction. In thin films, the situation is a little bit different because of the strain with the substrate.

7.2.2   Thin film on LAO crystallography

Manganite thin films have been grown on various substrates with compressive or tensile strain with the goal to change the magneto transport properties,

see for instance De Brion [19] or Nelson *et al.* [14]. It was observed that the electronic ordered phase only appear for the LaAlO$_3$ (LAO) substrate which provides a compressive strain. Other samples on substrates like SrTiO$_3$ have similar resistivity properties but it seems that one does not observe the charge and orbital order and the superstructure associated with from resonant diffraction techniques [14].

Several reports and our own results show that the films grow on LAO preferably along the (110) orthorhombic direction, see for instance ref. [18]. This orientation is preferred because it minimized the volume change of the unit cell, and let the lattice parameters almost unchanged. This accommodation is at the expense of the γ angle between $\boldsymbol{a}$ and $\boldsymbol{b}$. A second type of growth along the [001] axis is reported by Haghiri-Gosnet [18]. This is a minor phase however, within the [110]-axis growth, with a proportion of about 10%. We did not see a clear evidence of this phase in our data. However, one must say that once the thin film is oriented in the diffractometer, the exploration of the reciprocal space becomes limited to near the reciprocal space positions with Bragg reflections, and superstructure reflections. That is, we can not exclude another minor phase to occur. This is a concern when one looks for small superstructure reflections, one has to be sure that they belong to the major phase, not to the minor phase. Nevertheless, at the stage when we orient the sample, we never encountered strong reflections corresponding to a growth other than the (110) one.

Table 7.2: Lattice parameters from crystallographic refinements of single or powder crystals of Pr$_{1-x}$Ca$_x$MnO$_3$ thin films and related materials. References: Haghiri-Gosnet *et al.* [18].

Film	subs.	thick. (nm)	a	b	c	γ	T	T$_{CO}$	Ref.
Pr$_{0.5}$Ca$_{0.5}$MnO$_3$	LAO	100-150	5.403	5.403	7.6	90.9	RT	220 K	[18]

7.2.2.1 Monoclinic structure

Because of the strain of the substrate, the film can not have its bulk orthorhombic structure. Instead, it has a monoclinic structure with $a \approx b \neq c$ and $\gamma \neq 90$. In a referential frame where

$$\begin{aligned}
\boldsymbol{a} &= a\,(1,0,0) \\
\boldsymbol{b} &= b\,(\cos\gamma, \sin\gamma, 0) \\
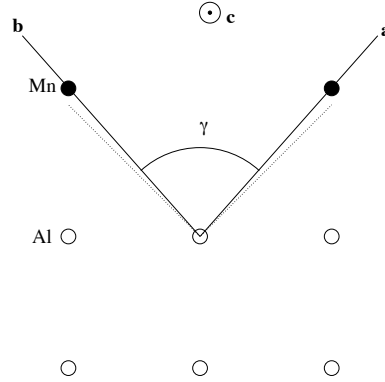\boldsymbol{c} &= c\,(0,0,1)
\end{aligned}$$

Figure 7.1: The orientation of the growth in understood by the small mismatch between the lattice parameter of LaAlO$_3$ and the c parameter, as well as the accommodation of the γ angle between $\boldsymbol{a}$ and $\boldsymbol{b}$. The sketch shows the interface between the manganite and LaAlO$_3$. The axis $\boldsymbol{c}$ is in the plane of the interface. The film grows along the [110] direction, by reducing the angle γ. Oxygens and rare earth are not represented.

the reciprocal space is then given by:

$$
\begin{aligned}
\boldsymbol{a}^* &= \frac{1}{a\sin\gamma}\left(\sin\gamma, -\cos\gamma, 0\right) \\
\boldsymbol{b}^* &= \frac{1}{b\sin\gamma}\left(0, 1, 0\right) \\
\boldsymbol{c}^* &= \frac{1}{c}\left(0, 0, 1\right)
\end{aligned}
$$

When finding a reflection using x-rays and a diffractometer, one notes the position of the detector, 2θ, which gives the value of the modulus of the diffraction vector that is being measured: $q = \frac{2\sin\theta}{\lambda}$. One can then identify the reflections that have this modulus and then calculates the lattice parameter and the angle γ using:

$$
\begin{aligned}
|q_{hkl}| &= \left(\left(\frac{h}{a\sin\gamma}\right)^2 + \left(\frac{k}{b\sin\gamma}\right)^2 + \left(\frac{l}{c} - \frac{2hk\cos\gamma}{ab\sin^2\gamma}\right)^2\right)^{1/2} \\
|q_{hk0}| &= \frac{1}{a\sin\gamma}\left(h^2 + k^2 - 2hk\cos\gamma\right)^{1/2} \quad \text{with a=b, l=0}
\end{aligned}
$$

We used these formula to estimate the lattice parameters.
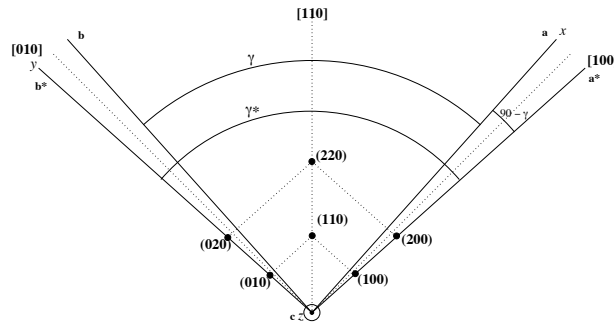
Figure 7.2: Reciprocal Space for a monoclinic lattice, with a=b, and $\gamma < 90$. For the $Pr_{0.6}Ca_{0.4}MnO_3$ thin film on $LaAlO_3$, typically $a = b = 5.40$, $c = 7.60$ and $\gamma = 89$.

7.2.2.2 Domains

We have seen a four-fold symmetry of the reciprocal space, which is due to the presence of domains placed perpendicular to each other, meaning that the c axis that lies in the plane can take the four perpendicular directions. This means also that some positions in the reciprocal space actually see superposed reflections. For instance the (222) reflections could also be the (310), the (130) and the (22$\bar{2}$) reflections.

7.2.2.3 Published reports on the occurrence of superstructure reflections

By superstructure reflections we mean the reflections that occur presumably because of the electronic ordering at low temperature. Now we know that at high temperature the reflections (h00) and (0K0), odd, are present in thin films. We call them high temperature superstructure reflections. In $Pr_{0.5}Ca_{0.5}MnO_3$ Haghiri-Gosnet *et al.* report the observation of superstructures with electron diffraction at the incommensurate positions $q = (0\ 0.38\ 0)$ and disappearing above 220 K [18]. They find that this value corresponds to the value of incommensurability measured for the bulk compound when its lattice parameter corresponds to the one locked-in by the substrate. They also report that the system is actually a ferromagnetic insulator, therefore the AF phase of the corresponding bulk compound is not realized. They propose two possibilities: either there are two phases, a ferromagnetic metallic phase embedded in a modulated insulating one, or a single ferromagnetic insulating modulated phase. Note that a charge/orbital order phase would have an antiferromagnetic order whose SQUID signal would be hidden by the ferromagnetic phase. Nevertheless one can see in their data a clear anomaly

around 220 K, also observed in the bulk, that corresponds to the bidimensionnal CO/OO ordering that implies bidimensionnal AF correlations. We therefore expect to find RXD superstructure reflections at the corresponding propagation vectors, even if the phase is embedded in a non-ordered ferromagnetic phase. The RXD technique is well adapted to the characterization of such mixed phase because the reflections of the AFI phase carry a different spectral signatures than reflections in the FM phase.
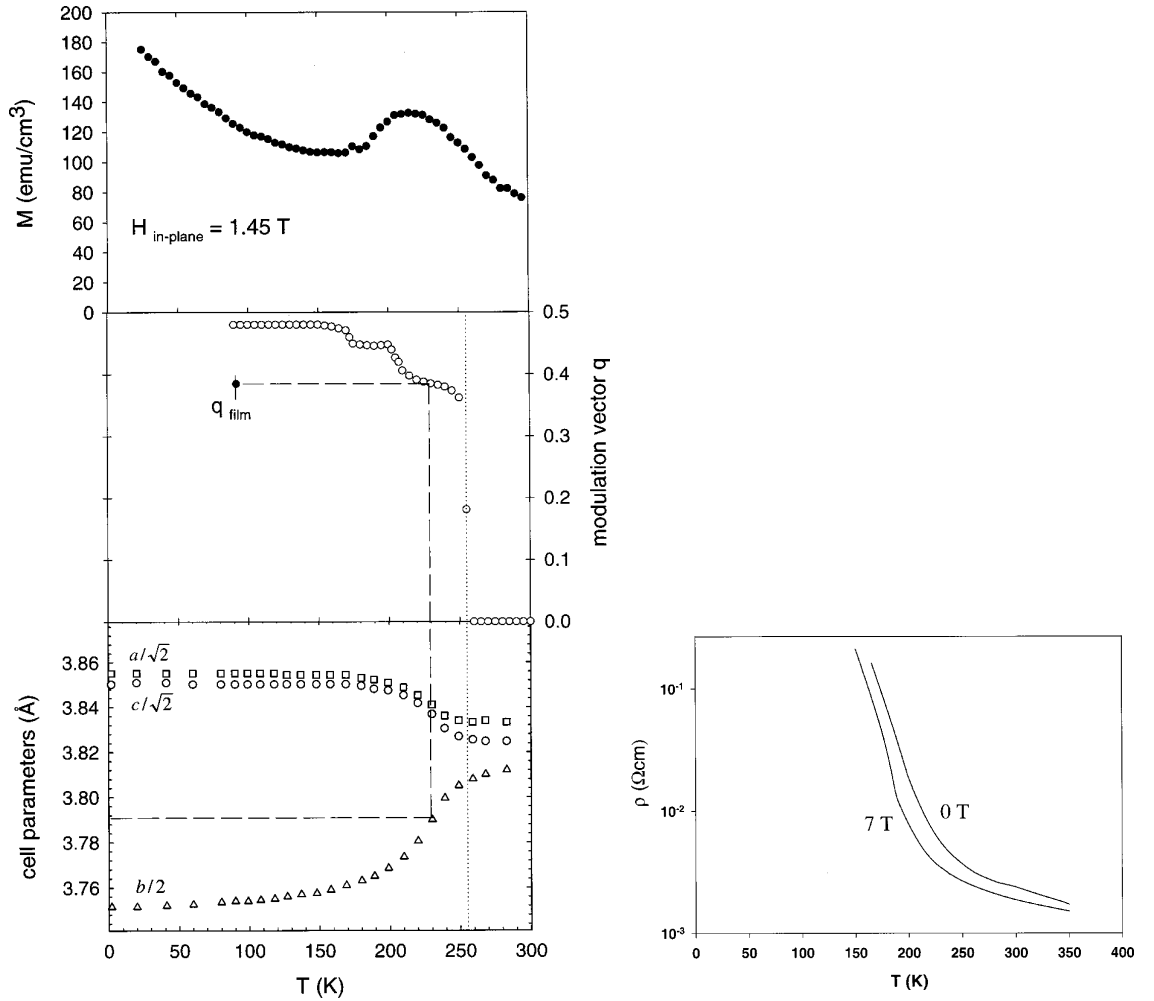
Figure 7.3: Left and right panels: Magnetization and resistivity of a $Pr_{0.5}Ca_{0.5}MnO_3$ thin film (100nm) on $LaAlO_3$. Middle panel are q and lattice parameters for the bulk compound. From Haghiri-Gosnet *et al.* [18]

In $Pr_{0.6}Ca_{0.4}MnO_3$ on the LAO substrate, C.S. Nelson *et al.* reported superstructure reflections using resonant x-ray diffraction in the low temperature ordered phase [14]. Figure 7.4 shows the intensity of the superstructure

Figure 7.4: RXD results from Nelson *et al.* [14] (300) charge (closed circle) and (2.5 00) orbital (open circle) order peak intensities, normalized to equal 1 at a temperature of 100 K. Insets show energy s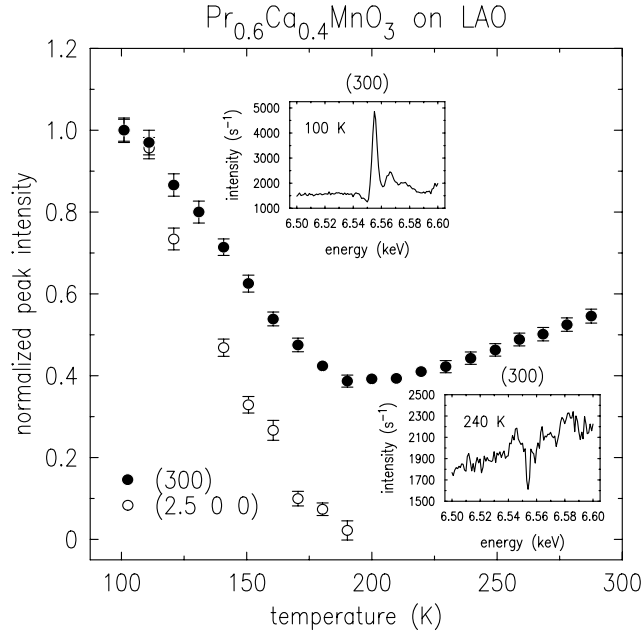cans carried out at the (300) peak at temperatures of 100 and 240 K. One note the very different RXD spectra for the two phases, providing their respective signatures.

reflection (300) with the temperature. The RXD technique offers a spectral signature of this reflection and an insight of the nature of the respective phases. In the two insets one sees the RXD spectra at two temperatures, below and above the phase transition temperature. In the CO/OO phase, the spectroscopic signal is typical with a narrow resonance at 6.555 keV, where the intensity nearly is multiplied by four. The same signal is observed in the bulk materials, it was analyzed, simulated and understood [3]. It corresponds to a checkerboard ordering of octahedra. Octahedra with a Jahn-Teller distortion alternate with regular octahedra. Mn^{4+} sit in the undistorted regular octahedra. In the distorted octahedra, the Mn is formally in a 3^+ state with an e_g orbital that is occupied. This e_g orbital realize an orbital order simultaneous to the charge ordering, giving rise to the $(0\frac{k}{2}0)$ reflections, as observed by Nelson *et al.*. This type of reflections only appears below the phase transition temperature, there is no signal above.

In our study, we have been looking for this (300) and equivalently for the (100) reflection, and for the $(0\frac{k}{2}0)$ reflections as well. We also paid

attention to the possibility of having incommensurate reflections for the $(0\frac{k}{2}0)$ reflections, like observed by Haghiri-Gosnet *et al.* [18]. Once found, the procedure was to apply the current, and follow the position of the reflections, their intensities and their resonant spectra in order to detect the slightest long-ranged structural change around the Mn atoms with the applied current.

7.3   Resonant X-ray Diffraction

7.3.1   Results on $Pr_{0.6}Ca_{0.4}MnO_3$/LAO

The experiment was conducted on the Cristal beamline at Soleil in May 2012 (see 'Tools' chapter for a brief description of the beamline). It was a collaboration with Silvana Mercone from the Laboratoire des Sciences des Procédés et des Matériaux, Villetaneuse, Wilfrid Prellier from Crismat, Caen.

7.3.1.1   The sample

The sample labeled "10286-1.5K001" (Fig. 7.5) was a $Pr_{0.6}Ca_{0.4}MnO_3$ thin film on a $LaAlO_3$ substrate grown by Pulsed Laser Deposition by the group of W. Prellier at the Crismat laboratory (Caen) in March 2012. This sample was 75 nm thick. Another sample was grown with a 150 nm thickness, labeled "10285-3K001". The latter sample was the closest to the one studied by Nelson *et al.* (only thinner by 100 nm). We tried to use the capabilities of the Nanofab platform of the Institut Néel in order to grow clean contacts by lithography and gold deposition. Unfortunately the 150nm thick sample was broken during the lithography process when it was glued and hard pushed on a support. We had then to use the 75 nm sample on which we made the traditional four contacts of silver paint and Pt wires (see the 'Tools' chapter). We will call this sample PCMO x=0.4.
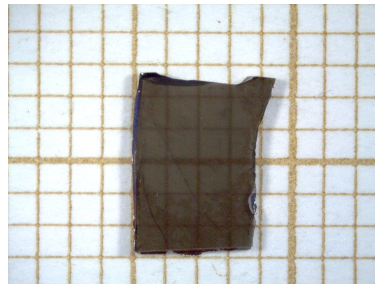

Figure 7.5: Sample $Pr_{0.6}Ca_{0.4}MnO_3$ on a LAO substrate, labeled "10286-1.5K001".

7.3.1.2 The I(V) data

Four point current voltage characterization of PCMO x=0.4 thin films are shown in figure **??**. These data were recolted during the experiments at SOLEIL synchrotron. From a fit of Fig. 7.6 we we get a value for the resistance of R = $6.05 \times 10^6 \pm 3 \times 10^4$ Ω and a resistivity of $\rho = 45\Omega$cm which have the same magnitudes as similar samples studied in the literature [10]. In this measurements we only applied a current up to $1\mu A$ because at higher currents the compliance of the nanovoltmeter was reached.
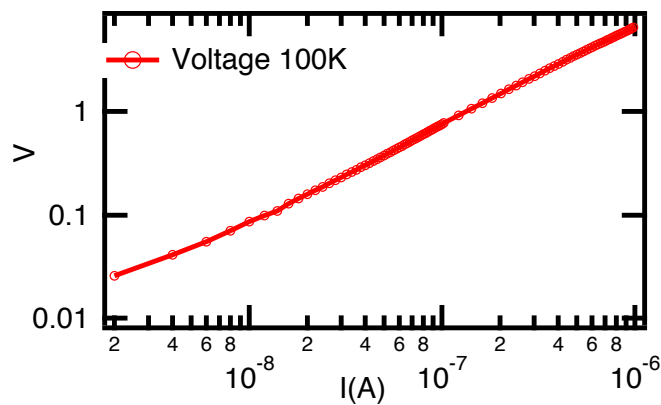
Figure 7.6: V(I) measurements at 100K for PCMO x=0.5

In figure 7.7 we show a resistivity curve of sample PCMO x=0.4. One sees the large increase in resistivity at low temperature, but no sign of a transition around the expected CO phase transition at 220K. From a plot of ln(R) versus 1/T one can determine the T_{CO} with a change it the curves slope. Figure 7.7b shows no change in the slope of the curve. Now Nelson and collaborators reported the occurrence of the CO/OO ordering without a clear step in the resistivity data. To get a direct information of a charge ordering one has to perform resonant diffraction experiments.

Figure 7.7: Resistivity curves of PCMO x=0.4 sample. No sign of a CO transition at T=220K or 1/T=0.0045 K^{-1} is observed

7.3.1.3   Crystallographic information of the thin film

The film is considered of good quality in the sense that the epitaxy is well realized, as seen from the in-plane lattice parameters, and the direction of the (110) direction of the 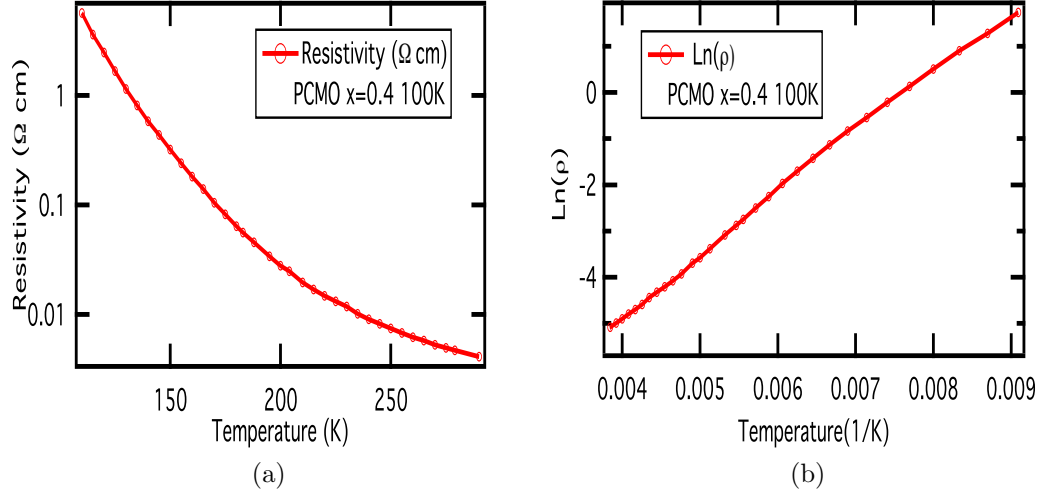film that is parallel to the (001) direction of the substrate. We observed the fringes related to the finite thickness of the manganite thin film, and evaluated it to about 70 nm (Fig. 7.8).

Alignments on several main Bragg reflections during the experiment allowed to estimate the lattice parameters. At 10K, using the reflections (300), (400), (330) and (222), the lattice parameters were obtained using the software of the beamline:

$$
\begin{aligned}
a &= 5.420 \text{ Å} \\
b &= 5.405 \text{ Å} \\
c &= 7.611 \text{ Å} \\
\gamma &= 88.511°
\end{aligned}
$$

No uncertainty was calculated, we will take these values as indicative. The difference between the a and b parameters is surprising. At first we considered them to be equal, and indeed we never found evidence of a double $(h00)/(0h0)$ reflections, for instance around the (400) reflection such difference in the a and b values could give two reflections separated by about 0.2 degree in the Bragg angle. We do not have the room temperature lattice parameters
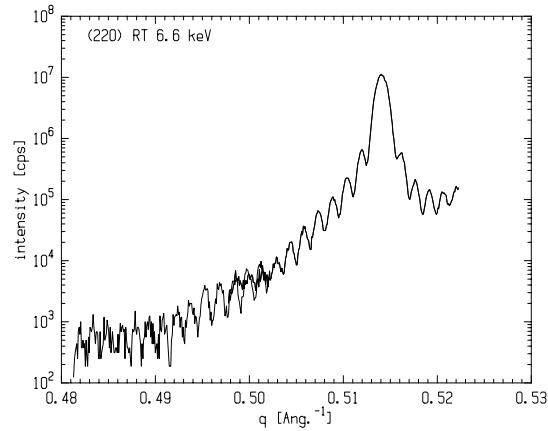
Figure 7.8: Sample $Pr_{0.6}Ca_{0.4}MnO_3$ on LAO. (220) reflection at room temperature and 6.6 keV showing the fringes due to the limited thickness of the thin film, indicating a thickness of about 70 nm. Above 0.52 nm^{-1} the intensity increases again because of the (002) reflection of the substrate.
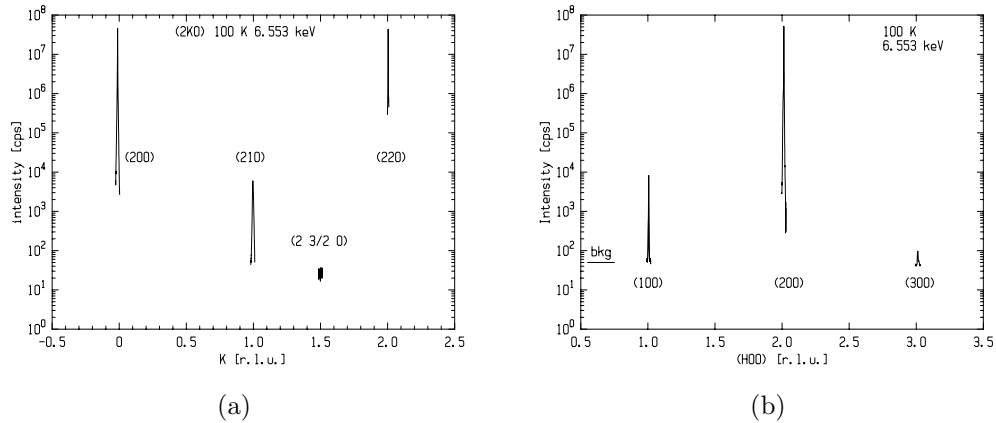
Figure 7.9: Sample $Pr_{0.6}Ca_{0.4}MnO_3$ on LAO. Reflections along the (a)(2K0) and along the (b) (H00) at 100K and resonant energy 6.553 keV showing thin film reflections at integer positions (100) (210) and (300), but not at half positions as expected for an orbitally ordered structure (only the $(2\frac{3}{2}0)$ position is shown). All these reflections are observable off resonance energy. The (300) is hardly above the background level.

because most of the beamtime was dedicated to finding reflections in the low temperature phase, once the Be windows were put into place, and the cryostat was cooled down. We note that the c parameter corresponds to twice

the in-plane value of the substrate, about 3.80 Å. These values at 10K can be compared to the bulk values of the same doping, which are significantly larger: The film is constrained in all three directions. We also see that, in the bulk, the c value undergoes a huge change from the non-ordered phase to the ordered phase. In the film, the c value is constrained to a value that would reduce the stability of the electronic orders. The γ angle however significantly departs from 90°.

7.3.1.4   In search for superstructure reflections

At all temperature, we found $(100)/(010)$-type reflections, but we did not find any $(0\frac{1}{2}0)$ reflections (Fig. 7.9). The $(100)/(010)$-type reflections are four to six orders of magnitude weaker than the main Bragg reflection, counting less than one hundred cps for the (300) reflection, see Table 7.3. It tells that in order to perform a thorough study of the superstructure reflections, a beam-line on an insertion device is mandatory, which makes the Cristal beamline the only one possible in France after the closure of the ID20 beamline of the ESRF. We note also that we get less counts than Nelson *et al.* by an order of magnitude on the (300) reflection. It is not straightforward to compare though, the beamlines (9ID at the APS) are different and their sample was also three times thicker which would account for the difference in counting.

Table 7.3: Orders of magnitude in the intensities of the reflections observed at the Cristal beamline, with relative intensities.

Reflections	Type of reflection	I_{obs} (cps)	I_{rel}
(220)	Main Bragg	$5\ 10^7$	1
(200)	Main Bragg	$5\ 10^7$	≈ 1
(222)	Main Bragg	10^6	$2\ 10^{-2}$
(330)	Main Bragg	$5\ 10^5$	10^{-2}
(400)	Main Bragg	$5\ 10^5$	10^{-2}
(310)	Main Bragg	10^5	$2\ 10^{-3}$
(221)	Main Bragg	10^4	$2\ 10^{-4}$
(210)	Thin film	$5\ 10^3$	10^{-4}
(100)	Thin film	$5\ 10^3$	10^{-4}
(300)	Thin film	10^2	$2\ 10^{-6}$

7.3.1.5 Energy scans

The energy scans gave us an important information: a confirmation that the sample is not in the ordered checkerboard phase as the bulk can be. Figure (7.10) shows an energy line shape that has little energy dependence. It can absolutely not be compared with what Nelson *et al.* have measured on their film at the same temperatures. The main result is that there seems to be a single Mn atom site, even down to the lowest temperature measured, about 10 K, even though the resistivity increases by orders of magnitude.
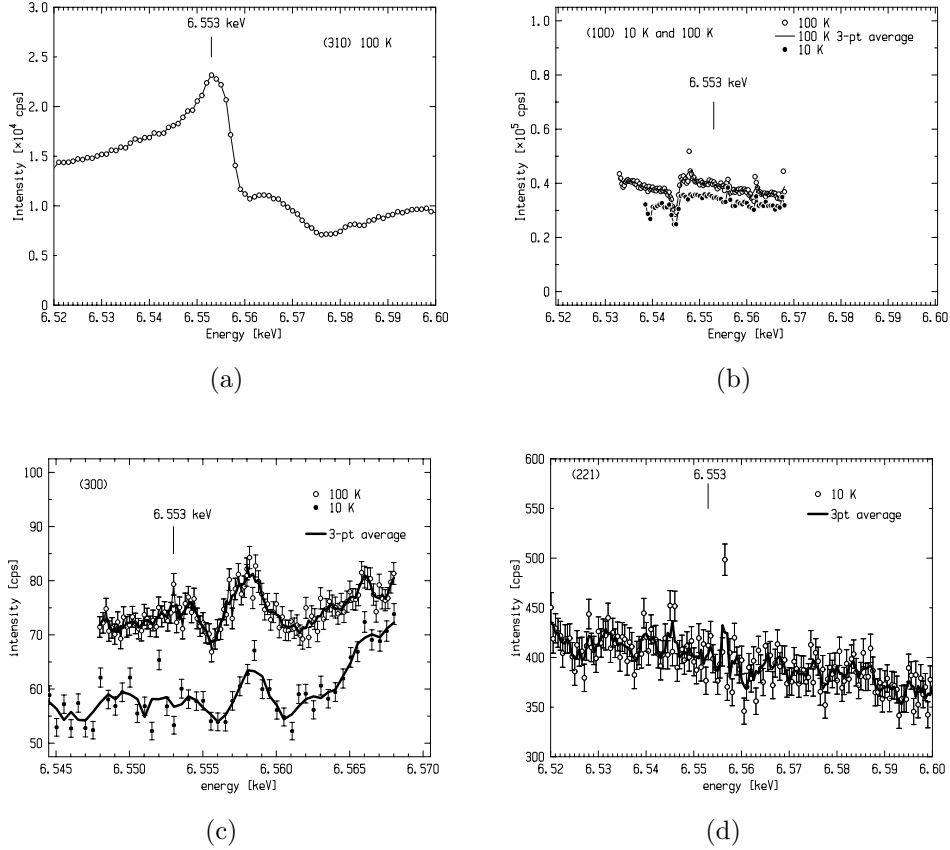
Figure 7.10: Sample $Pr_{0.6}Ca_{0.4}MnO_3$ on LAO. (a) Energy scan of the main bragg (310) reflection. A clear resonant is seen at this reflection. This is however a normal line shape, expected for the bulk material. (b) Energy scan of thin film (100) reflection. No resonant signal is seen, the anomaly lower than the edge, around 6.545 keV is probably due to multiple scattering. (c) Energy scan of thin film (300) reflection. Although very faint, we believe that the line shape is similar to the one measured by Nelson *et al.* at 240 K, see Fig. 7.4. (d) Energy scan of the main bragg (221) reflection, again without sign of differing Mn atoms. All in all, we believe that the sample at 100K and 10K is not in a charge and orbitally ordered phase.

7.3.1.6   Conclusion for the $Pr_{0.6}Ca_{0.4}MnO_3$ sample

The 70 nm thick $Pr_{0.6}Ca_{0.4}MnO_3$ thin film on LAO shows a high resistivity as if it were in an electronically, charge and orbitally ordered antiferromagnetic insulating phase. However, it does not show any resonant x-ray scattering spectroscopic sign of a checkerboard order of Jahn-Teller distorted manganese

octahedra, as observed in the same but thicker sample (250 nm) by Nelson *et al.* and in the bulk system as observed by several groups. Therefore we could say that in thin 75nm thick PCMO x=0.5 samples there is on charge or orbital ordering. If the resistivity increases, we believe it is not because of a long range order of charges or of distortions. It doesn't mean the octahedra are regular down to low temperature. Distortions could exist, but they are not ordered, or at least not ordered like they are in the bulk material, along the (100) and (010) directions.

7.3.2 Results on $Pr_{0.5}Ca_{0.5}MnO_3$/LAO

7.3.2.1 The sample

The sample was a 240 nm thick $Pr_{0.5}Ca_{0.5}MnO_3$ thin film on $LaAlO_3$, labeled "5832L". This sample was used in a number of other experiments, in particular in the studies performed by S. de Brion at the LCMI in Grenoble by Electron Spin Resonance measurements, *e.g.* [19]. In this latter study, it was found that the sample forms two phases, the ordered antiferromagnetic one, and a ferromagnetic phase. We will refer to this sample as PCMO x=0.5.
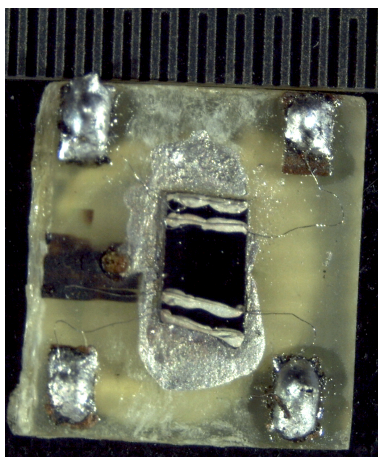

Figure 7.11: Sample PCMO x=0.5. It is seen here on the insulating plate used for the x-ray experiment with the four contacts and the Pt wires. The black mark on the left is a x-ray burn from ID20. The sample whose substrate had been thinned, was accidentally destroyed during a subsequent laboratory experiment.

7.3.2.2 The experiments

The data presented here were taken at the D2AM beamline of the ESRF. As explained in the 'Tools' section, we had used the 7 circle diffractometer which is now replaced by a Kappa diffractometer.

7.3.2.3 The I(V) and R(T) data

Here we show four point current voltage measurements of the PCMO x=0.5 sample. In figure 7.12a there are four I(V) curves at different temperatures with the applied current axis on logarithmic scale to point out the high resistance of the sample at low temperature. The maximum possible applied current is defined by the compliance of the nanovoltmeter. The fit of the linear part at 100K gives a value for the resistance of R $= 2.096 \times 10^6 \pm 7.5 \times 10^3$ Ω and a resistivity of $\rho = 50.28\Omega$cm.
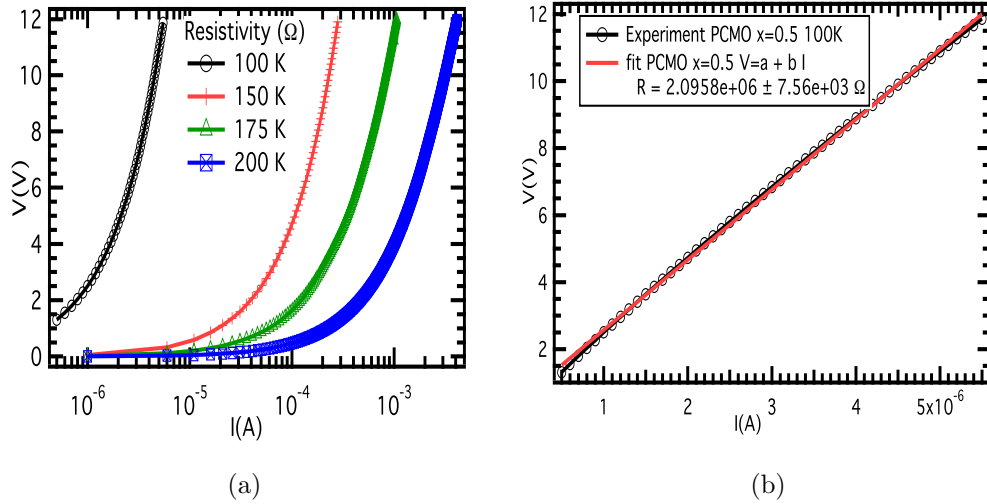
Figure 7.12: V(I) measurements at 100K for PCMO x=0.5 (a) the total curve (b) fit of the linear part to evaluate the resistivity.

Figure 7.13 shows a resistivity curve of PCMO x=0.5 sample. This measurement were made with different values of the applied currents I $= 10^{-7}$, 5×10^{-7}, I $= 10^{-6}$ and I $= 10^{-5}$A because of the large change of its resistivity with temperature. No sign of a CO transition appears in our resistivity experimental data. The figure 7.13b shows a $\log(\rho)$ versus $1/T$ plot where no signature of a CO appears either. In addition, with thin films the signal can be mask from the substrate or from another competing phases. Again, a direct determination is to use x-ray resonant diffraction.
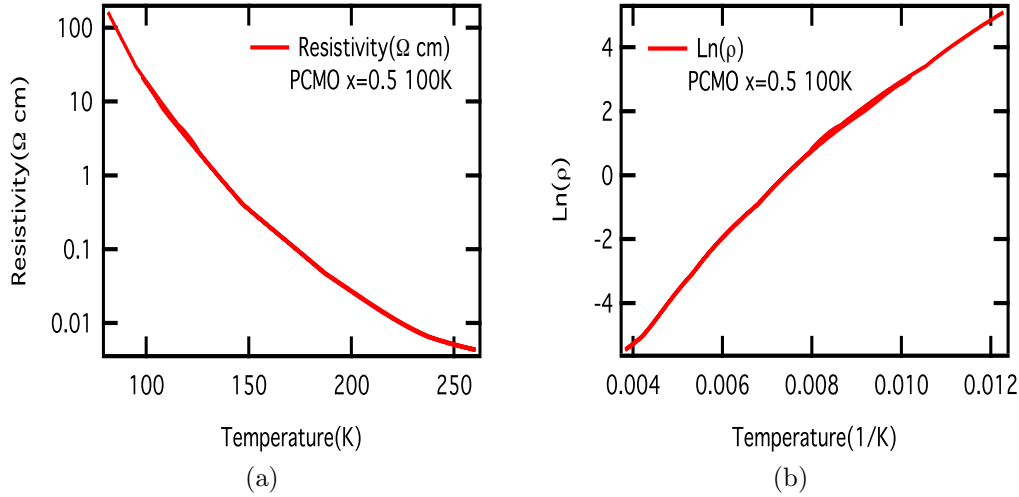
Figure 7.13: Resistivity curves of PCMO x=0.5 sample. No sign of any CO transition at T=220K or 1/T=0.0045 K^{-1} is observed.

7.3.2.4 The diffraction data (without applied current)

We observed reflections whose relative intensities are consistent with those measured at the Cristal beamline. We have seen the (200) with an intensity in the 10^4 cps range, and the (100) reflection in the 10^1 cps range thus with a relative intensity of 1 to 10^{-3} as seen on Cristal. We observe however a loss in intensity of 3 orders of magnitude at the D2AM beamline. This is of course explained first by the x-ray source, a bending magnet on D2AM, an undulator on Cristal, but also by the optics on D2AM (mirrors and monochromator) that have aged and that are planned to be replaced by 2013. The two samples are different, the larger thickness of the present sample should favored higher diffracted intensities.

We clearly found the (100) reflection, but not the (300) reflection. Considering the three orders of magnitude loss of the intensity on the (100), it is not surprising to not see the (300) reflection at the D2AM beamline. We also found another incommensurate superstructure reflection at (2 1.433 0). This latter reflection was also seen off resonance but with less intensity. In order to identify this incommensurate reflection to the manganite film, we looked for the $(2\ 2 - 0.443\ 0)$ reflection. We found however a large multiple-scattering reflection around this position which obscured the zone. The resonance spectra was not conclusive either because of the low counting rate of the reflection. We would therefore consider this reflection as a possible but not certain incommensurate reflection of the manganite thin film. We

nevertheless measured the dependence with the applied current of both reflections.

7.3.2.5   The diffraction data with applied current

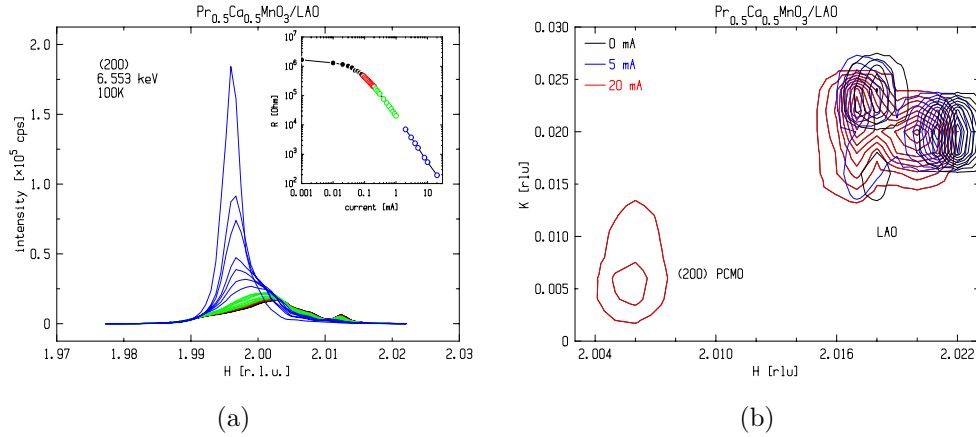(a)   (b)

Figure 7.14: (a) Intensity of the main bragg (200) reflection with applied current. The color code in the resistivity correspond to different regions in the reflection line shape. The strongest corresponds to the 20 mA applied current. (b) Intensity near the PCMO (200) reflection and the substrate reflection, with applied current, illustrating the heating by the applied current.

In Fig. 7.14a, we see the intensity line shape of the (200) reflection with various applied currents. We observe three regimes, one where the resistance is slowly decreasing, from 1 μA to about $20\mu A$ with nearly no change in the intensity line shape, a second one from about $20\mu A$ to the range about $200\mu A$ where the resistivity shows a stiffer decrease, but without significant change in the intensity or position of the reflections. and a third regime where the resistivity keeps decreasing at the same rate than in the second regime while the reflection changes in intensity and in position. The color code in the resistivity corresponds to different regions in the reflection line shape, the strongest intensity corresponds to the 20 mA applied current.

The third regime is of course ascribed to Joule heating. We have another hint in the heating of the sample by looking equivalently at the line shape of a reflection of the substrate. In Fig. 7.14b the change in the substrate peak position clearly shows that the heating by currents in the mA range has an effect in the crystallography of the substrate, with an increase in the lattice parameter as the reflection moves toward lower reciprocal space position.

Now, the sample seems to be heated above an applied current of 1 mA. We came however to a surprising observation indeed: two superstructure reflections had no change in position nor in intensity with the applied current. The figures in 7.15 show the (100) and the (2 1.433 0) reflections with none and several applied current including the maximal applied value. This is of course counter intuitive if the sample is supposed to be in thermal equilibrium. We are sure that the (100) does come from the thin film, and is not some scattered photon from the substrate or the Be domes. First, it is positioned exactly where expected, the orientation matrix of the sample in the diffractometer was reliable as to find any reflections at demand. Second, the energy dependence was measured, as shown in the following, showing the expected dependence of the position with the Bragg law and the expected anomaly at the Mn K-edge resonance [3]. We are therefore confident that the (100) reflection does not change with the applied current.

(a)   (b)
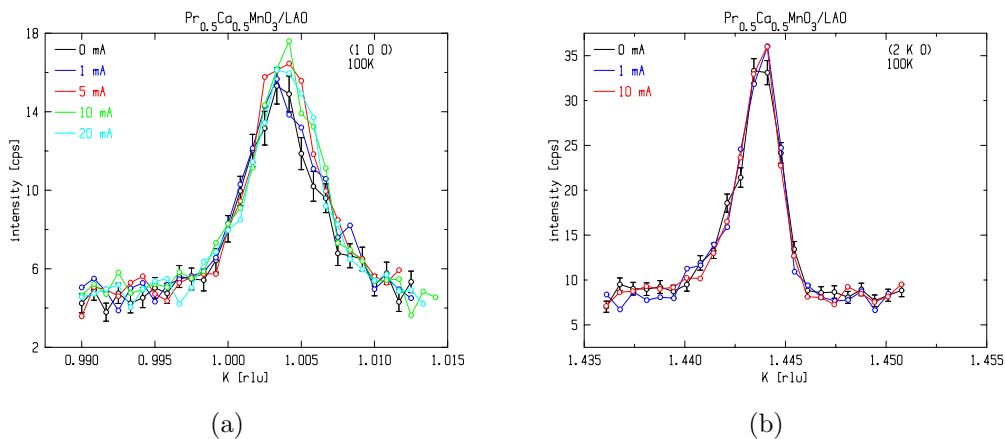
Figure 7.15: Intensity of the PCMO thin film (100) and superstructure (2 1.433 0) reflections with applied current, illustrating no effect of heating. Sample $Pr_{0.5}Ca_{0.5}MnO_3$ "5832L".

7.3.2.6   Energy line shape with applied current

First, we see that the energy line shape of the (100) reflection Fig. 7.16a is different for this sample than for the sample presented in the previous section Fig. 7.10b. Here we observe a signal that has the signature of the checkerboard order as seen in bulk materials [3]. The application of a current have not given any change in the energy line shape for the (100) reflection. Fig. 7.16b shows the resonant spectra of the (310) reflection for two applied
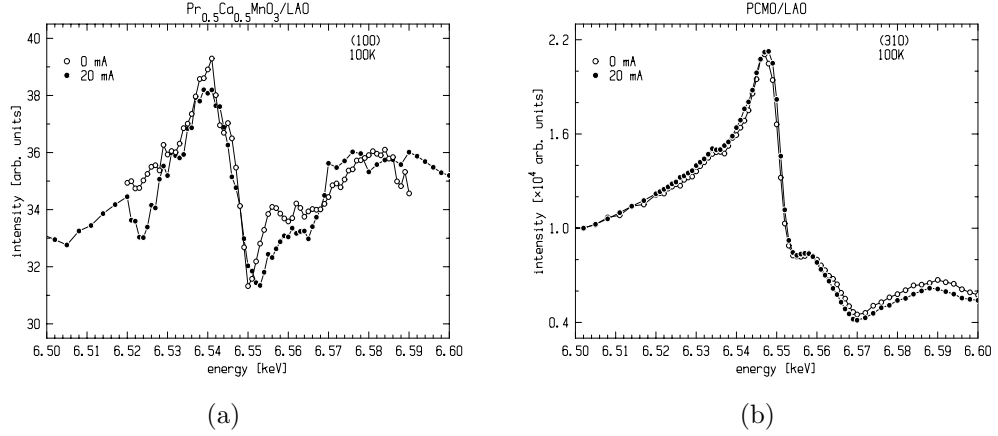
Figure 7.16: (a) Resonant spectra of the PCMO x=0.5 thin film refelction (100) without an applied current and a 20 mA applied current. (b) Resonant spectra of the main bragg (310) reflection without an applied current and a 20 mA applied current, the spectra have been rescaled and superposed.

currents. In this case too, the spectra are essentially unchanged meaning that the local crystallographic sites are unchanged for the Mn atoms when the current is applied. At the largest applied current, we are certainly in the non-linear regime of the resistivity, at least because of Joule heating.

7.3.2.7 Conclusion for the $Pr_{0.5}Ca_{0.5}MnO_3$ sample

The resistivity measurements on this sample do not show any sight of a ordered phase. In this sample we observed superstructure peaks that may be due to CO/OO: their position and their spectroscopic signature corresponds to a CO/OO phase. We observed an intriguing behavior of the reflection intensity with the applied current of these peaks. One possibility is that the (100) reflection measured does not see a change in the crystallographic structure when heated, or is not heated at all. This last possibility is unlikely because we expect some thermal equilibrium to occur within the thin sample and the substrate. We do not have a satisfactory explanation at this point.

7.4 Conclusion

In this chapter we have studied PCMO x=0.5 and PCMO x=0.4 samples which we expected to have a charge ordered phase. We have only seen superstructure peaks with a spectroscopic signal in the PCMO x=0.5 sample.

This may be related to the thickness of the manganite layer. At the interface the strain induced by the substrate is maximum and then the layer relaxes getting closer and closer to the bulk state. Of course this is a very rude explanation, but one can imagine that in thicker layers as PCMO x=0.5 (250nm) and Nelson's (240nm) the CO/OO phase appears at the top. On the contrary a very thin layer as PCMO x=0.4 (75nm) the layer it is not sufficiently relaxed to show a CO/OO phase.

This activity has left us with some mixed feelings. On one hand, we have learned how to perform these experiments of RXD characterization of electronically ordered and other CDW materials under applied current, from the installation of the current and voltage sources with their soft control, to the four contact set-up on the samples adapted to the x-ray scattering geometry, and low temperature. On the other hand the interpretation of the results is far from being complete. Like other authors we have to separate the effects of Joule heating and the real non-linear transport properties of the manganites. To this aim pulse current source could be a solution.

Nevertheless, and to the best of our knowledge, these resonant x-ray diffraction experiments under applied electrical current were the first intended on manganites. We believe that RXD could be an interesting technique in order to probe both the structural changes that are simultaneous to an electronic phase transition under applied current. In our particular case, we recognized a problem with the growth and the characterization of the samples. If measurements of magnetization, lab reflectivity and resistivity are necessary prior to the synchrotron experiments, it appears that the ultimate characterization can only be performed at the beamline, where we discover whether the sample is in an ordered phase or not, or in a mixed phase. In the case of manganites, a strong resistivity does not necessarily mean a long range order of charge and orbitals. We need to find a step in the resistivity and an anomaly in the magnetization which should show antiferromagnetism. Both measurements are not straightforward with thin films, with which signals from the substrate and from another competing phase can cover the signal from the phase we are interested in.

Bibliography

[1] Goodenough, "Theory of the Role of Covalence in the Perovskite-Type Manganites [La, M(II)]MnO3," *Physical Review B*, vol. 100, p. 564, 1955.

[2] H. Kuwahara, Y. Tomioka, A. Asamitsu, Y. Moritomo, and Y. Tokura, "A first-order phase transition induced by a magnetic field," *Science*, vol. 270, 1995.

[3] S. Grenier, J. P. Hill, D. Gibbs, J. K. Thomas, M. v. Zimmermann, C. S. Nelson, Y. Tokura, Y. Tomioka, D. Casa, T. Gog, and C. Venkataraman, "Resonant Diffraction study of the colossal-magnetoresistant $Pr_{0.6}Ca_{0.4}MnO_3$," *Physical Review B*, vol. 69, p. 134419, 2004.

[4] R. J. Goff and J. P. Attfield, "Charge ordering in half-doped manganites," *Physical Review B (Condensed Matter and Materials Physics)*, vol. 70, no. 14, p. 140404, 2004.

[5] A. Daoud-Aladine, J. Rodríguez-Carvajal, L. Pinsard-Gaudart, M. T. Fernández-Díaz, and A. Revcolevschi, "Zener polaron ordering in half-doped manganites," *Phys. Rev. Lett.*, vol. 89, p. 097205, Aug 2002.

[6] D. V. Efremov, J. van den Brink, and D. I. Khomskii, "Bond- versus site-centered ordering and possible ferroelectricity in manganites," *Nature Materials*, vol. 3, pp. 853–856, 2004.

[7] A. Wahl, S. Mercone, A. Pautrat, M. Pollet, C. Simon, and D. Sedmidubsky, "Nonlinear electrical response in a charge/orbital ordered $Pr_{0.63}Ca_{0.37}MnO_3$ crystal : The charge density wave analogy," *Physical Review B*, vol. 68, p. 9, 2003.

[8] S. Cox, J. Singleton, R.D.McDonald, A. Migliori, and P. Littlewood, "Sliding charge density wave in manganites," *Nature Materials*, vol. 7, no. 25, 2008.

[9] B. Fisher, J. Genossar, L. Patlagan, S. Kar-Narayan, X. Moya, D. Snchez, P. A. Midgley, and N. D. Mathur, "The absence of charge-density-wave sliding in epitaxial charge-ordered $Pr_{0.48}Ca_{0.52}MnO_3$ films," *Journal of Physics: Condensed Matter*, vol. 22, no. 27, p. 275602, 2010.

[10] P. Padhan, W. Prellier, C. Simon, and R. C. Budhani, "Current-induced metallic behavior in $Pr_{0.5}Ca_{0.5}MnO_3$ thin films: Competition between Joule heating and nonlinear conduction mechanisms," *Phys. Rev. B*, vol. 70, p. 134403, Oct 2004.

[11] S. Mercone, R. Fresard, V. Caignaert, C. Martin, D. Saurel, C. Simon, G. André, P. Monod, F. Fauth, C. Casa, D. Venkataraman, and T. Gog, "Nonlinear effects and Joule heating in I-V curves in manganites," *Journal of Applied Physics*, vol. 98, Aug 2005.

[12] A. Guha, A. K. Raychaudhuri, A. R. Raju, and C. N. R. Rao, "Nonlinear conduction in charge-ordered $Pr_{0.63}Ca_{0.37}MnO_3$: Effect of magnetic fields," *Phys. Rev. B*, vol. 62, pp. 5320–5323, Sep 2000.

[13] A. Guha, N. Khare, A. K. Raychaudhuri, and C. N. R. Rao, "Magnetic field resulting from nonlinear electrical transport in single crystals of charge-ordered $Pr_{0.63}Ca_{0.37}MnO_3$," *Phys. Rev. B*, vol. 62, pp. R11941–R11944, Nov 2000.

[14] C. Nelson, J. Hill, D. Gibbs, M. Rajeswari, M. Biswas, R. Shinde, S. Greene, T. Venkatesan, A. Millis, F. Yokaichiya, C. Giles, C. Casa, D. Venkataraman, and T. Gog, "Substrate-induced strain effects on Pr0.6Ca0.4MnO3 films," *Journal of Physics: Condensed Matter*, vol. 16, pp. 13–27, 2004.

[15] Z. Jirák, S. Krupicka, Z. Simsa, M. Dlouhá, and S. Vratislav, "Neutron diffraction study of $Pr_{1-x}Ca_xMnO_3$ perovskites," *Journal of Magnetism and Magnetic Materials*, vol. 53, pp. 153–166, 1985.

[16] E. E. Rodriguez, T. Proffen, A. Llobet, J. J. Rhyne, and J. F. Mitchell, "Neutron diffraction study of average and local structure in $La_{0.5}Ca_{0.5}MnO_3$," *Physical Review B (Condensed Matter and Materials Physics)*, vol. 71, no. 10, p. 104430, 2005.

[17] P. G. Radaelli, D. E. Cox, M. Marezio, and S.-W. Cheong, "Charge, orbital and magnetic ordering in $La_{0.5}Ca_{0.5}MnO_3$," *Physical Review B*, vol. 55, p. 3015, 1997.

[18] A. Haghiri-Gosnet, M. Hervieu, C. Simon, B. Mercey, and B. Raveau, "Charge ordering in $Pr_{0.5}Ca_{0.5}MnO_3$ thin films: A new form initiated by strain effects of $LaAlO_3$ substrate," *Journal of Applied Physics*, vol. 88, p. 3545, 2000.

[19] S. de Brion, G. Chouteau, A. Janossy, R. Rauwel Buzin, and W. Prellier, "Magnetic phase diagram in the charge-ordered $Pr_{0.5}Ca_{0.5}MnO_3$ strained thin films," *Journal of Magnetism and Magnetic Materials*, pp. 450–451, 2003.

Chapter 8

Tools for resonant X-ray diffraction

8.1   Introduction

In this chapter we show different experimental and theoretical tools that allow to perform resonant x-ray diffraction (RXD) studies. We first show some of the beamlines and diffractometers in european synchrotrons and then we show a program for the calculation of spectroscopic signatures, FDMNES. FDMNES code allows to perform simulations of either absorption or RXD experiments. It gives the electronic structure from the crystal structure and it allows to use different approximations and multipolar developments.

For the RXD experiments we need a high flux monochromatic beam with different polarization states. Synchrotrons are circular electron accelerators that create these high intensity x-rays of which the energy can be tuned and their polarization well defined. The x-ray sources are either Bending Magnets (BM) or Insertion Devices (ID). In a BM a magnetic field curves the trajectory of the electrons to emit an EM radiation with linear polarization. In an ID several magnets are aligned and the radiation emitted by the electrons is very intense and the polarization can be chosen to be linear or circular. For an ID beamline in the soft x-ray range the incident angle at the monochromator is small, then one can keep the polarization state of the incoming x-ray see table 3.1. In the hard x-ray range the incoming angle at the monochromator is much higher and therefore one cannot keep a circular polarized beam. To overcome this problem, the incident linear polarised radiation can be converted into circular polarisation using quarter phase-plates. These phase plates are very much used in hard- x ray diffraction beamlines. To have a broader overview of a synchrotron we propose the reader the book [1]. RXD experiments require a diffractometer as well as the possibility to scan the energy in a precise way. In the next section we present some european beamlines that fulfill these conditions.

8.1.1   Resonant x-ray scattering beamlines

The table:8.1 lists soft and hard x-ray beamlines from European synchrotrons that allow to perform RXD experiments. Here we mention the main characteristics of the beamlines, later we precise the possibilities of each beamline.

Most of the hard x-ray beamlines have commercial diffractometers. These diffractometers can be divided into two main groups: the ones constructed according to an Eulerian referential and the so called *Kappa* diffractometers. The main difference between these two types of diffractometers is that *Kappa* diffractometers have a large sample environment space. Most of the new hard-x ray beamlines have a *kappa* diffractometer and even old ones as D2AM

Table 8.1: Beamlines that allow to perform soft or hard RXD experiments.

Beamline	Source	Diffractometers	Synchrotron	Energy
D2AM	BM	Kappa(euler*)	ESRF	Hard x-ray
ID20**	ID	euler	ESRF	Hard x-ray
XMaS	BM	euler	ESRF	Hard x-ray
Cristal	ID	Kappa	SOLEIL	Hard x-ray
I16	ID	Kappa	Diamond	Hard x-ray
Sextants	ID	Home made	SOLEIL	Soft-x-ray
I06	ID	Home made	Diamond	Soft x-ray
magnetic reflectometer	ID	Home made	Bessy	Soft x-ray

*In our experiments we used an eulerian diffractometer.
Now there is a *Kappa* diffractometer.
** ID20 beamline was closed in sep2011   .

replace old Euler diffractometers also called 6-circle diffractometers for new kappa ones.

Soft x-ray diffractometers are very different from hard x-ray diffractometers. This is because soft x-ray are absorbed by the air and they can only be used in vacuum. This makes soft x-ray chamber more complex to handle and also this restricts the sample environment and the degrees of freedom the diffractometer will have.

The sample environment in each diffractometer is specific to the beamline. Here we note the sample environments of the diffractometers used during this thesis. A more detailed description of the beamlines can be found in the synchrotron internet pages.

D2AM: It is a french Cooperative Research Group (CRG) beamline. The Kappa diffractometer does not have a cryostat yet. RXD experiments at low temperature are therefore not possible at the D2AM beamline anymore. The detection is performed by a CCD or a photomultiplier.

XMas Xmas is hard x-ray British CRG at the ESRF. They have a commercial Huber diffractometer with a cryostat and polarization analyzers. The linear polarization is converted into circular by a phase- plate. They even have the so-called flipper in order to improve the signal-to-noise ratio for the XMCD measurements (both C^+ and C^- are used.)

ID20:   This beamline was closed in 2011. However during this thesis we performed one experiment there. The sample environment allowed to cool down and it was possible to apply a magnetic field and an electric field. With the polarization analyzers, this beamline was the ideal beamline to perform resonant magnetic hard x-ray scattering experiments.

Cristal: This beamline is not dedicated to RXD experiments, but it is very well suited to perform such experiments. In the *kappa* diffractometer it is possible to cool down the sample with a displex cryostat, apply an electric field/current, heat it and even apply a pressure. For the detection they have photomultipliers, 1D, as well as a CCD. In this beamline it is possible to perform coherent imaging experiments.

I16:   I16 is a hard x-ray beamline at Diamond Light Source dedicated to magnetism and material science. They have a diamond crystal phase retarder to convert the linearly polarized X-ray beam to circular polarisation. The large 6-circle kappa diffractometer supports several sample stages, giving temperatures down to 4-6 K and up to 800K. There is a wide variety of detectors including a Pilatus 100K photon-counting pixel detector.

I10:RASOR   This is the soft x-ray reflectivity-diffraction chamber at diamond light source. It has a cryostat which allows to cool down to around 15K. There are polarization analyzers and the sample holder allows to apply an electric field or electric current. The detection is done by a photodiode or by a channeltron. For more information see [2].

2circle diffractometer: This is a soft x-ray small diffractometer at Diamond Light Source. It only has two motorized rotation θ and 2θ. All other displacements are manual (x, y, z, χ). The main advantage of this chamber is that it allows to heat up to 460°C.

Magnetic reflectometer: It is a reflectometer to study reflectivity and absorption experiments at Bessy. It has a temperature range 28-480K , the magnetic coils are outside the chamber and the field inside is 260mT. There is full 360° azimuthal rotation. The main reflected detection is done by a diode, there is also an absorption detection TEY, and a fluorescence detection, for more information see [3].

Sextants:RESOXS   This diffractometer allows to perform reflectivity and diffraction experiments under applied magnetic and electric field and at low

temperature. Part of this thesis has been to work on the development of a new sample holder for this soft x-ray diffractometer RESOXS. In the next section we present the chamber more in detail.

8.2 Application of an electric current: hard x-ray scattering experiments

One part of this thesis has been to perform hard RXD experiments under an applied electric current. We performed 4 point measurements (apply a current and measure the voltage) at low temperature. Four point measurements are specially suited for low resistivity samples and to eliminate the impedance from the wires, contacts... In our case this will be very useful since during the measurements there are sometimes 15 m long wires and contacts on the sample may be of poor quality. The low temperature conditions demands a cryostat with four electric wires coming out. These wires are connected to a 2182 Keithley current source and 6221 Keithley nanovoltmeter. These Keithleys are remotely controlled by a Labview program written by Frederic Gay from the Inst. Néel. The connection scheme is shown in figure 8.1.
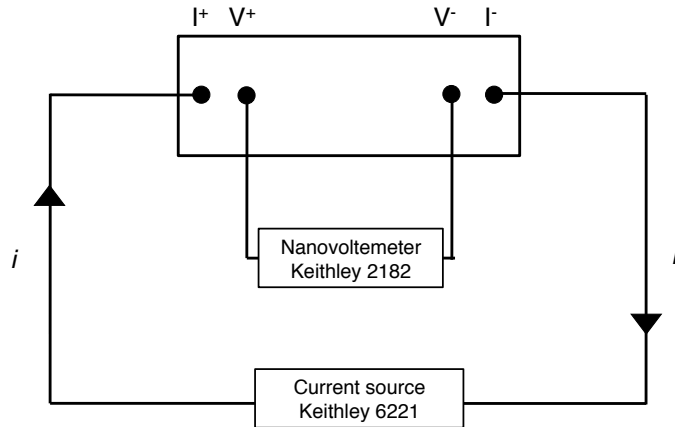
Figure 8.1: Schema of the electric connections set-up

Resonant hard x-ray scattering experiments with applied electric current were performed at three beamlines: ID20, Cristal and D2AM. The computer that controls the Keithley was in the control room and since in hard x-ray beamlines the experimental room is surrounded by lead one needs to have 4 wires passing through the walls. These are the four wires connected to the sample and they come from the cryostat. In ID20 beamline the set up was all

ready, the 4 wires from the cryostat as well as the connection to the control room. For Cristal beamline the four wires inside the cryostat were mounted and the wires coming to the control room were installed at out arrival. On the contrary for D2AM, the old cryostat (it is out of use now) did not have four wires and they had to be mounted specially for our experiment by S.Arnaud the engineer assistant. The connection from the experimental room to the control room was made by usb ports. The application of an electric current on the sample during the experiments was always a success.

The electrical contacts on the sample were done using stycast Epoxy glue which is a good thermal and electrical conductor. The density of this glue allows to make electrical contacts as show in Fig. 8.2. Nowadays, with techniques as lithography one makes clean and very precise electrical contacts. For our diffraction experiments we decided to try to make lithography contacts, but unfortunately one of our samples broke during the process. At this stage we have not tried to make any other lithography contacts.
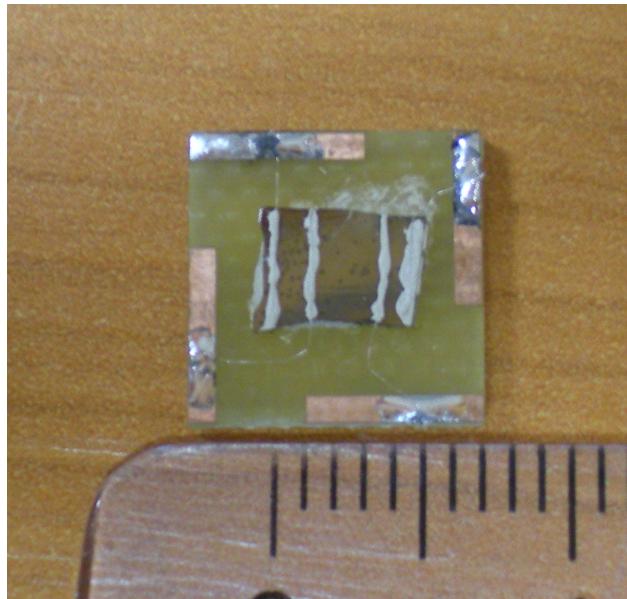

Figure 8.2: Photo of a PCMO thin film with the four sticast contacts.

8.2.1   RESOXS endstation: soft x-ray diffractometer

RESOXS is a ultra high vacuum (UHV) diffractometer at Sextants beamline in Synchrotron SOLEIL. It was designed and built at the Néel Institut by the SERAS and N. Jaouen and J.M Tonnerre and is managed by J.M. Tonnerre

at the Néel Institut and Nicolas Jaouen at SOLEIL. It allows to perform reflectivity and diffraction experiments and it was designed for the study of magnetic materials. It was one of the first soft x-ray chamber to have magnetic coils inside allowing to apply a magnetic field. In the past years, the research of the effect of applied electric fields/currents has attired the attention of many scientists. In this context our group decided to design and build a new sample holder that would allow to apply an electric field/current as well as to read the drain current from absorption.

This development become a part of this thesis. Here we present the choices made for the materials and the design. One has to keep in mind that since RESOXS is a UHV chamber any modification within the chamber demands a big amount of work and one has to use a very specific type of materials due to the vacuum and other parameters as magnetic field or temperature. Before presenting the new sample holder we briefly present RESOXS Fig.8.3.

RESOXS diffractometer is a soft x-ray chamber with two main parts. The bottom part holds the detector and a differentially pumped rotary seal. This is the so called 2θ assembly. The top part carries the sample holder, a cryostat system and a electromagnet as well as a differentially pumped rotary seal. For precise alignment of the chamber in the beam a new motorized support has recently been constructed. Further details of the chamber can be found in the paper [4] or at Soleil.

The materials used in the sample holder had to support both high and low temperatures and be amagnetic. The chamber is at low temperature during the experiments and therefore the properties of the wires have to be stable in a large range of temperature. The materials have to support high temperatures up to 100° because of the baking. In ultra high vacuum, the chamber have to be heated to outgas the inner part. This chamber is very much used to perform magnetic scattering measurements and one has to ensure that the materials inside the chamber do not move when the field is applied.

With all this under consideration we have developed a sample holder shown in Fig. 8.4.The new system for the sample holder consists of two main parts. The sample holder which is where the sample is glued is removable to the outside, and the cold finger part which remains inside the chamber. The system rotates ±180° giving a full azimuthal degree of freedom. To have this freedom the fixed part has three main parts, a cold finger made of copper (2) Fig.8.4 for good thermal contact, a rotating ring made of inox 304L(3) Fig.8.4 and a non rotating ring (4) Fig.8.4 made of a bronze nuance of PAN WBz 8 compatible with ultra high vacuum.
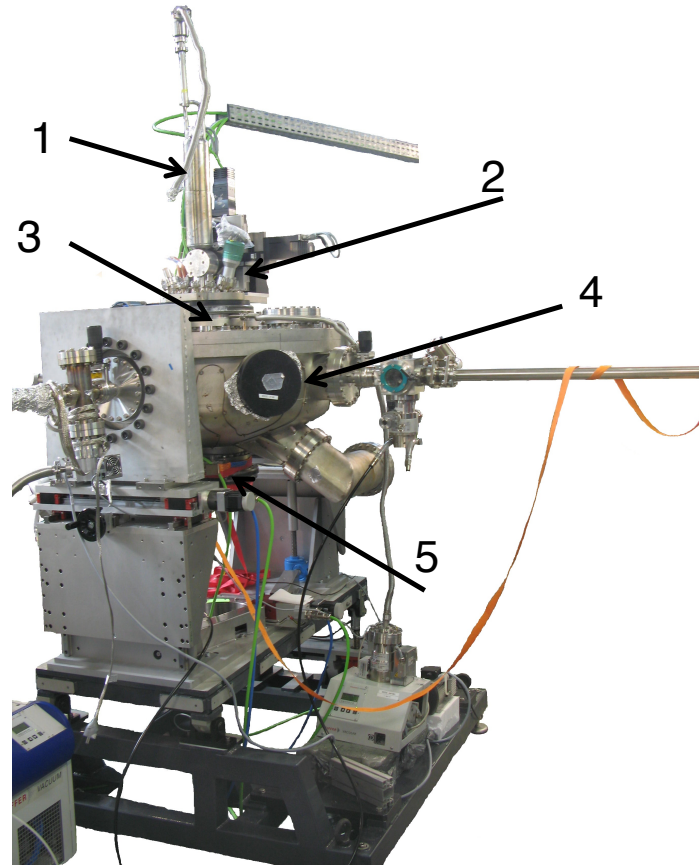
Figure 8.3: RESOXS diffractometer in the new support designed during this thesis. (1) cryostat, (2) top flange with x, y, z motors (3)differentially pumped rotary seal (θ motor), (4) bottom flange, (5) differentially pumped rotary seal (2θ motor).

In the picture the sample holder is upside down and it is possible to see six male pins (5) (Fig.8.4). These pins are tin-gold plated and their female counterpart are in the rotating ring (fixed inside the chamber) (7) Fig.8.4. These are the pins that allow the the electrical contact. The other two bigger pins are to help the transfer and to avoid damage of the electrical pins (6) Fig.8.4.

Figure 8.5 is a picture of the system mounted inside the diffractometer. The wires from the rotating ring are made of Constatan, a copper-nickel alloy. Since the system rotates $\pm 180 deg$ these wires are thin and flexible enough

Figure 8.4: New set-up for sample holder with electrical contacts. (1) Temperature sensor cap (2) cold finger (3) Rotating Ring (4) Non-Rotating ring, (5) male electrical pins, (6) transfer pins, (7) female electrical pins. with two 0.9 mm screws fixed on the cold finger.
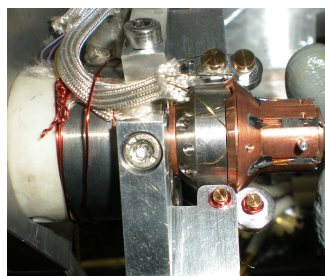
Figure 8.5: New set-up for sample holder in place inside the diffractometer.

to allow the azimuthal rotation. The wires are insulated and their resistivity is constant over a wide range of temperature. These six wires coming from the rotating ring are guided to a PEEK subminiature-C connector. From this connector to the air-vacuum feedthrough there is a UHV ribbon cable assembly, Kapton insulated, with PEEK subminiature-C connectors on both ends.

In chapter 6, we show the electric field application of this set up, where we applied 30kV/cm and recorded the reflectivity on and off field.

8.3   Theoretical tool: FDMNES

To support and explain resonant scattering experiments one needs theoretical simulations. The FDMNES program [5] calculates the spectra of different spectroscopies related to the real or virtual absorption of x-ray in material. It gives the absorption cross sections of photons around the ionization edge, that is in the energy range of XANES in the EXAFS. The calculations can be performed with all conditions of rectilinear or circular polarizations. In the same way, it calculates the structure factors and intensities of resonant x-ray diffraction spectra. One simulates not only diffraction spectra but also azimuthal scans very much used in resonant scattering to study orbital ordering for example.

One of the main characteristics of FDMNES is that it uses two techniques of fully relativistic monoelectronic calculations. The first one is based on the Finite Difference Method (FDM) to solve the Schrödinger equation. In that way the shape of the potential is free and in particular avoid the muffin-tin approximation. The second one uses the Green formalism (multiple scattering) on a muffin-tin potential. This approach can be less precise but is faster.

FDMNES uses monoelecronic calculations and it is very well suited for the calculations of delocalized states: K edges for light elements as transition metals and L edges of heavy element as Pt. For this reason especially with transition metal oxides the program is very much used for the K edges (see chapter 5). In these compounds the $3d$ orbitals are very localized and the simulations of the $L_{2,3}$ edges it is not easy. Multi electronic calculations are used for the calculations of localized electronic states. Yves Joly and Oana Bunau have developed a multi-electronic extension using the Time-Dependant DFT with a local kernel for FDMNES.

In chapter we show more in detail how to use FDMNES with some interesting results on ferroelectric thin films.

Bibliography

[1] Jens Als-Nielsen and Des McMorrow. *Elements of Modern X-Ray Physics*. Wiley, 2001.

[2] T. A. W. Beale, T. P. A. Hase, T. Iida, and K. et al. Endo. Rasor: An advanced instrument for soft x-ray reflectivity and diffraction. *Review of Scientific Instruments*, 81, 2010.

[3] S. Brck, S. Bauknecht, B. Ludescher, and E. Goering. An advanced magnetic reflectometer. *rsi*, 79(9), Aug 1999.

[4] N. Jaouen, J-M. Tonnerre, G. Kapoujian, P. Taunier, J-P. Roux, D. Raoux, and F. Sirotti. An apparatus for temperature-dependent soft x-ray resonant magnetic scattering. *jsr*, 11:363, 2004.

[5] Y. Joly. X-ray absorption near-edge structure calculations beyond the muffin-tin approximation. *Phys. Rev. B*, 63:125120, 2001.

Chapter 9

Conclusion

9.1   Conclusion

In this thesis I have developed a formalism to simulate reflectivity of stratified systems, simulated absorption and diffraction spectra of complex ferroelectric domains, worked at the improvement of a soft X-ray diffractometer and studied three different systems with resonant X-ray diffraction.

The resonant X-ray reflectivity formalism has been based on a boundary propagation method developed on an eigenwaves basis. We have applied this formalism to a magnetic system and to a system that shows an anisotropy along the normal axis. The formalism was implemented in a Matlab environment. It can simulate the reflectivity with different polarization states as well as Kerr measurements.

Very thin films of $PbTiO_3$ on $DyScO_3$ substrates show exotic ferroelectric phases and domain structures. Results have been obtained on a 30 nm-thick sample, for which a reflectivity refinement showed that the first 9 nm of this film were damaged. We have combined hard X-ray resonant scattering measurements and FDMNES simulations to obtain the ferroelectric domain structure and the ferroelectric polarization of these systems. The similarity between simulations and experiments confirms that RXD can successfully address nanostructured ferroelectrics and solve the polar displacements in ferroelectric unit cells.

We have evidenced a magnetic coupling between a soft ferromagnetic Co layer and a single crystal of the multiferroic $BiFeO_3$ with soft X-ray resonant magnetic scattering. We have observed the incommensurate structure that the BFO cycloids imprint onto the Co layer. With our results and simulations of the Co and BFO magnetization we propose a model for the distorted magnetic structure on the Co layer, in the form of a wriggle. XRMS experiments have been performed on monodomain FE crystals, with application of an electric field for the first-time utilization of the new sample holder developed during the thesis. We have also studied BFO multidomain FE single crystals with X-PEEM with no ferromagnetic layer deposited on top. A correlation between FE and AFM domains as well as the existence of several AFM domains in one same FE domain have been observed.

Our last systems were thin films of $Pr_{1-x}Ca_xMnO_3$ on LAO with $x = 0.4$ and $x = 0.5$. Both systems were supposed to show charge ordering which may be explained by Charge Density Wave and be related to charge order based multiferroicity. We have performed hard X-ray experiments on these systems with a set up to apply electric field *in situ*. No conclusive results have been obtained since some intriguing behaviours have been observed in the intensity of the peaks under applied electric current. To our knowledge, it was the first time that RXD experiments were performed with an injected

current.

At last, I have given a general overview of resonant X-ray scattering in Europe. Since the closure of ID20 at the ESRF, the possibilities to perform resonant scattering experiments in Europe have decreased. In spite of this, Insertion device beamlines such as Cristal at SOLEIL, and I16 at Diamond Light Source still allow to perform RXD experiments. In the soft X-ray range, many diffractometers are being created or improved. I have especially been involved in the improvement of RESOXS diffractometer and the development of a new sample holder that allows to apply an electric field down to $10\,K$.

The RXD thesis was also started in the framework of fundamental research to find new techniques for data storage. Systems with bulk BFO, such as the one studied in this thesis, are not suited for data storage because of ferroelectric domains building up. For this reason, multilayers with thin layer BFO are more promising candidates. Our experimental achievements with Resonant X-ray Diffraction open the possibility to study the magnetic coupling in such systems, which is a key point for research & development towards Multiferroic Random Access Memories.

This technique has to be combined with simulations along with other experiments to provide complementary information: microscopy techniques, transport measurements, magnetic measurements and many others. In my opinion, resonant experiments under applied electric current/fields have a very promising future. More and more scientists study the effect of currents on systems and along with the chemical and spatial selectivity that RXD offers many fundamental challenges could be answered. Specially in the field of multiferroicity.

Appendix A

Anisotropy ratios

A.1   Intensities with linear polarizations

We first look at the anisotropies for linear polarization. The polarization of the incoming beam is almost always known, but to know the polarization of the diffracted beam we need polarization analyzers in the synchrotrons. This is not always possible, or with difficulty, especially in the soft x-ray regime. For this reason here we calculate the intensities diffracted for a σ and π incident beam:

$$
\begin{aligned}
I^u_{\sigma \to \sigma + \pi} =& |F_0|^2 + |F_1|^2 (u_y \cos\theta + u_z \sin\theta)^2 \\
& + |F_2|^2 u_x^2 (u_x^2 + (u_y \sin\theta - u_z \cos\theta)^2) \\
& + \mathrm{Re}\{F_0 F_2^*\} 2 u_x^2 \\
& + \mathrm{Im}\{F_1 F_2^*\} u_x [(u_z^2 - u_y^2) \sin 2\theta + 2 u_y u_z \cos 2\theta] \\
I^u_{\pi \to \sigma + \pi} =& |F_0|^2 \cos^2 2\theta + |F_1|^2 (u_x^2 \sin^2 2\theta + (u_y \cos\theta - u_z \sin\theta)^2) \\
& + |F_2|^2 [(u_y^2 \sin^2\theta - u_z^2 \cos^2\theta)^2 + u_x^2 (u_y \sin\theta + u_z \cos\theta)^2] \\
& + \mathrm{Im}\{F_0 F_1^*\} u_x \sin 4\theta \\
& - 2\mathrm{Re}\{F_0 F_2^*\} (u_y^2 \sin^2\theta - u_z^2 \cos^2\theta) \cos 2\theta \\
& - \mathrm{Im}\{F_1 F_2^*\} u_x [(u_y^2 - u_z^2) \sin 2\theta + 2 u_y u_z] \cos 2\theta
\end{aligned}
\tag{A.1}
$$

A.1.1   Anisotropy ratio: fixed magnetization inverting the polarization

Once the intensities are calculated, we can follow to calculate the anisotropy ratio. For a fixed direction of the applied magnetic field $\pm u$, the two reflectivity measurements are done with two different incoming photon polarizations σ and π.

The ratio is given by:

$$
R^{\pm u \text{ fixed}}_{\sigma - \pi} = \frac{I^{\pm u}_\sigma - I^{\pm u}_\pi}{I^{\pm u}_\sigma + I^{\pm u}_\pi}
\tag{A.2}
$$

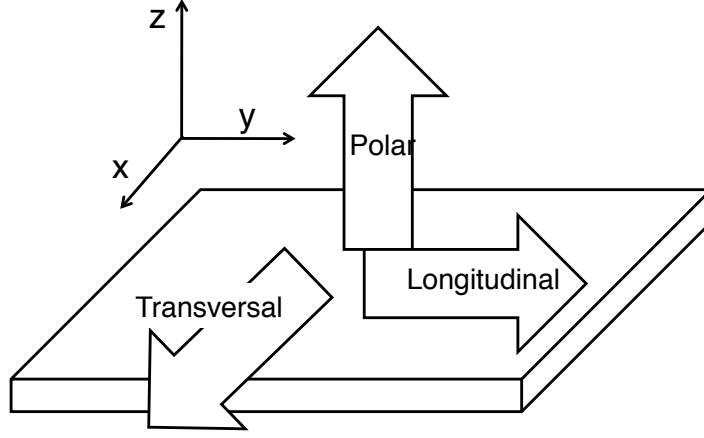- **Transverse geometry** applying the field along the x direction one

Figure A.1: Definition of the transversal, longitudinal and polar directions.

gets an anisotropy of:

$$
R_{\sigma-\pi}^{\pm u} =
$$

$$
\frac{|F_0|^2 \sin^2 2\theta - |F_1|^2 u_x^2 \sin^2 2\theta + |F_2|^2 u_x^4 + 2\mathrm{Re}\{F_0 F_2^*\} u_x^2 \mp \mathrm{Im}\{F_0 F_1^*\} u_x \sin 4\theta}{|F_0|^2 (1 + \cos^2 2\theta) + |F_1|^2 u_x^2 \sin^2 2\theta + |F_2|^2 u_x^4 + 2\mathrm{Re}\{F_0 F_2^*\} u_x^2 \pm \mathrm{Im}\{F_0 F_1^*\} u_x \sin 4\theta}
$$

$$(A.3)$$

In this configuration one only has an angular dependence to the first order of the magnetic term (F_1) with its maximun at $\theta = \pi/8$. There is also a constant contribution from the uniaxial term (F_2).

• If one looks at the ratio with a field applied along the y direction the anisotropy ratio in the **longitudinal geometry** is:

$$
R_{\sigma-\pi}^{\pm u} = \frac{|F_0|^2 \sin^2 2\theta + u_y^2 \sin^2 \theta (2\mathrm{Re}\{F_0 F_2^*\} \cos 2\theta - |F_2|^2 u_y^2 \sin^2 \theta)}{|F_0|^2 (1 + \cos^2 2\theta) + 2|F_1|^2 u_y^2 \cos^2 \theta - 2\mathrm{Re}\{F_0 F_2^*\} u_y^2 \cos 2\theta \sin^2 \theta + |F_2|^2 u_y^4 \sin^4 \theta}
$$

$$(A.4)$$

In this configuration one is only sensitive to a uniaxial anisotropy F_2 in the y direction and the contribution will be the largest at small angles.

• And with the **polar geometry** we have:

$$
R_{\sigma-\pi}^{\pm u} = \frac{|F_0|^2 \sin^2 2\theta - |F_2|^2 u_z^2 \cos^2 \theta - 2\mathrm{Re}\{F_0 F_2^*\} u_z^2 \cos 2\theta \cos^2 \theta}{|F_0|^2 (1 + \cos^2 2\theta) + 2|F_1|^2 u_z^2 \sin^2 \theta + |F_2|^2 u_z^2 \cos^2 \theta + 2\mathrm{Re}\{F_0 F_2^*\} u_z^2 \cos 2\theta \cos^2 \theta}
$$

$$(A.5)$$

With the polar configuration one measures the out-of-plane component of the magnetization at low angles (terms wit $\cos \theta$).

A.1.2 Anisotropy ratio: fixed polarization inverting the magnetization

Now let's look at the anisotropy ratio for a fix photon polarization inverting the applied field. The ratio for σ incident light is given by:

$$R_\sigma = \frac{I_\sigma^u - I_\sigma^{-u}}{I_\sigma^u + I_\sigma^{-u}}$$

$$= \frac{\operatorname{Im}\{F_1 F_2^*\} u_x [(u_z^2 - u_y^2) \sin 2\theta + 2 u_y u_z \cos 2\theta]}{|F_0|^2 + |F_1|^2 (u_y \cos\theta + u_z \sin\theta)^2 + |F_2|^2 (u_x^4 + u_x^2 (u_z \cos\theta - u_y \sin\theta)^2) + 2\operatorname{Re}\{F_0 F_2^*\} u_x^2}$$

For the incident π light one gets:

$$R_\pi = \frac{I_\pi^u - I_\pi^{-u}}{I_\pi^u + I_\pi^{-u}}$$

with

$$
\begin{aligned}
I_\pi^u - I_\pi^{-u} &= 2\operatorname{Im}\{F_0 F_1^*\} u_x \sin 4\theta \\
&\quad -2\operatorname{Im}\{F_1 F_2^*\} u_x \cos 2\theta (\sin^2\theta(u_y^2 - u_z^2) + 2 u_y u_z)
\end{aligned}
$$

and

$$
\begin{aligned}
I_\pi^u + I_\pi^{-u} &= 2|F_0|^2 \cos^2 2\theta \\
&\quad + 2|F_1|^2 (u_x^2 \sin^2 2\theta + (u_y \cos\theta - u_z \sin\theta)^2) \\
&\quad + 2|F_2|^2 ((u_y^2 \sin^2\theta + u_z^2 \cos^2\theta) + u_x^2 (u_y \sin\theta + u_z \cos\theta)^2) \\
&\quad - 4\operatorname{Re}\{F_0 F_2^*\} (u_y^2 \sin^2\theta - u_z^2 \cos^2\theta) \qquad\qquad \text{(A.6)}
\end{aligned}
$$

In the experiments one privileges one direction for the applied field. Looking again at the three configurations for σ and π one gets:

$$
\begin{aligned}
R_\sigma^{\text{LONG}} &= R_\sigma^{\text{TRANS}} = R_\sigma^{\text{POL}} = R_\pi^{\text{LONG}} = R_\pi^{\text{POL}} = 0 \\
R_\pi^{\text{TRANS}} &= \frac{\operatorname{Im}\{F_0 F_1^*\} u_x \sin 4\theta}{|F_0|^2 \cos^2 2\theta + |F_1|^2 u_x^2 \sin^2 2\theta}
\end{aligned}
$$

Therefore, reversing the applied field with σ polarization it is not useful since one will not get any information. However, with π polarization and reversing the applied field in the x direction one gets the information of the magnetic anisotropy along this direction. Noteworthy, this signal will be maximum at $\theta = \pi/8$.

A.2 Intensities with circular polarization

Circular polarized light is very used in soft x-ray experiments. We will see that with these polarizations one is mainly but not only sensitive to the magnetic anisotropy. With the right experimental configuration it is easy to distinguish between the out-of-plane and in-plane components of the magnetization.

A.2.1 Anisotropy ratio: fixed polar polarization inverting the magnetization

Let's first consider the anisotropy ratio calculated by inverting the applied field with a given photon polarization. The ratio between two opposite directions of the anisotropy, for one fixed incident polarization ($C_\pm$) is :

$$R_{C\pm}^{u\ inv} = \frac{I_{C\pm}^{+u} - I_{C\pm}^{-u}}{I_{C\pm}^{+u} + I_{C\pm}^{-u}} \tag{A.7}$$

with

$$
\begin{aligned}
I_{C\pm}^{+u} - I_{C\pm}^{-u} = {}& \pm 4\mathrm{Re}\{F_0 F_1^*\}(u_y \cos^3\theta - u_z \sin^3\theta) + \mathrm{Im}\{F_0 F_1^*\}u_x \sin 4\theta \\
& + 2\mathrm{Im}\{F_1 F_2^*\}u_x \sin 2\theta (u_x^2 + u_y^2 + u_z^2 \sin^2\theta) \\
& \pm 4\mathrm{Re}\{F_1 F_2^*\}(u_y \cos\theta + u_z \sin\theta)(-u_x^2 \cos 2\theta + u_y^2 \sin^2\theta - u_z^2 \cos^2\theta))
\end{aligned}
$$

and

$$
\begin{aligned}
I_{C\pm}^{+u} + I_{C\pm}^{-u} = {}& 2|F_0|^2(\cos^4\theta + \sin^4\theta) \\
& + |F_1|^2(u_x^2 \sin^2 2\theta + 2u_y^2 \cos^2\theta + 2u_z^2 \sin^2\theta) \\
& + |F_2|^2(u_x^4 + u_y^2 \sin^4\theta + u_z^4 \cos^4\theta \\
& + 2u_x^2 u_z^2 \cos^2\theta - 2u_y^2 u_z^2 \sin^2\theta \cos^2\theta + 2u_x^2 u_y^2 \sin^2\theta) \\
& + 4\mathrm{Re}\{F_0 F_2^*(-u_y^2 \sin^2\theta + u_z^2 \cos^2\theta \pm iu_x u_y \sin\theta \mp iu_x u_z \cos\theta)\}
\end{aligned}
$$

- For a **transversal configuration** the anisotropy ratio is:

$$R_{C\pm}^{\mathrm{u\ inv\ TRANS}} = \frac{\mathrm{Im}\{F_0 F_1^*\}u_x \sin 4\theta + 2\mathrm{Im}\{F_1 F_2^*\}u_x^3 \sin 2\theta}{2|F_0|^2(\cos^4\theta + \sin^4\theta) + |F_1|^2 u_x^2 \sin^2 2\theta + |F_2|^2 u_x^4}$$

In this configuration one will have a signal from the x component of the magnetization with its maximum at $\theta = \pi/8$. In the case of a spin-orbit coupling

term (F_2) it would appear at $\theta = \pi/4$.

- For a **longitudinal configuration** the anisotropy is:

$$R_{C\pm}^{\text{u inv LONG}} = \frac{\pm 2\text{Re}\{F_0 F_1^*\} u_y \cos^3\theta \pm 4\text{Re}\{F_1 F_2^*\} u_y^3 \cos\theta \sin^2\theta}{|F_0|^2(\cos^4\theta + \sin^4\theta) + |F_1|^2 u_y^2 \cos^2\theta + |F_2|^2 u_y^2 \sin^4\theta - 4\text{Re}\{F_0 F_2^*\} u_y^2 \sin^2\theta}$$

At small angles, one is sensible to the y component of the magnetization (F_1). with the maximum at $\theta = \pi/4$.

- Finally, with the **polar configuration** one gets:

$$R_{C\pm}^{\text{u inv POL}} = \frac{\mp 2\text{Re}\{F_0 F_1^*\} u_z \sin^3\theta \mp 4\text{Re}\{F_1 F_2^*\} u_z^3 \cos^2\theta \sin\theta}{|F_0|^2(\cos^4\theta + \sin^4\theta) + |F_1|^2 u_z^2 \sin^2\theta + 4\text{Re}\{F_0 F_2^*\} u_z^2 \cos^2\theta}$$

Here at higher angle one will have a magnetic contribution of the out-of-plane contribution.

It is important to point out that the $R_{C\pm}^{\text{u inv POL}}$ and $R_{C\pm}^{\text{u inv LONG}}$ terms have very similar expressions. They both depend on $u_{y,z}$ with $\cos^3\theta$ or $\sin^3\theta$. This resemblance make these two ratios a very good choice to study the y and z components of magnetization and compare them.

A.2.2 Anisotropy ratio: fixed magnetization inverting photon polarization

The ratio between two incident circular polarizations, with the magnetization fixed is given by:

$$R_{C_+ - C_-}^{\pm u \text{ fixed}} = \frac{I_{C_+}^{\pm u} - I_{C_-}^{\pm u}}{I_{C_+}^{\pm u} + I_{C_-}^{\pm u}} \tag{A.8}$$

$$
\begin{aligned}
I_{C_+}^{\pm u} - I_{C_-}^{\pm u} = {}& \pm 4\mathrm{Re}\{F_0 F_1^*\}(u_y \cos^3\theta - u_z \sin^3\theta) \\
& -4\mathrm{Im}\{F_0 F_2^*\}u_x(u_y\cos\theta + u_z\sin\theta)\sin 2\theta \\
& \pm 2\mathrm{Re}\{F_1 F_2^*\}[-u_y^3\cos\theta\sin^2\theta + u_z^3\sin\theta\cos^2\theta \\
& + u_x^2\cos 2\theta(u_y\cos\theta + u_z\sin\theta) \\
& + u_y u_z^2\cos^3\theta - u_z u_y^2\sin^3\theta] \qquad\qquad\text{(A.9)}
\end{aligned}
$$

$$
\begin{aligned}
I_{C_+}^{\pm u} + I_{C_-}^{\pm u} = {}& 2|F_0|^2(\cos^4\theta + \sin^4\theta) \\
& + |F_1|^2(u_x^2\sin^2 2\theta + 2u_y^2\cos^2\theta + 2u_z^2\sin^2\theta) \\
& + |F_2|^2(2u_x^4 + 2u_y^4\sin^4\theta + 2u_z^4\cos^4\theta + 4u_x^2 u_z^2\cos^2\theta \\
& \qquad - 4u_y^2 u_z^2\cos^2\theta\sin^2\theta + 4u_x^2 u_y^2\sin^2\theta) \\
& \pm \mathrm{Im}\{F_0 F_1^*\}u_x\sin 4\theta \\
& + 2\mathrm{Re}\{F_0 F_2^*\}(u_x^2 - \cos 2\theta(u_y^2\sin^2\theta - u_z^2\cos^2\theta)) \\
& \mp 2\mathrm{Im}\{F_1 F_2^*\}u_x\sin 2\theta(u_y^2\cos^2\theta + u_z^2\sin^2\theta) \qquad\text{(A.10)}
\end{aligned}
$$

Before writing down the particular cases lets have a look at $I_{C_+}^{\pm u} - I_{C_-}^{\pm u}$. Here the term $4\mathrm{Im}\{F_0 F_2^*\}u_x(u_y\cos\theta + u_z\sin\theta)\sin 2\theta$ is very interesting because it has only $F_0 F_2$ and it is dependent of the angle θ. In the community a circular dichroism is associated most of the time to a magnetic order, but here we see that this it is not mandatory: There will be a dichroic term in case of a non zero F_2, for instance due to a local structural anisotropy. This is suspected in a recent measurement on Fe_3O_4 magnetite [?].

The asymmetry relation for the three particular cases are:
• In the **Transversal configuration**, one has

$$
R^{\pm u\ \text{TRANS}} = 0
$$

There is no information from the transversal configuration.

• In the **longitudinal configuration**

$$
R^{\pm u\ \text{LONG}} = \frac{\pm 2\mathrm{Re}\{F_0 F_1^*\}u_y\cos^3\theta \mp \mathrm{Re}\{F_1 F_2^*\}u_y^3\cos\theta\sin^2\theta}{|F_0|^2(\cos^4\theta + \sin^4\theta) + |F_1|^2 u_y^2\cos^2\theta - \mathrm{Re}\{F_0 F_2^*\}u_y^2\sin^2\theta\cos 2\theta + |F_2|^2 u_y^4\sin^4\theta}
$$

At small angles, one is sensitive to the y component of the magnetization (F_1) with its maximum at $\theta = \pi/4$.

- For the **polar configuration**

$$R^{\pm u \text{ POL}} = \frac{\mp 2\text{Re}\{F_0 F_1^*\} u_z \sin^3 \theta + \text{Re}\{F_1 F_2^*\} u_z \sin \theta \cos^2 \theta}{|F_0|^2 (\cos^4 \theta + \sin^4 \theta) + |F_1|^2 u_z^2 \sin^2 \theta + \text{Re}\{F_0 F_2^*\} u_z^2 \cos^2 \theta \cos 2\theta + |F_2|^2 u_z^4 \cos^4 \theta}$$

Here at higher angle one will have a magnetic contribution of the out-of-plane contribution.

One sees that $R_{C\pm}^{u\ inv}$ and $R_{C_+ - C_-}^{\pm u}$ give the same information in the polar and longitudinal cases. The case $R_{C\pm}^{\text{u inv POL}}$ seems like a good option to study the z component of the magnetization. However one has to consider that not many experimental soft x-ray UHV chambers allow to apply and switch a magnetic field in the out-of-plane direction.

Abstract

The aim of this thesis is to explore the capabilities offered by resonant X-ray scattering for the study of multiferroic systems with a special emphasis on the feasibility of such experiments under applied electric field/current.

Boundary propagation matrices formalism has been developed for the simulation of resonant reflectivity, using a set of eigenwaves as a basis for the computation.

Resonant X-ray experiments were performed on three transition metal oxides. This technique combines chemical selectivity and reciprocal space information, and was used on very thin films of $PbTiO_3$ to solve the atomic structure of a periodic pattern of ferroelectric domains. The spectroscopic signatures observed in our hard X-ray experiments are well reproduced with FDMNES ab-initio simulations of complex super cells. In the soft X-ray range, we studied the cycloidal antiferromagnetic structure of multiferroic $BiFeO_3$ and especially the imprint of the cycloid on a 10 nm-thin layer of Co deposited on top of the multiferroic bulk material. We also present an experiment in which we tried to explore the effect of an electrical current applied on a thin film of charge-ordered $Pr_{1-x}Ca_xMnO_3$.

Last part is dedicated to instrumentation. We summarize the state of the art of european synchrotron beamlines and diffractometers which can host resonant X-ray diffraction experiments. Finally, we detail a new sample holder that we developed and tested in the high-vacuum diffractometer RESOXS, which allows for the application of an electric field/current.

Keyword: Resonant scattering, Multiferroics, nanostructures, thin films, transition metal oxides.

Résumé

Le but de cette thèse est d'explorer la faisabilité d'expériences de diffraction résonante sur des systèmes multiferroïques et en particulier avec un champ/courant électrique appliqué.

Un formalisme de matrices de propagation a été développé pour simuler la réflectivité résonante, en utilisant un ensemble d'ondes propres comme base arithmétique pour le calcul.

Des expériences de diffraction résonante ont été menées sur trois oxides de métaux de transition. Cette technique combinant la selectivité chimique et la sensibilité à l'espace réciproque, elle a été utilisée sur des films très minces de $PbTiO_3$ pour étudier la structure atomique d'un agencement périodique de domaines ferroélectriques. La signatures spectroscopiques observées par nos expériences de diffraction X durs sont reproduites par des simulations ab-initio FDMNES de super-cellules complexes. Dans le domaine X mous, nous avons étudié la structure antiferromagnétique cycloïdale du multiferroïque $BiFeO_3$, et plus spécialement l'empreinte de la cycloïde sur une couche mince de Co déposée sur le matériau multiferroïque. Nous présentons également une expérience dans laquelle nous avons tenté d'explorer l'effet d'un courant électrique appliqué sur un film mince du composé à ordre de charge $Pr_{1-x}Ca_xMnO_3$.

La dernière partie est consacrée à l'instrumentation. Nous passons en revue les lignes synchrotron européennes et les diffractomètres qui permettent de faire des expériences de diffraction résonante de rayons X. Pour finir, nous détaillons un nouveau porte-échantillon que nous avons développé et testé sur le diffractomètre RESOXS, et qui permet d'appliquer un champ/courant électrique.

Mots-clés: Diffusion résonante, Rayons X, Multiferroïques, nanostructures, films minces, oxides métaux de transition.